

The background of the cover features a stylized brain composed of various colored segments (yellow, orange, red, purple, blue, green) arranged in a circular pattern. A network of white lines connects small dots, resembling a neural network or a mesh, overlaid on the brain segments. The top half of the cover has a solid blue background, while the bottom half is white.

OPTICAL NEURAL INTERFACES

EDITED BY: Massimo De Vittorio, Ferruccio Pisanello and John A. Assad
PUBLISHED IN: Frontiers in Neuroscience



frontiers

Frontiers Copyright Statement

© Copyright 2007-2019 Frontiers Media SA. All rights reserved.

All content included on this site, such as text, graphics, logos, button icons, images, video/audio clips, downloads, data compilations and software, is the property of or is licensed to Frontiers Media SA ("Frontiers") or its licensees and/or subcontractors. The copyright in the text of individual articles is the property of their respective authors, subject to a license granted to Frontiers.

The compilation of articles constituting this e-book, wherever published, as well as the compilation of all other content on this site, is the exclusive property of Frontiers. For the conditions for downloading and copying of e-books from Frontiers' website, please see the Terms for Website Use. If purchasing Frontiers e-books from other websites or sources, the conditions of the website concerned apply.

Images and graphics not forming part of user-contributed materials may not be downloaded or copied without permission.

Individual articles may be downloaded and reproduced in accordance with the principles of the CC-BY licence subject to any copyright or other notices. They may not be re-sold as an e-book.

As author or other contributor you grant a CC-BY licence to others to reproduce your articles, including any graphics and third-party materials supplied by you, in accordance with the Conditions for Website Use and subject to any copyright notices which you include in connection with your articles and materials.

All copyright, and all rights therein, are protected by national and international copyright laws.

The above represents a summary only. For the full conditions see the Conditions for Authors and the Conditions for Website Use.

ISSN 1664-8714

ISBN 978-2-88963-080-6

DOI 10.3389/978-2-88963-080-6

About Frontiers

Frontiers is more than just an open-access publisher of scholarly articles: it is a pioneering approach to the world of academia, radically improving the way scholarly research is managed. The grand vision of Frontiers is a world where all people have an equal opportunity to seek, share and generate knowledge. Frontiers provides immediate and permanent online open access to all its publications, but this alone is not enough to realize our grand goals.

Frontiers Journal Series

The Frontiers Journal Series is a multi-tier and interdisciplinary set of open-access, online journals, promising a paradigm shift from the current review, selection and dissemination processes in academic publishing. All Frontiers journals are driven by researchers for researchers; therefore, they constitute a service to the scholarly community. At the same time, the Frontiers Journal Series operates on a revolutionary invention, the tiered publishing system, initially addressing specific communities of scholars, and gradually climbing up to broader public understanding, thus serving the interests of the lay society, too.

Dedication to Quality

Each Frontiers article is a landmark of the highest quality, thanks to genuinely collaborative interactions between authors and review editors, who include some of the world's best academicians. Research must be certified by peers before entering a stream of knowledge that may eventually reach the public - and shape society; therefore, Frontiers only applies the most rigorous and unbiased reviews.

Frontiers revolutionizes research publishing by freely delivering the most outstanding research, evaluated with no bias from both the academic and social point of view. By applying the most advanced information technologies, Frontiers is catapulting scholarly publishing into a new generation.

What are Frontiers Research Topics?

Frontiers Research Topics are very popular trademarks of the Frontiers Journals Series: they are collections of at least ten articles, all centered on a particular subject. With their unique mix of varied contributions from Original Research to Review Articles, Frontiers Research Topics unify the most influential researchers, the latest key findings and historical advances in a hot research area! Find out more on how to host your own Frontiers Research Topic or contribute to one as an author by contacting the Frontiers Editorial Office: researchtopics@frontiersin.org

OPTICAL NEURAL INTERFACES

Topic Editors:

Massimo De Vittorio, Istituto Italiano di Tecnologia and Università del Salento, Italy

Ferruccio Pisanello, Istituto Italiano di Tecnologia, Italy

John A. Assad, Harvard Medical School, United States

Citation: De Vittorio, M., Pisanello, F., Assad, J. A., eds. (2019). Optical Neural Interfaces. Lausanne: Frontiers Media. doi: 10.3389/978-2-88963-080-6

Table of Contents

- 04 *The Three-Dimensional Signal Collection Field for Fiber Photometry in Brain Tissue***
Marco Pisanello, Filippo Pisano, Minsuk Hyun, Emanuela Maglie, Antonio Balena, Massimo De Vittorio, Bernardo L. Sabatini and Ferruccio Pisanello
- 20 *Optogenetic Light Sensors in Human Retinal Organoids***
Marcela Garita-Hernandez, Laure Guibbal, Lyes Tualbi, Fiona Routet, Antoine Chaffiol, Celine Winckler, Marylin Harinquet, Camille Robert, Stephane Fouquet, Sebastien Bellow, José-Alain Sahel, Olivier Goureau, Jens Duebel and Deniz Dalkara
- 32 *Tapered Fibers Combined With a Multi-Electrode Array for Optogenetics in Mouse Medial Prefrontal Cortex***
Leonardo Sileo, Sebastian H. Bitzenhofer, Barbara Spagnolo, Jastyn A. Pöpplau, Tobias Holzhammer, Marco Pisanello, Filippo Pisano, Elisa Bellistri, Emanuela Maglie, Massimo De Vittorio, Patrick Ruther, Ileana L. Hanganu-Opatz and Ferruccio Pisanello
- 42 *Microscale Inorganic LED Based Wireless Neural Systems for Chronic in vivo Optogenetics***
Raza Qazi, Choong Yeon Kim, Sang-Hyuk Byun and Jae-Woong Jeong
- 48 *Synthetic Light-Activated Ion Channels for Optogenetic Activation and Inhibition***
Sebastian Beck, Jing Yu-Strzelczyk, Dennis Pauls, Oana M. Constantin, Christine E. Gee, Nadine Ehmann, Robert J. Kittel, Georg Nagel and Shiqiang Gao
- 64 *High-Density μ LED-Based Optical Cochlear Implant With Improved Thermomechanical Behavior***
Eric Klein, Christian Gossler, Oliver Paul and Patrick Ruther
- 79 *Organelle Optogenetics: Direct Manipulation of Intracellular Ca^{2+} Dynamics by Light***
Toshifumi Asano, Hiroyuki Igarashi, Toru Ishizuka and Hiromu Yawo



The Three-Dimensional Signal Collection Field for Fiber Photometry in Brain Tissue

Marco Pisanello^{1†}, Filippo Pisano^{1†}, Minsuk Hyun^{2†}, Emanuela Maglie^{1,3}, Antonio Balena^{1,3}, Massimo De Vittorio^{1,3}, Bernardo L. Sabatini^{2*} and Ferruccio Pisanello^{1*}

¹ Istituto Italiano di Tecnologia, Center for Biomolecular Nanotechnologies, Lecce, Italy, ² Department of Neurobiology, Howard Hughes Medical Institute, Harvard Medical School, Boston, MA, United States, ³ Dipartimento di Ingegneria dell'Innovazione, Università del Salento, Lecce, Italy

OPEN ACCESS

Edited by:

Stephen Louis Macknik,
Sunny Downstate Medical Center,
United States

Reviewed by:

Daniel Benjamin Aharoni,
University of California, Los Angeles,
United States
Stéphane Dieudonné,
École Normale Supérieure, France

*Correspondence:

Marco Pisanello
marco.pisanello@iit.it
Bernardo L. Sabatini
bernardo_sabatini@hms.harvard.edu
Ferruccio Pisanello
ferruccio.pisanello@iit.it

[†]These authors have contributed
equally to this work

Specialty section:

This article was submitted to
Neural Technology,
a section of the journal
Frontiers in Neuroscience

Received: 12 August 2018

Accepted: 25 January 2019

Published: 26 February 2019

Citation:

Pisanello M, Pisano F, Hyun M,
Maglie E, Balena A, De Vittorio M,
Sabatini BL and Pisanello F (2019) The
Three-Dimensional Signal Collection
Field for Fiber Photometry in Brain
Tissue. *Front. Neurosci.* 13:82.
doi: 10.3389/fnins.2019.00082

Fiber photometry is used to monitor signals from fluorescent indicators in genetically-defined neural populations in behaving animals. Recently, fiber photometry has rapidly expanded and it now provides researchers with increasingly powerful means to record neural dynamics and neuromodulatory action. However, it is not clear how to select the optimal fiber optic given the constraints and goals of a particular experiment. Here, using combined confocal/2-photon microscope, we quantitatively characterize the fluorescence collection properties of various optical fibers in brain tissue. We show that the fiber size plays a major role in defining the volume of the optically sampled brain region, whereas numerical aperture impacts the total amount of collected signal and, marginally, the shape and size of the collection volume. We show that ~80% of the effective signal arises from 10^5 to $10^6 \mu\text{m}^3$ volume extending ~200 μm from the fiber facet for 200 μm core optical fibers. Together with analytical and ray tracing collection maps, our results reveal the light collection properties of different optical fibers in brain tissue, allowing for an accurate selection of the fibers for photometry and helping for a more precise interpretation of measurements in terms of sampled volume.

Keywords: fiber photometry, optogenetics, optical fibers, collection volumes, collection fields

INTRODUCTION

In the last decade, optogenetics has become widely used for optical control of neural activity (Miesenböck, 2009; Deisseroth, 2011; Häusser, 2014). Simultaneously, new implantable devices, mainly based on waveguides (Zorzos et al., 2012; Pisanello et al., 2014, 2017, 2018; Canales et al., 2015; Segev et al., 2016; Park et al., 2017; Pisano et al., 2018) or micro light emitting diodes (μLEDs) (Kim et al., 2013; McAlinden et al., 2013, 2015; Goffler et al., 2014; Wu et al., 2015; Scharf et al., 2016), have been developed for light delivery in the living brain. Recently these optical approaches have been extended to monitor neural circuits by detecting time-varying signals from diverse genetically-encoded fluorescent indicators of neural activity, neuromodulator action, and membrane potential (Fluhler et al., 1985; Loew, 1996; Miyawaki et al., 1997; Slovins et al., 2002; Petersen et al., 2003; Emiliani et al., 2015). While new devices utilizing integrated photodetectors and μLEDs have been described (Lu et al., 2018), traditional flat-cleaved optical fibers are broadly used for both triggering and collecting fluorescence *in vivo* in freely behaving animals.

This approach is typically referred to as fiber photometry (Lütcke et al., 2010; Grienberger et al., 2012; Cui et al., 2013, 2014; Stroh et al., 2013; Adelsberger et al., 2014; Gunaydin et al., 2014; Chen et al., 2015; Fuhrmann et al., 2015; Kim et al., 2016; Matthews et al., 2016; Nieh et al., 2016; Lovett-Barron et al., 2017; Muir et al., 2017; Schwalm et al., 2017; Selimbeyoglu et al., 2017; He et al., 2018; Luo et al., 2018; Meng et al., 2018; Simone et al., 2018).

While the influence of optical fibers' constitutive parameters on emission properties and light delivery geometries in the brain are well-known (Aravanis et al., 2007; Yizhar et al., 2011; Schmid et al., 2016), similar information for fluorimetry performances is not yet available. Even though analytical models to estimate light collection field of optical fibers in quasi-transparent medium has been derived (Engelbrecht et al., 2009), the use of Monte Carlo simulations (Pfefer et al., 2001, 2002; Bargo et al., 2002, 2003a,b) or direct experimental measurements (Tai et al., 2007; Ryu et al., 2015) are required to properly assess spatial dependence of fluorimetry performances with high spatial resolution. Such information is necessary in order to select the optimal optical fibers to collect light from the brain region of interest as well as to interpret photometry measurements.

Here we evaluate the fluorescence collection properties of optical fibers typically employed in fiber photometry. We characterize the extension and shape of the probed volume and collected signal, evaluating the effects of fibers' constitutive parameters. Through a combined confocal/2-photon laser-scanning microscope we measured the light *collection* and *emission* fields in brain tissue whose combination determines the photometry efficiency field $\rho(x,y,z)$ (Zhu and Yappert, 1992; Tai et al., 2007). These provide a quantitative estimation of collection volumes as a function of fiber numerical aperture (NA) and core diameter (a), together with an assessment of signal decay as a function of the position with respect to the fiber facet. Comparing data between different fibers, we found that NA has a secondary effect on photometry properties and that fiber core size is the chief parameter in defining the collection volume. Together with analytical and ray tracing collection maps, our data highlight aspects of light collection from brain tissue often overlooked in biological fiber photometry applications, with optical fibers having different NAs that have not been quantitatively compared yet.

RESULTS

Numerical Estimation of Optical Fibers Collection Field

As schematically represented in **Figure 1A**, the light generated from an isotropic fluorescent source is collected by an optical fiber with a certain efficiency that depends on the optical fiber's properties (numerical aperture and diameter) and on the properties of the medium between the source and the fiber (refractive index, absorption and scattering). For a given fiber with core diameter a and numerical aperture NA, immersed in a homogeneous medium with refractive index n , the analytical approach provided by Engelbrecht et al. (2009) estimates the 2D map of collection efficiency $\psi(NA, n, a, x, z)$ as the fraction

of the power collected by the fiber core from an isotropic point source located in the (x, z) plane (see **Figure 1A** for axis definition). To numerically estimate the collection field of optical fibers typically employed for *in vivo* fiber photometry (i.e., considering tissue absorption and scattering) we combined the approach in Engelbrecht et al. (2009) with a ray tracing model. In the following, we first extend the method proposed by Engelbrecht et al. (2009) to take into account the light entering the waveguide from the cladding front face; we then use the results to validate a ray tracing model that numerically estimates the fiber collection field in scattering brain tissue (see section Materials and Methods).

The collection efficiency η for a fiber with core diameter a , cladding diameter b , core refractive index n_{core} , and cladding refractive index n_{clad} can be written as

$$\eta(NA, n_{\text{core}}, n, a, b, x, z) = \psi(NA, n, a, x, z) + \psi(NA_{\text{eq}}, n, b, x, z) - \psi(NA_{\text{eq}}, n, a, x, z), \quad (1)$$

where $NA_{\text{eq}} = \sqrt{n_{\text{clad}}^2 - n^2} = \sqrt{n_{\text{core}}^2 - NA^2 - n^2}$ is the equivalent numerical aperture of the cladding/external medium interface (Snyder and Love, 1983), with the term $\psi(NA_{\text{eq}}, n, b, x, z) - \psi(NA_{\text{eq}}, n, a, x, z)$ accounting for light collected by the cladding. Taking advantage of the axial symmetry of the system, values of η throughout the whole space filled by the external medium can be obtained. Meridional slices ($y = 0$) of such volumes are shown in **Figure 1B** for optical fibers with three different configurations of NA/core diameter commonly used for fiber photometry experiments (0.22/50 μm , 0.39/200 μm , and 0.50/200 μm , respectively), for a homogeneous medium with $n = 1.335$. These maps show the presence of a region with constant collection efficiency next to the fiber core, roughly described by a cone with base coincident with the fiber facet surface and vertex lying on the waveguide axis at z_0 (Engelbrecht et al., 2009), where

$$z_0 = \frac{a}{2 \cdot \tan \left[\sin^{-1} \left(\frac{NA}{n} \right) \right]} \approx \frac{a}{2 \cdot \tan \left(\frac{NA}{n} \right)}. \quad (2)$$

Interestingly, for 0.39/200 μm fiber the maximum collection efficiency region lies along the lateral surface of the cone, due to the fact that $NA_{\text{eq}} > NA$, whereas this does not happen in the case of the 0.50/200 μm fiber for which $NA_{\text{eq}} < NA$. This difference between 0.39/200 μm and 0.50/200 μm fibers is clearly visible also in the axial collection profiles (blue lines in **Figure 1E**). In the case of the 0.39/200 μm fiber, as a result of cladding collection, a peak in the collection efficiency is observed at the boundary of the constant region close to the fiber (red arrow in **Figure 1E**, middle panel). In contrast, for the 0.50/200 μm fiber cladding collection leads only to a small plateau indicated by the red arrow in the bottom panel of **Figure 1E**. The influence of cladding on collected signal for different parameters is summarized in **Supplementary Figure 1**, showing the comparison between the volumes enclosed by iso-surfaces at several values of η for fibers with NA = 0.22, 0.39, 0.50, 0.66, and core cladding/diameters $a/b = 200 \mu\text{m}/225 \mu\text{m}$, 400 $\mu\text{m}/425 \mu\text{m}$. Cladding contribution leads to a general increase

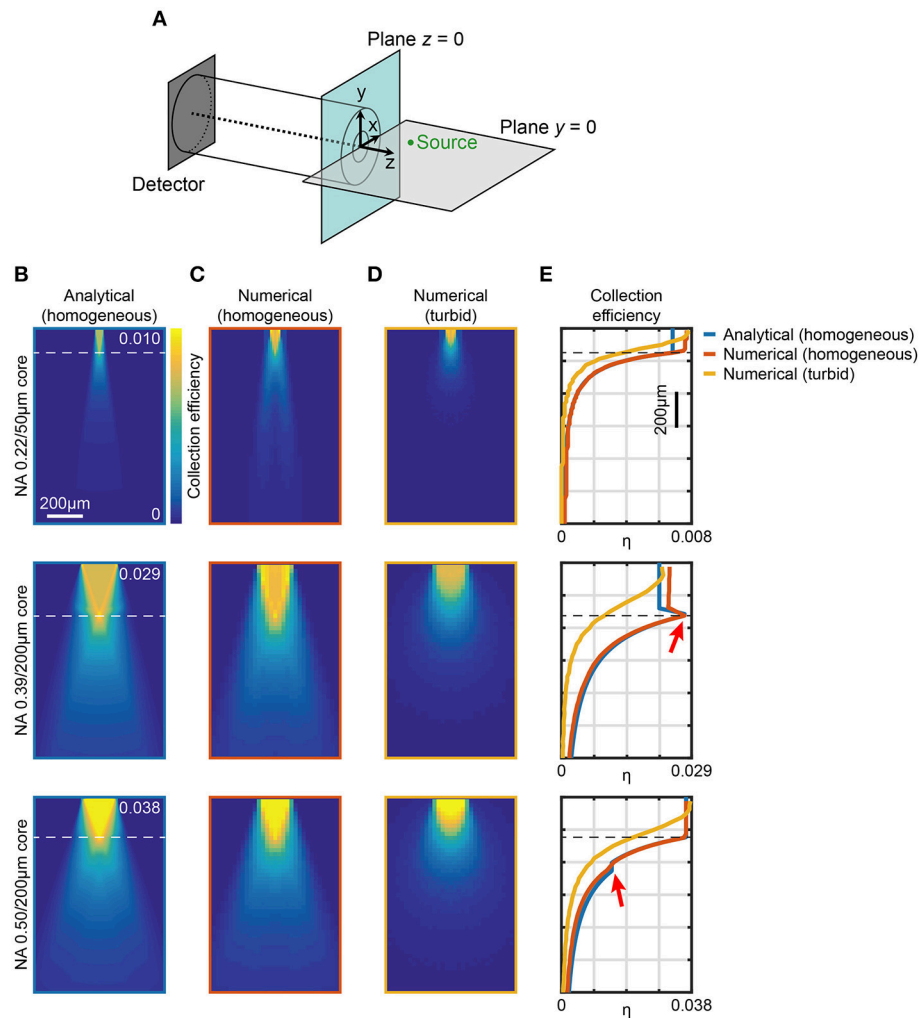


FIGURE 1 | Computational models of light collection efficiency for optical fibers. **(A)** Reference system used throughout the manuscript. An example point source (green) is shown in the plane $y = 0$. **(B)** Analytical calculations of collection efficiency diagrams for light emitting from point sources locating in the xz ($y = 0$) plane for three different fibers. Data are shown for 0.22NA/50 μm , 0.39NA/200 μm , and 0.50NA/200 μm optical fibers, as indicated, immersed in a transparent homogeneous medium ($n = 1.335$). The horizontal dashed lines represent $z_0 = a \cdot \left[2 \tan \left(\frac{NA}{n} \right) \right]^{-1}$. **(C,D)** Ray tracing simulations of collection efficiency diagrams from a point source ($\lambda = 520 \text{ nm}$) for same fibers as **(B)** immersed in a transparent homogeneous medium ($n = 1.335$) **(C)** or in a turbid medium (Henvey-Greenstein scattering, $n = 1.360$, $l = 48.95 \mu\text{m}$, $g = 0.9254$, $T = 0.9989$) **(D)**. **(E)** Comparison of axial collection efficiency ($x = 0$, $y = 0$) for 0.22NA/50 μm , 0.39NA/200 μm , and 0.50NA/200 μm optical fibers at $\lambda = 520 \text{ nm}$ immersed in a homogeneous medium (blue curve and orange curve for analytical and numerical data, respectively) and in a turbid medium (yellow curve). The red arrows indicate the effect of light collection through the cladding. The horizontal dashed lines represent z_0 .

of the collection volume, more pronounced for fibers where $NA_{eq} > NA$: for the 0.39 NA fiber considered in this work, the cladding generates $\sim 57\%$ and $\sim 27\%$ volume increase for 200 and 400 μm core, respectively. Performances of fibers with higher a/b ratio or with $NA_{eq} < NA$ are less affected by the cladding collection.

Ray-tracing simulations were performed by scanning an isotropic point source at $\lambda = 520 \text{ nm}$ across the xz plane (the ray tracing setup is shown in **Supplementary Figure 2**). Modeled light rays entering the fiber within NA_{eq} were propagated through a short length of patch fiber (10 mm) and registered if they reached a hypothetical detector at the distal end of

the fiber. Results for core/cladding fibers are displayed in **Figure 1C**. This configuration simulated the potential leakage of light rays outside NA_{eq} that propagate in the cladding. A comparison in terms of axial collection profiles (**Figure 1E**) shows a very good agreement with the analytical model for both the geometrical behavior and the absolute collection efficiency values. In particular, the maximum collection efficiency η for the 0.39/200 μm fiber was found to be ~ 0.03 whereas in the case 0.50/200 μm it was estimated to be ~ 0.04 . The model matches well also with the analytical approach of Engelbrecht et al. (2009) when cladding collection is neglected (inset of **Supplementary Figure 2**).

Since the ray-tracing approach and the analytical method gave consistent results, we extended the numerical simulations to model turbid media, such as scattering brain tissue. We modeled the medium around the fiber with a Henyey-Greenstein scattering function to simulate absorption and scattering properties of brain tissue (Zinter and Levene, 2011; Yona et al., 2016) (refractive index $n = 1.360$, mean free path $l = 48.95 \mu\text{m}$, anisotropy parameter $g = 0.9254$, transmission coefficient $T = 0.9989$). The resulting maps of collection efficiency for $0.22/50 \mu\text{m}$, $0.39/200 \mu\text{m}$, and $0.50/200 \mu\text{m}$ fibers are shown in **Figure 1D**. As a comparison, the axial profiles of analytical and numerical estimation of η for both transparent and turbid media are reported in **Figure 1E** for all the investigated fibers. When absorption and scattering of the medium are considered, the constant region in collection efficiency almost disappears, and η starts decreasing immediately after the fiber facet. The maximum η value remains $\sim 65\%$ higher for the $0.50/200 \mu\text{m}$ fiber with respect to $0.39/200 \mu\text{m}$. However, the collection efficiency decrease is slightly steeper for the $0.50/200 \mu\text{m}$ fiber, reaching 50% of the maximum at $250 \mu\text{m}$ from the fiber facet, compared to $300 \mu\text{m}$ observed for the $0.39/200 \mu\text{m}$ fiber.

Empirical Model for Collection Volumes

Collection fields returned from both analytical model and ray-tracing simulations were used to obtain an empirical model of the probed volume as a function of fiber NA and size, assuming axially symmetric distribution, in quasi-transparent medium and brain tissue. Volumetric data for different values of η for fibers with NA = 0.22, 0.39, 0.50, 0.66, and $a/b = 200 \mu\text{m}/225 \mu\text{m}$, $400 \mu\text{m}/425 \mu\text{m}$ are reported in **Figures 2A,B** for the analytical and the ray tracing models, respectively. These plots highlight that core size plays an important role in defining the volume from which light is gathered, with increased NA impacting for a lower amount in the volume increase.

On the base of the good match between the empirical and ray-tracing models, this latter is used to estimate the collection volumes also in turbid medium, as shown in **Figure 2C**. The overall behavior is the same observed in quasi-transparent medium, with collection volumes in turbid medium being ~ 2 times smaller than volumes in transparent medium. Even though **Figure 2C** covers common NAs and core/cladding sizes, a rough estimation of the collected volumes from fibers with parameters in between the data points can be interpolated from the plots.

Direct Measurement of Collection Field in Quasi-Transparent Fluorescent Media

A two-photon (2P) laser scanning system has been designed and built to directly measure the light collection field of optical fibers, in a configuration similar to Tai et al. (2007). A block diagram of the optical path is illustrated in **Figure 3A**: the optical fiber was submerged in a fluorescent PBS:fluorescein solution ($30 \mu\text{M}$) and a fs-pulsed near-infrared laser ($\lambda_{\text{ex}} = 920 \text{ nm}$) was used to generate a fluorescent voxel that was scanned in three dimensions close to the fiber facet. Scan in the xz plane was obtained by a two-axis galvanometric scanhead on a $\sim 1.4 \times 1.4 \text{ mm}^2$ field of view (FOV), with the microscope objective (Olympus XLFluor 4x/340 NA 0.28) mounted on a y -axis piezo focuser to obtain

a volumetric scan. The voxel emission was collected by the same objective and detected by a non-descanned photomultiplier tube ("*μscope PMT*"). This gave a measurement of the total fluorescence generated and, if needed, can be used to compensate for changes in excitation efficiency of the scanning point source. Simultaneously, the fraction of the voxel's fluorescence that was collected by the optical fiber and guided to a second PMT ("*fiber PMT*") was measured. The point spread function (PSF) of the two-photon epifluorescence system was measured to be $3 \mu\text{m}$ laterally and $32 \mu\text{m}$ axially (see **Supplementary Figure 3** and section Materials and Methods for details).

During volumetric raster scanning of the 2P spot, Scanimage software (Vidrio Technologies) was used to reconstruct images from both the *μscope PMT* and the *fiber PMT* signals, allowing for a point-by-point mapping of the light intensity collected from the optical fiber within the scanned volume. **Figure 3B** shows the signal collected by the *fiber PMT* when the excitation was scanned across the $y = 0$ plane for three different type of optical fiber: $0.22/50 \mu\text{m}$ (Thorlabs FG050UGA, top panel), $0.39/200 \mu\text{m}$ (Thorlabs FT200UMT, middle panel), and $0.50/200 \mu\text{m}$ (Thorlabs FP200URT, bottom panel), with overlay of the isolines at 10%, 20%, 40%, 60%, and 80% of the maximum number of photons collected. **Supplementary Figure 4** shows the signal collected along the $x = 0$ plane. A typical full volumetric scan is shown in the video of **Supplementary Video 1**, obtained with a $0.50/200 \mu\text{m}$ fiber. These images were corrected for unevenness of illumination within the FOV by using the related signal on the *μscope PMT* (see **Supplementary Figure 5**). In addition, the gain G of the system was estimated by noise analysis at each measurement session and used to convert the PMTs signals into numbers of photons (see Materials and Methods for details). A direct measurement of η as ratio between the collected photons (the signal read by the *fiber PMT*) and the photons emitted by the fluorescent source (the signal read by the *μscope PMT* corrected by the solid angle of collection of the microscope objective) can also be obtained. For a direct comparison, analytical collection maps were also computed convolving η and a three-dimensional function modeling the experimental PSF (**Figure 3C**) (details on this calculation are reported in Materials and Methods). The related axial profiles, shown normalized to the to the average of the points within the firsts $80 \mu\text{m}$ in **Figure 3D**, indicate good agreement between numerical predictions and the experimental data. Both analytical and experimental results show a difference between $0.39/200 \mu\text{m}$ and $0.50/200 \mu\text{m}$ fibers (**Figures 3B–D**). For $0.39/200 \mu\text{m}$ fibers, the region of maximum collection does not lie on the optical axis, but in two lobes near the boundary of the core: this can be ascribed to the fact that light is efficiently guided not only by the core-cladding interface, but also by the waveguide formed by the cladding and the external medium (i.e., the PBS:fluorescein solution).

By assembling the data collected from adjacent xz -planes in the sampled volume, the full three-dimensional collection fields can be reconstructed and used to illustrate the iso-intensity surfaces at 10%, 20%, 40%, 60%, and 80% of the maximum number of collected photons (**Figure 4A**). The volumes enclosed by these surfaces reflect those from which a given fraction of the

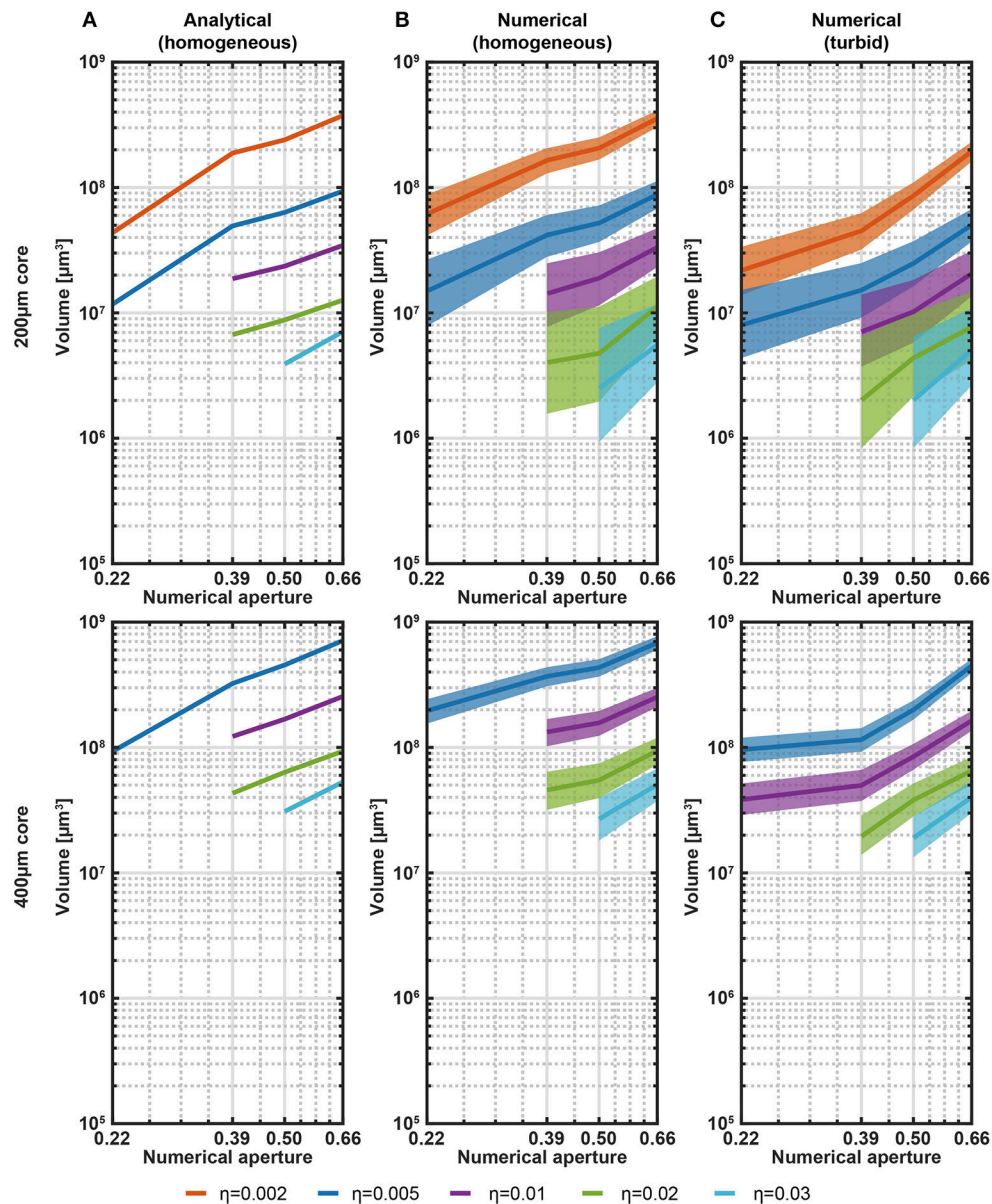


FIGURE 2 | Analytical and numerical estimation of collection volumes. **(A)** Volume iso-surfaces at different η estimated with the analytical model in transparent medium as a function of NA. Data are shown for $\eta = 0.002, 0.005, 0.01, 0.02, 0.03$ and for fibers with core/cladding diameters $a/b = 200 \mu\text{m}/225 \mu\text{m}$, $400 \mu\text{m}/425 \mu\text{m}$ (top and bottom panels, respectively). Missing data at low NA means null volume. **(B)** Same analysis of **(A)** shown for the ray-tracing model in transparent medium. The width of the curves represents the error in the volume estimation introduced by the domain discretization. **(C)** Same analysis of **(B)** shown for the ray-tracing model in a turbid medium to simulate brain tissue. Scattering was modeled with Henyey-Greenstein formulation ($\eta = 1.360$, $l = 48.95 \mu\text{m}$, $g = 0.9254$, $T = 0.9989$). The width of the curves represents the error in the volume estimation introduced by the domain discretization.

collected photons arise and hence determine the effective volume from which functional signals can be detected (**Figure 4B**, left). Collection volumes of $0.39\text{NA}/200 \mu\text{m}$ and $0.50\text{NA}/200 \mu\text{m}$ fibers behave very similar for relative intensities $\leq 60\%$. The $0.22\text{NA}/50 \mu\text{m}$ (which has a 16 times smaller core surface) shows consistently lower collection volumes. When the volumetric data for the $0.22\text{NA}/50 \mu\text{m}$ fiber are multiplied by a factor 16 (dotted yellow line in **Figure 4B**, left), collection volumes

are close to those of $0.39/200 \mu\text{m}$ and $0.50/200 \mu\text{m}$ fibers. The same consideration can be done by evaluating collected photons within the iso-intensity surfaces at fixed value of absolute collection efficiency η (**Figure 4B**, right): $0.39\text{NA}/200 \mu\text{m}$ and $0.50\text{NA}/200 \mu\text{m}$ fibers behave similarly, with the $0.50\text{NA}/200 \mu\text{m}$ fiber providing lower variation among different fibers at higher collection efficiency. As users of fiber photometry are interested in the overall signal collected from a certain depth or from a

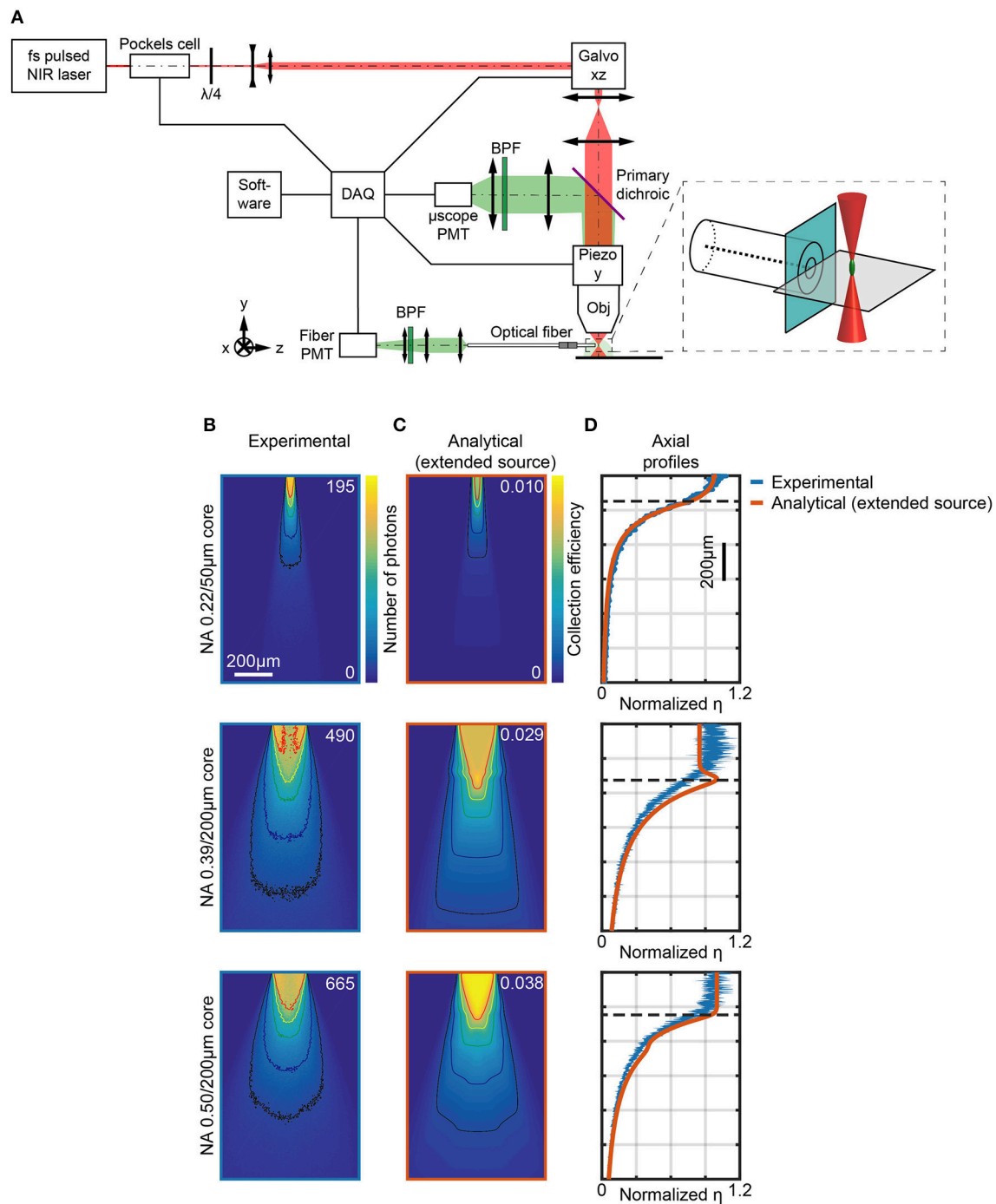


FIGURE 3 | Measurements of light collection efficiency using 2-photon generated fluorescent point sources. **(A)** Schematic representation of the two-photon microscope used to measure the collection field of optical fibers in quasi-transparent fluorescent medium. The inset shows a magnification of the fiber facet surroundings. **(B)** Section $y = 0$ of the collection field of 0.22/50 μ m, 0.39/200 μ m, and 0.50/200 μ m optical fibers, as indicated, in a 30 μ M PBS:fluorescein solution, obtained through the *fiber PMT* as shown in **(A)**. Isolines at 10%, 20%, 40%, 60%, and 80% of the maximum number of photons are shown (in black, blue, green, yellow, and red, respectively). **(C)** Analytical calculations of collection efficiency diagrams for the three fibers in **(B)** immersed in a transparent homogeneous medium ($n = 1.335$) assuming a gaussian source with lateral FWHM $r_{x,z} = 3 \mu$ m, axial FWHM $r_y = 32 \mu$ m. Isolines at 10%, 20%, 40%, 60%, and 80% of the maximum number of photons are shown (in black, blue, green, yellow, and red, respectively). **(D)** Comparison of normalized experimentally-measured (blue curve) and analytically-calculated (orange curve) axial collection efficiency profiles ($x = 0$, $y = 0$) for the same fibers in **(B)**. Normalization is done with respect to the average of the data points within the firsts 80 μ m. The horizontal dashed lines represent z_0 . The width of the blue curves for the 0.39 NA/200 μ m and 0.50 NA/200 μ m fibers represents mean \pm standard deviation over four different fibers.

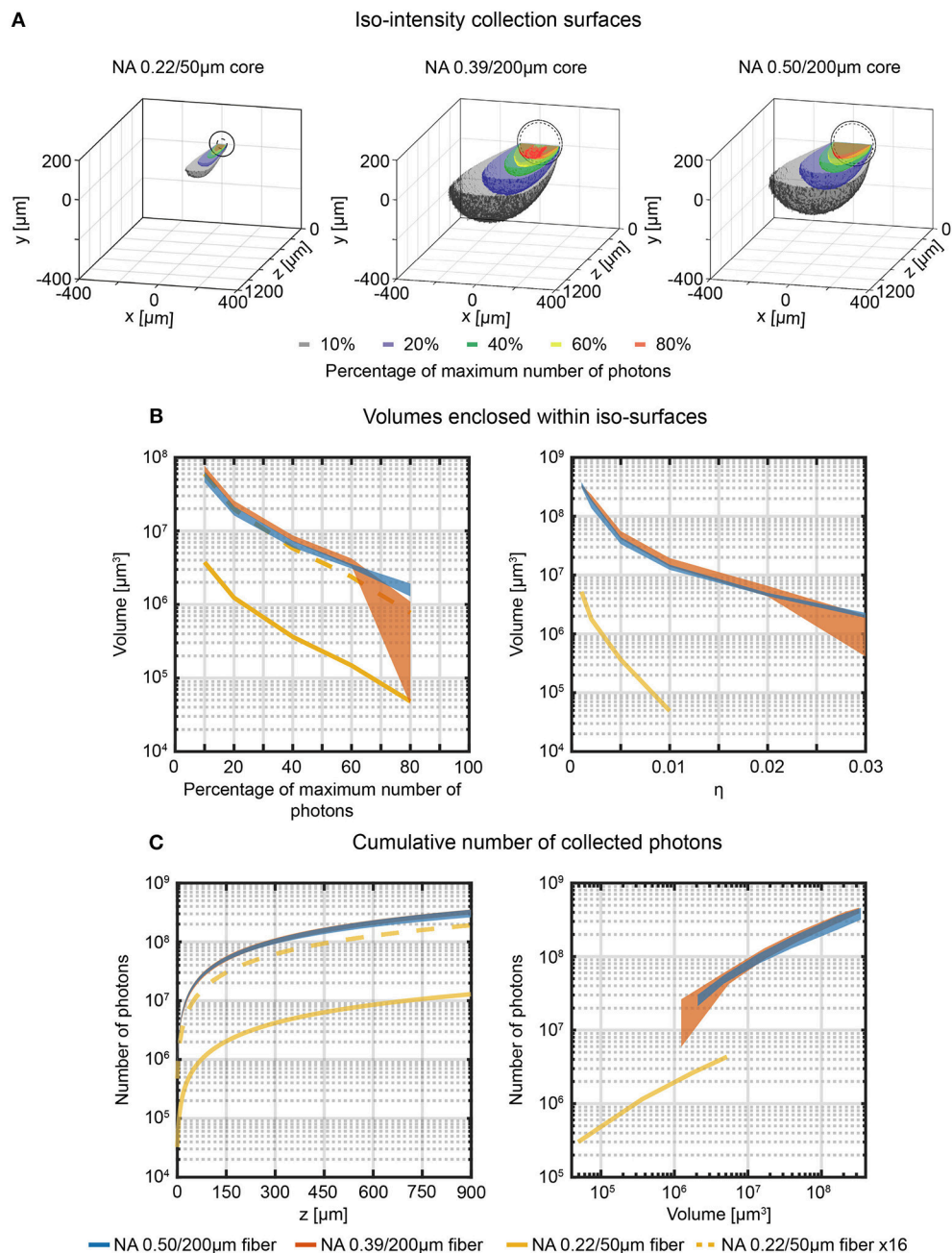


FIGURE 4 | Effective light collection volumes in quasi-transparent medium. **(A)** Cross-sectional views of the 3-dimensional reconstructions of the collection field for 0.22/50 μm , 0.39/200 μm , and 0.50/200 μm fibers in quasi-transparent solution. Iso-intensity surfaces defining the boundaries at which the number of collected photons falls to 10%, 20%, 40%, 60%, and 80% of its maximum are shown (in black, blue, green, yellow and red, respectively). The continuous and dashed circles in the xy plane represent the cladding and the core boundaries, respectively. **(B)** Volumes enclosed by the iso-intensity surfaces at 10%, 20%, 40%, 60%, and 80% of the maximum number of photons (left panel) and at $\eta = 0.001, 0.002, 0.005, 0.01, 0.02, 0.03$ (right panel) for 0.22/50 μm , 0.39/200 μm , and 0.50/200 μm fibers (yellow, orange, and blue curves, respectively). The dashed yellow curve represents the data for the 0.22/50 μm fiber multiplied by a factor 16 to adjust for the smaller cross-sectional area of this fiber. The width of the curves for the 0.39NA/200 μm and 0.50NA/200 μm fibers represents mean \pm standard deviation over four different fibers. **(C)** Cumulative number of photons collected by the three fibers as a function of the distance from the fiber facet (left panel, number of photons are shown in a volume 900 $\mu\text{m} \times 600\mu\text{m} \times z$) and as a function of the volume enclosed within the iso-surfaces at fixed η (right panel). The dashed yellow curve represents the data points relative to the 0.22/50 μm fiber multiplied by a factor 16. The width of the curves for the 0.39NA/200 μm and 0.50NA/200 μm fibers represents mean \pm standard deviation over four different fibers.

certain volume, these parameters have been extracted from the volumetric collection fields. The absolute cumulative number of collected photons as a function of collection depth is shown in **Figure 4C**, left, while the photons flux emerging from a specific volume (defined within iso-intensity surfaces at fixed value of η) is displayed in **Figure 4C** (right). These data highlight that in quasi-transparent media these two figures of merit behave very similarly for 0.39NA/200 μm and 0.50NA/200 μm fibers (the ratio of the average number of photons collected throughout the range $z = 0 \mu\text{m} - 900 \mu\text{m}$ is ~ 1 , as shown in **Supplementary Figure 6A**), while 0.22NA/50 μm fiber collects less photons from smaller volumes.

Direct Measurement of Collection Field in Brain Slices

The system depicted in **Figure 3A** was also used to measure the light collection field of 0.39/200 μm and 0.50/200 μm optical fibers in 300 μm thick brain slices stained with fluorescein. This was done to estimate the influence of tissue absorption and scattering on the geometrical features of light collection. **Figure 5A** shows the results of these measurements for the two investigated fibers on the plane $y = 0$, with overlay of the isolines at 10%, 20%, 40%, 60%, and 80% of the maximum signal detected from the fiber PMT. A clear difference compared to the measurement in PBS:fluorescein solutions is that the flat collection efficiency region was disrupted by tissue scattering so that it was not possible to define the characteristic point at z_0 for either fibers. This was also seen in the axial collection profiles reported normalized to the average of the points within the firsts 80 μm in **Figure 5B**, which show a steep decrease of the collection curve starting at the fiber face. These findings were confirmed by comparing the results to those obtained using the ray-tracing model discussed above for both axial collection profiles (orange lines in **Figure 5B**) and their derivatives (**Supplementary Figure 7A**). It is also important to mention that, although collection diagrams in quasi-transparent media are fully symmetric (**Supplementary Figure 8**), the data in tissue present a certain degree of asymmetry due to the tissue conformation, which could also induce slightly uneven staining.

The $y = 0, x < 0$ half-planes of the measurements in **Figure 5A** were used to reconstruct the collection volume. The collection volume was reconstructed by 360° rotation after applying a 11×11 pixel moving average filter (details on the procedure are given in Materials and Methods). Iso-intensity surfaces of the reconstructed 3D collection field at 10%, 20%, 40%, 60%, and 80% of the maximum PMT counts value were calculated (**Figure 5C**), and collection volumes at the same relative threshold and for fixed value of η were determined (**Figure 5D**, left and right, panel, respectively). As expected, the collection volumes in tissue are smaller with respect to the volumes in fluorescent solution due to light absorption and scattering. In addition, the 0.50/200 μm fiber increased the average collection volume by a factor ~ 1.6 compared to the average volume collected by the 0.39/200 μm fiber (see **Supplementary Figure 7B** for a detailed plot of volumes ratio between 0.50 and 0.39 fibers for each η iso-intensity curve). The absolute value of collected photons as

a function of collection depth and as a function of volume within iso-efficiency collection surfaces at fixed value of η are displayed in **Figure 5E**. 0.50NA/200 μm fiber collect slightly more photons than the 0.39NA/200 μm fiber (the ratio of the average number of photons collected throughout the range $z = 0 \mu\text{m} - 900 \mu\text{m}$ is ~ 1.24 , matching with a 3% tolerance the ratio of 1.28 between the NAs, as shown in **Supplementary Figure 6B**).

Photometry Efficiency in Brain Tissue

We described the approach used to estimate the collection efficiency of an optical fiber by scanning a point like source in the proximity of the fiber facet. However, in fiber photometry experiments fluorescence is generated by delivering excitation light (typically at 473 nm or 488 nm) and collecting the generated fluorescence (usually in the range 500 nm–550 nm) through the same fiber. Therefore, light intensity obtained from a specific position depends not only on how photons are collected from that point, but also on the efficiency at which fluorescence is excited at that point. A *photometry efficiency* parameter ρ can therefore be defined as:

$$\rho(x, y, z) = \eta(x, y, z) \cdot \beta(x, y, z) \quad (3)$$

where η is the collection efficiency and β is the normalized light emission diagram of the same optical fiber used to collect light (Zhu and Yappert, 1992; Tai et al., 2007). In brain tissue, η can be estimated with the 2P scanning method detailed in paragraph Direct Measurement of Collection Field In Quasi-Transparent Fluorescent Media. To estimate β in the same location where η is measured, a pinhole detection system was implemented in a de-scanned collection path (**Figure 6A**). The scanning pinhole allows light to reach the detector only if it arises from a conjugate location in the tissue; thus, its intensity is determined by the efficiency at which light reaches the point from the fiber. In this way fiber emission diagram is measured in brain slices uniformly stained with fluorescein. A block diagram of the experimental setup is shown in **Figure 6A**. A 473 nm CW laser source was coupled to the fiber distal end and provided the excitation light. The fluorescence light excited in the brain slice by the optical fiber was imaged on the galvanometric mirrors and scanned through a pinhole aperture that conveyed it on a *pinhole PMT*. This detector was used to reconstruct the fluorescence intensity map within the same FOV (same magnification and position) of the 2P scan used to estimate η (**Figures 6B,C**, respectively). A comparison of η and β in terms of axial decay is shown in **Supplementary Figure 9**. Upon normalization, β maps give an estimation of the light emission diagram and can be used in conjunction with the collection fields to estimate ρ (pixel by pixel product of η and β).

The resulting maps (**Figure 6D**, with overlay of the isolines at 10%, 20%, 40%, 60%, and 80% of the maximum photometry efficiency) contain in each pixel a value proportional to (i) the amount of fluorescence light excited by the fiber in that pixel and (ii) to the amount of light collected from that pixel. These values describe the relative contribution of signal arising from each voxel and thus determine the spatial distribution of the sources of signal collected during a fiber photometry recording.

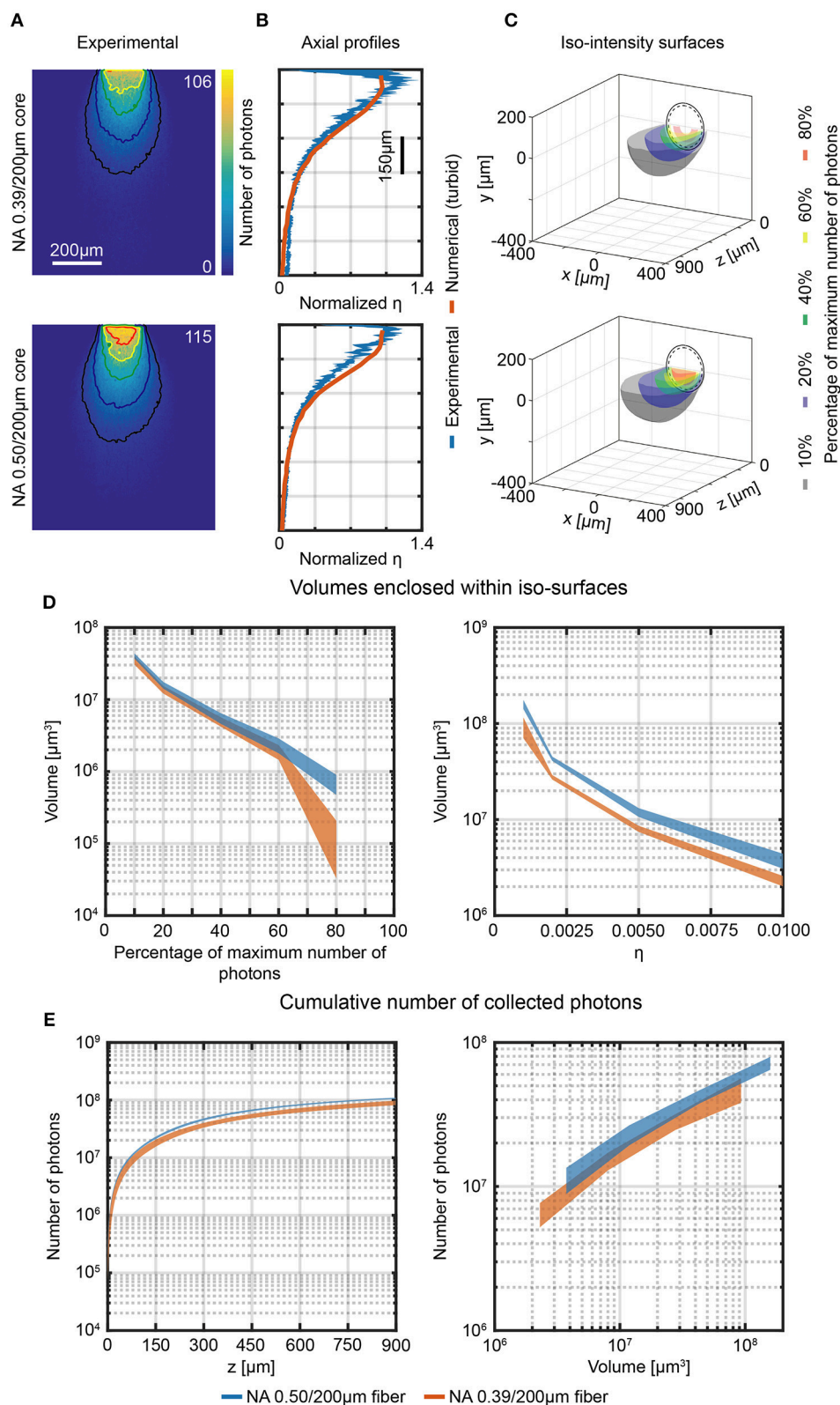


FIGURE 5 | Photon collection efficiency and effective collective volumes in brain slice. **(A)** Section $y = 0$ of the collection field of 0.39/200 μm and 0.50/200 μm optical fibers, measured in a 300 μm thick fluorescently stained brain slice using the 2-photon scanning system shown in **Figure 3**. Isolines at 10%, 20%, 40%, 60%, and 80% of maximum number of photons. *(Continued)*

FIGURE 5 | 80% of the maximum number of photons are shown (in black, blue, green, yellow and red, respectively). **(B)** Comparison of normalized axial profiles ($x = 0$, $y = 0$) of experimental (in brain slices, blue curves) and numerical data (in turbid medium, orange curves) for 0.39/200 μm and 0.50/200 μm optical fibers. Normalization is done with respect to the average of the data points within the firsts 80 μm . The width of the blue curves represents mean \pm standard deviation over four different fibers. **(C)** Cross-sections of the 3-dimensional reconstruction of the collection field of 0.39/200 μm and 0.50/200 μm fibers. Iso-intensity surfaces defining the boundaries at which the number of collected photons falls to 10%, 20%, 40%, 60%, and 80% of its maximum are shown (in black, blue, green, yellow, and red, respectively). The continuous and dashed circles represent the cladding and the core boundaries, respectively. **(D)** Volumes enclosed by the iso-intensity surfaces at 10%, 20%, 40%, 60%, and 80% of the maximum number of photons (left panel) and at $\eta = 0.001$, 0.002, 0.005, 0.01 (right panel) for 0.39/200 μm and 0.50/200 μm fibers (orange, and blue curves, respectively). The width of the curves represents mean \pm standard deviation over three different fibers. **(E)** Cumulative number of photons collected by 0.39/200 μm and 0.50/200 μm fibers as a function of the distance from the fiber facet (left panel, number of photons are shown in a volume 900 $\mu\text{m} \times 600 \mu\text{m} \times z$) and as a function of the volume enclosed within the iso-surfaces at fixed η (right panel). The width of the curves represents mean \pm standard deviation over three different fibers.

This analysis reveals that, as expected from the effect of tissue scattering, the axial profile of ρ falls off faster with distance from the fiber face than the collection only diagram (**Figure 6E**, profiles are normalized to the average of the points within the firsts 80 μm) for both the 0.39/200 μm and 0.50/200 μm fibers. Transversal profile of ρ along x at $z = 0 \mu\text{m}$, 100 μm , 200 μm , 300 μm for both fibers are shown in **Figure 6F**.

Similarly, volumetric analysis analogous to the ones described in section Direct Measurement of Collection Field in Quasi-Transparent Fluorescent Media can be extended to photometry efficiency (**Figure 7A**) to determine the volumes enclosed by the iso-intensity surfaces at 10%, 20%, 40%, 60%, and 80% of the maximum photometry efficiency and at fixed values of ρ (**Figure 7B** left and right panel, respectively). The higher numerical aperture 0.50/200 μm fiber results in a collection volume ~ 2.2 times higher than the 0.39/200 μm fiber (on average: the plot of the ratio between the two datasets for the different ρ iso-intensity surfaces is reported in **Supplementary Figure 10**).

DISCUSSION AND CONCLUSION

Although fiber photometry is regularly employed to investigate the relationship between neural activity and behavior as well as connectivity in neural circuits (Lütcke et al., 2010; Grienberger et al., 2012; Cui et al., 2013, 2014; Stroh et al., 2013; Adelsberger et al., 2014; Gunaydin et al., 2014; Chen et al., 2015; Fuhrmann et al., 2015; Kim et al., 2016; Matthews et al., 2016; Nieh et al., 2016; Lovett-Barron et al., 2017; Muir et al., 2017; Schwalm et al., 2017; Selimbeyoglu et al., 2017; He et al., 2018; Luo et al., 2018; Meng et al., 2018; Simone et al., 2018), the fluorimetry properties of optical fibers inserted into the brain have not been well-characterized yet. In this work we evaluated the illumination and collection fields for widely-used multimode optical fibers in brain tissue, quantitatively estimating signal collection efficiency as well as size and shape of collection volumes.

This was achieved by implementing a combined confocal/two-photon laser-scanning microscope to measure both the collection and emission diagrams from the same fiber in the same region (**Figures 3, 6**) (Tai et al., 2007). The 2P path was used to estimate collection volumes in both quasi-transparent media and brain slices (**Figures 4, 5**, respectively), showing that collection volumes for 0.39 NA and 0.50 NA fibers with 200 μm core are almost the same in fluorescein and only slightly higher for 0.50 NA fibers in brain slices. The geometric distribution of the collection volume consistently agrees with analytical

and numerical estimations based on theory and ray tracing models. The latter can therefore be confidently used to estimate the spatial dependence of light collection intensity once the scattering and absorption parameters in the Henyey-Greenstein model are known in terms of mean free path, anisotropy parameter, and transmission coefficient (all scripts are provided in **Supplementary Material**).

The observations on collection fields measured for 0.39 NA and 0.50 NA hold true also for the photometry efficiency fields $\rho(x, y, z)$. According to our data, 0.39/200 μm and 0.50/200 μm fibers behave very similarly in terms of on-axis spatial decay of ρ (**Figure 6E**). The 0.50/200 μm fiber, however, interface with a volume approximatively two times bigger with respect to the 0.39/200 μm fiber (**Figures 5D, 7B**), mainly due to out-of-axis contributions. Our results suggest that the influence of the numerical aperture in defining the axial extension of the brain volume under investigation is marginal with respect to the effect of the fiber diameter. Optical fibers with smaller core, such as the 0.22/50 μm one, can be utilized to collect functional fluorescence signals from a restricted tissue volume, when localized information is needed.

From a practical perspective, our data can serve as a resource for researchers in choosing the optical fiber to use in a specific experiment: (i) increase the core size rather than the NA to enlarge the collection volume; (ii) if on-axis contribution is preferred (e.g., cortical columns), a lower NA should be used; (iii) if a low count rate is expected, high NA fibers can help by detecting additional out-of-axis fluorescence.

MATERIALS AND METHODS

Fiber Stubs Fabrication

Fiber stubs were realized from 0.22/50 μm (Thorlabs FG050UGA), 0.39/200 μm (Thorlabs FT200UMT), and 0.50/200 μm (Thorlabs FP200URT) multimode optical with cladding diameters of 125 μm and 225 μm , for 0.22/50 μm and 0.39/200 μm –0.50/200 μm fibers, respectively. After peeling off the buffer, stubs were trimmed to size using a fiber cleaver (Fujikura CT-101) and connectorized to a stainless-steel 1.25 mm ferrule. The connectorized ends of the stubs were then manually polished. Fiber patches were realized from the same fiber types and connectorized using a stainless-steel ferrule on the proximal end and a SMA connector on the distal end, with respect to the stub. During experiments, the stubs were connected to a patch fiber of matching NA and core/cladding sizes via ferrule to ferrule butt-coupling. The patch fiber has

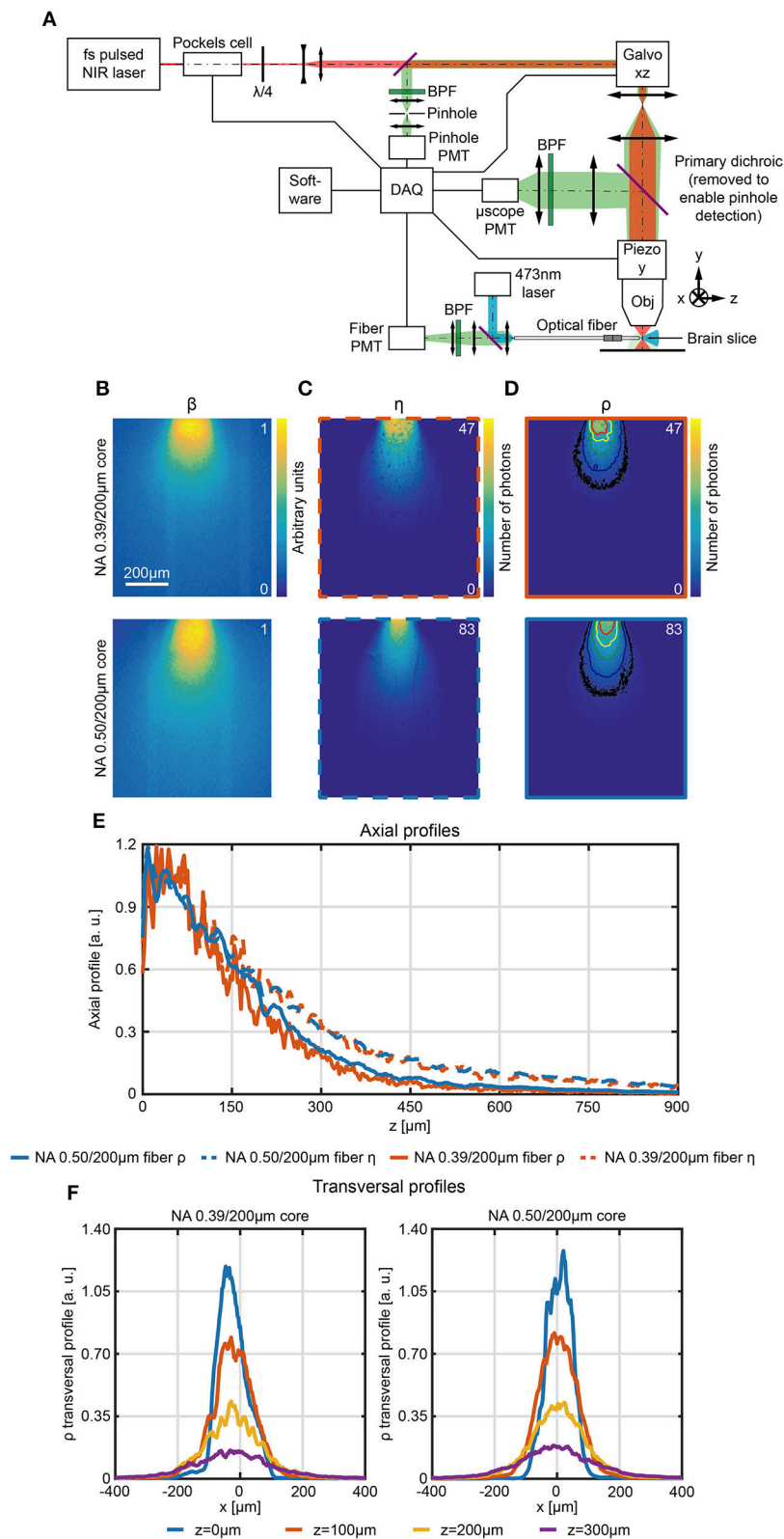


FIGURE 6 | Scanning pinhole detection of the excitation light field for fiber optics. **(A)** Schematic representation of the optical path used to measure the photometry efficiency diagram of optical fibers in fluorescently stained brain slices. **(B–D)** Section $y = 0$ of the normalized light emission diagram β **(B)**, the collection efficiency η **(C)**, and the number of photons ρ **(D)**. **(E)** Axial profiles of the normalized light emission diagram β **(B)**, the collection efficiency η **(C)**, and the number of photons ρ **(D)**. **(F)** Transversal profiles of the normalized light emission diagram β **(B)**, the collection efficiency η **(C)**, and the number of photons ρ **(D)**. *(Continued)*

FIGURE 6 | (C) and the photometry efficiency ρ **(D)** of 0.39/200 μm and 0.50/200 μm optical fibers, as indicated, measured in a 300 μm thick fluorescently stained brain slice. In **(D)** isolines at 10%, 20%, 40%, 60%, and 80% of the maximum efficiency are shown (in black, blue, green, yellow, and red, respectively). **(E)** Comparison of normalized axial profiles ($x = 0, y = 0$) between 0.39/200 μm and 0.50/200 μm fibers for photometry efficiency (orange and blue continuous curve, respectively) and collection efficiency (orange and blue dashed curve, respectively). Normalization is done with respect to the average of the points within the firsts 80 μm . **(F)** Normalized photometry efficiency transversal profiles at different depths ($z = 0 \mu\text{m}, 100 \mu\text{m}, 200 \mu\text{m}, 300 \mu\text{m}, y = 0$) for 0.39NA/200 μm and 0.50NA/200 μm fibers (left and right panel, respectively).

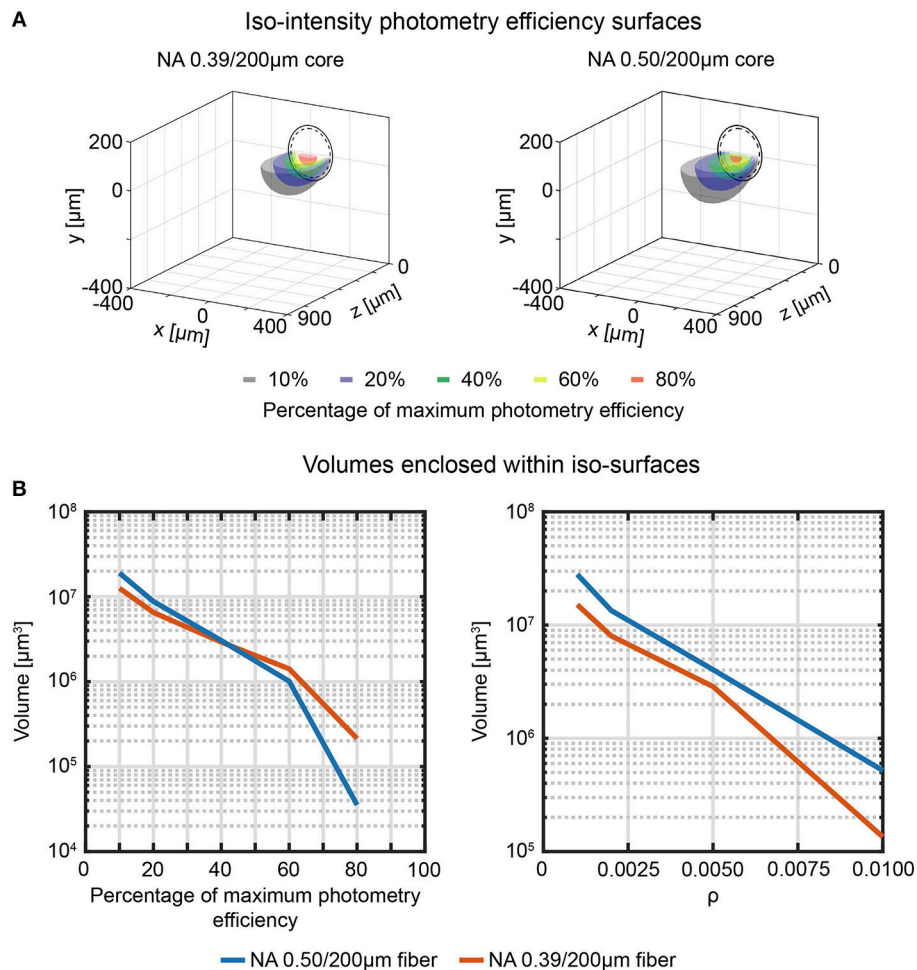


FIGURE 7 | Effective fiber photometry sampling volumes in tissue. **(A)** Cross-sections of the 3-dimensional reconstruction of the photometry efficiency diagram of 0.39/200 μm and 0.50/200 μm fibers (left and right, respectively). Iso-intensity surfaces at 10%, 20%, 40%, 60%, and 80% efficiency are shown (in black, blue, green, yellow, and red, respectively). The continuous and dashed circles represent the cladding and the core boundaries, respectively. **(B)** Volumes enclosed by the iso-intensity surfaces at 10%, 20%, 40%, 60%, and 80% of the maximum photometry efficiency (left) and at $\rho = 0.001, 0.002, 0.005, 0.01$ (right) for 0.39/200 μm and 0.50/200 μm fibers (orange and blue curves, respectively).

a fully preserved core/cladding/buffer structure, that influence propagation of light collected and guided by the cladding of the fiber stub. For the 0.39/200 μm and 0.50/200 μm fibers, light entering the cladding can propagate in the patch fiber since the buffer has a refractive index $n_{\text{buf}} < n_{\text{clad}}$. For 0.22/50 μm fiber, instead, the acrylate buffer refractive index is $n_{\text{buf}} = 1.4950$ at 520 nm (Polyanskiy, 2018), higher than $n_{\text{clad}} = 1.4440$, thus preventing light to be guided into the cladding of the patch fiber.

Analytical Calculation of Fiber Collection Fields

Analytical 3D maps of fiber collection fields for an ideal point source were calculated for 0.22/50 μm , 0.39/200 μm , and 0.50/200 μm fibers following Engelbrecht et al. (2009). We extended their work to include the cladding front face contribution to the collection fields of 0.39/200 μm , 0.50/200 μm and 0.66/200 μm fibers by implementing Equation (1). The refractive index of the core ($n_{\text{core}} = 1.4613$ at 520 nm for

0.39 NA and 0.50 NA with silica core, and $n_{\text{core}} = 1.5202$ at 520 nm for 0.66 NA with borosilicate core) has been retrieved from the online database (Filmetrics, 2018), while the refractive index of the cladding (n_{clad}) has been calculated to provide the nominal numerical aperture. In Equation (1), $\psi(\text{NA}, n, a, x, z)$ is the same as in Ref. Engelbrecht et al. (2009), while the term $\psi(\text{NA}_{\text{eq}}, n, b, x, z) - \psi(\text{NA}_{\text{eq}}, n, a, x, z)$ takes into account light collection from the cladding facet (see **Supplementary Script 1**). In particular, $\psi(\text{NA}_{\text{eq}}, n, b, x, z)$ is the collection efficiency of a fiber with diameter b that guides light by virtue of the refractive index contrast between the surrounding medium and the cladding with numerical aperture NA_{eq} . However, the cladding has a thickness $b-a$ with circular crown shape, and therefore the collection efficiency from the region overlapped to the core, $\psi(\text{NA}_{\text{eq}}, n, a, x, z)$, should be subtracted. This modeling was used for obtaining the collection efficiency maps for point-like sources shown in **Figure 1B**. To extend these data to the case of an extended source, three dimensional maps for point-like source were obtained by rotating collection efficiency maps in the $y = 0$ plane around the fiber axis (see **Supplementary Script 1**). The obtained 3D maps were then convolved with a 3D representation of the actual focal spot generated by the microscope (see **Supplementary Script 1**). This latter was modeled as a Gaussian function with lateral FWHM $r_{x,z} = 3 \mu\text{m}$, and axial FWHM $r_y = 32 \mu\text{m}$, modeling the PSF of the used experimental configuration (see below for details in the PSF measurements).

Ray Tracing Simulation of Fiber Collection Fields

Ray tracing simulations were performed using an optical model designed with commercial optical ray-tracing software Zemax-OpticStudio to simulate the behavior of light collected by the optical fibers. The implemented layout is shown in **Supplementary Figure 2**. Flat fibers were represented as two nested cylinders simulating core and cladding of nominal diameters ($50 \mu\text{m}/125 \mu\text{m}$ for 0.22NA Thorlabs FG050UGA fiber, $200 \mu\text{m}/225 \mu\text{m}$ for 0.39NA Thorlabs FT200UMT and 0.50NA Thorlabs FP200URT fibers, and $400 \mu\text{m}/425 \mu\text{m}$). Numerical apertures of the fibers were defined by setting the respective core/cladding refractive indexes $n_{\text{core}}/n_{\text{clad}}$ as 1.4613/1.4440 for 0.22NA fibers, 1.4613/1.4079 for 0.39NA fibers, 1.4613/1.3730 for 0.50NA fibers, and 1.5202/1.3694 for 0.66NA fibers (Filmetrics, 2018). One of the two fiber facets was included within an optically homogeneous cylinder volume that simulated the PBS:fluorescein droplet or the stained brain slice. A fluorescence source was modeled as a 520 nm point source emitting $500 \cdot 10^3$ rays for a total power of 1W. To reproduce the experimental acquisition, the source was raster scanned across the half-plane $y = 0, x > 0$ (**Figure 1A**). To optimize simulation time, steps along z and x were set to $25 \mu\text{m}$; for simulations concerning 0.22/50 μm fiber the region in the proximity of the fiber ($600 \mu\text{m}$ along z and $500 \mu\text{m}$ along x) was simulated with a grid step of $12.5 \mu\text{m}$, to better sample the smaller core. For each source position, the rays were collected from both core and cladding surfaces on the facet, propagated into the fiber and they were detected on a single-pixel squared

detector placed at the distal end of the fiber. The detector size was matched to the cladding diameter. Refractive indexes were set as $n = 1.335$ for PBS:fluorescein solution and as 1.360 for brain-like scattering volume (Sun et al., 2012). Scattering in the PBS:fluorescein solution was not modeled. Scattering in brain tissue was simulated following a Henyey-Greenstein model with parameters: mean free path $m = 0.04895 \text{ mm}$, anisotropy value $g = 0.9254$ and transmission $T = 0.9989$ (Zinter and Levene, 2011; Yona et al., 2016).

From the computational point of view, the most demanding part of the simulation is rays propagation into the fiber, that experimentally is $\sim 1 \text{ m}$ long and requires $> 24 \text{ h}$ per simulation. To shorten simulation times, a relatively short length of the fibers was implemented (10 mm). This short length does not allow, however, to consider losses of light entering the fiber outside the maximum accepted angle. Therefore, only rays describing an angle with the fiber input facet smaller than a threshold θ_{th} were considered in the power count, with

$$\theta_{\text{th}} = \sin^{-1} \frac{\max\{\text{NA}, \text{NA}_{\text{eq}}\}}{n}. \quad (4)$$

For the 0.22 NA fibers the cladding sidewalls were modeled as an absorbing interface to take into account for the leakage of light from the cladding ($n_{\text{clad}} = 1.4440$ at 520 nm) to the buffer ($n_{\text{buf}} = 1.4950$ at 520 nm Polyanskiy, 2018) into the patch fiber.

Brain Slices Treatment

Brain slices $\sim 300 \mu\text{m}$ thick were cut with a vibratome from wild-type mice brain. Slices were then fixed in PFA and permeabilized for 30 min in 0.3% Triton X-100 (Sigma-Aldrich). Slices were then incubated with fluorescein (1mM in PBS) for 30 min.

Acquisition and Analysis of Fiber Collection Fields

A combined confocal/two-photon laser scanning microscope was designed and built in a configuration similar to Ref. Tai et al. (2007). A full block diagram of the path used to measure collection fields is illustrated in **Figure 3A**. The power of a fs-pulsed near-infrared (NIR) laser beam (Coherent Chameleon Discovery, emission tuned at $\lambda_{\text{ex}} = 920 \text{ nm}$) is modulated by means of a Pockels cell (Conoptics 350-80-02), and a quarter wave plate (Thorlabs AQWP05M-980) has been used to obtain circularly polarized light. The laser beam is expanded by a factor 5 and xz -scanned with a galvo/galvo head (Sutter). The microscope objective (Olympus XLFluor 4x/340) is mounted on a y -axis piezo focuser (Phisik Instrument P-725.4CD), and fluorescence signal is excited into a quasi-transparent $30 \mu\text{M}$ PBS:Fluorescein solution or into a fluorescently stained brain slice. Fluorescence light is re-collected by the same objective and conveyed without descanning on the entrance window of a photomultiplier tube (PMT, Hamamatsu H10770PA-40, the “ $\mu\text{scope PMT}$ ”) through a dichroic mirror (Semrock FF665-Di02), two spherical lenses (Thorlabs LA1708-A and LA1805-A), and a bandpass filter (BPF, Semrock FF01-520/70-25). During experiments in solution, fiber stubs were submerged in a PBS:Fluorescein droplet held in the sample plane by a hydrophobic layer. After a butt-to-butt

coupling with a patch fiber of matched NA and core/cladding diameter, the light back emitted from the fiber was collected through a microscope objective (Olympus Plan N 40x) and sent to the entrance window of a PMT (Hamamatsu H7422P-40, the “*fiber PMT*”), through two spherical lenses (Thorlabs LA1050-A and LA1805-A) and a BPF (Semrock FF03-525/50-25).

A focal spot was then generated and scanned in the vicinity of the fiber facet covering a field of view of $\sim 1.4 \times 1.4 \text{ mm}^2$ with 512×512 pixels, with the beam resting on each pixel for $\sim 3.2 \text{ } \mu\text{s}$. Laser power and PMTs gain were adjusted to optimize signal to noise ratio. For each measurement, a $400 \text{ } \mu\text{m}$ thick stack was acquired with a $5 \text{ } \mu\text{m}$ step along y , starting slightly below the fiber axis and finishing above the fiber. Each slice in the stack was averaged out of 5 frames.

The number of photons for each frame was calculated as $N_{ph} = \frac{PMT_{counts}}{G}$, where G represents the gain of the acquisition system. G was measured as $G = \sigma_{counts}^2 / \langle PMT_{counts} \rangle$, where the average number of counts $\langle PMT_{counts} \rangle$ and the variance σ_{counts}^2 were acquired by illuminating a confined and homogeneous region in the fluorescein drop. Stacks acquired through the *fiber PMT* were corrected slice-by-slice for unevenness in excitation, by scaling them against the normalized corresponding image collected by the *μscope PMT* (see **Supplementary Figure 5**). The frame acquired for gain measurement of the epi-fluorescence path has been used to correct for slight variability of laser power between measurements, proportionally to the pixel average value. Uncertainty σ_c on the cumulative number of photons shown in **Figure 4C** were evaluated propagating the Poisson

nominal fiber were averaged, and twice the standard deviation was considered as error bar.

Point Spread Function Measurement

The PSF of the two-photon microscope was measured by imaging sub-resolution nanoparticles (100 nm) at 920 nm with 160 nm lateral steps and $2 \text{ } \mu\text{m}$ axial steps. For the 4X/0.28NA Olympus XLFluor 4x/340 objective, this resulted in a PSF with lateral FWHM $r_{x,z} = 3 \text{ } \mu\text{m} \pm 1 \text{ } \mu\text{m}$, and axial FWHM $r_y = 32 \text{ } \mu\text{m} \pm 5 \text{ } \mu\text{m}$ (**Supplementary Figure 3**). Lateral and axial profiles were fitted with a gaussian function. Two nanoparticles were considered in this measurement, values shown are mean \pm standard deviation.

Acquisition of Spatially Sampled Fiber Emission Diagrams

The setup schematically shown in **Figure 6A** was used to measure the emission diagrams of flat-cleaved optical fibers in tissue. Fibers were inserted into a $300 \text{ } \mu\text{m}$ thick fluorescently stained brain slice, 473 nm light was coupled into the fiber through an objective lens (Olympus Plan N 40x), and the primary dichroic of the 2P microscope was removed from the system. Light emission from the tissue was collected through the microscope objective, descanned by the scan-head, focused into a pinhole (Thorlabs MPH-16), and detected by a PMT (Hamamatsu H7422P-40, the “*pinhole PMT*”). A BPF (Thorlabs MF525/39) isolated the wavelength band of interest. The pinhole size was set to $100 \text{ } \mu\text{m}$.

$$\sigma_c(z) = \sqrt{\sum_{x,y,z} \left\{ N_{ph}(x,y,z) \sqrt{\left(\frac{1}{\sqrt{PMT_{counts}^{fiber}(x,y,z)}} \right)^2 + \left(\frac{1}{\sqrt{PMT_{counts}^{\mu scope}(x,y,z)}} \right)^2 + \left[\frac{\text{std}(G^{fiber})}{\langle G^{fiber} \rangle} \right]^2} \right\}} \quad (5)$$

noise on the photon count of every pixel and the error on gain determination as where the superscript *fiber* and *μscope* identify the PMT, mean and standard deviation of G are evaluated over five consecutive frames, and the sum indexes span across the whole xy plane and up to z . The value of σ_c resulted to be $< 1\%$ of N_c at all z for all fibers. Collection efficiency η was evaluated pixel by pixel as

$$\eta(x,y,z) = \frac{PMT_{counts}^{fiber}(x,y,z)/G^{fiber}}{PMT_{counts}^{\mu scope}(x,y,z)/[G^{\mu scope} \cdot 0.5\gamma(1 - \cos(NA_{obj}/n))]}, \quad (6)$$

where $\gamma = 1.11$ is a factor compensating for the loss in the patch fiber and the term $0.5(1 - \cos(NA_{obj}/n))$ is the fraction of solid angle accepted by the microscope objective. Data processing was done through **Supplementary Script 2** and **Supplementary Script 3** for images collected in quasi-transparent medium and in brain slice, respectively. One $0.22\text{NA}/50 \text{ } \mu\text{m}$ fiber, four $0.39\text{NA}/200 \text{ } \mu\text{m}$ and four $0.50\text{NA}/200 \text{ } \mu\text{m}$ fibers were characterized in quasi-transparent medium, three $0.39\text{NA}/200 \text{ } \mu\text{m}$ and three $0.50\text{NA}/200 \text{ } \mu\text{m}$ fibers were characterized in brain slice; data among the same

Photometry Efficiency Calculation

Images acquired on the $y = 0$ plane by the *fiber PMT* and the *pinhole PMT* were used to determine the photometry efficiency. The image acquired through the pinhole was registered over the collection field to obtain a pixel-to-pixel spatial correspondence. The photometry efficiency maps were determined as the pixel by pixel product of normalized version of illumination and collection fields (see **Supplementary Script 4**). One half of the photometry efficiency maps was employed to obtain a volumetric representation of this quantity, as reported previously.

Matlab Programming

Data processing was implemented in Matlab. Scripts are reported in **Supplementary Materials**, with **Supplementary Script 5** containing all the undefined functions called in **Supplementary Scripts 1–4**.

DATA AVAILABILITY

Data will be made available by authors after the publication of the paper at cbn.iit.it/openfiberphotometry and can be requested to the authors at any time.

AUTHOR CONTRIBUTIONS

All authors listed have made a substantial, direct and intellectual contribution to the work, and approved it for publication.

FUNDING

FeP, FiP, EM, and AB acknowledge funding from the European Research Council under the European Union's Horizon 2020 research and innovation program (#677683). MP and MDV acknowledge funding from the European Research Council

under the European Union's Horizon 2020 research and innovation program (#692643). MDV and BS are funded by the US National Institutes of Health (U01NS094190).

SUPPLEMENTARY MATERIAL

The Supplementary Material for this article can be found online at: <https://www.frontiersin.org/articles/10.3389/fnins.2019.00082/full#supplementary-material>

Supplementary Video 1 | Volumetric scan of the collection field of a 0.50NA/200 μm fiber in a 30 μm PBS: Fluorescein solution.

REFERENCES

- Adelsberger, H., Zainos, A., Alvarez, M., Romo, R., and Konnerth, A. (2014). Local domains of motor cortical activity revealed by fiber-optic calcium recordings in behaving nonhuman primates. *Proc. Natl. Acad. Sci. U.S.A.* 111, 463–468. doi: 10.1073/pnas.1321612111
- Aravanis, A. M., Wang, L. P., Zhang, F., Meltzer, L. A., Mogri, M. Z., Schneider, M. B., et al. (2007). An optical neural interface: *in vivo* control of rodent motor cortex with integrated fiberoptic and optogenetic technology. *J. Neural Eng.* 4, S143–S156. doi: 10.1088/1741-2560/4/3/S02
- Bargo, P. R., Prael, S. A., and Jacques, S. L. (2002). "Collection efficiency of a single optical fiber in turbid media for reflectance spectroscopy," in *Biomedical Topical Meeting* (Optical Society of America), 604–606.
- Bargo, P. R., Prael, S. A., and Jacques, S. L. (2003a). Collection efficiency of a single optical fiber in turbid media. *Appl. Opt.* 42, 3187–3197. doi: 10.1364/AO.42.003187
- Bargo, P. R., Prael, S. A., and Jacques, S. L. (2003b). Optical properties effects upon the collection efficiency of optical fibers in different probe configurations. *IEEE J. Sel. Top. Q. Electron.* 9, 314–321. doi: 10.1109/JSTQE.2003.811287
- Canales, A., Jia, X., Froriep, U. P., Koppes, R. A., Tringides, C. M., Selvidge, J., et al. (2015). Multifunctional fibers for simultaneous optical, electrical and chemical interrogation of neural circuits *in vivo*. *Nat. Biotechnol.* 33, 277–284. doi: 10.1038/nbt.3093
- Chen, Y., Lin, Y. C., Kuo, T. W., and Knight, Z. A. (2015). Sensory detection of food rapidly modulates arcuate feeding circuits. *Cell* 160, 829–841. doi: 10.1016/j.cell.2015.01.033
- Cui, G., Jun, S. B., Jin, X., Luo, G., Pham, M. D., Lovinger, D. M., et al. (2014). Deep brain optical measurements of cell type-specific neural activity in behaving mice. *Nat. Protoc.* 9, 1213–1228. doi: 10.1038/nprot.2014.080
- Cui, G., Jun, S. B., Jin, X., Pham, M. D., Vogel, S. S., Lovinger, D. M., et al. (2013). Concurrent activation of striatal direct and indirect pathways during action initiation. *Nature* 494, 238–242. doi: 10.1038/nature11846
- Deisseroth, K. (2011). Optogenetics. *Nat. Methods* 8, 26–29. doi: 10.1038/nmeth.f.324
- Emiliani, V., Cohen, A. E., Deisseroth, K., and Hausser, M. (2015). All-optical interrogation of neural circuits. *J. Neurosci.* 35, 13917–13926. doi: 10.1523/JNEUROSCI.2916-15.2015
- Engelbrecht, C. J., Göbel, W., and Helmchen, F. (2009). Enhanced fluorescence signal in nonlinear microscopy through supplementary fiber-optic light collection. *Opt. Express* 17, 6421–6435. doi: 10.1364/OE.17.006421
- Filmetrics (2018). *Refractive Index Database*. Available online at: <https://www.filmetrics.com/refractive-index-database>
- Fluhler, E., Burnham, V. G., and Loew, L. M. (1985). Spectra, membrane binding, and potentiometric responses of new charge shift probes *Biochemistry* 24, 5749–5755. doi: 10.1021/bi00342a010
- Fuhrmann, F., Justus, D., Sosulina, L., Kaneko, H., Beutel, T., Friedrichs, D., et al. (2015). Locomotion, theta oscillations, and the speed-correlated firing of hippocampal neurons are controlled by a medial septal glutamatergic circuit. *Neuron* 86, 1253–1264. doi: 10.1016/j.neuron.2015.05.001
- Göfller, C., Bierbrauer, C., Moser, R., Kunzer, M., Holc, K., Pletschen, W., et al. (2014). GaN-based micro-LED arrays on flexible substrates for optical cochlear implants. *J. Phys. D. Appl. Phys.* 47:205401. doi: 10.1088/0022-3727/47/20/205401
- Grienberger, C., Adelsberger, H., Stroth, A., Milos, R. I., Garaschuk, O., Schierloh, A., et al. (2012). Sound-evoked network calcium transients in mouse auditory cortex *in vivo*. *J. Physiol.* 590, 899–918. doi: 10.1113/jphysiol.2011.222513
- Gunaydin, L. A., Grosenick, L., Finkelstein, J. C., Kauvar, I. V., Fenno, L. E., Adhikari, A., et al. (2014). Natural neural projection dynamics underlying social behavior. *Cell* 157, 1535–1551. doi: 10.1016/j.cell.2014.05.017
- Häusser, M. (2014). Optogenetics: the age of light. *Nat. Methods* 11, 1012–1014. doi: 10.1038/nmeth.3111
- He, Y., Wang, M., Chen, X., Pohmann, R., Polimeni, J. R., Scheffler, K., et al. (2018). Ultra-slow single-vessel BOLD and CBV-based fMRI spatiotemporal dynamics and their correlation with neuronal intracellular calcium signals. *Neuron* 97, 925–939.e5. doi: 10.1016/j.neuron.2018.01.025
- Kim, C. K., Yang, S. J., Pichamoorthy, N., Young, N. P., Kauvar, I., Jennings, J. H., et al. (2016). Simultaneous fast measurement of circuit dynamics at multiple sites across the mammalian brain. *Nat. Methods* 13, 325–328. doi: 10.1038/nmeth.3770
- Kim, T. I., McCall, J. G., Jung, Y. H., Huang, X., Siuda, E. R., Li, Y., et al. (2013). Injectable, cellular-scale optoelectronics with applications for wireless optogenetics. *Science* 340, 211–216. doi: 10.1126/science.1232437
- Loew, L. M. (1996). Potentiometric dyes: Imaging electrical activity of cell membranes. *Pure Appl. Chem.* 68, 1405–1409. doi: 10.1351/pac199668071405
- Lovett-Barron, M., Andalman, A. S., Allen, W. E., Vesuna, S., Kauvar, I., Burns, V. M., et al. Ancestral circuits for the coordinated modulation of brain state. *Cell* (2017). 171:1411–1423.e17. doi: 10.1016/j.cell.2017.10.021
- Lu, L., Gutruf, P., Xia, L., Bhatti, D. L., Wang, X., Vazquez-Guardado, A., et al. (2018). Wireless optoelectronic photometers for monitoring neuronal dynamics in the deep brain. *Proc. Natl. Acad. Sci. U.S.A.* 115, E1374–E1383. doi: 10.1073/pnas.1718721115
- Luo, L., Callaway, E. M., and Svoboda, K. (2018). Genetic dissection of neural circuits: a decade of progress. *Neuron* 98, 256–281. doi: 10.1016/j.neuron.2018.03.040
- Lütcke, H., Murayama, M., Hahn, T., Margolis, D. J., Astori, S., Zum Alten Borgloh, S. M., et al. (2010). Optical recording of neuronal activity with a genetically-encoded calcium indicator in anesthetized and freely moving mice. *Front. Neural Circuits* 4:9. doi: 10.3389/fncir.2010.00009
- Matthews, G. A., Nieh, E. H., Vander Wee, C. M., Halbert, S. A., Pradhan, R. V., Yosafat, A. S., et al. (2016). Dorsal raphe dopamine neurons represent the experience of social isolation. *Cell* 164, 617–631. doi: 10.1016/j.cell.2015.12.040
- McAlinden, N., Gu, E., Dawson, M. D., Sakata, S., and Mathieson, K. (2015). Optogenetic activation of neocortical neurons *in vivo* with a sapphire-based micro-scale LED probe. *Front. Neural Circuits* 9:25. doi: 10.3389/fncir.2015.00025
- McAlinden, N., Massoubre, D., Richardson, E., Gu, E., Sakata, S., Dawson, M. D., et al. (2013). Thermal and optical characterization of micro-LED probes for *in vivo* optogenetic neural stimulation. *Opt. Lett.* 38, 992. doi: 10.1364/OL.38.000992

- Meng, C., Zhou, J., Papaneri, A., Peddada, T., Xu, K., and Cui, G. (2018). Spectrally resolved fiber photometry for multi-component analysis of brain circuits. *Neuron* 98, 707–717.e4. doi: 10.1016/j.neuron.2018.04.012
- Miesenböck, G. (2009). The optogenetic catechism. *Science* 326, 395–399. doi: 10.1126/science.1174520
- Miyawaki, A., Llopis, J., Heim, R., McCaffery, J. M., Adams, J. A., Ikura, M., et al. (1997). Fluorescent indicators for Ca²⁺ based on green fluorescent proteins and calmodulin. *Nature* 388, 882–887. doi: 10.1038/42264
- Muir, J., Lorsch, Z. S., Ramakrishnan, C., Deisseroth, K., Nestler, E. J., Calipari, E. S., et al. (2017). *In vivo* fiber photometry reveals signature of future stress susceptibility in nucleus accumbens. *Neuropsychopharmacology* 43, 255–263. doi: 10.1038/npp.2017.122
- Nieh, E. H., Vander Weele, C. M., Matthews, G. A., Presbrey, K. N., Wichmann, R., Leppla, C. A., et al. (2016). Inhibitory input from the lateral hypothalamus to the ventral tegmental area disinhibits dopamine neurons and promotes behavioral activation. *Neuron* 90, 1286–1298. doi: 10.1016/j.neuron.2016.04.035
- Park, S., Guo, Y., Jia, X., Kyoung Choe, H., Grena, B., Kang, J., et al. (2017). One-step optogenetics with multifunctional flexible polymer fibers. *Nat. Neurosci.* 20, 612–619. doi: 10.1038/nn.4510
- Petersen, C. C., Grinvald, A., and Sakmann, B. (2003). Spatiotemporal dynamics of sensory responses in Layer 2/3 of rat barrel cortex measured *in vivo* by voltage-sensitive dye imaging combined with whole-cell voltage recordings and neuron reconstructions. *J. Neurosci.* 23, 1298–1309. doi: 10.1523/JNEUROSCI.23-04-01298.2003
- Pfefer, T., Schomacker, K., Ediger, M., and Nishioka, N. S. (2001). Light propagation in tissue during fluorescence spectroscopy with single-fiber probes. *IEEE J. Sel. Top. Q. Electron.* 7, 1004–1012. doi: 10.1109/2944.983306
- Pfefer, T. J., Schomacker, K. T., Ediger, M. N., and Nishioka, N. S. (2002). Multiple-fiber probe design for fluorescence spectroscopy in tissue. *Appl. Opt.* 41, 4712–4721. doi: 10.1364/AO.41.004712
- Pisanello, F., Mandelbaum, G., Pisanello, M., Oldenburg, I. A., Sileo, L., Markowitz, J. E., et al. (2017). Dynamic illumination of spatially restricted or large brain volumes via a single tapered optical fiber. *Nat. Neurosci.* 20, 1180–1188. doi: 10.1038/nn.4591
- Pisanello, F., Sileo, L., Oldenburg, I. A., Pisanello, M., Martiradonna, L., Assad, J. A., et al. (2014). Multipoint-emitting optical fibers for spatially addressable *in vivo* optogenetics. *Neuron* 82, 1245–1254. doi: 10.1016/j.neuron.2014.04.041
- Pisanello, M., Pisano, F., Sileo, L., Maglie, E., Bellistri, E., Spagnolo, B., et al. (2018). Tailoring light delivery for optogenetics by modal demultiplexing in tapered optical fibers. *Sci. Rep.* 8:4467. doi: 10.1038/s41598-018-22790-z
- Pisano, F., Pisanello, M., Sileo, L., Qaltieri, A., Sabatini, B., L., De Vittorio, M., et al. (2018). Focused ion beam nanomachining of tapered optical fibers for patterned light delivery. *Microelectron. Eng.* 195, 41–49. doi: 10.1016/j.mee.2018.03.023
- Polyanskiy, M. N. (2018). *Refractive Index Database*. Available Online at: <https://refractiveindex.info>
- Ryu, Y., Shin, Y., Lee, D., Altarejos, J. Y., Chung, E., and Kwon, H. S. (2015). Lensed fiber-optic probe design for efficient photon collection in scattering media. *Biomed. Opt. Express* 6:191. doi: 10.1364/BOE.6.000191
- Scharf, R., Tsunematsu, T., McAlinden, N., Dawson, M. D., Sakata, S., and Mathieson, K. (2016). Depth-specific optogenetic control *in vivo* with a scalable, high-density μ LED neural probe. *Sci. Rep.* 6:28381. doi: 10.1038/srep28381
- Schmid, F., Wachsmuth, L., Schwalm, M., Prouvot, P. H., Jubal, E. R., Fois, C., et al. (2016). Assessing sensory versus optogenetic network activation by combining (o)fMRI with optical Ca²⁺ recordings. *J. Cereb. Blood Flow Metab.* 36, 1885–1900. doi: 10.1177/0271678X15619428
- Schwalm, M., Schmid, F., Wachsmuth, L., Backhaus, H., Kronfeld, A., Aedo Jury, F., et al. (2017). Cortex-wide BOLD fMRI activity reflects locally-recorded slow oscillation-associated calcium waves. *Elife* 6:e27602. doi: 10.7554/eLife.27602
- Segev, E., Reimer, J., Moreaux, L. C., Fowler, T. M., Chi, D., Sacher, W. D., et al. (2016). Patterned photostimulation via visible-wavelength photonic probes for deep brain optogenetics. *Neurophotonics* 4:011002. doi: 10.1117/1.NPh.4.1.011002
- Selimbeyoglu, A., Kim, C. K., Inoue, M., Lee, S. Y., Hong, A. S. O., Kauvar, I., et al. (2017). Modulation of prefrontal cortex excitation/inhibition balance rescues social behavior in CNTNAP2-deficient mice. *Sci. Transl. Med.* 9:eaah6733. doi: 10.1126/scitranslmed.aah6733
- Simone, K., Füzesi, T., Rosenegger, D., Bains, J., and Murari, K. (2018). Open-source, cost-effective system for low-light *in vivo* fiber photometry. *Neurophotonics* 5:025006. doi: 10.1117/1.NPh.5.2.025006
- Slovin, H., Arieli, A., Hildesheim, R., and Grinvald, A. (2002). Long-term voltage-sensitive dye imaging reveals cortical dynamics in behaving monkeys. *J. Neurophysiol.* 88, 3421–3438. doi: 10.1152/jn.00194.2002
- Snyder, A. W., and Love, J. D. (1983). *Optical Waveguide Theory*. New York, NY: Chapman and Hall.
- Stroh, A., Adelsberger, H., Groh, A., Rühlmann, C., Fischer, S., Schierloh, A., et al. (2013). Making waves: initiation and propagation of corticothalamic Ca²⁺ waves *in vivo*. *Neuron* 77, 1136–1150. doi: 10.1016/j.neuron.2013.01.031
- Sun, J., Lee, S. J., Wu, L., Sarntinoranont, M., and Xie, H. (2012). Refractive index measurement of acute rat brain tissue slices using optical coherence tomography. *Opt. Express* 20:1084. doi: 10.1364/OE.20.001084
- Tai, D. C., Hooks, D. A., Harvey, J. D., Smaill, B. H., and Soeller, C. (2007). Illumination and fluorescence collection volumes for fiber optic probes in tissue. *J. Biomed. Opt.* 12:034033. doi: 10.1117/1.2750288
- Wu, F., Stark, E., Ku, P. C., Wise, K. D., Buzsáki, G., and Yoon, E. (2015). Monolithically integrated μ LEDs on silicon neural probes for high-resolution optogenetic studies in behaving animals. *Neuron* 88, 1136–1148. doi: 10.1016/j.neuron.2015.10.032
- Yizhar, O., Fenno, L. E., Davidson, T. J., Mogri, M. Z., and Deisseroth, K. (2011). Optogenetics in neural systems. *Neuron* 71, 9–34. doi: 10.1016/j.neuron.2011.06.004
- Yona, G., Weissler, Y., Meitav, N., Guzi, E., Rifold, D., Kahn, I., et al. (2016). Realistic modeling of optogenetic neuronal excitation in light-scattering brain tissue. *Biomed. Opt. Express* 7:1634. doi: 10.1364/CANR.2016.JW3A.21
- Zhu, Z. Y., and Yappert, M. C. (1992). Determination of effective depth and equivalent pathlength for a single-fiber fluorometric sensor. *Appl. Spectrosc.* 46, 912–918. doi: 10.1366/0003702924124411
- Zinter, J. P., and Levene, M. J. (2011). Maximizing fluorescence collection efficiency in multiphoton microscopy. *Opt. Express* 19, 15348. doi: 10.1364/OE.19.015348
- Zorz, A. N., Scholvin, J., Boyden, E. S., and Fonstad, C. G. (2012). Three-dimensional multiwaveguide probe array for light delivery to distributed brain circuits. *Opt. Lett.* 37:4841. doi: 10.1364/OL.37.004841

Conflict of Interest Statement: The authors declare that the research was conducted in the absence of any commercial or financial relationships that could be construed as a potential conflict of interest.

Copyright © 2019 Pisanello, Pisano, Hyun, Maglie, Balena, De Vittorio, Sabatini and Pisanello. This is an open-access article distributed under the terms of the Creative Commons Attribution License (CC BY). The use, distribution or reproduction in other forums is permitted, provided the original author(s) and the copyright owner(s) are credited and that the original publication in this journal is cited, in accordance with accepted academic practice. No use, distribution or reproduction is permitted which does not comply with these terms.



Optogenetic Light Sensors in Human Retinal Organoids

Marcela Garita-Hernandez^{1*}, Laure Guibbal^{1†}, Lyes Toualbi^{1†}, Fiona Routet¹, Antoine Chaffiol¹, Celine Winckler¹, Marylin Harinquet¹, Camille Robert¹, Stephane Fouquet¹, Sebastien Bellow², José-Alain Sahel^{1,3,4}, Olivier Goureau¹, Jens Duebel^{1†} and Deniz Dalkara^{1†}

¹ Institut de la Vision, Sorbonne Université, INSERM, CNRS, Paris, France, ² BioAxial, Paris, France, ³ CHNO des Quinze-Vingts, DHU Sight Restore, INSERM-DGOS CIC 1423, Paris, France, ⁴ Department of Ophthalmology, The University of Pittsburgh School of Medicine, Pittsburgh, PA, United States

OPEN ACCESS

Edited by:

John A. Assad,
Harvard Medical School,
United States

Reviewed by:

Masahiro Kono,
Medical University of South Carolina,
United States
Pere Garriga,
Universitat Politècnica de Catalunya,
Spain

*Correspondence:

Marcela Garita-Hernandez
mgaritah@gmail.com

[†] These authors have contributed
equally to this work

Specialty section:

This article was submitted to
Neural Technology,
a section of the journal
Frontiers in Neuroscience

Received: 06 August 2018

Accepted: 12 October 2018

Published: 02 November 2018

Citation:

Garita-Hernandez M, Guibbal L,
Toualbi L, Routet F, Chaffiol A,
Winckler C, Harinquet M, Robert C,
Fouquet S, Bellow S, Sahel J-A,
Goureau O, Duebel J and Dalkara D
(2018) Optogenetic Light Sensors
in Human Retinal Organoids.
Front. Neurosci. 12:789.
doi: 10.3389/fnins.2018.00789

Optogenetic technologies paved the way to dissect complex neural circuits and monitor neural activity using light in animals. In retinal disease, optogenetics has been used as a therapeutic modality to reanimate the retina after the loss of photoreceptor outer segments. However, it is not clear today which ones of the great diversity of microbial opsins are best suited for therapeutic applications in human retinas as cell lines, primary cell cultures and animal models do not predict expression patterns of microbial opsins in human retinal cells. Therefore, we sought to generate retinal organoids derived from human induced pluripotent stem cells (hiPSCs) as a screening tool to explore the membrane trafficking efficacy of some recently described microbial opsins. We tested both depolarizing and hyperpolarizing microbial opsins including CatCh, ChrimsonR, ReaChR, eNpHR 3.0, and Jaws. The membrane localization of eNpHR 3.0, ReaChR, and Jaws was the highest, likely due to their additional endoplasmic reticulum (ER) release and membrane trafficking signals. In the case of opsins that were not engineered to improve trafficking efficiency in mammalian cells such as CatCh and ChrimsonR, membrane localization was less efficient. Protein accumulation in organelles such as ER and Golgi was observed at high doses with CatCh and ER retention lead to an unfolded protein response. Also, cytoplasmic localization was observed at high doses of ChrimsonR. Our results collectively suggest that retinal organoids derived from hiPSCs can be used to predict the subcellular fate of optogenetic proteins in a human retinal context. Such organoids are also versatile tools to validate other gene therapy products and drug molecules.

Keywords: hiPSC, retinal organoids, optogenes, trafficking, localization, ER stress

Abbreviations: AAV, adeno-associated virus; BET1L, Bet1 Golgi vesicular membrane trafficking protein like; BiP, binding immunoglobulin protein; CAG, CMV early enhancer/chicken β actin; CHOP, C/EBP homologous protein; CoDiM, conical diffraction microscope; CRX, cone-rod homeobox; DAPI, 4'-6'-diamino-2-dihydrochloride; ER, endoplasmic reticulum; GFP, green fluorescent protein; GOS28, Golgi snap receptor complex 1; HEK, human embryonic kidney; hiPSCs, human induced pluripotent stem cells; KDEL, proteic sequence Lys-Asp-Glu-Leu; PRs, photoreceptors; RCVRN, recoverin; RGCs, retinal ganglion cells; RP, retinitis pigmentosa; RPE, retinal pigmented epithelium; RT-PCR, real-time polymerase chain reaction; UPR, unfolded protein response; WGA, wheat germ agglutinin.

INTRODUCTION

Optogenetics uses light to control cells genetically modified to express light-sensitive membrane proteins, generically known as opsins. A major breakthrough was the discovery that the introduction of these opsins into neurons made them responsive to light allowing their modulation within a precise timeframe (Boyden et al., 2005). Optogenetics has opened new ways of experimentation in neuroscience, that enables optical modulation of selected cells within variety of complex tissues, but also holds promising therapeutic potential in retinal degenerative diseases (Deisseroth et al., 2006; Herlitze and Landmesser, 2007; Häusser, 2014). Today, there are two ongoing clinical trials using microbial opsins for vision restoration in patients affected with RP (NCT02556736 and NCT03326336).

The neural retina is composed of six major types of neurons in a laminar organization. The primary retinal neurons, PRs, are found in the outermost layer supported by the RPE. The PRs convey the light signal to an intermediate layer of interneurons, which synapse, to a final layer of RGCs, sending their axons to form the optic nerve toward the brain for visual processing. Patients affected by retinal diseases such as RP exhibit a progressive degeneration of PRs, starting with the loss of PR outer segments and leading to complete blindness. With a worldwide prevalence of 1:4000 (Pagon, 1988), RP has been associated with a wide number of mutations hampering the development of a universal gene therapy (Berger et al., 2010). However, optogenetic therapies can treat RP patients regardless of the specific mutation causing the disease. Indeed, using viral vectors carrying an optogene, any remaining retinal neuron can be transformed into an artificial PR. The strategy to convert surviving inner retinal cells into light-sensitive cells has been proposed first using the channelrhodopsin 2 (ChR2) light-sensor in the *rd1* mouse model (Bi et al., 2006). Nowadays, the available optogenetic toolbox offers the possibility to use hyperpolarizing opsins to activate dormant cones lacking light-sensitive outer segments (Busskamp et al., 2010; Khabou et al., 2018) and more depolarizing opsins to target the downstream retinal neurons such as bipolar cells (Macé et al., 2015) and RGCs (Sengupta et al., 2016; Chaffiol et al., 2017).

Our work aims to optimize each key-element to establish better optogenetic therapies based on microbial opsins for inherited retinal diseases to ensure their efficacy and safety. In our previous work, we identified the most efficient AAV vectors and optimized their doses to target mouse and primate retinal cells via various intraocular administration routes (Dalkara et al., 2013; Khabou et al., 2016). We also tested other vector components such as promoters in retinal organoids derived from hiPSCs (Khabou et al., 2018). One of the remaining questions is the choice of the best microbial opsin among the expanded selection that is currently available for research and therapy (Table 1). Since the discovery of channelrhodopsin in early 2000s, there has been over 15 years of research leading to the discovery of microbial opsins with desirable biophysical properties suiting various applications (Zhang et al., 2011).

Unfortunately, microbial opsins often show an impaired subcellular localization and poor membrane trafficking in

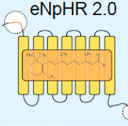
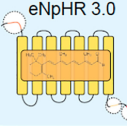
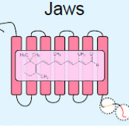
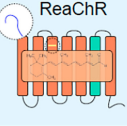
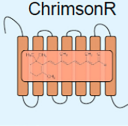
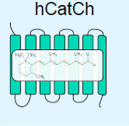
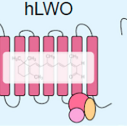

mammalian cells (Gradinaru et al., 2010). Introducing proteins coming from prokaryotic organisms that do not have a nucleus or ER to Golgi trafficking is likely responsible for this suboptimal expression. Safety concerns may arise in the host cells due to excess accumulation of opsins, which may lead to adverse effects potentially triggering an UPR. Thus, assessing and enhancing the trafficking is a critical point to determine the safety and efficacy of microbial opsins. Molecular modifications aiming to improve membrane trafficking have been undertaken for several opsins (Table 1). The use of signal peptides, additional exports motifs and trafficking signals led to more effective versions of NpHR (*Natromonas pharaonis*, HaloRhodopsin) (Gradinaru et al., 2008). Following this work several microbial opsins were engineered for better membrane expression leading to improved light responses such as the ones observed with Jaws (Chuong et al., 2014).

However, among the existing diversity of opsins, it is unclear which ones are best suited for expression in human retinal cells. The patterns of expression obtained with these opsins in primary neurons, cell lines (like HEK cells) or mouse models do not accurately predict expression patterns in human retinal cells. Human retinal explants might be a good model but their accessibility and maintenance in culture (Fradot et al., 2011) limit their use. Here, we propose to use retinal organoids derived from hiPSCs as an accessible, easy to produce and relevant human cell model, to study membrane trafficking of microbial opsins in a tissue of interest.

In this study, we assessed the trafficking efficiency and safety of hyperpolarizing opsins such as eNpHR 3.0 and Jaws but also depolarizing opsins such as ReaChR, ChrimsonR and humanized CatCh (hCatCh) in retinal organoids derived from hiPSCs. Microbial opsins need to be expressed in the cell membrane in order to be functional. Even though all of the microbial opsins we tested triggered light responses in retinal organoids, they displayed heterogeneous membrane trafficking efficacies. ChrimsonR and hCatCh were less efficient in membrane trafficking compared to the microbial opsins that have been engineered for improved trafficking. We characterized the trafficking deficiency of hCatCh and ChrimsonR by first localizing where it occurred, and then determining whether it induced ER stress. We observed that hCatCh sometimes colocalized with ER markers, whereas ChrimsonR was found in the cytosol in absence of membrane insertion suggesting that these microbial opsins can benefit from additional signal sequences for more efficient ER release and membrane trafficking. Nevertheless, we did not observe any toxicity related to the opsin expression in organoids.

Retinal organoids can thus be used to predict the expression pattern of optogenetic tools in human tissues shedding light onto the subcellular and transcellular trafficking in relation to safety. Moreover, the use of human cells can be advantageous for designing the next generation of optogenetic technologies for therapeutic use in humans. Potential additional molecular modifications for enhancing trafficking efficiency of microbial opsins might include human signal peptides or ER export motifs, Golgi trafficking signals and transport signals of human origin—all of which can enable better transport of these proteins along

TABLE 1 | Microbial opsins used in the present study.

HYPERPOLARIZING OPSINS			DEPOLARIZING OPSINS			VERTEBRATE OPSINS	
							
Signal peptide for membrane insertion ER export signal to facilitate ER to Golgi trafficking	Signal peptide for membrane insertion ER export to prevent aggregates Trafficking Signal KGC and ER2 sequences from Kir2.1	ER export to prevent aggregates Trafficking Signal KGC and ER2 sequences from Kir2.1	Replacing the N-ter from a better trafficking opsin (ChIEF)				
590nm	590nm	600nm	590nm	600nm	474nm	600nm	380-400nm
Gradinaru et al. 2008	Gradinaru et al. 2010	Chuong et al. 2014	Lin et al. 2013	Klapoetke et al. 2014	Kleinlogel et al. 2011	Masseeck et al. 2014	

We tested hyperpolarizing opsins (eNpHR 2.0, eNpHR 3.0 and Jaws), depolarizing opsins (ReaChR, ChrimsonR, and hCatCh) but also vertebrate opsins (hLWO for human long-wavelength opsin and mSWO for mouse short-wavelength opsin). Some of the following opsins have been engineered to enhance their membrane trafficking in eukaryotic cells. Peak activation wavelength for each opsin is indicated for each opsin.

the secretory pathway to the cell surface where they exert their activity.

MATERIALS AND METHODS

HEK Cells

HEK-293 cells were cultured in DMEM medium (Thermo Fisher Scientific) supplemented with 10% of fetal bovine serum (FBS) and 1% of penicillin/streptomycin (Thermo Fisher Scientific). Cells were kept at 37°C, under 5% CO₂/95% air atmosphere, 20% oxygen tension and 80–85% of humidity. Sterilized cover glasses were coated with poly-D-lysine (2 µg/cm², Sigma-Aldrich) for 45 min at 37°C followed by laminin coating (1 µg/cm², Sigma-Aldrich) at 37°C overnight and then placed in 24-well plates. At day 1, 100,000 cells per well were seeded in 24-well plates in DMEM supplemented with 10% FBS without antibiotic. At day 2, PEI and a plasmid carrying an optogene (ChrimsonR, hCatCh, ReaChR, eNpHR 2.0, eNpHR 3.0, Jaws, hLWO, mSWO) fused with GFP or yellow fluorescent protein (YFP) under the control of a ubiquitous CAG promoter, were mixed together and incubated for 10 min at RT. After 24–48 h, the medium was completely removed and replaced with fresh DMEM supplemented with 10% FBS without antibiotic. At day 3–4, the transfected cells were rinsed with PBS and stained with WGA before being fixed with 4% PFA for 10 min at room temperature.

WGA Staining

Wheat germ agglutinin, which binds to sialic acid and *N*-acetylglucosamine sugar residues, was used to stain the cellular plasma membrane in HEK cells. On living cells, in dark conditions, the conjugated lectin WGA-Rhodamine (Vector Laboratories) was incubated for 10 min. After 2–5 min washes in PBS, the cells were fixed with 4% PFA at RT for 10 min and kept in PBS until performing of classical immunostaining described below.

AAV Production

Recombinant AAVs were produced as previously described using the co-transfection method and purified by iodixanol gradient ultracentrifugation (Choi et al., 2007). Concentration and buffer exchange were performed against PBS containing 0.001% Pluronic. AAV titers were then determined based on real-time quantitative PCR titration method (Aurnhammer et al., 2012) using SYBR Green (Thermo Fisher Scientific).

Maintenance of hiPSC Culture

All experiments conducted in this study were carried out using hiPSC 2A cell line, previously established from human fibroblasts (Reichman et al., 2014) and recently adapted to feeder-free conditions (Reichman et al., 2017). Cells were kept at 37°C, under 5% CO₂/95% air atmosphere, and 20% oxygen tension and 80–85% of humidity. Colonies were cultured with Essential 8TM medium (Thermo Fisher Scientific) in culture dishes coated with truncated recombinant human vitronectin (Thermo Fisher Scientific) and passaged once a week.

Generation of Retinal Organoids From hiPSCs

Human iPSC were differentiated toward retinal organoids following a modified protocol based on previous publications (Reichman et al., 2014, 2017). Briefly, hiPSC lines were expanded to 80% confluence in Essential 8TM medium were switched in Essential 6TM medium (Thermo Fisher Scientific). After 2 days, cells were cultured to a proneural medium (Table 2). The medium was changed every 2–3 days. At day 28, neural retina-like structures grew out of the cultures and were mechanically isolated and further cultured in a 3D system in maturation medium for 70 days. Floating organoids were cultured in a six well-plate and supplemented with 10 ng/ml FGF2 (fibroblast growth factor 2, PeproTech) until D35. Additionally, between D44–D50, 10 µM DAPT (*N*-[*N*-(3,5-difluorophenacetyl)-L-alanyl]-S-phenylglycine t-butyl ester, Selleckchem) was added to the maturation medium in order to promote the PR lineage

TABLE 2 | Medium composition.

Proneural medium	Maturation medium
Essential 6 TM Medium (Thermo Fisher Scientific, A1516401)	DMEM/F-12 (Thermo Fisher Scientific, 11320074)
N-2 supplement (100X) 1% (Thermo Fisher Scientific, 17502048)	B27 Supplement (100X), 2% (Thermo Fisher Scientific, 17504044)
Penicillin-streptomycin 1% (Thermo Fisher Scientific, 15140122)	MEM non-essential amino acids solution (100X), 1% (Thermo Fisher Scientific, 11140035)
	Penicillin-streptomycin 1% (Thermo Fisher Scientific, 15140122)

TABLE 3 | List of primers and taqman probes.

Gene	Taqman probe
<i>BRN3B</i>	Hs00231820_m1
<i>CRX</i>	Hs00230899_m1
<i>18S</i>	Hs99999901_s1

commitment of retinal progenitors. Medium was changed every 2 days (**Figure 2A**).

Infection of Retinal Organoids With AAV

Introduction of each optogene was done by a single infection at day 44 at a 5×10^{10} vg per organoid using AAV2-7m8 (Dalkara et al., 2013) carrying each optogene (ChrimsonR, hCatCh, ReaChR, eNpHR 2.0, eNpHR 3.0, Jaws, hLWO, mSWO) under the control of ubiquitous CAG promoter and fused to the fluorescent reporter GFP. For GFP-only-expressing controls, an infection with AAV2-7m8-CAG-GFP was used.

RNA Isolation and Real-Time RT-qPCR

Total RNA isolation was performed using a RNeasy Mini Kit (Qiagen), according to the manufacturer's instructions. RNA concentration and purity were determined using a NanoDrop ND-1000 Spectrophotometer (Thermo Fisher Scientific).

Reverse transcription was carried out with 250 ng of total RNA using the QuantiTect retrotranscription kit (Qiagen). Quantitative PCR (qPCR) reactions were performed using Taqman Array Fast plates and Taqman Gene expression master mix (Thermo Fisher Scientific) for *CRX* and *BRN3B* and *S18* in an Applied Biosystems real-time PCR machine (7500 Fast System). All samples were normalized against a housekeeping gene (*18S*) and the gene expression was determined based on the $\Delta\Delta CT$ method relative to D35. Average values were obtained from at least four biological replicates. The primer sets and MGB probes (Thermo Fisher Scientific) labeled with FAM for amplification are listed in **Table 3**.

Tissue Preparation and Immunostaining

Seventy-day-old organoids were washed in PBS and fixed in 4% paraformaldehyde for 10 min at 4°C before they were incubated overnight in 30% sucrose (Sigma-Aldrich) in PBS. Organoids were embedded in gelatin blocks (7.5% gelatin (Sigma-Aldrich), 10% sucrose in PBS) and frozen using isopentane at -50°C.

TABLE 4 | List of primary antibodies.

Antibody (antigen)	Reference	Specie	Clonality	Dilution
CRX	Atlas	Rabbit	Polyclonal	1/50
BET1L	Abcam	Rabbit	Polyclonal	1/250
BIP (GRP78)	Abcam	Rabbit	Polyclonal	1/1000
BRN3A	Millipore	Mouse	Monoclonal	1/250
GFP	Abcam	Chicken	Polyclonal	1/500
GOS28 (GosR1)	Antibodies-online	Mouse	Polyclonal	1/250
KDEL (GRP78 and GRP94)	Abcam	Mouse	Monoclonal	1/500
RCVRN	Millipore	Rabbit	Polyclonal	1/2000
WGA-rhodamine (lectin)	Vector Laboratories			1/2000

10 μ m thick sections were obtained using a Cryostat Microm and mounted on Super Frost Ultra Plus[®] slides (Menzel Gläser, Braunschweig, Germany).

Cryosections were permeabilized in PBS containing 0.5% Triton X-100 during 1 h at RT. Blocking was done with PBS containing 0.2% gelatin, 0.25% Triton X-100 for 30 min at RT and incubation with primary antibodies was performed overnight at 4°C. Primary antibodies used are listed in **Table 4**. After incubation with primary antibodies, sections were washed with PBS containing 0.25% Tween20 and incubated with fluorochrome-conjugated secondary antibodies (1/500 dilution) for 1 h at RT. Nuclei were counterstained with DAPI (4'-6'-diamino-2-phenylindole dihydrochloride, Sigma-Aldrich) at a 1/1000 dilution. After washing, the slides were mounted with fluoro-gel (Electron Microscopy Sciences) mounting medium.

Retinal Organoid Immunostaining and Clearing

The protocol is based on the 3D imaging of solvent-cleared organ (3DISCO) clearing procedure (Belle et al., 2014), recently adapted to retinal organoids (Reichman et al., 2017). After 4% PFA fixation, 10 min at 4°C and PBS-washing, the organoids were permeabilized and blocked in 1X PBS + 0.2% gelatin + 0.5% Triton X-100 (PBSGT) overnight under rotation. Primary antibodies were incubated for 3 days at 37°C under rotation. The samples were washing for 1 day in PBSGT changing the bath four times. Secondary antibodies were incubated with the organoids at 37°C overnight under rotation. After four times washing in PBSGT the samples were embedded in agarose prior to clearing and processing in confocal microscopy. For clearing procedure, the samples were dehydrated in tetrahydrofuran solution (THF) anhydrous, containing 250 ppm butylated hydroxytoluene inhibitor (Sigma-Aldrich), in ascending concentrations (50%, 80%, and 100%) diluted in H₂O. All washes lasted 1 h at RT in the dark, on a tube rotator. Next, the samples were placed in the lipid-removal solution dichloromethane (DCM; Sigma-Aldrich) for 30 min under rotation followed by an overnight clearing step in dibenzyl ether (DBE; Sigma-Aldrich). Samples

were kept in light-protection glass vials in DBE at RT until confocal acquisitions.

Image Acquisition

Immunofluorescence was observed using a Leica DM6000 microscope (Leica Microsystems) equipped with a CCD CoolSNAP-HQ camera (Roper Scientific) or using an inverted or upright laser scanning confocal microscope (FV1000, Olympus) with 405, 488, 515, and 635 nm pulsing lasers. The images were acquired sequentially with the step size optimized based on the Nyquist–Shannon theorem. The analysis was conducted in FIJI (NIH). Images were put into a stack, Z-sections were projected on a 2D plane using the MAX intensity setting in the software's Z-project feature, and the individual channels were merged.

CODIM

Confocal Imaging

The microscope used includes a commercial Nikon C2 confocal system (Nikon Corporation). The confocal scan head is plugged to a Nikon TiE Eclipse inverted microscope. All confocal images were acquired using a 1024×1024 pixels format with an averaging of two frames with a pixel dwell time of 4.9 μ s.

Super-Resolution Imaging

Super-resolution imaging was performed with a commercial CoDiM (Caron et al., 2014; Fallet et al., 2014). The BioAxial super-resolution module (CODIM100, BioAxial) is an add-on integrated to the Nikon confocal system previously described. The CODIM module acts as a powerful beam shaper generating local structured illumination. A sCMOS camera plugged at the back port of the microscope (Orca Flash 4.0, Hamamatsu Photonics) is used for the detection generating individual micro-images for each scanning point containing independent information. The set of all micro-images obtained from the scan procedure are processed and reconstructed by CODIM algorithm (Nesterov, 2005) to generate a super-resolved image. In both confocal and super-resolution modalities, a 60x 1.49NA Oil immersion Nikon Plan Apo TIRF objective was used to focus the laser beam and collect of the emitted fluorescence. The 488 and 561 excitation wavelengths of a multi laser engine (iChrome MLE, Toptica Photonics Inc.) are used for fluorescence excitation. The confocal image captures were performed using Nikon Nis-Elements software (Nikon Instruments Europe). The laser power was properly chosen to be out of the saturation regime. Confocal and super-resolution montages were subsequently built in ImageJ (NIH).

Cell Counts

For image analysis at least 12 microscopic fields from each sample were taken randomly using a 40x lens objective in an Olympus FV1000 confocal microscope. To reduce human bias, a semi-automated image analysis system was used to determine the percentage of immunoreactive cells from digital images using Metamorph NX[®] v7.5.1.0 Software.

Live Two-Photon Imaging and Patch-Clamp Recordings of Photocurrents in Optogenetically Engineered Retinal Organoids

Retinal organoids were placed in the recording chamber of the microscope at 36°C in oxygenated (95% O₂/5% CO₂) Ames medium (Sigma-Aldrich) during the whole experiment.

A custom-made two-photon microscope equipped with a 25x water immersion objective (XLPlanN-25x-W-MP/NA1.05, Olympus) equipped with a pulsed femto-second laser (InSight[™] DeepSee[™] – Newport Corporation) was used for imaging and targeting AAV-transduced fluorescent retinal organoids (GFP-positive cells). Two-photon images were acquired using the excitation laser at a wavelength of 930 nm. Images were processed offline using ImageJ (NIH).

For patch-clamp recordings, AAV-transduced fluorescent cells were targeted with a patch electrode under visual guidance using the reporter tag's fluorescence. Whole-cell recordings were obtained using the Axon Multiclamp 700B amplifier (Molecular Device Cellular Neurosciences). Patch electrodes were made from borosilicate glass (BF100-50-10, Sutter Instrument) pulled to 6–9 M Ω and filled with 115 mM K gluconate, 10 mM KCl, 1 mM MgCl₂, 0.5 mM CaCl₂, 1.5 mM EGTA, 10 mM HEPES, and 4 mM ATP-Na₂ (pH 7.2). Photocurrents were recorded while voltage-clamping cells at a potential of –60 mV.

A monochromatic light source [Polychrome V, TILL photonics (FEI)] was used to stimulate cells with a pair of 450 or 590 nm full-field light pulses during electrophysiological experiments and hence record photocurrents. Stimuli were generated using custom-written software in LabVIEW (National Instruments) and output light intensities, of 1×10^{16} and 3.2×10^{17} photons cm⁻² s⁻¹, were calibrated using a spectrophotometer (USB2000+, Ocean Optics).

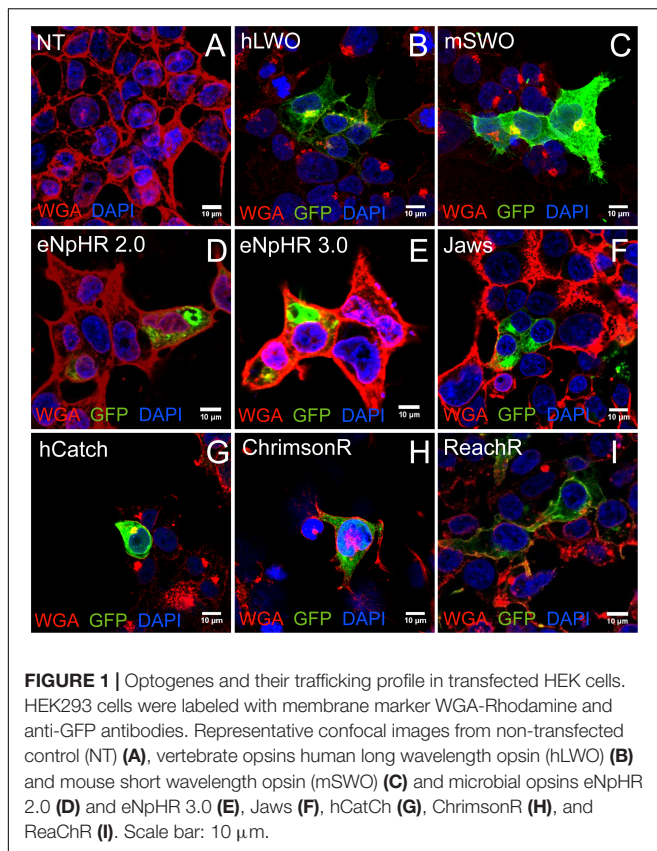
Statistical Analyses

Data was analyzed with GraphPad Prism and it was expressed as mean \pm standard error of mean (SEM) of at least four independent biological replicates, except for immunocytochemistry for which a representative image from at least three independent assays was depicted in the figures. Comparisons between values were analyzed using unpaired non-parametric Mann–Whitney Student's *t*-test. A level of $p < 0.05$ was considered significant. The labels used were: * for $p < 0.05$, ** for $p < 0.01$, *** for $p < 0.0001$.

RESULTS

Subcellular Localization of Microbial and Vertebrate Opsins in HEK Cells

Given the widespread use of HEK cells, we aimed to determine the expression and localization of several microbial opsins in relation to mouse and human opsins in this cell type. Depolarizing channelrhodopsins (hCatCh, ChrimsonR, and ReaChR), halorhodopsins from prokaryotes (eNpHR 2.0, eNpHR 3.0 and Jaws), Vertebrate Opsins such as mouse Short-Wave



Opsin (OPN1SW, referred to as mSWO) and human Long-Wave Opsin (OPN1LW referred to as hLWO) (Masseck et al., 2014) were used in this assay (Table 1). Confocal imaging was used to assess subcellular distribution of each opsin (Figure 1). The vertebrate opsins hLWO and mSWO (Figures 1B,C) localized to the membrane and were also found in the ER to Golgi pathway and cytoplasm. ReachR and Jaws (Figures 1F,I) displayed almost as efficient membrane trafficking as hLWO whereas hCatCh and ChrimsonR (Figures 1G,H) were found mostly in the perinuclear region. Despite the ER escape and membrane trafficking sequences introduced into eNpHR 2.0 and eNpHR 3.0 (Figures 1D–E) we did not observe significant improvement in membrane trafficking in HEK cells.

Even though developmentally, it has been suggested that HEK cells may have features of a neuronal lineage (Shaw et al., 2002) and are likely to display similar biological functions such as protein folding and trafficking, they do not represent the human retinal context and therefore may not recapitulate all of the features of human retinal neurons. Hence, we sought to complement our data in a model, representing the human retinal context.

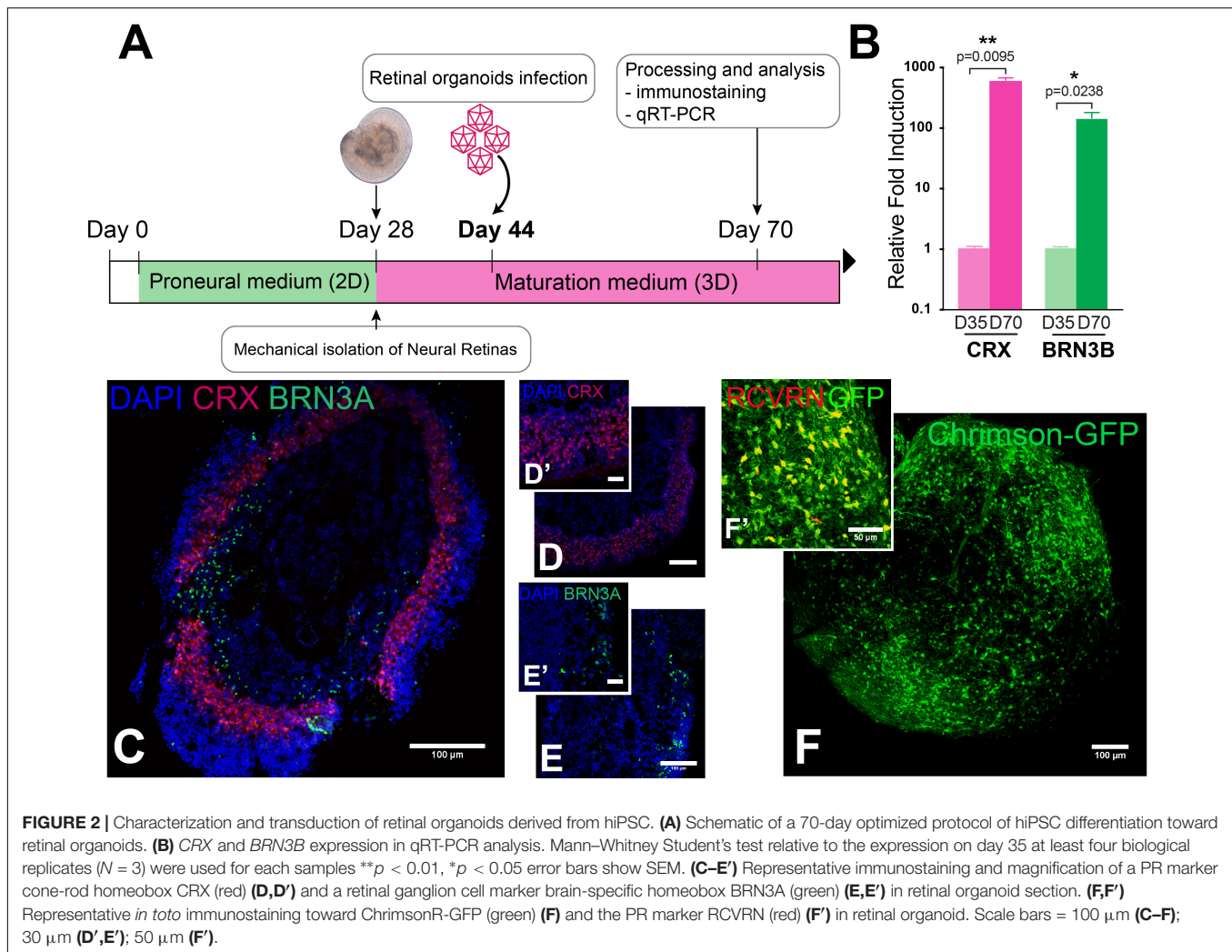
Opsin Expression in Retinal Organoids Derived From hiPSC

Human induced pluripotent stem cell-derived retinal organoids mimic the human retinal environment and can be used to rapidly screen optogenetic tools in human retinal cells both in terms of

membrane trafficking efficiency and functional light responses. HiPSCs were differentiated toward retinal organoids in 70 days following an optimized procedure based on a previously published 2D/3D protocol allowing the growth of neural retinal structures (Reichman et al., 2017). The 2D steps take 28 days, then differentiated 3D structures are mechanically isolated and matured in pro-neural medium (Figure 2A). Gene delivery in retinal organoids was achieved using a single infection with AAV2-7m8 encoding the microbial opsin or GFP at day 44 of differentiation, (Figure 2A). In all the constructs, the optogene was fused to GFP to track down the localization of the protein. After infection, cell cycle arrest is induced by addition of the gamma secretase inhibitor DAPT, which also allows for the enrichment of the more abundant PR population (Osakada et al., 2008; Reichman et al., 2014). Immunofluorescence on cryosections of day 70 retinal organoids identified a large number of cells expressing specific markers of PR lineage such as CRX (Figures 2C,D,D') and RCVRN (Figure 2F'). The PR precursors lacked outer segments indicating they were not fully mature. Interestingly the PR precursor cells were found in a layer in the outer border of the retinal organoids, getting closer to the *in vivo* conditions, instead of forming the rosettes as described in absence of DAPT (Reichman et al., 2017). A sparse population of RGCs, positive for BRN3A, was also present at day 70 (Figures 2C,E,E'). The presence of these two cell populations were confirmed with RT-qPCR analysis of relative expression of *CRX* and *POU4F2* (*BRN3B*) genes, which were upregulated at day 70 compared to expression at day 35 (Figure 2B). To study the spatial localization of different optogenes in the organoids we performed whole-mount labeling against GFP and the PR marker RCVRN followed by 3 DISCO clearing. This technique, allowed us to visualize all infected cells without the need for sectioning as shown here for cleared-organoids expressing ChrimsonR-GFP (Figure 2F). Confocal acquisitions and 3D analyses of the cleared-samples showed colocalization of GFP and RCVRN confirming the PR-enriched nature of our organoids (Figure 2F') and the AAV transduction pattern obtained in this context.

Membrane Trafficking and Light Responses of Optogenes in Engineered hiPSC-Derived Retinal Organoids

Five engineered optogenes were analyzed in this study including eNpHR 3.0, Jaws, hCatCh, ChrimsonR and ReaChR (Figure 3). We did not include eNpHR 2.0 as it showed an almost identical membrane expression to eNpHR 3.0 (Figures 1D,E). The membrane localization of each opsin was compared to a GFP-only control. As expected, the cells transduced with the GFP-only control presented cytosolic expression (Figure 3A). Among the several optogenes we tested, the depolarizing opsins hCatCh and ChrimsonR (Figures 3D,G) showed reduced trafficking compared to ReaChR (Figure 3J), optimized for membrane expression. Concerning the hyperpolarizing opsins, Jaws (Figure 3M) showed a better membrane localization compared to eNpHR 3.0 (Figure 3P). Live two-photon imaging of transduced cells, showing endogenous cells fluorescence, confirmed these results



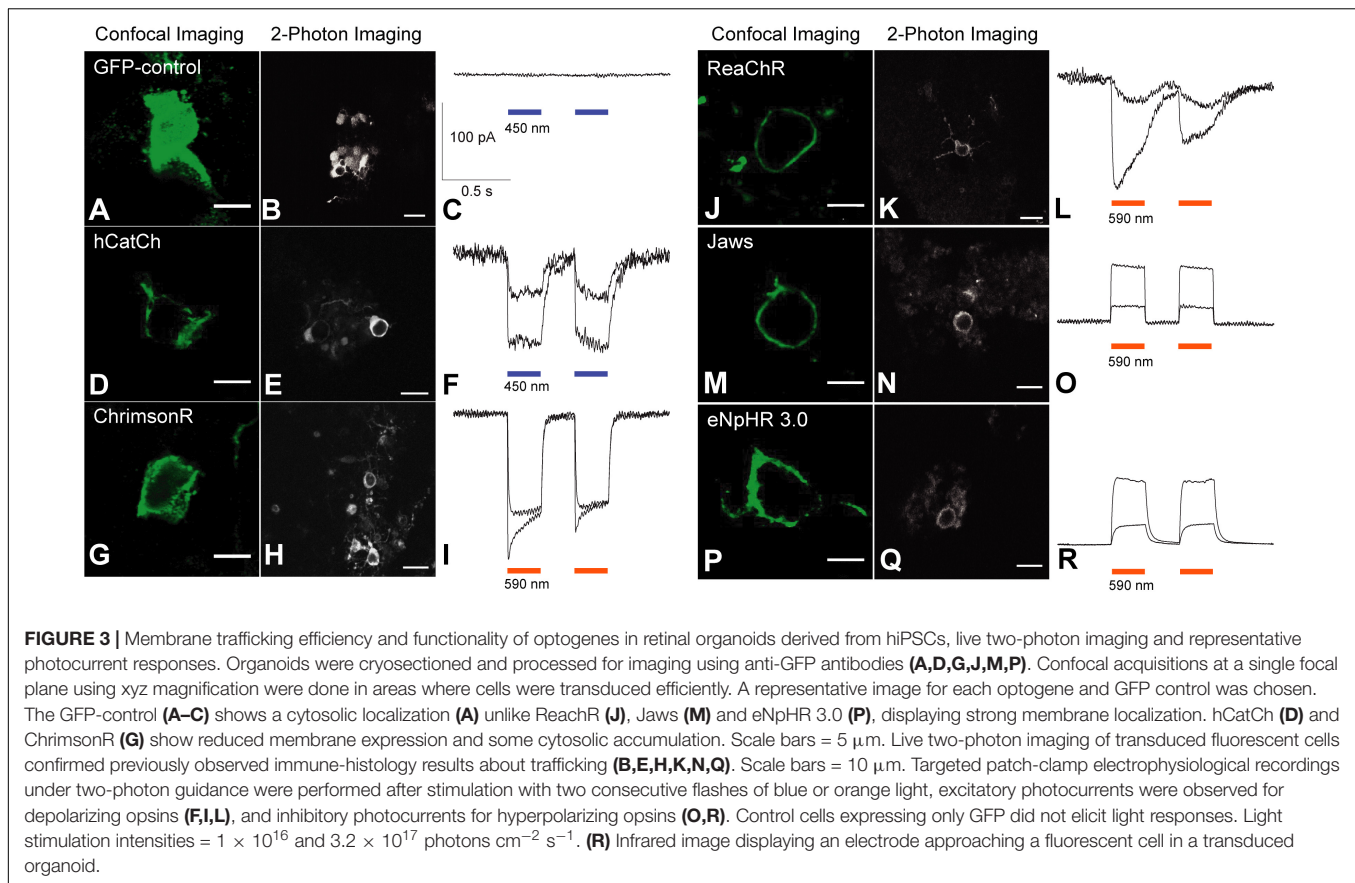
(Figures 3B,E,H,K,N,Q). To test for functionality, two-photon targeted patch-clamp electrophysiological recordings were performed. Light stimulation either in blue or orange depending on the spectral characteristics of each opsin were used, at two different intensities. Flashes of light elicited excitatory photocurrents in the case of depolarizing opsins (Figures 3F,I,L), and inhibitory photocurrents for hyperpolarizing opsins (Figure 3O), while no responses were recorded in control cells expressing only GFP (Figure 3C). Hence, despite their differential membrane expression, all of the microbial opsins drove light-responses in retinal organoids.

Subcellular Localization of Optogenes in Retinal Organoids Derived From hiPSCs

Expression of optogenetic tools in retinal neurons must lead to sufficient membrane trafficking to prevent ER stress associated safety concerns. For example, it is known that mutations on the rhodopsin gene can impair its folding and membrane trafficking leading to cell death (Athanasίου et al., 2018). In a similar way, deficiencies in membrane trafficking of microbial opsins can

lead to negative consequences such as ER stress. We sought to characterize the subcellular localization of ChromsonR and hCatCh, the two assayed microbial opsins showing deficient membrane expression and cytoplasmic protein retention.

In order to study this, we used antibodies marking endogenous ER-resident proteins containing the KDEL retention signal (KDEL), Golgi SNAP receptor complex member 1 (GOS28) and BET1L, which stain the ER, the Golgi apparatus, and the post-Golgi trafficking vesicles, respectively. As shown in the Figure 4, hCatCh and ChromsonR showed heterogeneous distribution across the secretory pathway in different cells. hCatCh showed some co-localization with ER and Golgi markers (Figures 4A,B) whereas ChromsonR did not display major accumulation in any of these organelles based on colocalization of GFP immunofluorescence with organelle markers (Figures 4D–F). To confirm the possible opsin retention in cell organelles, we thus used a super-resolution microscope incorporated with the CODIM technology to strengthen our analysis. We focused on the ER marker for this study as ER retention is more likely to be associated with adverse events whereas the presence of opsins in the Golgi and vesicles would be expected to some extent as part



of the continual process of protein production. Using CODIM we could distinguish colocalization of GFP and KDEL marker in some cells and no colocalization in others (**Supplementary Figure S1**). Altogether these results suggest that there was no major difficulty in endosomal release for these opsins but that colocalization was found as a normal part of the continual processing of opsins on the secretory pathway.

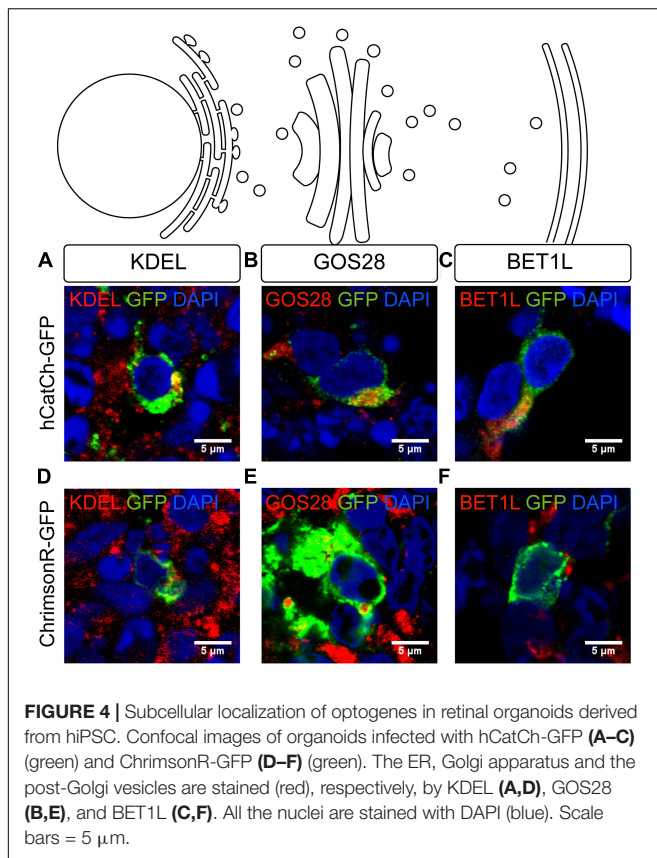
UPR Responses of Transduced Retinal Cells ChrimsonR and hCatCh

Endoplasmic reticulum accumulation of unfolded proteins can result in ER stress and eventually lead to toxicity (Saliba et al., 2002; Nemet et al., 2015). The production and accumulation of unfolded proteins within the ER must be resolved to restore cell homeostasis. Activating UPR leads to enhanced protein folding or degradation. To achieve this, UPR triggers the dissociation of the chaperone BiP from the mediators of UPR, which are PKR-like ER kinase (PERK), activating transcription factor (ATF6) and inositol-requiring kinase/endo-RNase 1 (IRE1). However, if UPR does not resolve the ER stress, UPR switches from its pro-survival function to activate the pro-apoptotic transcription factor CHOP (**Figure 5A**). It has been recently suggested that ER stress might contribute to the degenerative PR process, using hiPSCs from an RP patient carrying a *RHODOPSIN* mutation (Yoshida et al., 2014). Similarly, we aimed to determine if hCatCh and ChrimsonR led to UPR activation in retinal organoids. To

follow the UPR activation, we quantified the number of cells positive for BiP in retinal organoids expressing hCatCh and ChrimsonR (**Figure 5E**). In hCatCh-expressing retinal organoids, BiP was higher than in control organoids (**Figures 5B,C,E**), indicating activation of the UPR response, while ChrimsonR expression did not increase the number of BiP-positive cells (**Figures 5B,D,E**). This data suggests that the occasional labeling of ER observed with hCatCh-expressing organoids is indicative of an ER accumulation and activation of UPR, which could eventually induce apoptotic pathways and have an adverse effect on cell health.

DISCUSSION

Several optogenetic-based therapeutic strategies have successfully targeted different retinal neurons in mouse models of retinal degeneration. AAV-mediated delivery achieved stable expression of ChR2 variants in the RGCs of rodent models of retinal degeneration (Bi et al., 2006; Tomita et al., 2009, 2014; Sugano et al., 2011; Sengupta et al., 2016). ChR2 has also been used to target bipolar cells in the *rd1* mouse model (Lagali et al., 2008; Doroudchi et al., 2011; Macé et al., 2015) and resensitization of dormant cone PRs has been achieved in mice and monkeys using eNpHR and Jaws (Busskamp et al., 2010; Chuong et al., 2014; Khabou et al., 2018). Based on these works, two recent clinical trials were started to test the potential of microbial



opsin-based vision restoration in the clinic (NCT02556736 and NCT03326336). Promising results from these initial trials will pave the way to refinements leading to second-generation optogenetic therapies for vision restoration. Refinements in parameters such as the use of better AAV vectors and promoters have already been subject of previous studies by our group (Chaffiol et al., 2017; Khabou et al., 2018). However, thus far there has been no systematic comparison of the trafficking profile of the various opsins on a representative human neuronal cell model. Cultured rodent neurons or HEK cells have been extensively used to screen trafficking profiles and to monitor light response properties of optogenes with whole-cell patch clamp recordings (Gradinaru et al., 2008; Mattis et al., 2011; Chuong et al., 2014; Klapoetke et al., 2014). However, neuronal cultures from rodents and mouse models of RP are suboptimal for studying the trafficking efficiency of opsins since rodent and primate cells use different trafficking signals and handle protein folding differently. HEK cells on the other hand, are an easy-to-use, human-cell model but they are not neurons. To study trafficking patterns of microbial opsins in a human retinal context, we thus used hiPSC-derived retinal organoids.

Retinal organoids derived from hiPSCs constitute an excellent model for gene delivery studies providing the human context and disease modeling possibilities (Quinn et al., 2018). Our robust protocol of differentiation produces large amounts of cones but lacking outer segment structures. What could be seen as a disadvantage for cell therapy is an advantage for

the better prediction of optogene behavior in RP patients given that in early stages the first hallmark of disease is the loss of PR outer segments. We extensively optimized AAV-mediated transduction of our retinal organoids; which allowed the efficient delivery of optogenes without compromising cell viability on day 44. This might correspond to the timepoint of differentiation where the organoids are mature enough to be stably infected. Trafficking efficiency and good membrane expression of microbial opsins remains crucial for clinical applications of optogenetics. Membrane trafficking plays a fundamental role in the efficacy but also in the potential toxicity induced by opsin expression. Screening optogenes using this relevant retinal organoid model uncovered a range of trafficking profiles among the tested optogenes. eNpHR 3.0, Jaws and ReachR displayed an almost exclusive membrane expression while ChrimsonR and hCatCh presented some percentage of non-membrane bound expression in the immature cones of a human retinal organoids. This result might be partially explained by the lack of membrane trafficking sequences in ChrimsonR and hCatCh (Table 1). Trafficking defects are well known among certain microbial opsins (Gradinaru et al., 2010; Bedbrook et al., 2017) and are a concern that needs to be addressed considering trafficking defects may lead to unwanted toxicity. For instance, rhodopsin mutations like P23H, P347S, S334ter lead to aggresome formation, ER accumulation or post-Golgi trafficking defects of rhodopsin (Saliba et al., 2002; Athanasiou et al., 2018). The trafficking between ER and the membrane involves several quality controls through the intracellular organelles for a proper sorting of transmembrane proteins. Hence, the occasional labeling of ER observed with hCatCh is indicative of an ER accumulation with adverse effects on cell health.

Retinal organoids are useful for predicting expression patterns of ectopic proteins, such as microbial opsins providing opportunities to evaluate their folding and localization. Despite some trafficking issues, cells expressing ChrimsonR and hCatCh showed light responses consistent with the literature (Kleinlogel et al., 2011; Klapoetke et al., 2014; Chaffiol et al., 2017). The subcellular characterization of opsin trafficking suggests some colocalization with ER but no systematic retention in this structure. Moreover, all microbial opsins tested in this work showed functional activation with light and did not lead to visible toxicity or cell death within the organoids. It is important to note that the choice of a microbial opsin for vision restoration is also driven by other parameters such as the target cell type, the action spectrum of the opsin and temporal response properties. Moreover, expression profile of the same opsin can differ in different subsets of neurons. In our study, we restricted the analysis of opsin expression patterns to the PR precursors as this population is enriched and localized on the outside of the organoids. The fact that this population is enriched and more easily accessible than the sparse RGC population localized in the center of the organoids did not allow us to study the behavior of optogenes in different neuronal subtypes. It should also be noted that we could not make any conclusions on the potential immunogenicity of microbial opsins based on screening in an *in vitro* organoid system. Nevertheless, keeping the parameters such as vector, promoter, fluorescent protein, expression time,

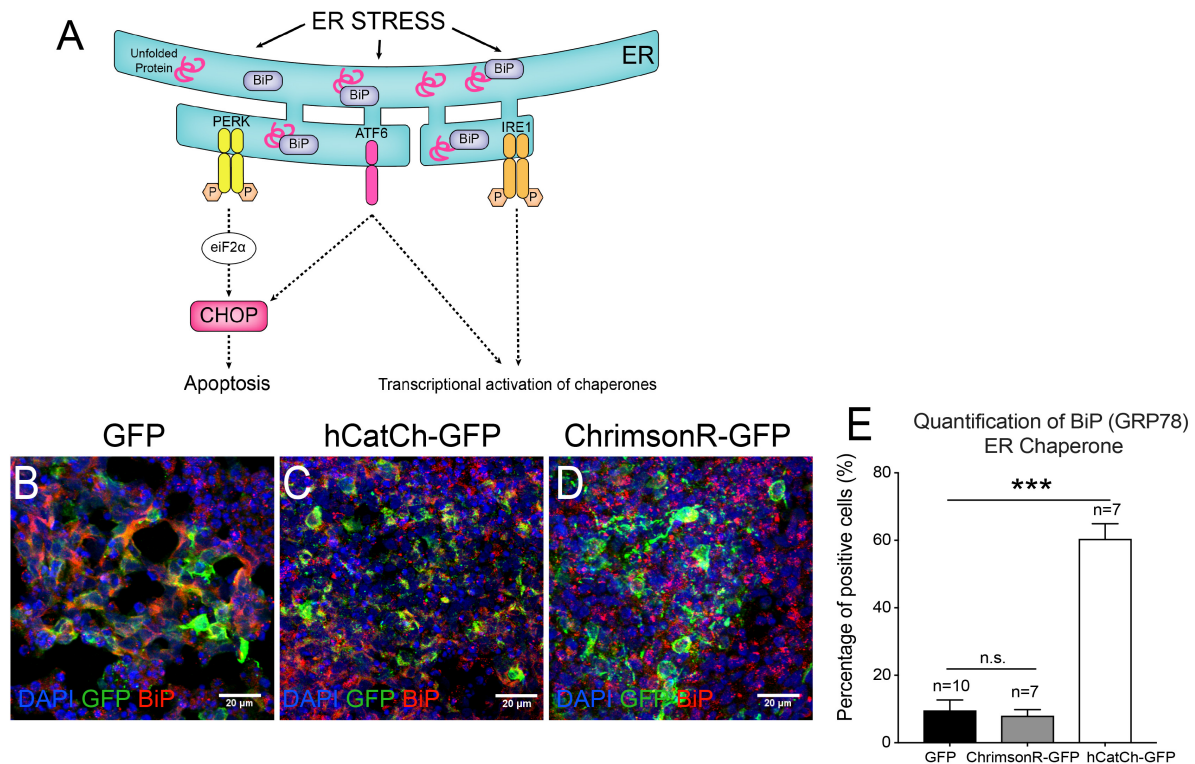


FIGURE 5 | UPR responses of retinal cells expressing microbial opsins. Unfolded proteins in the ER trigger the dissociation of the chaperone BiP (binding immunoglobulin protein) from the mediators of unfolded protein response, which are PKR-like ER kinase (PERK), activating transcription factor (ATF6) and inositol-requiring kinase/endo-RNase 1 (IRE1). It initiates biochemical cascades leading to an increase of the pro-apoptotic C/EBP homologous protein (CHOP) expression but also a transcriptional activation of chaperones (A). Confocal images (B–D) and histogram quantification (E) from hiPSC-derived organoids infected with CAG-GFP (B), CAG-hCatCh-GFP (C) or CAG-ChrimsonR-GFP (D) expressing BiP (in red). Mann-Whitney Student's test relative to the percentage of positive cells on CAG-GFP control organoids. $N = 3$, *** $p < 0.0001$.

illumination, and cell type granted us an unbiased side-by-side comparison of the different opsins. The optogenes tested here might show different trafficking properties in different retinal neurons or when coupled with different fluorescent proteins allowing better solubility and membrane trafficking (Allen et al., 2015).

CONCLUSION

In this study, we used for the first time human retinal organoids derived from hiPSCs to evaluate membrane trafficking efficiency and toxicity of microbial opsins that have been used for vision restoration studies in the past. This model has allowed us to evaluate the expression patterns and their effect on cell health, which can be useful for future opsin engineering studies with clinical application in mind.

AUTHOR CONTRIBUTIONS

MG-H optimized the generation of optogenetically transformed hiPSC-derived retinal organoids, performed culture, imaging, RT-qPCR, optimized histology, designed the experiments,

analyzed the data, lead the project, and wrote the manuscript. LG and LT generated optogenetically transformed hiPSC-derived retinal organoids, performed immunostainings, imaging, RT-qPCR, and helped to write the manuscript. FR maintained the hiPSC lines and generated hiPSC-derived retinal organoids, helped with imaging and histology. AC designed and performed patch-clamp recordings and 2-photon imaging and contributed with the manuscript. CW performed HEK cell cultures, transfections, and stainings. MH performed histology and imaging. CR produced the AAV virus. SF helped with confocal acquisitions of 3D-cleared transformed organoids. SB acquired and analyzed the CODIM images. J-AS gave feedback on the manuscript, provided scientific input, and financial and administrative support. OG provided hiPSCs and gave feedback on the manuscript. JD gave feedback on the manuscript. DD designed the experiments and wrote the manuscript.

FUNDING

This work was supported by ERC Starting Grant (OPTOGENRET, 309776/JD) the Centre National de la Recherche Scientifique (CNRS), the Institut National de la Santé et de la Recherche Médicale (INSERM), Sorbonne Université,

The Foundation Fighting Blindness (Wynn-Gund translational research award) (J-AS), Marie Curie CIG (334130, RETINAL GENE THERAPY) ERC Starting Grant (REGENETHER, 639888/DD) and ANR RHU Light4Deaf (DD), INSERM, Labex-Lifesenses (JD and DD), LCL Foundation (DD).

ACKNOWLEDGMENTS

We thank Emilie Keomani for her help producing viral vectors, Eleonor Bombard for help with cloning, Amelie Slembrouck-Brec for her help in the maintenance of the iPSC cultures, Karen Daoud and Parisa Khalilian for their assistance cryosectioning the organoids. We are grateful to Morgane Belle for assistance with 3DISCO clearing protocol. This work has benefited from the

Photonic Bio Imaging platform of Imagopole (Institut Pasteur). We thank Stefan Herlitze for providing the hLWO and mSWO plasmids and Serge Picaud for feedback and discussions.

SUPPLEMENTARY MATERIAL

The Supplementary Material for this article can be found online at: <https://www.frontiersin.org/articles/10.3389/fnins.2018.00789/full#supplementary-material>

FIGURE S1 | CODIM Super-resolution imaging for trafficking characterization. Heterogeneous colocalization results observed for Chrimson-GFP and hCatch-GFP and the ER marker KDEL (red). GFP displayed a cytosolic distribution that in some cases escaped the ER and in others clearly colocalized with KDEL indicating ER retention (arrowhead). Scale bars = 1 μ m.

REFERENCES

- Allen, B. D., Singer, A. C., and Boyden, E. S. (2015). Principles of designing interpretable optogenetic behavior experiments. *Learn. Mem.* 22, 232–238. doi: 10.1101/lm.038026.114
- Athanasios, D., Aguila, M., Bellingham, J., Li, W., McCulley, C., Reeves, P. J., et al. (2018). The molecular and cellular basis of rhodopsin retinitis pigmentosa reveals potential strategies for therapy. *Prog. Retin. Eye Res.* 62, 1–23. doi: 10.1016/j.preteyeres.2017.10.002
- Aurnhammer, C., Haase, M., Muether, N., Hausl, M., Rauschhuber, C., Huber, I., et al. (2012). Universal real-time PCR for the detection and quantification of adeno-associated virus serotype 2-derived inverted terminal repeat sequences. *Hum. Gene Ther. Methods* 23, 18–28. doi: 10.1089/hgtb.2011.034
- Bedbrook, C. N., Yang, K. K., Rice, A. J., Gradinaru, V., and Arnold, F. H. (2017). Machine learning to design integral membrane channelrhodopsins for efficient eukaryotic expression and plasma membrane localization. *PLoS Comput. Biol.* 13:5786. doi: 10.1371/journal.pcbi.1005786
- Belle, M., Godefroy, D., Dominici, C., Heitz-Marchaland, C., Zelina, P., Hellal, F., et al. (2014). A simple method for 3D analysis of immunolabeled axonal tracts in a transparent nervous system. *Cell Rep.* 9, 1191–1201. doi: 10.1016/j.celrep.2014.10.037
- Berger, W., Kloeckener-Gruissem, B., and Neidhardt, J. (2010). The molecular basis of human retinal and vitreoretinal diseases. *Prog. Retin. Eye Res.* 29, 335–375. doi: 10.1016/j.preteyeres.2010.03.004
- Bi, A., Cui, J., Ma, Y.-P., Olshevskaya, E., Pu, M., Dizhoor, A. M., et al. (2006). Ectopic expression of a microbial-type rhodopsin restores visual responses in mice with photoreceptor degeneration. *Neuron* 50, 23–33. doi: 10.1016/j.neuron.2006.02.026
- Boyden, E. S., Zhang, F., Bamberg, E., Nagel, G., and Deisseroth, K. (2005). Millisecond-timescale, genetically targeted optical control of neural activity. *Nat. Neurosci.* 8, 1263–1268. doi: 10.1038/nn1525
- Busskamp, V., Duebel, J., Balya, D., Fradot, M., Viney, T. J., Siebert, S., et al. (2010). Genetic reactivation of cone photoreceptors restores visual responses in retinitis pigmentosa. *Science* 329, 413–417. doi: 10.1126/science.1190897
- Caron, J., Fallet, C., Tinevez, J. Y., Moisan, L., Braitbart, L. P., Sirat, G. Y., et al. (2014). Conical diffraction illumination opens the way for low phototoxicity super-resolution imaging. *Cell Adhes. Migr.* 8, 430–439. doi: 10.4161/cam.29358
- Chaffiol, A., Caplette, R., Jaillard, C., Brazhnikova, E., Desrosiers, M., Dubus, E., et al. (2017). A new promoter allows optogenetic vision restoration with enhanced sensitivity in macaque retina. *Mol. Ther.* 25, 2546–2560. doi: 10.1016/j.ymthe.2017.07.011
- Choi, V. W., Asokan, A., Haberman, R. A., and Samulski, R. J. (2007). Production of recombinant adeno-associated viral vectors. *Curr. Protoc. Hum. Genet.* 15, 4.17.1–4.17.30. doi: 10.1002/0471142905.hg1209s53
- Chuong, A. S., Miri, M. L., Busskamp, V., Matthews, G. A. C., Acker, L. C., Sorensen, A. T., et al. (2014). Noninvasive optical inhibition with a red-shifted microbial rhodopsin. *Nat. Neurosci.* 17, 1123–1129. doi: 10.1038/nn.3752
- Dalkara, D., Byrne, L. C., Klimczak, R. R., Visel, M., Yin, L., Merigan, W. H., et al. (2013). In vivo-directed evolution of a new adeno-associated virus for therapeutic outer retinal gene delivery from the vitreous. *Sci. Transl. Med.* 5:189ra76. doi: 10.1126/scitranslmed.3005708
- Deisseroth, K., Feng, G., Majewska, A. K., Miesenböck, G., Ting, A., Schnitzer, M. J., et al. (2006). Next-generation optical technologies for illuminating genetically targeted brain circuits. *J. Neurosci.* 26, 10380–10386. doi: 10.1523/JNEUROSCI.3863-06.2006
- Doroudchi, M. M., Greenberg, K. P., Liu, J., Silka, K. A., Boyden, E. S., Lockridge, J. A., et al. (2011). Virally delivered channelrhodopsin-2 safely and effectively restores visual function in multiple mouse models of blindness. *Mol. Ther.* 19, 1220–1229. doi: 10.1038/mt.2011.69
- Fallet, C., Caron, J., Oddos, S., Tinevez, J.-Y., Moisan, L., Sirat, G. Y., et al. (2014). “Conical diffraction as a versatile building block to implement new imaging modalities for superresolution in fluorescence microscopy,” in *Proceedings of the SPIE 9169, Nanoimaging Nanospectroscopy II*, Washington, DC, doi: 10.1117/12.2061059
- Fradot, M., Busskamp, V., Forster, V., Cronin, T., Léveillard, T., Bennett, J., et al. (2011). Gene therapy in ophthalmology: validation on cultured retinal cells and explants from postmortem human eyes. *Hum. Gene Ther.* 22, 587–593. doi: 10.1089/hum.2010.157
- Gradinaru, V., Thompson, K. R., and Deisseroth, K. (2008). eNpHR: a *Natronomonas halorhodopsin* enhanced for optogenetic applications. *Brain Cell Biol.* 36, 129–139. doi: 10.1007/s11068-008-9027-6
- Gradinaru, V., Zhang, F., Ramakrishnan, C., Mattis, J., Prakash, R., Diester, I., et al. (2010). Molecular and cellular approaches for diversifying and extending optogenetics. *Cell* 141, 154–165. doi: 10.1016/j.cell.2010.02.037
- Häusser, M. (2014). Optogenetics: the age of light. *Nat. Methods* 11, 1012–1014. doi: 10.1038/nmeth.3111
- Herlitze, S., and Landmesser, L. T. (2007). New optical tools for controlling neuronal activity. *Curr. Opin. Neurobiol.* 17, 87–94. doi: 10.1016/j.conb.2006.12.002
- Khabou, H., Desrosiers, M., Winckler, C., Fouquet, S., Auregan, G., Bemelmans, A.-P., et al. (2016). Insight into the mechanisms of enhanced retinal transduction by the engineered AAV2 capsid variant -7m8. *Biotechnol. Bioeng.* 113, 2712–2724. doi: 10.1002/bit.26031
- Khabou, H., Garita-hernandez, M., Chaffiol, A., Reichman, S., Jaillard, C., Brazhnikova, E., et al. (2018). Noninvasive gene delivery to foveal cones for vision restoration. *JCI Insight* 3:e96029. doi: 10.1172/jci.insight.96029
- Klapoetke, N. C., Murata, Y., Kim, S. S., Pulver, S. R., Birdsey-Benson, A., Cho, Y. K., et al. (2014). Independent optical excitation of distinct neural populations. *Nat. Methods* 11, 338–346. doi: 10.1038/nmeth.2836
- Kleinlogel, S., Feldbauer, K., Dempski, R. E., Fotis, H., Wood, P. G., Bamann, C., et al. (2011). Ultra light-sensitive and fast neuronal activation with the Ca²⁺-permeable channelrhodopsin CatCh. *Nat. Neurosci.* 14, 513–518. doi: 10.1038/nn.2776
- Lagali, P. S., Balya, D., Awatramani, G. B., Münch, T. A., Kim, D. S., Busskamp, V., et al. (2008). Light-activated channels targeted to ON bipolar cells restore visual

- function in retinal degeneration. *Nat. Neurosci.* 11, 667–675. doi: 10.1038/nn.2117
- Lin, J. Y., Knutsen, P. M., Muller, A., Kleinfeld, D., and Tsien, R. Y. (2013). ReaChR: a red-shifted variant of channelrhodopsin enables deep transcranial optogenetic excitation. *Nat. Neurosci.* 16, 1499–1508. doi: 10.1038/nn.3502
- Macé, E., Caplette, R., Marre, O., Sengupta, A., Chaffiol, A., Barbe, P., et al. (2015). Targeting channelrhodopsin-2 to ON-bipolar cells with vitreally administered AAV Restores ON and OFF visual responses in blind mice. *Mol. Ther.* 23, 7–16. doi: 10.1038/mt.2014.154
- Masseck, O. A., Spoida, K., Dalkara, D., Maejima, T., Rubelowski, J. M., Wallhorn, L., et al. (2014). Vertebrate cone opsins enable sustained and highly sensitive rapid control of Gi/o signaling in anxiety circuitry. *Neuron* 81, 1263–1273. doi: 10.1016/j.neuron.2014.01.041
- Mattis, J., Tye, K. M., Ferenczi, E. A., Ramakrishnan, C., O'Shea, D. J., Prakash, R., et al. (2011). Principles for applying optogenetic tools derived from direct comparative analysis of microbial opsins. *Nat. Methods* 9, 159–172. doi: 10.1038/nmeth.1808
- Nemet, I., Ropelewski, P., and Imanishi, Y. (2015). Rhodopsin trafficking and mistrafficking: signals, molecular components, and mechanisms. *Prog. Mol. Biol. Transl. Sci.* 132, 39–71. doi: 10.1016/bs.pmbts.2015.02.007
- Nesterov, Y. (2005). Smooth minimization of non-smooth functions. *Math. Program.* 103, 127–152. doi: 10.1007/s10107-004-0552-5
- Osakada, F., Ikeda, H., Mandai, M., Wataya, T., Watanabe, K., Yoshimura, N., et al. (2008). Toward the generation of rod and cone photoreceptors from mouse, monkey and human embryonic stem cells. *Nat. Biotechnol.* 26, 215–224. doi: 10.1038/nbt1384
- Pagon, R. A. (1988). Retinitis pigmentosa. *Surv. Ophthalmol.* 33, 137–177. doi: 10.1016/0039-6257(88)90085-9
- Quinn, P. M., Buck, T. M., Ohonin, C., Mikkers, H. M. M., and Wijnholds, J. (2018). Production of iPS-derived human retinal organoids for use in transgene expression assays. *Methods Mol. Biol.* 1715, 261–273. doi: 10.1007/978-1-4939-7522-8_19
- Reichman, S., Slembrouck, A., Gagliardi, G., Chaffiol, A., Terray, A., Nanteau, C., et al. (2017). Generation of storable retinal organoids and retinal pigmented epithelium from adherent human iPS cells in Xeno-free and feeder-free conditions. *Stem Cells* 35, 1176–1188. doi: 10.1002/stem.2586
- Reichman, S., Terray, A., Slembrouck, A., Nanteau, C., Orieux, G., Habeler, W., et al. (2014). From confluent human iPS cells to self-forming neural retina and retinal pigmented epithelium. *Proc. Natl. Acad. Sci. U.S.A.* 111, 8518–8523. doi: 10.1073/pnas.1324212111
- Saliba, R. S., Munro, P. M. G., Luthert, P. J., and Cheetham, M. E. (2002). The cellular fate of mutant rhodopsin: quality control, degradation and aggresome formation. *J. Cell Sci.* 115, 2907–2918.
- Sengupta, A., Chaffiol, A., Macé, E., Caplette, R., Desrosiers, M., Lampiè, M., et al. (2016). Red-shifted channelrhodopsin stimulation restores light responses in blind mice, macaque retina, and human retina. *EMBO Mol. Med.* 8, 1–17. doi: 10.15252/emmm.201505699
- Shaw, G., Morse, S., Ararat, M., and Graham, F. L. (2002). Preferential transformation of human neuronal cells by human adenoviruses and the origin of HEK 293 cells. *FASEB J.* 16, 869–871. doi: 10.1096/fj.01-0995fje
- Sugano, E., Isago, H., Wang, Z., Murayama, N., Tamai, M., and Tomita, H. (2011). Immune responses to adeno-associated virus type 2 encoding channelrhodopsin-2 in a genetically blind rat model for gene therapy. *Gene Ther.* 18, 266–274. doi: 10.1038/gt.2010.140
- Tomita, H., Sugano, E., Isago, H., Hiroi, T., Wang, Z., Ohta, E., et al. (2009). Channelrhodopsin-2 gene transduced into retinal ganglion cells restores functional vision in genetically blind rats. *Exp. Eye Res.* 90, 429–436. doi: 10.1016/j.exer.2009.12.006
- Tomita, H., Sugano, E., Murayama, N., Ozaki, T., Nishiyama, F., Tabata, K., et al. (2014). Restoration of the majority of the visual spectrum by using modified volvox channelrhodopsin-1. *Mol. Ther.* 22, 1434–1440. doi: 10.1038/mt.2014.81
- Yoshida, T., Ozawa, Y., Suzuki, K., Yuki, K., Ohya, M., Akamatsu, W., et al. (2014). The use of induced pluripotent stem cells to reveal pathogenic gene mutations and explore treatments for retinitis pigmentosa. *Mol. Brain* 7:45. doi: 10.1186/1756-6606-7-45
- Zhang, F., Vierock, J., Yizhar, O., Fenno, L. E., Tsunoda, S., Kianianmomeni, A., et al. (2011). The microbial opsin family of optogenetic tools. *Cell* 147, 1446–1457. doi: 10.1016/j.cell.2011.12.004

Conflict of Interest Statement: DD is a consultant for GenSight Biologics and an inventor on a patent of adeno-associated virus virions with variant capsid and methods of use thereof with royalties paid to Avalanche Biotech (WO2012145601 A2). OG and J-AS are inventors on a patent on iPSC retinal differentiation (WO2014174492 A1). J-AS is a founder and consultant for Pixium Vision and GenSight Biologics and is a consultant for Sanofi Fovea, Genesignal, and Vision Medicines.

The remaining authors declare that the research was conducted in the absence of any commercial or financial relationships that could be construed as a potential conflict of interest.

Copyright © 2018 Garita-Hernandez, Guibbal, Tualbi, Routet, Chaffiol, Winckler, Harinquet, Robert, Fouquet, Bellow, Sahel, Goureau, Duebel and Dalkara. This is an open-access article distributed under the terms of the Creative Commons Attribution License (CC BY). The use, distribution or reproduction in other forums is permitted, provided the original author(s) and the copyright owner(s) are credited and that the original publication in this journal is cited, in accordance with accepted academic practice. No use, distribution or reproduction is permitted which does not comply with these terms.



Tapered Fibers Combined With a Multi-Electrode Array for Optogenetics in Mouse Medial Prefrontal Cortex

Leonardo Sileo^{1†}, Sebastian H. Bitzenhofer^{2†}, Barbara Spagnolo^{1†}, Jastyn A. Pöpplau^{2†}, Tobias Holzhammer^{3,4}, Marco Pisanello¹, Filippo Pisano¹, Elisa Bellistri¹, Emanuela Maglie^{1,5}, Massimo De Vittorio^{1,5}, Patrick Ruther^{3,6†}, Ileana L. Hanganu-Opatz^{2†} and Ferruccio Pisanello^{1*†}

OPEN ACCESS

Edited by:

Mikhail Lebedev,
Duke University, United States

Reviewed by:

Sotiris Masmanidis,
University of California, Los Angeles,
United States
Kuan Hong Wang,
National Institute of Mental Health
(NIMH), United States

*Correspondence:

Ferruccio Pisanello
ferruccio.pisanello@iit.it

[†] These authors have contributed
equally to this work as first authors

[‡] These authors have contributed
equally to this work as last authors

Specialty section:

This article was submitted to
Neural Technology,
a section of the journal
Frontiers in Neuroscience

Received: 31 July 2018

Accepted: 04 October 2018

Published: 26 October 2018

Citation:

Sileo L, Bitzenhofer SH,
Spagnolo B, Pöpplau JA,
Holzhammer T, Pisanello M, Pisano F,
Bellistri E, Maglie E, De Vittorio M,
Ruther P, Hanganu-Opatz IL and
Pisanello F (2018) Tapered Fibers
Combined With a Multi-Electrode
Array for Optogenetics in Mouse
Medial Prefrontal Cortex.
Front. Neurosci. 12:771.
doi: 10.3389/fnins.2018.00771

¹ Istituto Italiano di Tecnologia, Center for Biomolecular Nanotechnologies, Arnesano, Italy, ² Developmental Neurophysiology, Institute of Neuroanatomy, University Medical Center Hamburg-Eppendorf, Hamburg, Germany, ³ Department of Microsystems Engineering (IMTEK), University of Freiburg, Freiburg im Breisgau, Germany, ⁴ ATLAS Neuroengineering bvba, Leuven, Belgium, ⁵ Dipartimento di Ingegneria dell'Innovazione, Università del Salento, Lecce, Italy, ⁶ Cluster of Excellence BrainLinks-BrainTools, University of Freiburg, Freiburg im Breisgau, Germany

Optogenetics offers many advantages in terms of cell-type specificity, allowing to investigate functional connectivity between different brain areas at high spatial and neural population selectivity. In order to obtain simultaneous optical control and electrical readout of neural activity, devices called “optrodes” are employed. They are typically composed of a linear array of microelectrodes integrated on a slender probe shafts combined with flat-cleaved optical fibers (FF) placed above the recording sites. However, due to tissue absorption and scattering, light delivered by the FF unevenly illuminates the region of interest. This issue is of particular relevance when cellular populations are disposed along the dorso-ventral axis, such as in medial prefrontal cortex (mPFC) where cortical layers are aligned vertically. The study presented here aims at using tapered optical fibers (TFs) in combination with a 16-electrode neural probe to better access neural populations distributed along the dorso-ventral axis in the mPFC of newborn mice, restricting light delivery over a specific portion of the cortical layer of interest. Half of the TF surface is coated with a reflecting metal blocking the light to enable light delivery from one side of the probe's shaft only, with the probe base being designed to host the fiber without interfering with the wire-bonds that connect the recording sites to a printed circuit board. Monte-Carlo simulations have been implemented to define the relative TF-probe position and to identify the light intensity distribution above the recording sites. *In vivo* recordings indicate that simultaneous optical stimulation and electrical readout of neural activity in the mPFC benefit from the use of the engineered TF-based optrode in terms of a more uniform light distribution along the dorso-ventral axis and the possibility of restricting light delivery to a subset of electrical recording sites of interest.

Keywords: optogenetics, optrode, optical fibers, medial prefrontal cortex, tapered fibers

INTRODUCTION

With the increasing use of optogenetics to investigate functional connectivity in the mouse brain, the development of implantable devices for the simultaneous optical control and electrical monitoring of neural activity has been a major research focus in recent years (Grosenick et al., 2015; Cho et al., 2016; Pisanello et al., 2016). In their earlier implementation, these opto-electrodes (optrodes) were composed of a single light source and a single recording electrode (Gradinaru et al., 2007). More than 10 years of development have allowed obtaining different configurations, in which multiple optical stimulation channels can be accompanied with multi electrode arrays (MEA), providing multi-point optical control and electrical readout of neural activity. This can be obtained with several technologies, including μ LEDs realized on one substrate comprising multiple recording sites (Wu et al., 2015) or on separate substrates (Ayub et al., 2016, 2017), flexible electronics (Kim et al., 2013; Goßler et al., 2014) or solid state waveguides (Segev et al., 2016; Schwaerzle et al., 2017; Lanzio et al., 2018) potentially providing multiple diffraction gratings for the outcoupling of light (Lanzio et al., 2018).

Although these technologies have the potential to help neuroscientists to better match stimulation and recording patterns with the anatomy of the brain region of interest, devices commonly used in neuroscience labs are still based on flat-cleaved optical fibers (FF) placed above linear arrays of electrodes for extracellular recording (Neuronexus, 2015; Atlas Neurotechnologies, 2017; Cambridge Neurotechnologies, 2017). However, this widely used approach encounters important limitations when the cellular population of interest is distributed along the dorso-ventral direction. Indeed, light emitted above the recording sites undergoes tissue attenuation and scattering. This results in a highly inhomogeneous distribution of power density, that can span several orders of magnitudes along the recording sites if they are positioned along more than 1 mm (Yizhar et al., 2011; Stujenske et al., 2015; Schmid et al., 2016). This fact is illustrated in **Figure 1A** with a Monte-Carlo simulation indicating the power density in brain tissue generated by an optical fiber with a numerical aperture NA = 0.22 and a core size of 100 μ m, emitting light above a linear array of 16 electrodes. As indicated by the iso-power density lines, one obtains a decrease in optical power by about two orders of magnitude from the top most recording site to the bottom one. The above-mentioned technologies based in microsystems engineering can help in challenging this issue by placing multiple emitters very close to the individual recording sites. However, these discrete sets of light delivery points face different pitfalls, such as a potential tissue heating induced by Joule's effects for μ LEDs, limited outcoupling efficiencies of diffraction gratings and the high commercialization costs to make these probes available to neuroscience labs. In this scenario, tapered optical fibers (TFs) (Pisanello et al., 2014, 2017) represent on the other hand a valid alternative to these approaches, allowing to tailor the light delivery pattern to the anatomy of the functional region of interest (Pisanello et al., 2018; Pisano et al., 2018). This is possible by exploiting two main features of these devices: (i) the narrowing waveguide

allows to exploit mode division demultiplexing to deliver light gradually along a specific segment of the taper (Pisanello et al., 2018); indeed, as the taper narrows, the number of guided modes supported by the waveguide decreases, with modes not allowed to propagate toward the tip being outcoupled around the taper, and (ii) the possibility of using metal coatings to mask emission and to direct light to specific sites and directions (Pisano et al., 2018).

In this work we describe the engineering of an optrode based on a TF placed besides a 16-electrodes silicon-based neural probe following the Michigan style. The tapered fiber is designed to deliver light to the tissue above a subset of recording sites by exploiting a gold coating deposited on one half of the taper. Monte-Carlo simulations are implemented to define the relative TF-shank placement to obtain a fairly uniform power density in the tissue above the selected electrodes. The geometrical assembly is specifically thought to deliver light on (and to record signal from) pyramidal neurons in layers 2/3 of the prelimbic (PL) region of the medial prefrontal cortex (mPFC), in which Channelrhodopsin (ChR2) was selectively expressed by means of *in utero* electroporation (IUE). Extracellular electrophysiology data in mice at postnatal day (P) 8–10 confirm that the device can be used to monitor both local field potentials and single unit action potentials, with the TF design allowing for a more uniform illumination above the chosen subset of recording sites.

RESULTS

Optrode Design and Fabrication

The optrode presented in this work has been designed with the goal of engineering light delivery in the mPFC of rodents. Area- and layer-specific stimulation in prefrontal networks is critical to understand the origin and significance of neuronal activity patterns. Layer-specific optogenetic stimulation in the mPFC can be achieved by layer-specific expression of ChR2 by IUE (**Figure 1C**) (Bitzenhofer et al., 2017a,b). However, the restriction of transfection to specific subdivisions of the mPFC is difficult to achieve with *in utero* electroporation, but critical to study prefrontal function due to different or even opposing functions of dorsal and ventral subdivisions of the mPFC (Hardung et al., 2017). The alternative approach to restrict stimulation is to limit the area of illumination in transfected tissue. However, most commercially available optrodes are often based on linear array of electrodes for extracellular recording combined with a FF placed above the probe shank, as illustrated in **Figure 1A**. This configuration results in a highly inhomogeneous illumination of neurons directly facing the recording sites, as quantified by the displayed iso-power density lines, obtained with the Monte-Carlo method published by Stujenske et al. (2015) to assess the power density distribution along the electrode carrying probe shank.

To overcome this limitation and to obtain a more uniform light intensity across specific recording sites, we engineered an optrode design consisting of a silicon-based probe in combination with a TF emitting light from one side of the silicon shank (**Figure 1B**). The optical design of the TF is optimized

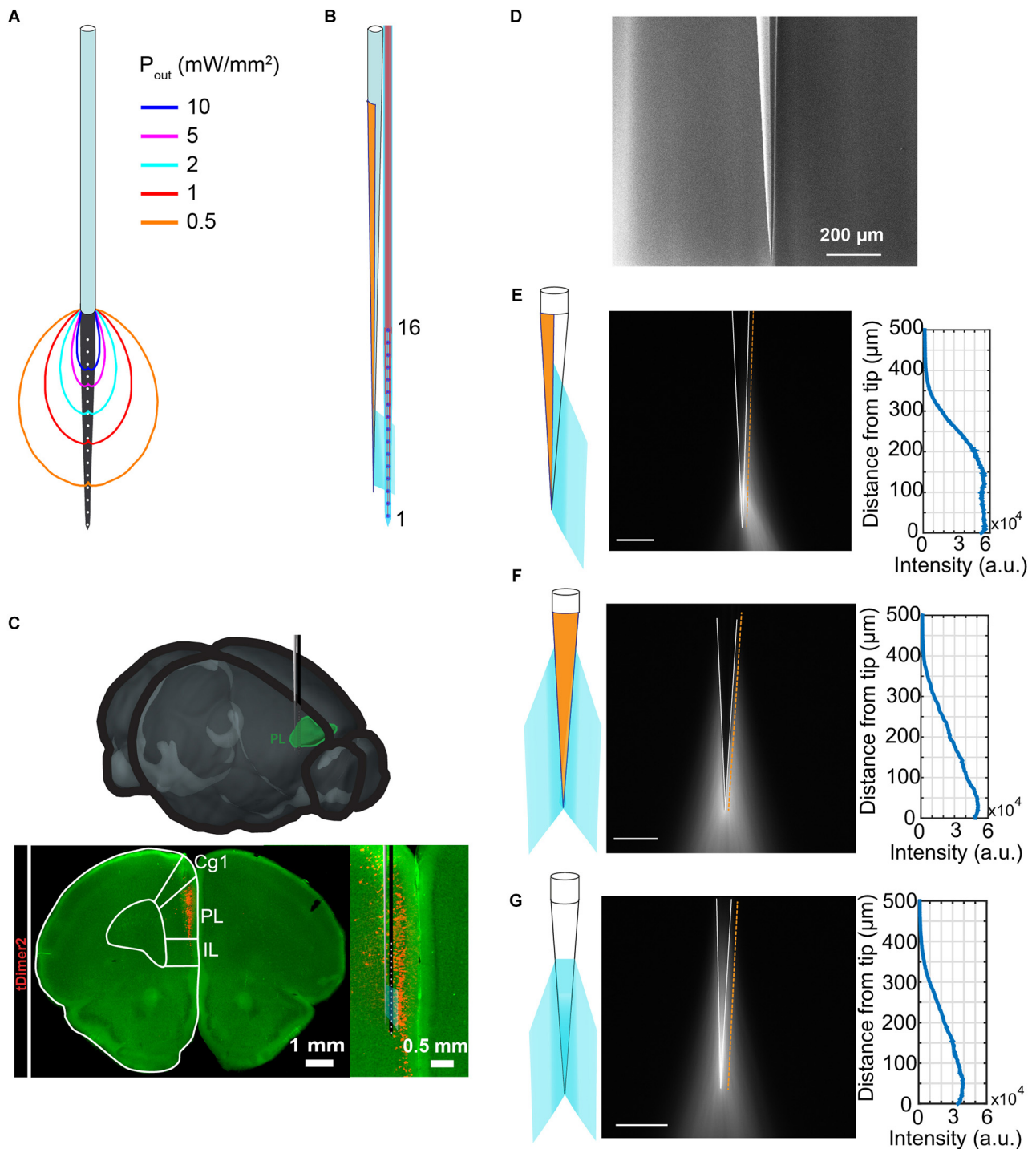


FIGURE 1 | Tailoring light delivery to a subregion of mPFC. **(A)** Representation of a commercially available optrode (A1 × 16-3mm-100-703-OA16LP, light fiber terminates 200 μm from the top recording site) and power density distribution iso-lines obtained with Monte-Carlo simulations for a total power of 1 mW delivered to the tissue. **(B)** Schematic representation of the optrode designed in this work, consisting of a half-metallized TF beside a multielectrode array. **(C)** Schematic overview of recording setup of the prelimbic subdivision of the mPFC. Digital photomontage reconstructing the position of the designed opto-electrode in the PL of a P9 mouse after IUE with ChR2(ET/TC) and tDimer2 (red) at embryonic age (E)15.5. Inset, optical light fiber (gray) and electrode shank (black) including the position of the recording sites (white) over the prelimbic depth are displayed at higher magnification. **(D)** Typical scanning electron microscope image of the realized TF. **(E–G)** Emission properties of the realized TF (side view) in a cartoon (left) and with the TF submerged in fluorescein:PBS droplet (center). Half of the taper is coated with ~5 nm of Cr and ~200 nm of Au. The graph (right) shows the emission profile acquired along the orange line in the center panel (scale bars represent 100 μm).

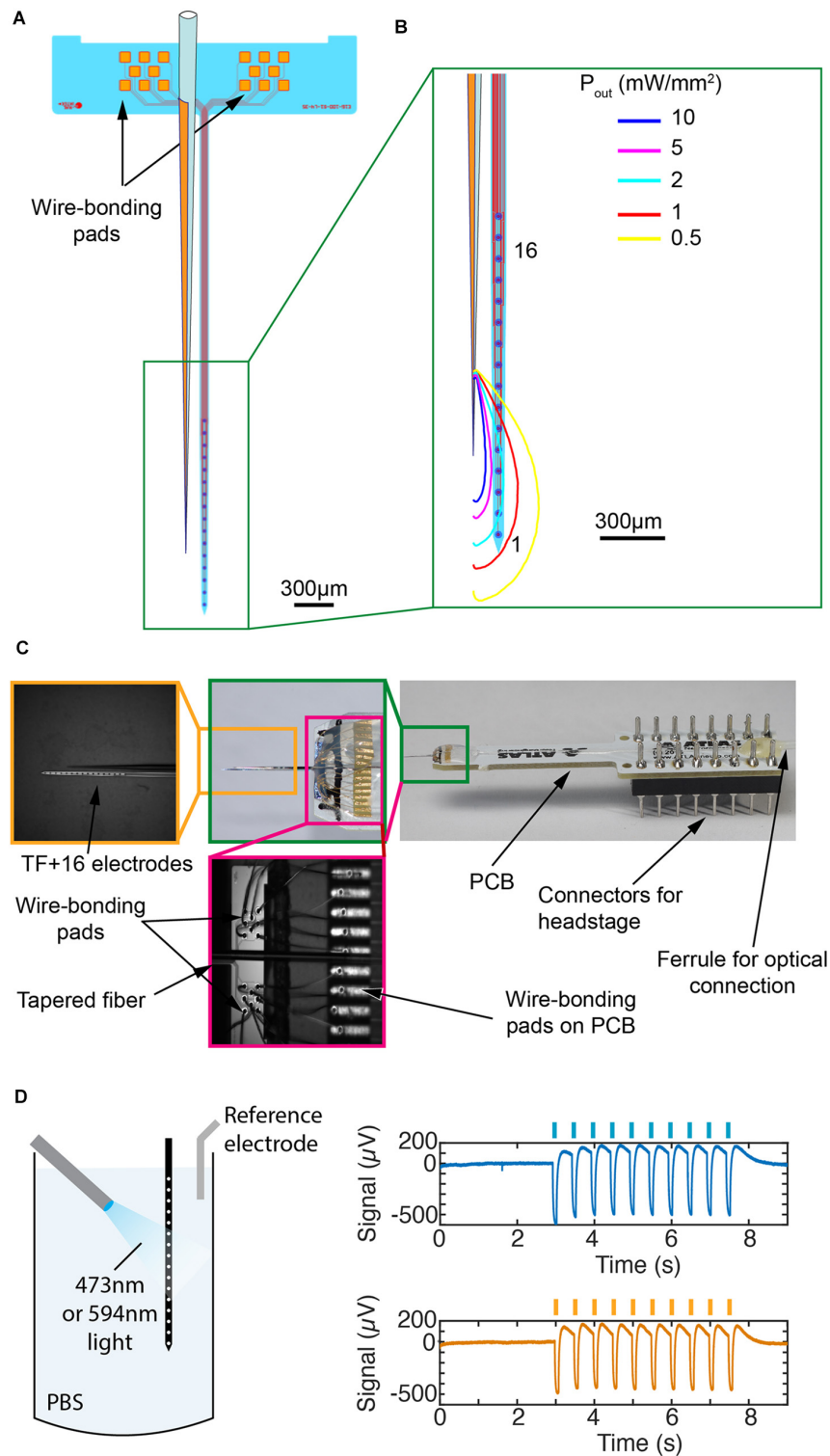


FIGURE 2 | Engineering of the TF-based optrode. **(A)** Layout of the silicon-based probe array with 16 IrO_x recording sites (diameter 35 μm) arranged at a pitch of 100 μm along a 4-mm-long probe shank and two groups of bonding pads arranged on the probe base (2.5 mm × 0.58 mm). Fiber position is also reported. **(B)** Monte-Carlo simulations of power density distribution iso-lines generated by the realized TF and overlapped with a sketch of the microelectrodes array. **(C)** Final optrode assembly on a PCB (right side) with enlarged view of the wire bonds on the probe base and PCB (center) and the tip region indicating the electrodes and TF (left). **(D)** Test of photoelectric effect induced by blue or yellow light in PBS. An optical fiber was placed 900 μm in front of the shank and delivers 200-ms-long pulses of 10 mW at wavelengths of 473 or 594 nm. The two graphs on the right show photoelectric effects generated by both wavelengths (the non-filtered signal is shown). Peak-to-peak amplitudes are 687 μV ± 13 μV and 624 μV ± 8 μV (mean ± std, $n = 10$) for the 473 and 594 nm lasers, respectively.

with the aim of providing a relatively uniform light intensity only in a region above selected recording sites along the probe shank. Further, the light emission geometry matches the dorso-ventral extension of the neural population of interest. Among the available TFs configurations (Pisano et al., 2018), we chose an optical fiber with core/cladding diameters of 105 μm /125 μm and a numerical aperture of $\text{NA} = 0.22$. The TF was realized by the heat-and-pull technique, resulting in a taper angle Ψ of $\sim 4^\circ$, which has already been shown to provide a tissue illumination over an extent of $\sim 400 \mu\text{m}$ (Pisanello et al., 2018). To deliver light only toward the shank, half of the taper is coated with a 200-nm-thick, thermally evaporated gold layer. A typical output of the fabrication process is shown in the scanning electron microscope image in **Figure 1D**, while the light delivery behavior of a TF with these geometrical characteristics is illustrated in **Figures 1E–G** for three different angular views, with the TF submerged in a fluorescent liquid. By virtue of the metal reflectivity, light delivery is confined to about 180° around the waveguide.

The neural probe applied here (see probe layout in **Figure 2A**) comprises a slender, tapered probe shaft with a maximum width of 75 μm at the probe base. The shaft carries 16 recording sites with a diameter of 35 μm arranged at a center-to-center distance of 100 μm . The probe shaft is connected to a rectangular probe base (2.5 mm \times 0.58 mm) on which two groups of eight contact pads (80 μm \times 80 μm) are arranged, interfacing the individual recording sites. The probe metallization is made of a layer stack of titanium/gold/titanium with the electrode metallization being realized by reactive sputter deposition and lift-off of iridium oxide. Probe shaft and base have a thickness of 50 μm and are realized using standard micro-electromechanical systems (MEMS) technologies combined with the etching before grinding (EBG) approach (Herwik et al., 2011).

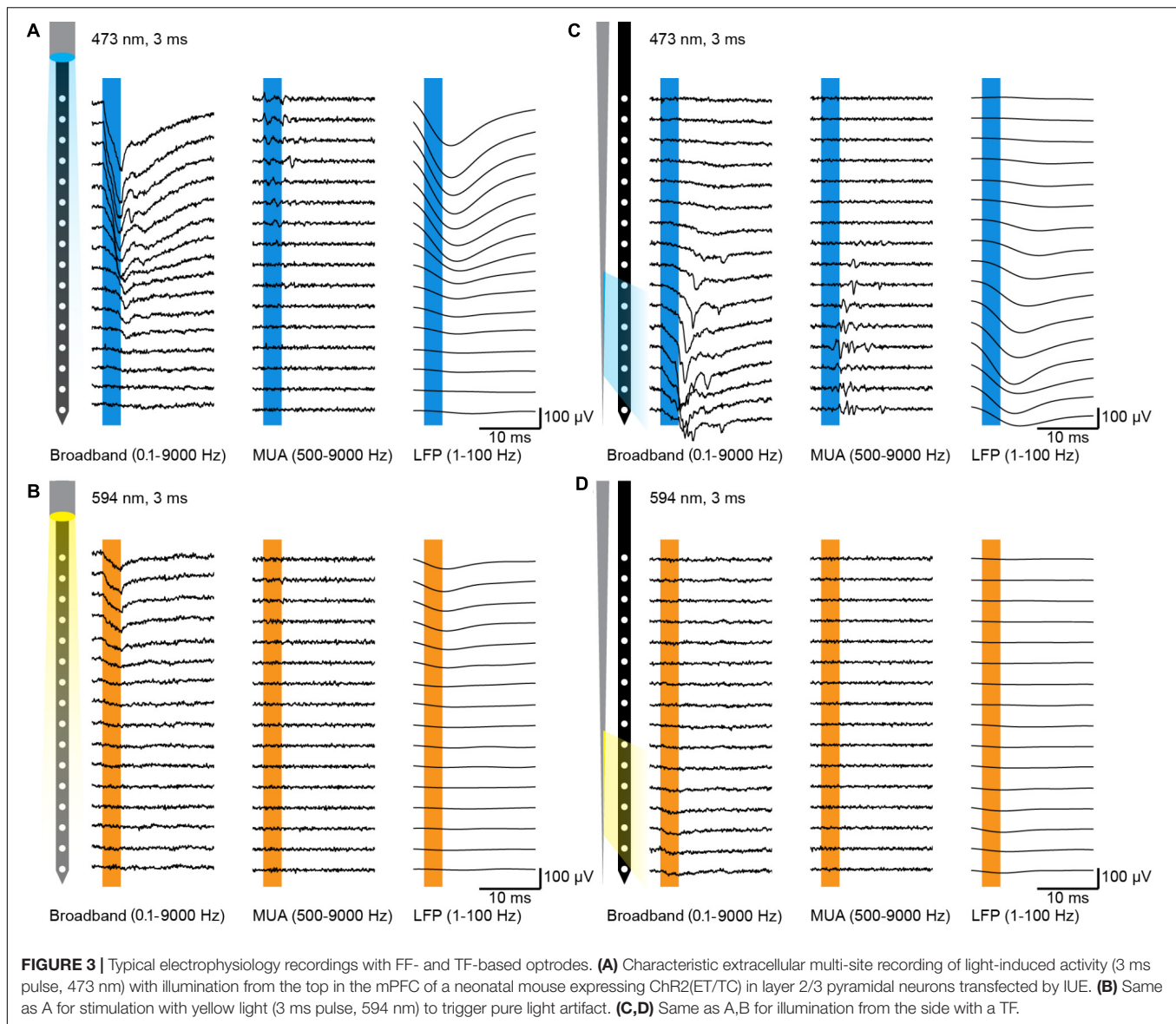
To estimate light delivery properties in scattering tissue and to define the relative TF-shank placement, a modified Monte-Carlo algorithm was implemented to take into account light emission along a tapered waveguide. This approach allows to estimate light distribution around the taper and to engineer the relative position between the TF and the probe shank. **Figure 2B** shows iso-power density lines for a TF which is placed at $\sim 150 \mu\text{m}$ beside the shank emitting a total optical power of 1 mW. Tissue above the electrodes #1 through #6 receive a relatively uniform power density of about 2 mW/mm². Recording sites #8 to #16 receive an optical power density $< 0.5 \text{ mW/mm}^2$, with a steep decrease across electrode #7. This represents a key difference between the TF-based optrode design and the commercially available system shown in **Figure 1A**, in which tissue above electrodes from #7 to #16 receive a power density above 2 mW/mm², but in a highly inhomogeneous way.

In order to position the TF within the above-mentioned distance relative to the probe shank, the electrical contact pads on the probe base interfacing the recording sites on the shank are laid out as depicted in **Figure 2A**, i.e., the two groups of eight pads are positioned off-center on the probe base with respect to the probe shaft position. This allows for

wire bonding the pads to a printed circuit board (PCB) while the optical fiber is positioned in-between the two groups of contact pads. The resulting optrode is shown in **Figure 2C**, assembled by using two computer-controlled micromanipulators to obtain a precise relative positioning and axial alignment between TF, probe shank and PCB. Once in place, the TF is adhesively fixed to the probe base using UV curable epoxy glue, which at the same time mechanically protects the wire bonds between the pads on the probe base pads and PCB. The optical microscopy image in **Figure 2C** illustrates the highly parallel alignment between TF and probe shank expected to minimize tissue damage during optrode insertion into the brain.

Optical Control and Electrical Readout of Neuronal Activity in the mPFC of Neonatal Mice

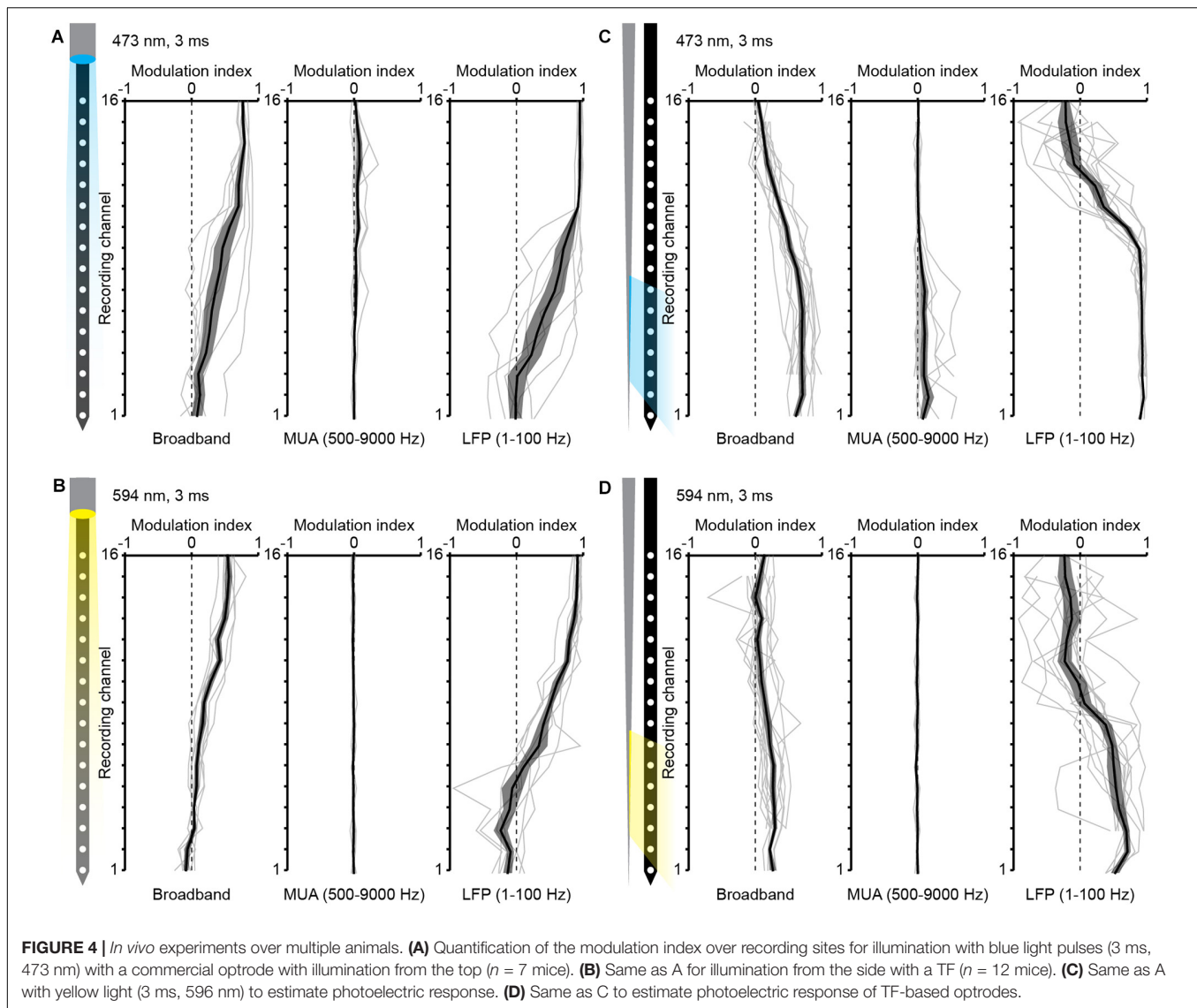
Light fibers on commercially available optrodes typically end above the top recording sites, i.e., the electrode positioned closest to the probe base. With this configuration light can be easily restricted to local patches of cortex at the surface of the brain, such as somatosensory or motor cortices. The mPFC is located at the midline of the forebrain with vertically oriented layers. With the available optrodes it is hard to restrict the inhomogeneous illumination of cortical patches to prefrontal subdivisions, especially for small sized neonatal mouse brains. In order to evaluate whether the TF-based optrode engineered in this work overcomes these limitations, we compared it to a commercially available FF-based optrode (NeuroNexus, A1 \times 16-3 mm-100-703-OA16LP, light fiber terminates 200 μm from the top recording site, **Figure 1A**) by using *in vivo* optogenetics in neonatal mice. For extracellular recordings the optrodes were inserted (2.4 mm) into the mPFC to reach ChR2-expressing pyramidal neurons in layers 2/3 of the prelimbic subdivision in mice at the age of (P) 8–10 (**Figure 1C**). Laser power for light delivery was adjusted to trigger neuronal spiking in response to $> 20\%$ of 3 ms-long light pulses at 16 Hz. Typical single channel local field potentials (LFPs, right column) and multi-unit activity (MUA, middle column), defined as activity in the frequency band from 500–9000 Hz, are displayed in **Figures 3A–D** for FF and TF optrodes, respectively. TF and FF induced neural activity was compared in response to blue light pulses (473 nm, total output power $\sim 1 \text{ mW}$, **Figures 3A,C**). Blue light pulses evoked comparable LFP and MUA for light delivery with TF and FF at the recording sites close to the fiber output, with the TF optrode eliciting neural activity on about 7 recordings sites starting from the tip, as expected from the Monte-Carlo simulations shown in **Figure 2B**. To characterize light artifacts of the probes and to distinguish them from induced activity in the same position where light-triggered activity is measured, yellow light pulses (594 nm, **Figures 3B,D**) that do not activate ChR2 were used. *Ex vivo* recordings of photoelectric effects with pulsed light of 473 and 594 nm induced similar light artifacts (**Figure 2D**). To evaluate the evoked responses over multiple animals, a modulation index was defined as $(x_{\text{stim}} - x_{\text{pre}})/(x_{\text{stim}} + x_{\text{pre}})$, where x_{stim} is the median amplitude of the



broadband signal, LFP or MUA in response to the light pulse and x_{pre} is the median signal amplitude before the pulse. Results of this analysis are reported in **Figure 4**. For both LFP and MUA channels, top illumination with FF evoked strong activity at the topmost recording sites with waning modulation toward the shaft's tip, whereas illumination with TF triggered activity mainly in the illuminated recording sites, as shown in **Figures 4A,C**, respectively. Compared to FF, TF-based optrodes illuminate a subset of recording sites more homogeneously resulting in more evenly distributed activity. Light artifacts recorded with yellow light stimulation were present in the frequency band of LFP, but not in MUA for TF and FF, as shown by the single channel data in **Figures 3B,D** and multiple animal averages in **Figures 4B,D**. Thus, TFs provide sufficient light output to trigger comparable activity in mPFC of neonatal mice as FF, with TF allowing for a more homogenous illumination of local cortical patches.

DISCUSSION AND CONCLUSION

In this work we propose an optrode design thought to better distribute light on cellular populations distributed in the dorso-ventral direction and to restrict illumination to subregions of the mPFC. It is based on a half-coated TF placed beside a 16-electrode silicon-based neural probe, whose relative position allows for delivering light to brain tissue addressed by a subset of the 16 recording sites. The system was tested on neonatal mice expressing ChR2 in layers 2/3 pyramidal neurons in the mPFC, distributed dorso-ventrally over ~ 2 mm, as shown in **Figure 1C**. To reduce the invasiveness of the optrode, also because of the mice's young age at the time of the experiment, we chose to work with the smallest-available TF (NA = 0.22, core/cladding diameters 105 μm /125 μm , taper angle $\Psi \approx 4^\circ$, sub-micrometer tip). FF commonly used to reach this region,



have diameters of 125 μm causing increased tissue damage. They generate light-stimulated activity over ~ 7 recording sites (Figure 3A) with a highly inhomogeneous power density, ranging from 20 mW/mm^2 to 2 mW/mm^2 , exponentially decreasing as the distance from facet increases (Figure 1A). Moreover, the geometrical configuration of FF-based optrodes has an intrinsic limitation related to fiber positioning: electrodes close to the shaft's tip interfacing with the less-damaged tissue can hardly be reached with a high-enough optical power density, unless light power delivered to the fiber is increased by two orders of magnitude (Schmid et al., 2016). Instead, placing a side-emitting TF beside the neural probe allows to direct light on the tissue above the selected recording sites. Although the data reported here are shown for illumination of recording sites close to the shank's tip, the TF/probe design enables using any subset of adjacent recording sites by changing the relative position of the TF along the probe shaft. To define the set of illuminated recording sites, a Monte-Carlo simulation

approach was implemented, allowing to identify the geometrical distribution of photons and the above-threshold region prior to the experiment. This, coupled with the possibility to engineer light delivery geometries by tailoring the taper angle (Pisanello et al., 2018) or using micro and nano fabrication approaches to structure the fiber taper (Pisanello et al., 2014, 2015; Pisano et al., 2018; Rizzo et al., 2018), let us envision that the TF-based optrode configuration can be extended to several experimental designs.

The activation of cells adjacent to specific subsets of recordings sites can be obtained also by other technologies, including optrodes based on μLEDs and solid-state waveguides. However, these approaches are based on different technological platforms that require complex fabrication processes, highly increasing the costs and time to bring them to market. Our design is instead based on a well-established combination between optical fibers and silicon-based neural probes following the Michigan style, and it requires only a few process steps to be modified: (i) layout of the

wire-bonding pads on the probe base and (ii) precise alignment and assembly of the TF relative to the probe shaft.

TF-based optrodes provide a better control of neuronal activity, due to homogenous illumination of several recording sites induced by the highly different distribution of light typically seen for FF-based optrodes. They also improve spatial restriction of illumination to local patches of vertically oriented cortical areas. The ability to homogeneously illuminate locally restricted patches in vertically oriented cortices, such as the mPFC, allows to investigate functions and interactions of prefrontal subdivisions, such as the prelimbic and infralimbic PFC throughout development. Overall, the optrode configuration proposed in this work allows for a better access to dorso-ventrally distributed neuronal populations, improving light delivery uniformity and to choose the position and the number of the recording sites to be illuminated.

MATERIALS AND METHODS

Realization of the Multi-Electrodes Probe

The silicon-based electrode array, as illustrated in **Figure 2A** with the respective mask layout, is realized using the etching before grinding (EBG) technology detailed elsewhere (Herwik et al., 2011). It applies 4-inch silicon (Si) wafers which are covered on their front side with a stress-compensated 1- μm -thick layer stack of silicon-oxide (SiO_x) and silicon nitride (Si_xN_y) realized by plasma enhanced chemical vapor deposition (PECVD). Next, the probe metallization which interfaces the recording sites with the contact pads via 1.5- μm -wide metal tracks is deposited and patterned using sputter deposition of titanium (Ti, 30 nm), gold (Au, 250 nm) and Ti (30 nm) and lift-off applying an image reversal resist, respectively. The metallization is covered by another, stress-compensated PECVD stack of $\text{Si}_x\text{O}/\text{Si}_x\text{N}_x$ (total thickness 1.5 μm). This layer stack is patterned using reactive ion etching (RIE) in combination with a positive photoresist serving as the masking layer to electrically access the contact pads ($80 \times 80 \mu\text{m}^2$) on the probe base and the recording sites through respective vias (diameter 5 μm). This etch step removes as well the upper Ti layer exposing the Au of the probe metallization. Next, the electrode metallization (diameter 35 μm) is deposited by sputter deposition and reactive sputter deposition of iridium (Ir, 100 nm) and iridium oxide (IrO_x , 200 nm), respectively. The Ir/ IrO_x layer stack is patterned using lift-off as well. Subsequently, we pattern the dielectric PECVD layer stacks (total thickness 2.5 μm) using RIE followed by deep reactive ion etching (DRIE) of the bulk silicon substrate to generate trenches (width 40 μm) defining to probe shape. These trenches are etched to a depth t_{etch} exceeding the intended probe shaft thickness t_{shaft} by 20 μm . Finally, the silicon wafer is ground from the rear using a commercial grinding process by DISCO Hi-TEC Europe GmbH (Kirchheim, Germany) to a thickness of 50 μm by which the probes are automatically released. Once peeled from an adhesive tape used during wafer grinding, the probes are ready for assembly. For this, probes are adhesively fixed onto a PCB and wire bonded using gold wires with a diameter of 25.4 μm .

Tapered Fibers Fabrication and Assembly With the Neural Probe

Tapered fibers were obtained from OptogeniX¹ with a taper angle of $\psi \approx 4^\circ$ and a numerical aperture of $\text{NA} = 0.22$ (core/cladding diameters 105/125 μm) (Pisanello et al., 2018). A 5-nm-thick Cr layer and a 200-nm-thick gold layer were deposited along the taper using evaporation which blocks ca. 180° of the TF from light emission. In order to ensure a correct deposition of the layers also close to the tip of the TF, the fiber was slightly tilted toward the crucibles during evaporation. After metal deposition, the obtained fibers were connectorized with a ceramic ferrule (diameter 1.25 mm) resulting in an overall fiber length that matches with the neural probe-PCB assembly (**Figure 2C**). Optical properties of the waveguide were tested in a PBS:fluorescein bath and emission profiles were determined by recording the fluorescence counts on a line parallel to the taper edge (**Figures 1E–G**).

The as prepared TF is fixed on a micromanipulator (Scientifica) and placed in parallel to the probe shank at a distance of $\sim 100 \mu\text{m}$ aligning the TF tip with the fifth electrode. The non-tapered fiber section is positioned in the space between the two groups of probe base bonding pads and fixed with UV curable epoxy glue.

Monte-Carlo Simulations

Monte-Carlo simulations were implemented in Matlab to estimate the power density distribution generated by flat-flat cleaved fibers (**Figure 1A**) or TFs (**Figure 2B**). In the case of FFs, the method proposed by Stujenske et al. (2015) was used to model an optical fiber with $\text{NA} = 0.22$ and core/cladding diameters of 105/125 μm , emitting a total power of 1 mW. In the case of metal-coated TFs, the code described in Stujenske et al. (2015) was modified in order to account for light emission from the conical surface of the taper. This was implemented by modifying the initial conditions of emitted photons in terms of emission position and output angles. Photon emission probability along the taper was estimated from the direct measurement of the light emission profile (see measurement in **Figure 1E**), while output angles were obtained by ray tracing simulations (Pisanello et al., 2018). Around the taper axis, photons emission probability was considered uniform in the angular range 0° to 180° and zero from 180° to 360° , to simulate the presence of the metal layer. Scattering was simulated in a domain of size 3 mm \times 3 mm, discretized with a mesh of 5 $\mu\text{m} \times 5 \mu\text{m}$. The matrix resulting from the simulation represents a spatial distribution of photons, weighted in intensity according to the energy left in a steady state (Stujenske et al., 2015). To draw the iso-power density lines in **Figures 1A** and **2B**, a 2-dimensional filter and a threshold were applied according to the examined power density volume. Output power was set to 1 mW and the Henyey–Greenstein scattering model was used at $\lambda = 473 \text{ nm}$, with absorption

¹www.optogenix.com

coefficient $a = 0.37 \text{ mm}^{-1}$, scattering coefficient $s = 11 \text{ mm}^{-1}$ and anisotropy parameter $g = 0.89$.

In utero Electroporation

All experiments were performed in compliance with the German laws and the guidelines of the European Community for the use of animals in research and were approved by the local ethical committee (Behörde für Gesundheit und Verbraucherschutz/Lebensmittelsicherheit und Veterinärwesen) (132/12, N18/015). Timed-pregnant C57Bl/6J mice were housed individually in breeding cages at a 12 h light/12 h dark cycle and fed *ad libitum*. Vaginal plug detection was defined embryonic day (E) 0.5, while birth was assigned as postnatal day (P) 0. Additional wet food supplemented with 2–4 drops Metacam (0.5 mg/ml, Boehringer-Ingelheim, Germany) was given from 1 day before until 2 days after surgery. At E15.5 pregnant mice were injected subcutaneously with buprenorphine (0.05 mg/kg body weight) 30 min before surgery. Surgery was performed under isoflurane anesthesia (induction: 5%, maintenance: 3.5%) on a heating blanket, eyes were covered with eye ointment, and toe pinch reflex and breathing were monitored throughout the surgery. Uterine horns were exposed and moistened with warm sterile PBS. 0.75–1.25 μl solution containing 1.25 $\mu\text{g}/\mu\text{l}$ DNA pAAV-CAG-ChR2(E123T/T159C)-2A-tDimer2 and 0.1% fast green dye were injected in the right lateral ventricle of each embryo using pulled borosilicate glass capillaries. Each embryo was placed between the electroporation tweezer-type paddles (5 mm diameter, Protech, TX, United States) oriented at a 20° leftward angle from the midline and a 10° angle downward from anterior to posterior to transfect neural precursor cells of layer 2/3 medial prefrontal pyramidal cells. Five electrode pulses (35 V, 50 ms, 950 ms interval) were applied with an electroporator (CU21EX, BEX, Japan). Uterine horns were placed back into the abdominal cavity after electroporation and abdominal muscles and skin were sutured.

In vivo Tests

Multi-site extracellular recordings were performed in the mPFC of P8–10 mice. Mice were injected i.p. with urethane (1 mg/kg body weight; Sigma-Aldrich, MO, United States) prior to surgery. Under isoflurane anesthesia (induction: 5%, maintenance: 2.5%) the head was fixed into a stereotaxic apparatus using two plastic bars mounted on the nasal and occipital bones with dental cement. The bone above the PFC (0.5 mm anterior to bregma, 0.1 mm right to the midline for layer 2/3) was carefully removed by drilling a hole of $< 0.5 \text{ mm}$ in diameter. After a 10–20 min recovery period on a heating blanket, linear multi-site optrodes with a flat-cleaved light fiber attached

ending 200 μm above the first recording site (NeuroNexus, MI, United States), or linear multi-site neural probes with a tapered light fiber attached were inserted 2.4 mm deep into the mPFC perpendicular to the skull surface. A silver wire in the cerebellum served as ground and reference electrode. Extracellular signals were band-pass filtered (0.1–9000 Hz) and digitized (32 kHz) with a multi-channel extracellular amplifier (Digital Lynx SX, Neuralynx, Bozeman, MO, United States) and the Cheetah acquisition software (Neuralynx, Bozeman, MO, United States). Pulsed light stimulations were performed with an arduino uno (Arduino, Italy) controlled laser (473 nm/594 nm, Omicron, Austria). Recording signals were band pass filtered to isolate local field potential (LFP, 1–100 Hz) and multi-unit activity (MUA, 500–9000 Hz) using a third-order Butterworth filter forward and backward to preserve phase information. To reduce signal contamination by photoelectric effects, 10-ms-long time windows starting 1 ms after the end of the light pulse were analyzed.

DATA AVAILABILITY STATEMENT

The datasets for this study are available upon request to the authors.

AUTHOR CONTRIBUTIONS

All authors listed have made a substantial, direct and intellectual contribution to the work, and approved it for publication.

FUNDING

FiP, BS, FeP, EB, and EM acknowledge funding from the European Research Council under the European Union's Horizon 2020 research and innovation program (#677683). MDV acknowledge funding from the European Research Council under the European Union's Horizon 2020 research and innovation program (#692943). SB, JP, and IH-O acknowledge funding from the European Research Council under the European Union's Horizon 2020 research and innovation program (#681577) and from the German Research Foundation [SFB 936 (B5) and SPP 1665 (Ha4466/12-1)]. LS, MP, and MDV are funded by the US National Institutes of Health (U01NS094190). This work was partly supported by BrainLinks-BrainTools, Cluster of Excellence funded by the German Research Foundation (DFG, Grant No. EXC 1086).

REFERENCES

- Atlas Neurotechnologies (2017). Available at: <http://www.atlasneuro.com/>
- Ayub, S., Barz, F., Paul, O., and Ruther, P. (2016). "Heterogeneous 3D optrode with variable spatial resolution for optogenetic stimulation and electrophysiological recording," in *Proceedings of the 38th Annual International Conference of the IEEE Engineering in Medicine and Biology Society (EMBC)*, (Piscataway, NJ: IEEE), 1762–1765. doi: 10.1109/EMBC.2016.7591058
- Ayub, S., Gentet, L. J., Fiáth, R., Schwaerzle, M., Borel, M., David, F., et al. (2017). Hybrid intracerebral probe with integrated bare LED chips for optogenetic studies. *Biomed. Microdevices* 19:49. doi: 10.1007/s10544-017-0190-3
- Bitzenhofer, S. H., Ahlbeck, J., and Hanganu-Opatz, I. L. (2017a). Methodological approach for optogenetic manipulation of neonatal neuronal networks. *Front. Cell. Neurosci.* 11:239. doi: 10.3389/fncel.2017.00239
- Bitzenhofer, S. H., Ahlbeck, J., Wolff, A., Wiegert, J. S., Gee, C. E., Oertner, T. G., et al. (2017b). Layer-specific optogenetic activation of pyramidal neurons

- causes beta–gamma entrainment of neonatal networks. *Nat. Commun.* 8:14563. doi: 10.1038/ncomms14563
- Cambridge Neurotechnologies (2017). Available at: <https://www.cambridgeurotech.com/>
- Cho, Y. K., Zheng, G., Augustine, G. J., Hochbaum, D., Cohen, A., Knöpfel, T., et al. (2016). Roadmap on neurophotonics. *J. Opt.* 18:093007. doi: 10.1088/2040-8978/18/9/093007
- Goßler, C., Bierbrauer, C., Moser, R., Kunzer, M., Holc, K., Pletschen, W., et al. (2014). GaN-based micro-LED arrays on flexible substrates for optical cochlear implants. *J. Phys. D Appl. Phys.* 47:205401. doi: 10.1088/0022-3727/47/20/205401
- Gradinaru, V., Thompson, K. R., Zhang, F., Mogri, M., Kay, K., Schneider, M. B., et al. (2007). Targeting and readout strategies for fast optical neural control in vitro and in vivo. *J. Neurosci.* 27, 14231–14238. doi: 10.1523/JNEUROSCI.3578-07.2007
- Grosenick, L., Marshel, J. H., and Deisseroth, K. (2015). Closed-loop and activity-guided optogenetic control. *Neuron* 86, 106–139. doi: 10.1016/J.NEURON.2015.03.034
- Hardung, S., Eppler, R., Jäckel, Z., Eriksson, D., Uran, C., Senn, V., et al. (2017). A functional gradient in the rodent prefrontal cortex supports behavioral inhibition. *Curr. Biol.* 27, 549–555. doi: 10.1016/j.cub.2016.12.052
- Herwik, S., Paul, O., and Ruther, P. (2011). Ultrathin silicon chips of arbitrary shape by etching before grinding. *J. Microelectromech. Syst.* 20, 791–793. doi: 10.1109/JMEMS.2011.2148159
- Kim, T., McCall, J. G., Jung, Y. H., Huang, X., Siuda, E. R., Li, Y., et al. (2013). Injectable, cellular-scale optoelectronics with applications for wireless optogenetics. *Science* 340, 211–216. doi: 10.1126/science.1232437
- Lanzio, V., West, M., Koshelev, A., Telian, G., Micheletti, P., Lambert, R., et al. (2018). High-density electrical and optical probes for neural readout and light focusing in deep brain tissue. *J. Micro Nanolithogr. MEMS MOEMS* 17:1. doi: 10.1117/1.JMM.17.2.025503
- Neuronexus (2015). Available at: <http://neuronexus.com/>
- Pisanello, F., Mandelbaum, G., Pisanello, M., Oldenburg, I. A., Sileo, L., Markowitz, J. E., et al. (2017). Dynamic illumination of spatially restricted or large brain volumes via a single tapered optical fiber. *Nat. Neurosci.* 20, 1180–1188. doi: 10.1038/nn.4591
- Pisanello, F., Sileo, L., and De Vittorio, M. (2016). Micro- and nanotechnologies for optical neural interfaces. *Front. Neurosci.* 10:70. doi: 10.3389/fnins.2016.00070
- Pisanello, F., Sileo, L., Oldenburg, I. A., Pisanello, M., Martiradonna, L., Assad, J. A., et al. (2014). Multipoint-emitting optical fibers for spatially addressable in vivo optogenetics. *Neuron* 82, 1245–1254. doi: 10.1016/j.neuron.2014.04.041
- Pisanello, M., Della Patria, A., Sileo, L., Sabatini, B. L., De Vittorio, M., and Pisanello, F. (2015). Modal demultiplexing properties of tapered and nanostructured optical fibers for in vivo optogenetic control of neural activity. *Biomed. Opt. Express* 6, 4014–4026. doi: 10.1364/BOE.6.004014
- Pisanello, M., Pisano, F., Sileo, L., Maglie, E., Bellistri, E., Spagnolo, B., et al. (2018). Tailoring light delivery for optogenetics by modal demultiplexing in tapered optical fibers. *Sci. Rep.* 8:4467. doi: 10.1038/s41598-018-22790-z
- Pisano, F., Pisanello, M., Sileo, L., Qualtieri, A., Sabatini, B. L., De Vittorio, M., et al. (2018). Focused ion beam nanomachining of tapered optical fibers for patterned light delivery. *Microelectron. Eng.* 195, 41–49. doi: 10.1016/j.mee.2018.03.023
- Rizzo, A., Lemma, E. D., Pisano, F., Pisanello, M., Sileo, L., De Vittorio, M., et al. (2018). Laser micromachining of tapered optical fibers for spatially selective control of neural activity. *Microelectron. Eng.* 192, 88–95. doi: 10.1016/J.MEE.2018.02.010
- Schmid, F., Wachsmuth, L., Schwalm, M., Prouvot, P.-H., Jubal, E. R., Fois, C., et al. (2016). Assessing sensory versus optogenetic network activation by combining (o)fMRI with optical Ca²⁺ recordings. *J. Cereb. Blood Flow Metab.* 36, 1885–1900. doi: 10.1177/0271678X15619428
- Schwaerzle, M., Paul, O., and Ruther, P. (2017). Compact silicon-based optrode with integrated laser diode chips, SU-8 waveguides and platinum electrodes for optogenetic applications. *J. Micromech. Microeng.* 27:065004. doi: 10.1088/1361-6439/aa6ad4
- Segev, E., Reimer, J., Moreaux, L. C., Fowler, T. M., Chi, D., Sacher, W. D., et al. (2016). Patterned photostimulation via visible-wavelength photonic probes for deep brain optogenetics. *Neurophotonics* 4:011002. doi: 10.1117/1.NPH.4.1.011002
- Stujenske, J. M., Spellman, T., and Gordon, J. A. (2015). Modeling the spatiotemporal dynamics of light and heat propagation for in vivo optogenetics. *Cell Rep.* 12, 525–534. doi: 10.1016/j.celrep.2015.06.036
- Wu, F., Stark, E., Ku, P.-C., Wise, K. D., Buzsáki, G., and Yoon, E. (2015). Monolithically integrated μ LEDs on silicon neural probes for high-resolution optogenetic studies in behaving animals. *Neuron* 88, 1136–1148. doi: 10.1016/j.neuron.2015.10.032
- Yizhar, O., Fenno, L. E., Davidson, T. J., Mogri, M., and Deisseroth, K. (2011). Optogenetics in neural systems. *Neuron* 71, 9–34. doi: 10.1016/J.NEURON.2011.06.004

Conflict of Interest Statement: TH had an academic [Department of Microsystems Engineering (IMTEK), Albert-Ludwigs-Universität Freiburg, Germany] and company (ATLAS Neuroengineering bvba, Leuven, Belgium) affiliation.

The remaining authors declare that the research was conducted in the absence of any commercial or financial relationships that could be construed as a potential conflict of interest.

Copyright © 2018 Sileo, Bitzenhofer, Spagnolo, Pöplau, Holzhammer, Pisanello, Pisano, Bellistri, Maglie, De Vittorio, Ruther, Hanganu-Opatz and Pisanello. This is an open-access article distributed under the terms of the Creative Commons Attribution License (CC BY). The use, distribution or reproduction in other forums is permitted, provided the original author(s) and the copyright owner(s) are credited and that the original publication in this journal is cited, in accordance with accepted academic practice. No use, distribution or reproduction is permitted which does not comply with these terms.



Microscale Inorganic LED Based Wireless Neural Systems for Chronic *in vivo* Optogenetics

Raza Qazi^{1,2}, Choong Yeon Kim¹, Sang-Hyuk Byun¹ and Jae-Woong Jeong^{1*}

¹ School of Electrical Engineering, Korea Advanced Institute of Science and Technology (KAIST), Daejeon, South Korea,

² Department of Electrical, Computer & Energy Engineering, University of Colorado Boulder, Boulder, CO, United States

OPEN ACCESS

Edited by:

Massimo De Vittorio,
University of Salento, Italy

Reviewed by:

Patrick Ruther,
Albert-Ludwigs-Universität Freiburg,
Germany

Shaoyu Ge,
Stony Brook University, United States

*Correspondence:

Jae-Woong Jeong
jjeong1@kaist.ac.kr

Specialty section:

This article was submitted to
Neural Technology,
a section of the journal
Frontiers in Neuroscience

Received: 27 July 2018

Accepted: 03 October 2018

Published: 23 October 2018

Citation:

Qazi R, Kim CY, Byun S-H and
Jeong J-W (2018) Microscale
Inorganic LED Based Wireless Neural
Systems for Chronic *in vivo*
Optogenetics.
Front. Neurosci. 12:764.
doi: 10.3389/fnins.2018.00764

Billions of neurons in the brain coordinate together to control trillions of highly convoluted synaptic pathways for neural signal processing. Optogenetics is an emerging technique that can dissect such complex neural circuitry with high spatiotemporal precision using light. However, conventional approaches relying on rigid and tethered optical probes cause significant tissue damage as well as disturbance with natural behavior of animals, thus preventing chronic *in vivo* optogenetics. A microscale inorganic LED (μ -ILED) is an enabling optical component that can solve these problems by facilitating direct discrete spatial targeting of neural tissue, integration with soft, ultrathin probes as well as low power wireless operation. Here we review recent state-of-the art μ -ILED integrated soft wireless optogenetic tools suitable for use in freely moving animals and discuss opportunities for future developments.

Keywords: chronic, microscale LED, optogenetics, soft, wireless

INTRODUCTION

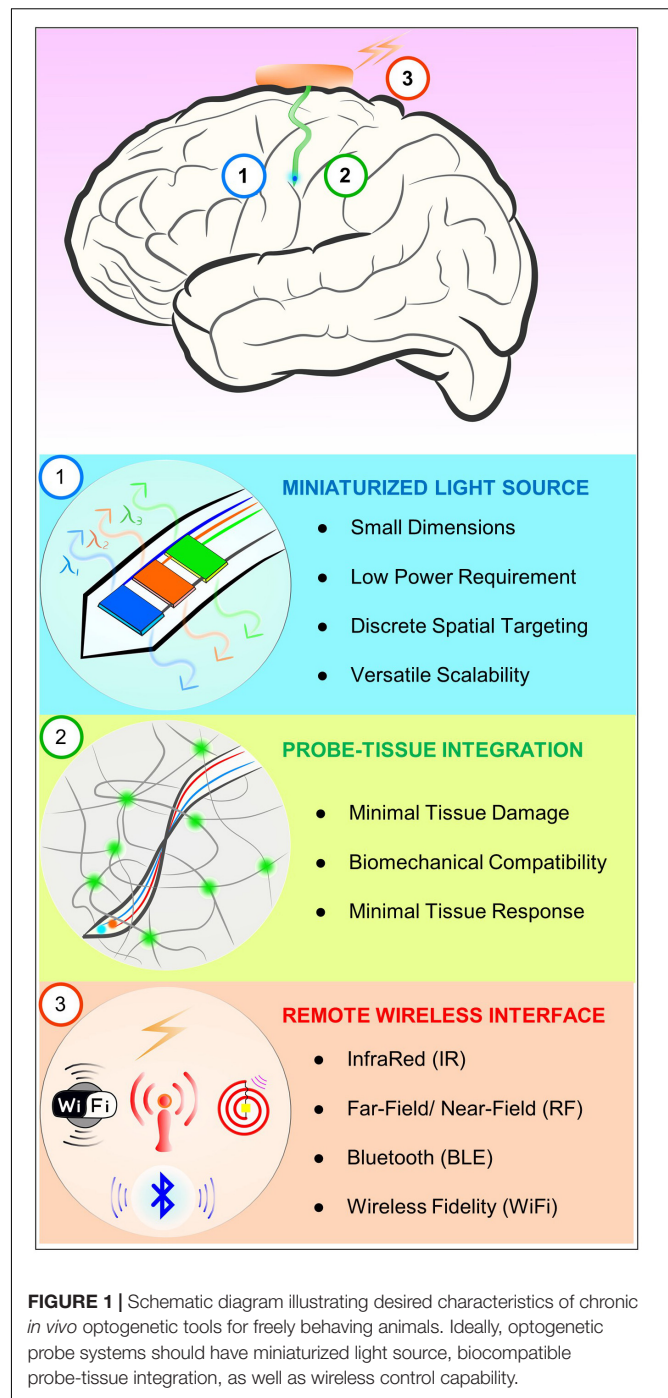
Precision in spatiotemporal control of a specific neuronal population is the key to dissect complex neural pathways within the nervous system. Optogenetics, a combination of optical and genetic technique, is an emerging approach that enables such highly precise, selective neuromodulation through photostimulation of genetically modified, light-sensitive target neurons. The photon sensitivity of these genetically modified cells empowers neuroscientists to study neural circuitry by stimulating or inhibiting them through exposure to different wavelengths of light (Boyden et al., 2005). Conventional tools for optogenetic studies rely on rigid and tethered silica-based optical fibers to deliver light to the deep brain from external bulky optical sources (Sparta et al., 2012), resulting in tissue damage over a relatively large volume of neural tissue. Researchers have tried to minimize tissue stress and damage by reducing device footprints in the form of small laser diode coupled SU-8 waveguides (Schwaerzle et al., 2017) and microscale inorganic light-emitting diodes (μ -ILEDs) integrated silicon probes (Wu et al., 2015; Scharf et al., 2016). However, their stiff mechanics still create unfavorable mismatch with the soft brain tissue [optical fiber: 73 GPa; silicon: 130–170 GPa vs. brain tissue: < 6 kPa (Sim et al., 2017)], which causes significant tissue lesions and inflammation over time. Recent developments helped address this issue by using biocompatible polymers to make probes flexible (Cao et al., 2013; Canales et al., 2015; Yamagiwa et al., 2015), but they still rely on tethered apparatus and fixtures with external connections which cause undue stress and constant irritation in freely moving animals by impeding their natural movement.

Recent advances in material science, micro/nanofabrication, and wireless techniques have enabled chronic, tether-free optoelectronic systems that can facilitate long-term *in vivo*

optogenetics in freely moving animals. A microscale inorganic light-emitting diode is an enabling core component for such systems due to its cellular-scale form factor allowing integration onto soft, flexible probes, low power requirement making them suitable for wireless operation, and ability for precise spatial targeting of specific neurons. In this mini review article, we summarize the state-of-the-art μ -ILED integrated wireless optogenetic devices that overcome fundamental limitations of conventional rigid and tethered approaches. The article starts with discussion on requirements for an ideal neural device for chronic *in vivo* optogenetics. The following sections introduce cutting-edge soft wireless μ -ILED integrated systems in two categories – that is, head-mounted and fully implantable systems, and discuss prospects for directions of further developments to make breakthroughs in neuroscience.

REQUIREMENTS FOR CHRONIC *IN VIVO* OPTOGENETICS

Figure 1 illustrates desired features of a neural probe system for chronic *in vivo* optogenetics. First of all, ideally, neural probe systems need a miniaturized light source. A tiny light source allows its seamless integration onto the shank of a neural probe, enabling direct light source interface with neural tissue. It can help not only reduce tissue damage and inflammation response due to its small dimensions, but also achieve more power-efficient optogenetic excitation by being right next to the target neural circuits, eliminating optical power loss associated with coupling waveguides of external light sources in the conventional waveguide-based method. Furthermore, the small size facilitates discrete, spatial targeting of a specific neuron or neural circuit for more precise, targeted optical manipulation. It can be easily extended to have multiple light sources with the same or distinct emission wavelengths on a single probe. This scalability is another beneficial attribute of miniature light sources that allow highly versatile optogenetic controls. Secondly, biocompatible probe-tissue integration should be achieved for chronic neural interface. Key factors required for chronic biocompatibility are a miniaturized neural probe for minimal tissue damage, mechanical property of the probe that matches with that of neural tissue, and material biocompatibility that causes negligible immune response. For these reasons, ultrathin, soft and flexible biocompatible polymeric platforms are considered to be an ideal solution to minimize the adverse tissue response over long periods of time. To enable chronic *in vivo* functionality while maintaining flexibility, these probes must be encapsulated with polymer with negligible water permeability (such as SU-8 and Parylene C) to provide a critical hermetic barrier against surrounding biofluids for several months (Kim et al., 2013; Shin et al., 2017). Lastly, implantable optogenetic systems should provide wireless interfaces to allow tether-free neural circuit controls to guarantee naturalistic behavior of animals. This can be realized by implementing miniaturized standalone wireless systems using widely available wireless techniques such as infrared (IR) and radiofrequency (RF) remote controls.



A μ -ILED is a core enabling element that facilitates realization of all of the above three requirements. The μ -ILEDs have dimensions smaller than $100\ \mu\text{m} \times 100\ \mu\text{m}$ with the thickness of only several microns, require very low electrical input power (1–1.5 mW) for optical output intensity needed for optogenetic excitation ($1\ \text{mW}/\text{mm}^2$) (Kim et al., 2013), and provide various color options (e.g., blue, orange, etc.) (Park et al., 2016) as well as thermally safe operation within tissue (temperature increase of the surrounding tissue: only $\sim 0.1^\circ\text{C}$

when operating a μ -ILED with 10 ms pulse width at 20 Hz, which produces a peak optical output power of 17.7 mW/mm² at an electrical input power of 8.65 mW (Kim et al., 2013). This favorable tiny optoelectronic component can be easily integrated with ultrathin, flexible polymeric platforms by transfer printing (McCall et al., 2013), therefore permitting minimally invasive, chronically biocompatible integration with neural tissue for *in vivo* optogenetics. For small scale integration of μ -ILEDs on flexible substrates, the polymer stamp-based transfer printing technique is favorable. Although sequential, it allows for simple and easy transfer of off-the-shelf or custom-fabricated μ -ILEDs without requiring expensive equipment and special processes, which is in contrast to wafer-level transfer using conventional laser lift-off (LLO) techniques (Delmdahl et al., 2013). LLO can allow single-step, mass transfer of custom-fabricated μ -ILEDs to other substrates, but require special thermal considerations, equipment setups, as well as careful layout design to ensure high yield and reliability for large scale transfer. Moreover, μ -ILEDs ease wireless operation due to its low operation current density requirement [> 44 times smaller than required current density for laser coupled waveguides for optogenetic stimulation (Schwaerzle et al., 2017)], which can be easily supplied through wireless power transfer or small batteries. In comparison to laser diodes, μ -ILEDs generally operate on lower voltages and currents [2.7 V, 0.5 mA for μ -ILEDs (Jeong et al., 2015) vs. > 3 V, > 22 mA for laser diode (Schwaerzle et al., 2017)], where they demonstrate relatively higher power efficiencies and lower heat generation. Their efficiency can be further improved by limiting operational currents without affecting their capability to generate sufficient optical output power to achieve optogenetic excitation, unlike laser diodes whose threshold currents lie above tens of milliamps, making them relatively inefficient for low power wireless systems. In this short review, we discuss designs of recent μ -ILEDs integrated, soft wireless neural systems that may provide insights for future development of *in vivo* optogenetic tools.

SOFT WIRELESS μ -ILED INTEGRATED OPTOGENETIC TOOLS

Combinatorial integration of μ -ILEDs based soft neural probes with different schemes of wireless controls and power supplies have created various types of soft wireless optoelectronics (Kim et al., 2013; McCall et al., 2013, 2017; Jeong et al., 2015; Park et al., 2015a,b, 2016; Shin et al., 2017; Noh et al., 2018), which have small form factors and light weights suitable for unleashed optogenetics in freely moving animals. These state-of-the art wireless neural systems allow complex behavioral studies in more natural conditions and improve chronic impact on animals by removing undue stress or irritation that can be caused by rigid implants and tethered operation. Based on implanted configurations, which mainly depend on wireless and powering schemes, the soft wireless optoelectronics can be classified into two broad categories, that is, (A) head-mounted and (B) fully implantable wireless systems, as illustrated in **Figure 2** and **Table 1**.

Head-Mounted Solutions

The head-mounted solutions allow highly compact, lightweight electronic systems to be exposed on the head while offering deep brain optogenetic access through soft, ultra-thin penetrating μ -ILED probes. Because the bulk of the system lies outside the body, the design can be modified with high versatility to realize diverse multi-modal platforms with less restrictions on size, powering schemes, and sensor and actuation designs. However, this approach prohibits its use in peripheral nervous systems due to relative bulkiness of the devices and is more prone to physical damage by external shocks caused during animal behavior. The following three sub-sections present head-mounted solutions based on (1) RF energy harvesting, (2) battery-powered infrared control, and (3) photovoltaic powering, respectively.

Injectable, Cellular-Scale Wireless Optoelectronic Systems (Kim et al., 2013; McCall et al., 2013)

Minimally invasive, standalone, soft and flexible optoelectronic probe systems were realized through transfer printing of custom fabricated gallium nitride μ -ILEDs ($50 \mu\text{m} \times 50 \mu\text{m} \times 6.45 \mu\text{m}$) on thin ($6 \mu\text{m}$) polyethylene terephthalate (PET) films. The cellular-scale of μ -ILEDs features highly localized targeting capabilities, minimal tissue damage and enhanced power efficiency by generating light directly near the target neurons. Owing to its design architecture utilizing transfer printing, multi-modal flexible probes can be achieved simply by stacking probes with μ -ILEDs, photodetectors (μ -IPD), and platinum (Pt) electrodes together to allow simultaneous optical modulation and electrophysiological sensing. This flexible optoelectronic probe shows reduced immune response in comparison to conventional optical fibers due to its high mechanical compliance. The design facilitates wireless control by allowing integration of detachable head-mounted RF (910 MHz) power scavenging circuits. The study demonstrated its potential for wireless optogenetics through real-time place-preference and anxiety modulation experiments in mice. Even so, the power harvested through this device is quite sensitive to directionality of the transmission panel antenna, therefore careful experimental design is necessary to cover various positions and orientations of freely moving animals during *in vivo* studies.

Battery-Powered, Programmable, IR Optofluidic Systems (Jeong et al., 2015; McCall et al., 2017)

To provide reliable wireless control of flexible μ -ILED probes for *in vivo* optogenetics, researchers have developed a head-mounted system that utilizes IR control, a microcontroller, and rechargeable, lightweight lithium polymer (LiPo) batteries (~ 0.3 g). This IR wireless system facilitates wireless control via a simple press of button on a portable remote control, provides long range of operation (~ 2 m) as well as modulation of frequency and pulse width of photostimulation in a pre-programmed way using the microcontroller. These features allow it to overcome fundamental limitations of the RF wireless power transfer and control (Kim et al., 2013), which are significantly influenced by angles and orientations of freely behaving mice. Moreover, high discharge capabilities of the rechargeable batteries (~ 80 mA) allows for integration of

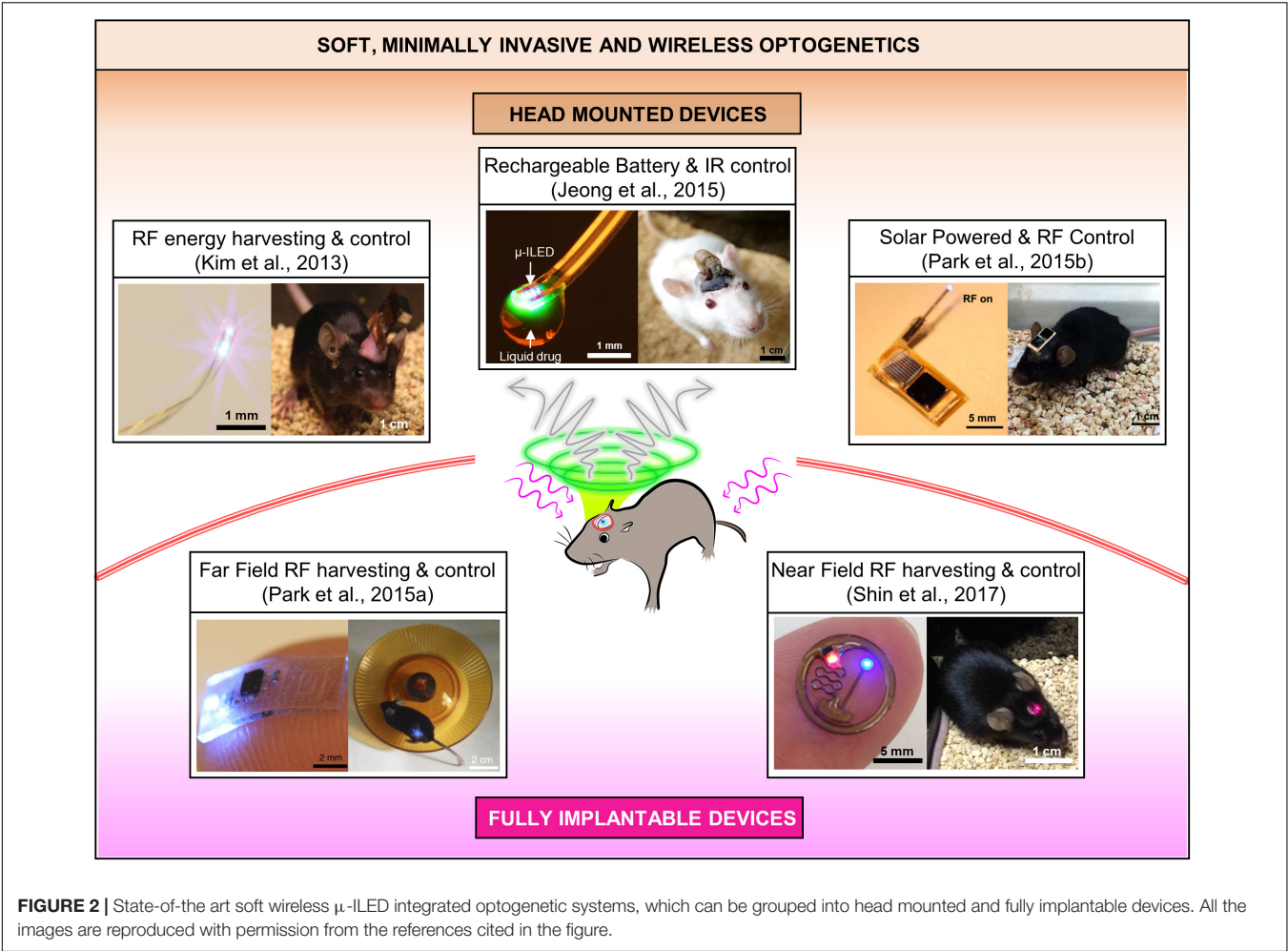


TABLE 1 | Comparison of the recent head-mounted and fully implantable wireless μ -ILED optogenetic tools.

Property	Head Mounted			Fully Implantable	
Reference	Kim et al., 2013; McCall et al., 2013	Jeong et al., 2015; McCall et al., 2017	Park et al., 2015b	Park et al., 2015a, 2016; Noh et al., 2018	Shin et al., 2017
μ -ILED	GaN (50 μ m \times 50 μ m \times 6.45 μ m)			InGaN (220 μ m \times 270 μ m \times 50 μ m)	
Probe (thickness)	PET (20 μ m)	PET + PDMS (80 μ m)	PI (~ 30 μ m)	PDMS (80–700 μ m)	PI (80–130 μ m)
Encapsulation material (thickness)	SU 8 (2 μ m)	SU 8 (2 μ m)	SU 8 (2 μ m)	Parylene C (6 μ m)	Parylene C (5 μ m)
Power	Wireless RF scavenging	LiPo batteries	Photovoltaic cells	RF capacitive coupling	Magnetic resonant coupling
Control (Frequency)	Far-field RF (910 MHz)	Infrared (38 kHz)	Far-field RF (1.6–2.5 GHz)	Far-field RF (1.8–3.2 GHz)	Near-field RF (13.56 MHz)
Range	~1 m	~2 m	~0.2 m	~0.2 m	~0.1 m
Weight	2 g	1.8 g	70 mg	~16–220 mg	~30 mg
SAR	0.77 mW/cm ²	No impact	< 18 mW/kg	~ 69 mW/kg	< 20 mW/kg

microfluidic pumping systems for drug delivery, which require a relative high power (on the order of hundreds of mW) for operation. Empowered by this battery-powered architecture, wireless optofluidic systems could be realized for simultaneous administration of light and pharmacological agents for highly selective, versatile manipulation of neural circuit in the brain of conscious, behaving animals. Further developments that can conquer the line-of-sight handicap of IR wireless communication

and inconvenience of replacing batteries would make this technology more attractive for complex behavior neuroscience research.

Photovoltaic-Powered RF Wireless Optoelectronic Systems (Park et al., 2015b)

Solar cells, which harvest energy from light, are another fascinating option to power wireless optogenetic systems. To eliminate the need for rechargeable batteries for continuous operation of devices, optoelectronic systems consisting of small, lightweight gallium arsenide solar cells (5 mg), RF wireless control module and soft μ -ILEDs probes, have been developed. The wireless control was enabled by rectifying a relatively low power RF signal to manipulate a switch that connected the solar cells to the μ -ILEDs. In comparison to the same device without solar cells, this photovoltaic-assisted RF wireless optoelectronics helps increase the range of operation about three times (~ 3 m) and reduce required RF power transmission levels almost by a factor of 10 (i.e., requires only 1 mW from ~ 1.2 m away to realize optogenetic threshold of 1 mW/mm^2), thus substantially decreasing electromagnetic exposure of animals. These devices also significantly minimize disturbance with animals' free behavior by unnecessitating replacement of rechargeable batteries. However, the power reliability of solar cells can be affected by proximity, direction and nature (i.e., intensity and wavelength spectrum) of light sources in the vicinity of a freely moving mouse. Integration of solar cells with tiny chip batteries that can store back-up energy may be a potential solution to improve operation reliability.

Fully Implantable Solutions

Advances in flexible/stretchable electronics design (Liu et al., 2016) and wireless power transfer technologies (Kim et al., 2013; McCall et al., 2013, 2017; Jeong et al., 2015; Park et al., 2015a,b, 2016; Shin et al., 2017; Noh et al., 2018) have allowed neuroscientists to implant soft optoelectronic devices completely inside the body for *in vivo* optogenetics. The compact, fully implantable soft devices guarantee more naturalistic behavior conditions to animals and provide potentials for integration with various central and peripheral nervous systems in addition to the brain. On the downside, their fully implantable nature limits their reconfigurability and functional scalability for versatile, multi-modal operation. The following sub-sections introduce fully implantable solutions based on (1) far-field and (2) near-field RF wireless energy harvesting.

Soft, Stretchable Optoelectronics With Far-Field RF Energy Harvester (Park et al., 2015a, 2016)

Advances in hard/soft integration techniques for electronics packaging (Liu et al., 2016) have allowed for creation of fully implantable, soft, and flexible polymeric (PDMS) implants, encapsulating μ -ILEDs and a stretchable RF energy harvester. This packaging technique not only insulates the entire device from surrounding biofluids but also provides adaptation with curvilinear surfaces of tissue. The wireless device is small ($6 \text{ mm} \times 3.8 \text{ mm} \times 0.7 \text{ mm}$) and very light (16 mg), therefore can be subdermally implanted in various space-critical

regions of both the central and peripheral nervous systems for *in vivo* optogenetics. The device can be made thinner, lighter and more flexible by further reducing the thickness of its encapsulation, thus enhancing its conformal integration with tissue. A key to miniaturization is a stretchable RF antenna design that allows capacitive coupling of ultra-high frequency (or far-field) electromagnetic waves (2.34 GHz) for energy harvesting and μ -ILED modulation. This tiny RF harvester removes the need for bulky batteries or solar cells, therefore significantly decreasing the size of the overall system. For more complicated experiments, the number of the antenna traces (i.e., operation channels) can be increased to achieve independent control of multiple μ -ILEDs at different control frequencies (Park et al., 2016; Noh et al., 2018). Wireless optogenetic excitation of spinal and peripheral nerves in live mice highlighted its versatile capabilities for *in vivo* wireless optogenetics within discrete, space-critical locations inside the body. Although showing unprecedented features, the stretchable RF antenna of this system needs design optimization to minimize the operational center frequency shift by deformation of the antenna structure caused by tissue deformation of animals in motion.

Flexible, Near-Field Subdermal Optoelectronics (Shin et al., 2017)

To reduce complexity in antenna designs, sensitivity to angular orientation, and RF power exposure of subjects, researchers have developed wireless subdermal flexible optoelectronics that can be powered inductively through thin coil antenna (Cu) in the near-field domain (13.56 MHz). In this device, PDMS and parylene encapsulation prevents electrical shorting of μ -ILEDs and the energy harvesting circuit due to subdermal fluid. The wireless device operated in the near-field domain considerably reduces specific absorption rate (SAR) in animal subjects compared to far-field devices as well as its dependence to surrounding environmental factors. To demonstrate their *in vivo* capabilities, dopaminergic neurons in ventral tegmental area (VTA) of mice were wirelessly triggered using the subdermally implanted device to promote their rewarding behavior. Although enabling robust wireless optogenetics in naturalistic conditions, the operation of these near-field optoelectronics require special cages installed with loop antennas parallel to the implanted optoelectronics for efficient wireless power transfer. Therefore, before experiments, care must be taken to ensure that the loop antenna and implanted devices are properly oriented each other for effective magnetic induction.

CONCLUSION

Here, we review various recent soft wireless μ -ILED based optoelectronic systems that have tremendous potential for chronic optogenetics in freely behaving animals. A μ -ILED is the key to enable minimally invasive wireless optogenetic systems, which offers cellular dimensions for discrete spatial targeting of neurons and functional scalability, heterogeneous integration

with flexible probes for enhanced biocompatibility, as well as power-efficient operation desired for wireless control. One of the most debated concerns regarding *in vivo* use of μ -ILEDs is the possibility of thermal damage to interfacing tissue due to their local heat generation. However, several studies have shown that this can be mitigated by controlling the output power of μ -ILEDs by limiting its operational currents and duty cycles without compromising on its ability to achieve optogenetic excitation (Kim et al., 2013; Park et al., 2015a). Moreover, tissue, working as a heat sink, facilitates fast heat dissipation, thus significantly negating the heat issue for thermally safe *in vivo* operation (Kim et al., 2013). While technologies to date focus on wireless control of neural circuitry of a specific animal, the concepts implemented here might be extended to achieve fully automated, closed loop wireless optogenetic control for high throughput neural manipulations of multiple animals. Such future development will pave the way for highly multiplexed behavioral studies to

accelerate advancement of our knowledge on complex brain circuitry.

AUTHOR CONTRIBUTIONS

RQ and J-WJ conceived the review focus. RQ, CK, S-HB, and J-WJ reviewed literature, wrote the first draft, and finalized the manuscript. All authors approved the final version of the manuscript.

FUNDING

This work was supported by the Basic Science Research Program through the National Research Foundation of Korea (NRF) funded by the Ministry of Science and ICT (NRF-2018R1C1B6001706 and NRF-2018025230).

REFERENCES

- Boyden, E. S., Zhang, F., Bamberg, E., Nagel, G., and Deisseroth, K. (2005). Millisecond-timescale, genetically targeted optical control of neural activity. *Nat. Neurosci.* 8, 1263–1268. doi: 10.1038/nn1525
- Canales, A., Jia, X., Froriep, U. P., Koppes, R. A., Tringides, C. M., Selvidge, J., et al. (2015). Multifunctional fibers for simultaneous optical, electrical and chemical interrogation of neural circuits in vivo. *Nat. Biotechnol.* 33, 277–284. doi: 10.1038/nbt.3093
- Cao, H., Gu, L., Mohanty, S. K., and Chiao, J. C. (2013). An integrated μ LED optrode for optogenetic stimulation and electrical recording. *IEEE Trans. Biomed. Eng.* 60, 225–229. doi: 10.1109/TBME.2012.2217395
- Delmdahl, R., Pätzelt, R., and Brune, J. (2013). Large-Area laser-lift-off processing in microelectronics. *Phys. Proc.* 41, 241–248. doi: 10.1016/j.phpro.2013.03.075
- Jeong, J.-W., McCall, J. G., Shin, G., Zhang, Y., Al-Hasani, R., Kim, M., et al. (2015). Wireless optofluidic systems for programmable in vivo pharmacology and optogenetics. *Cell* 162, 662–674. doi: 10.1016/j.cell.2015.06.058
- Kim, T., McCall, J. G., Jung, Y. H., Huang, X., Siuda, E. R., Li, Y., et al. (2013). Injectable, cellular-scale optoelectronics with applications for wireless optogenetics. *Science* 340, 211–216. doi: 10.1126/science.1232437
- Liu, Y., Norton, J. J. S., Qazi, R., Zou, Z., Ammann, K. R., Liu, H., et al. (2016). Epidermal mechano-acoustic sensing electronics for cardiovascular diagnostics and human-machine interfaces. *Sci. Adv.* 2:e1601185. doi: 10.1126/sciadv.1601185
- McCall, J. G., Kim, T., Shin, G., Huang, X., Jung, Y. H., Al-Hasani, R., et al. (2013). Fabrication and application of flexible, multimodal light-emitting devices for wireless optogenetics. *Nat. Protoc.* 8, 2413–2428. doi: 10.1038/nprot.2013.158
- McCall, J. G., Qazi, R., Shin, G., Li, S., Ikram, M. H., Jang, K.-I., et al. (2017). Preparation and implementation of optofluidic neural probes for in vivo wireless pharmacology and optogenetics. *Nat. Protoc.* 12, 219–237. doi: 10.1038/nprot.2016.155
- Noh, K. N., Park, S. I., Qazi, R., Zou, Z., Mickle, A. D., Grajales-Reyes, J. G., et al. (2018). Miniaturized, battery-free optofluidic systems with potential for wireless pharmacology and optogenetics. *Small* 14:1702479. doi: 10.1002/smll.201702479
- Park, S. I., Brenner, D. S., Shin, G., Morgan, C. D., Copits, B. A., Chung, H. U., et al. (2015a). Soft, stretchable, fully implantable miniaturized optoelectronic systems for wireless optogenetics. *Nat. Biotechnol.* 33, 1280–1286. doi: 10.1038/nbt.3415
- Park, S. I., Shin, G., Banks, A., McCall, J. G., Siuda, E. R., Schmidt, M. J., et al. (2015b). Ultraminiaturized photovoltaic and radio frequency powered optoelectronic systems for wireless optogenetics. *J. Neural Eng.* 12:056002. doi: 10.1088/1741-2560/12/5/056002
- Park, S. I., Shin, G., McCall, J. G., Al-Hasani, R., Norris, A., Xia, L., et al. (2016). Stretchable multichannel antennas in soft wireless optoelectronic implants for optogenetics. *Proc. Natl. Acad. Sci. U.S.A.* 113, E8169–E8177. doi: 10.1073/pnas.1611769113
- Scharf, R., Tsunematsu, T., McAlinden, N., Dawson, M. D., Sakata, S., and Mathieson, K. (2016). Depth-specific optogenetic control in vivo with a scalable, high-density μ LED neural probe. *Sci. Rep.* 6:28381. doi: 10.1038/srep28381
- Schwaerzle, M., Paul, O., and Ruther, P. (2017). Compact silicon-based optrode with integrated laser diode chips, SU-8 waveguides and platinum electrodes for optogenetic applications. *J. Micromech. Microeng.* 27:065004. doi: 10.1088/1361-6439/aa6ad4
- Shin, G., Gomez, A. M., Al-Hasani, R., Jeong, Y. R., Kim, J., Xie, Z., et al. (2017). Flexible near-field wireless optoelectronics as subdermal implants for broad applications in optogenetics. *Neuron* 93, 509.e3–521.e3. doi: 10.1016/j.neuron.2016.12.031
- Sim, J. Y., Haney, M. P., Park, S. I., McCall, J. G., and Jeong, J.-W. (2017). Microfluidic neural probes: in vivo tools for advancing neuroscience. *Lab. Chip* 17, 1406–1435. doi: 10.1039/C7LC00103G
- Sparta, D. R., Stamatakis, A. M., Phillips, J. L., Hovelsø, N., Zessen, R., and Stuber, G. D. (2012). Construction of implantable optical fibers for long-term optogenetic manipulation of neural circuits. *Nat. Protoc.* 7, 12–23. doi: 10.1038/nprot.2011.413
- Wu, F., Stark, E., Ku, P.-C., Wise, K. D., Buzsáki, G., and Yoon, E. (2015). Monolithically Integrated μ LEDs on silicon neural probes for high-Resolution optogenetic studies in behaving animals. *Neuron* 88, 1136–1148. doi: 10.1016/j.neuron.2015.10.032
- Yamagiwa, S., Ishida, M., and Kawano, T. (2015). Flexible parylene-film optical waveguide arrays. *Appl. Phys. Lett.* 107:083502. doi: 10.1063/1.4929402

Conflict of Interest Statement: The authors declare that the research was conducted in the absence of any commercial or financial relationships that could be construed as a potential conflict of interest.

Copyright © 2018 Qazi, Kim, Byun and Jeong. This is an open-access article distributed under the terms of the Creative Commons Attribution License (CC BY). The use, distribution or reproduction in other forums is permitted, provided the original author(s) and the copyright owner(s) are credited and that the original publication in this journal is cited, in accordance with accepted academic practice. No use, distribution or reproduction is permitted which does not comply with these terms.



Synthetic Light-Activated Ion Channels for Optogenetic Activation and Inhibition

Sebastian Beck^{1†}, Jing Yu-Strzelczyk^{1†}, Dennis Pauls², Oana M. Constantin³, Christine E. Gee³, Nadine Ehmann^{4,5,6}, Robert J. Kittel^{4,5,6}, Georg Nagel^{1*} and Shiqiang Gao^{1*}

¹ Julius-von-Sachs-Institute, University of Würzburg, Würzburg, Germany, ² Neurobiology and Genetics, Theodor-Boveri Institute, Biocenter, University of Würzburg, Würzburg, Germany, ³ Institute for Synaptic Physiology, University Medical Center Hamburg-Eppendorf, Hamburg, Germany, ⁴ Department of Neurophysiology, Institute of Physiology, University of Würzburg, Würzburg, Germany, ⁵ Department of Animal Physiology, Institute of Biology, Leipzig University, Leipzig, Germany, ⁶ Carl-Ludwig-Institute for Physiology, Leipzig University, Leipzig, Germany

OPEN ACCESS

Edited by:

Massimo De Vittorio,
University of Salento, Italy

Reviewed by:

Anna Moroni,
Università degli Studi di Milano, Italy
Matthew R. Banghart,
University of California, San Diego,
United States
Sonja Kleinlogel,
Universität Bern, Switzerland

*Correspondence:

Georg Nagel
nagel@uni-wuerzburg.de
Shiqiang Gao
gao.shiqiang@uni-wuerzburg.de

[†]These authors have contributed
equally to this work

Specialty section:

This article was submitted to
Neural Technology,
a section of the journal
Frontiers in Neuroscience

Received: 30 April 2018

Accepted: 29 August 2018

Published: 02 October 2018

Citation:

Beck S, Yu-Strzelczyk J, Pauls D,
Constantin OM, Gee CE, Ehmann N,
Kittel RJ, Nagel G and Gao S (2018)
Synthetic Light-Activated Ion
Channels for Optogenetic Activation
and Inhibition.
Front. Neurosci. 12:643.
doi: 10.3389/fnins.2018.00643

Optogenetic manipulation of cells or living organisms became widely used in neuroscience following the introduction of the light-gated ion channel channelrhodopsin-2 (ChR2). ChR2 is a non-selective cation channel, ideally suited to depolarize and evoke action potentials in neurons. However, its calcium (Ca^{2+}) permeability and single channel conductance are low and for some applications longer-lasting increases in intracellular Ca^{2+} might be desirable. Moreover, there is need for an efficient light-gated potassium (K^+) channel that can rapidly inhibit spiking in targeted neurons. Considering the importance of Ca^{2+} and K^+ in cell physiology, light-activated Ca^{2+} -permeant and K^+ -specific channels would be welcome additions to the optogenetic toolbox. Here we describe the engineering of novel light-gated Ca^{2+} -permeant and K^+ -specific channels by fusing a bacterial photoactivated adenylyl cyclase to cyclic nucleotide-gated channels with high permeability for Ca^{2+} or for K^+ , respectively. Optimized fusion constructs showed strong light-gated conductance in *Xenopus laevis* oocytes and in rat hippocampal neurons. These constructs could also be used to control the motility of *Drosophila melanogaster* larvae, when expressed in motoneurons. Illumination led to body contraction when motoneurons expressed the light-sensitive Ca^{2+} -permeant channel, and to body extension when expressing the light-sensitive K^+ channel, both effectively and reversibly paralyzing the larvae. Further optimization of these constructs will be required for application in adult flies since both constructs led to eclosion failure when expressed in motoneurons.

Keywords: optogenetics, calcium, potassium, cAMP, bPAC, CNG channel, *Drosophila melanogaster* motoneuron, rat hippocampal neurons

INTRODUCTION

With the discovery of channelrhodopsin-1 (Nagel et al., 2002) and the demonstration of light-induced membrane depolarization via ChR2 (Nagel et al., 2003), optical manipulation of cell physiology with transgenic photoreceptors became the method of choice for manipulating genetically defined cells (Boyden et al., 2005; Li et al., 2005; Nagel et al., 2005; Bi et al., 2006);

(Ishizuka et al., 2006). The opsin-based toolbox has expanded and includes the earlier discovered and characterized pump rhodopsins (Zhang et al., 2007; Chow et al., 2010), engineered channel rhodopsins (Kleinlogel et al., 2011; Lin et al., 2013; Dawydow et al., 2014; Scholz et al., 2017), and more recently, light-gated anion channels and nucleotidyl cyclases (Klapoetke et al., 2014; Gao et al., 2015; Govorunova et al., 2015; Scheib et al., 2015).

The optogenetic toolkit is not restricted to rhodopsins. The first optogenetic application employing a light-activated enzyme was light-induced increase of cytosolic cAMP with the photoactivated adenylyl cyclases PAC α and PAC β (Schröder-Lang et al., 2007). These flavoproteins with a BLUF domain (blue light using FAD) were discovered in the unicellular flagellate *Euglena gracilis* (Iseki et al., 2002). Several years later, in the genome of the soil bacterium *Beggiatoa*, a smaller photoactivated adenylyl cyclase (bPAC) was found and characterized (Ryu et al., 2010; Stierl et al., 2011).

Despite the success of Chr2 and certain mutants, there are also some limitations. Chr2 is a non-selective cation channel and its Ca²⁺ permeability and single channel conductance are low (Nagel et al., 2003; Kleinlogel et al., 2011). The point mutation L132C enhanced its Ca²⁺ permeability which is, however, still weaker than for H⁺, Na⁺, and K⁺ (Kleinlogel et al., 2011). Therefore, a more conductive light-sensitive channel with high Ca²⁺ permeability is of interest. Airan et al. generated chimeric OptoXRs from rhodopsin and GPCRs (G-protein coupled receptors) to manipulate intracellular second messengers and further regulate downstream ion channel activity (Airan et al., 2009). Recently introduced optogenetic tools for Ca²⁺ manipulation such as OptoSTIM1 (Kyung et al., 2015) or Opto-CRAC (He et al., 2015) are based on the interaction of light-regulated STIM1 and CRAC (Ca²⁺ release-activated Ca²⁺) channel. This method requires endogenous CRAC to be regulated by engineered STIM1. These tools are slow and highly dependent on background levels of STIM and CRAC.

As inhibitory tools, highly efficient Cl[−] conducting anion channelrhodopsins (ACRs) have been introduced (Govorunova et al., 2015), but whether they hyperpolarize or depolarize cells depends on the intracellular Cl[−] concentration (Mahn et al., 2016; Wiegert and Oertner, 2016). A light-gated K⁺ channel is therefore highly desirable for light-induced hyperpolarization. Already in 2004, Banghart et al. designed a light activated K⁺ channel with addition of a photoisomerizable azobenzene (Banghart et al., 2004). The light-sensitive light-oxygen-voltage (LOV) domain had also been applied to control the K⁺ channel together with a peptide toxin (Schmidt et al., 2014). Also to this end, the light-gated potassium channel BLINK1 was designed, by fusing the photosensory domain LOV2-J α from the oat photoreceptor phototropin with the small viral K⁺ channel Kcv (Cosentino et al., 2015). BLINK1 has advantages as it is small and requires only the ubiquitous chromophore flavin mononucleotide (FMN). BLINK1 has been expressed in HEK293 cells and zebrafish. However, in our hands the photocurrent of BLINK1, expressed in *Xenopus* oocytes is almost undetectable. This might be due to low expression or poor plasma membrane targeting (data not shown).

In this study, we generated light-gated Ca²⁺ permeant and K⁺ selective channels by fusing bPAC to cyclic nucleotide-gated (CNG) channels. Light-gated cAMP production from bPAC leads to activation of the CNG channel. The bovine olfactory organ CNG channel mutant T537S (OLF for short) is highly Ca²⁺ permeant (Altenhofen et al., 1991; Frings et al., 1995; Dzeja et al., 1999) and SthK from *Spirochaeta thermophila* (Brams et al., 2014; Kesters et al., 2015) is a selective K⁺ channel with a single channel conductance of 71 picosiemens (Brams et al., 2014).

Combining OLF and SthK with bPAC showed strong light-gated conductance in *Xenopus* oocytes. Fusing bPAC to CNG as one construct facilitated the subsequent transgenic handling, showed faster kinetics and required less cAMP for channel opening than the co-expressed proteins, presumably because of the close spatial proximity of cyclase and channel. These constructs were also effective in hippocampal neurons depolarizing or blocking spiking, respectively. Expression in *Drosophila* motoneurons allowed us to light-control the motility of larvae. Illumination led to body contraction with the OLF fusion construct, and to body extension with the SthK fusion construct. Thus, we have engineered new optogenetic tools that depolarize and increase intracellular Ca²⁺ or hyperpolarize cells and demonstrate that they can be used to activate and inhibit neurons, respectively.

MATERIALS AND METHODS

Molecular Biology

The bovine olfactory organ CNG (*Bos taurus* CNGA2) channel mutant T537S was already used in a previous study with PAC α and PAC β from *E. gracilis* (Schröder-Lang et al., 2007). The bPAC sequence is as previously published (Stierl et al., 2011). The SthK channel DNA sequence was synthesized by GeneArt Strings DNA Fragments (Life technologies, Thermo Fisher Scientific) according to the published amino acid sequence (Brams et al., 2014; Kesters et al., 2015) with codon usage optimized for *Mus musculus*. The DNA fragments were ligated and inserted into the oocyte expression vector pGEM-HE within N-terminal BamHI and C-terminal HindIII restriction sites. For the fly transgenic vector, the DNA insert was ligated into the KpnI and BamHI restriction sites of the expression vector pJFRC7, instead of Chr2-XXL (Dawydow et al., 2014).

Sequences were confirmed by complete DNA sequencing (GATC Biotech). Exact DNA sequences of all different constructs are shown in the **Supplementary Data Sheet 1**. Plasmids were linearized by NheI digestion. cRNAs were generated by *in vitro* transcription with the AmpliCap-MaxT7 High Yield Message Maker Kit (Epicentre Biotechnologies), using the linearized plasmid DNA as template.

Xenopus Oocyte Expression and Two Electrode Voltage Clamp Recording

Xenopus oocytes were injected with *in-vitro* generated cRNA and maintained at 16°C in ND96 solution: 96 mM NaCl, 2 mM KCl, 1 mM CaCl₂, 1 mM MgCl₂, 10 mM HEPES, pH 7.4, and 50 μ g/mL gentamycin. Injected oocytes were incubated at 16°C for 3 days.

Electrophysiological measurements with *Xenopus* oocytes were performed in Standard Ringer's solution (110 mM NaCl, 5 mM KCl, 2 mM BaCl₂, 1 mM MgCl₂, 10 mM HEPES, pH 7.4), unless specified. A 532 nm laser and a 473 nm laser (Changchun New Industries Optoelectronics Tech) were used as light sources. The light intensities at different wavelengths were measured with a Laser Check optical power meter (Coherent Inc.). Currents were measured at room temperature (20–23°C) with a two-electrode voltage clamp amplifier (TURBO TEC-03X, npI electronic GmbH, Tamm, Germany). Electrode capillaries ($\Phi = 1.5$ mm, wall thickness 0.178 mm, Hilgenberg) were filled with 3 M KCl, with tip openings yielding a resistance of 0.4–1 M Ω . Stimulation and data acquisition were controlled with an AD-DA converter (Digidata 1322A, Axon Instruments) and WinWCP software (v4.1.7, Strathclyde University, United Kingdom).

Rat Hippocampal Neuron Expression, Electrophysiology, and Imaging

Single-cell electroporation was used to introduce plasmid DNA into rat hippocampal neurons in organotypic slice cultures prepared from P5-P7 Wistar rats (Janvier), as described (Gee et al., 2017; Wiegert et al., 2017). Neurons were electroporated with plasmids encoding either OLF-T-YFP-bPAC-Ex (50 ng/ μ l) or SthK-T-YFP-bPAC-Ex (100 ng/ μ l), together with mKate2 (10 ng/ μ l).

After allowing 3 (SthK-T-YFP-bPAC-Ex) to 6 (OLF-T-YFP-bPAC-Ex) days for expression, slices were transferred to the perfusion chamber of an upright microscope (Olympus BX61WI) fitted with an LED (Mightex Systems), which was coupled through the camera port using a multimode fiber (1.0 mm) and collimator (Thorlabs) to photostimulate through the 40 \times water immersion objective (Plan-Apochromat, 40 \times 1.0 numerical aperture, Zeiss). Radiant power was determined using a silicon photodiode (Newport) positioned in the specimen plane and divided by the illuminated field (0.244 mm²).

The extracellular solution contained (in mM): NaCl 119, NaHCO₃ 26.2, D-glucose 11, KCl 2.5, NaH₂PO₄ 1, MgCl₂ 4, CaCl₂ 4, pH 7.4, 310 mOsm/kg, saturated with 95% O₂/5% CO₂. Recording temperature was 28–30°C. The following were added to the perfusate to block synaptic activity unless otherwise indicated: NBQX 10 μ M, CPPene 10 μ M, picrotoxin 100 μ M (Tocris). Wash-in of the antagonists did not affect the light evoked currents. The intracellular solution contained (in mM): K-gluconate 135, HEPES 10, EGTA 0.2, Na₂-ATP 4, Na-GTP 0.4, Magnesium chloride (MgCl₂) 4, ascorbate 3, Na₂-phosphocreatine 10, pH 7.2, 295 mOsm/kg. The liquid junction potential was measured (−14.4 mV) and compensated. Patch electrodes were made from thick-walled borosilicate glass and had resistances of 3–5 M Ω . Neurons were voltage-clamped at −70 mV using an Axopatch 200B amplifier. National Instruments A/D boards and Ephus software were used to record and control the experiment. Series resistance was <15 M Ω and was not compensated during voltage clamp recordings. The bridge balance compensation circuitry was used during current clamp recordings.

Drosophila Culture Conditions and Stocks

The following strains were generated in this study:

RJK 342, y[1] w[1118]; [UAS-OLF-T-YFP-bPAC-Ex]/CyO; +
LAT388, y[1] w[1118]; [UAS-SthK-T-YFP-bPAC-Ex]/CyO; +
RJK560, y[1] w[1118]; [UAS-CD8-YFP-bPAC]/CyO; +
RJK 564, y[1] w[1118]; [UAS-OLF-T-YFP-Ex]/CyO; +

Transgenic flies carrying UAS-OLF-T-YFP-bPAC-Ex, UAS-SthK-T-YFP-bPAC-Ex, UAS-OLF-T-YFP-Ex and UAS-CD8-YFP-bPAC were generated by targeted PhiC31 recombinase-mediated insertion into the genomic P[acman] landing site attP-9A[VK18] located on the second chromosome (Venken et al., 2006) (BestGene Inc.).

All larvae were reared on standard cornmeal/agar medium at 25°C and 70% relative humidity in constant darkness.

Abbreviations used in the figures for larvae of different genotypes were as below:

OLF-bP = UAS-OLF-T-YFP-bPAC-Ex/ok6-Gal4;
SthK-bP = UAS-SthK-T-YFP-bPAC-Ex/ok6-Gal4;
OLF = UAS-OLF-T-YFP-Ex/ok6-Gal4;
CD8-bP = ok6-Gal4/UAS-CD8-YFP-bPAC;
Ctrl-G = +/ok6-Gal4;
Ctrl-O = UAS-OLF-T-YFP-bPAC-Ex/+;
Ctrl-S = UAS-SthK-T-YFP-bPAC-Ex/+.

Recording Larval Locomotor Activity

For recording larval locomotion, 5–6 day old third instar larvae were selected and placed on a circular disc of 1.5% agarose, 85 mm in diameter. The agarose disk was seated on top of a FIM recording setup, built as previously described (Risse et al., 2013). Larval locomotion was recorded by an infrared-camera underneath, picking up the infrared light waves scattered by the larva and the agarose disk. The camera resolution was 2,592 \times 1,944 pixels, the recording frame-rate was set to one frame per second.

Blue light illumination was applied through an LED array (470 nm, light intensities applied are indicated in figure legends). Control conditions were recorded under ambient red room lighting (620 nm, 0.1 μ W/cm²). LED spectrum was determined using the QE65000 Spectrometer (Ocean Optics, Dunedin FL 34698) and intensity was measured using the Laser Check optical power meter (Coherent Inc.).

The open source tracking software FIMtrack (Risse et al., 2017) was used for tracking and analyzing various parameters of larval locomotion. We used two parameters “body length” (distance from larval head to tail) and “momentum distance” (distance between the larval center of mass from one recording frame to the next). The average momentum distance divided by the recording frame rate yields the velocity.

cAMP Assay With *Xenopus* Oocytes and *Drosophila* Larvae

Xenopus oocytes injected with different constructs were incubated at 16°C for 3 days in ND96. Oocytes were either kept in the dark or illuminated for 20 s with blue light (473 nm, 0.3 mW/mm²). 4–6 oocytes injected with the same construct were

homogenized by simply pipetting with a 20–200 μ l pipette in Sample Diluent (containing 0.1 N HCl and pH indicator, Arbor Assays). Samples were then centrifuged at 10,000 rpm for 10 min at room temperature. The supernatant was collected for cAMP assays.

Drosophila larvae were prepared in the dark or after 20 min blue light illumination (473 nm, 0.3 mW/mm²). Larvae in the dark or after illumination were frozen immediately in liquid N₂. The larvae were then homogenized with the micropestle for eppitubes (Eppendorf). Sample Diluent was used to suspend the ground samples. Samples were heated up to 95°C for 5 min and then centrifuged 10 min at 10,000 rpm room temperature for cAMP assays.

cAMP concentrations in the prepared samples were determined using DetectX High Sensitivity Direct Cyclic AMP Chemiluminescent Immunoassay Kit (Arbor assays).

Imaging

Fluorescence images of *Xenopus* oocytes were taken 3 days after injection with a confocal microscope (Leica DM6000). Movies of *Drosophila* larvae were obtained with a Leica DMI8 fluorescence microscope. Images of pupae and flies were obtained with a Keyence digital microscope equipped with VH-Z20 (20–200X) Ultra Small High-performance Zoom Lens.

Images of transfected hippocampal neurons were acquired with a confocal laser scanning microscope (Olympus FLUOVIEW FV1000). The signal from YFP and mKate2 were acquired individually by using the 488 nm (YFP) and 559 nm (mKate2) laser lines, emission channels used were 495–595 nm (YFP) and 565–665 nm (mKate2).

Immunohistochemistry

Staining of *Drosophila* larval NMJs and VNCs followed a standard protocol (Ljaschenko et al., 2013). In brief, male third instar larvae were dissected in Ca²⁺-free HL-3 (Haemolymph-like solution) (Stewart et al., 1994), fixed in 4% paraformaldehyde for 10 min at room temperature and blocked with PBT (0.05% Triton X-100; T8787, Sigma Aldrich) supplemented with 5% normal goat serum (G9023, Sigma Aldrich) for 30 min. The primary antibody, rabbit anti-GFP (1:400; A11122, Invitrogen), was diluted in blocking solution and incubated at 4°C overnight. This was followed by 2 short and 3 \times 20 min washing steps with PBT and incubation with secondary antibodies, goat anti-rabbit-AlexaFluor488 (1:250; A11034, Invitrogen) and HRP-Cy3 (1:250; 123-165-021, Dianova) in blocking solution for 2 h at room temperature. Subsequently, samples were washed (2 short, 3 \times 20 min washing steps) before mounting in Vectashield (H-1000, Vector laboratories). Images were acquired with a Zeiss Imager.Z2 confocal system (objective: 63x, numerical aperture 1.4, oil). For visualization, HRP-signals of NMJs were background subtracted, blurred (Gauss blur σ = 1 px) and normalized (ImageJ, National Institutes of Health). For VNCs, only a subset of the whole confocal stack was maximum projected. All genotypes were stained in the same vial.

Data Analysis

OriginPro 2017 (OriginLab Corporation, Northampton, MA, United States) and Microsoft Excel were used for oocyte and

Drosophila data analysis. All data are expressed as mean \pm standard error of the mean (SEM) or standard deviation (SD), as indicated. Paired Student's *t*-tests were used for statistical comparisons for all data other than larval behavior. For larval locomotion data, *p*-values of datasets were calculated using R. First each dataset was tested for normal gaussian distribution using a Shapiro-Wilk test. If all data of one dataset followed normal gaussian distribution, a pairwise-*t*-test was performed with Bonferroni correction. If at least one of the tested datasets did not follow normal gaussian distribution, a pairwise Wilcoxon test was performed with Bonferroni correction.

Differences were considered significant ****p* < 0.001, ***p* < 0.01, **p* < 0.05.

Data from hippocampal neurons were analyzed with custom routines programmed in MATLAB. Graphs, curve-fitting and non-parametric statistical analyses of the neuron data were performed with GraphPad Prism 6.0. Data are shown as median and interquartile range.

Ethics Statement

The laparotomy to obtain oocytes from *Xenopus laevis* was carried out in accordance with the principles of the Basel Declaration and recommendations of Landratsamt Würzburg Veterinaeramt. The protocol under License #70/14 from Landratsamt Würzburg, Veterinaeramt, was approved by the responsible veterinarian. Rats were housed and bred at the University Medical Center Hamburg animal facility. All procedures were performed according to protocols approved by the Behörde für Gesundheit und Verbraucherschutz (BGV), Hamburg.

RESULTS

Generation and Optimization of a Light-Gated Highly Ca²⁺-Permeant Cation Channel

Previously, soluble bPAC was shown to activate CNG channels, when co-expressed in *Xenopus* oocytes and hippocampal neurons (Stierl et al., 2011). Co-expression of the CNG channel OLF/T537S from the bovine olfactory organ (abbreviated OLF) together with bPAC in oocytes generated a pronounced inward photocurrent when exposed to a short light flash [473 nm, 1 mW/mm², 0.2 s, **Figure 1A**, OLF-YFP + bPAC (1:1)]. As the bovine OLF channel highly fluxes Ca²⁺ (Frings et al., 1995; Dzeja et al., 1999), recordings were performed with Ba²⁺ instead of Ca²⁺ as the permeant ion to prevent activation of endogenous Ca²⁺-activated Cl[−] channels in the oocytes.

We then tested several OLF and bPAC fusion constructs in oocytes. Very few oocytes expressing bPAC directly attached to the C-terminus of OLF had photocurrents, therefore the averaged photocurrent is very small (**Figure 1A**, OLF-bPAC). Inserting a YFP domain between the channel and bPAC did not improve this significantly (**Figure 1A**, OLF-YFP-bPAC) although light induced cAMP production by both OLF-bPAC and OLF-YFP-bPAC (**Figure 1B**). We hypothesized that the plasma membrane trafficking of the channel might be hampered when fusing bPAC or YFP-bPAC to the C terminus of OLF.

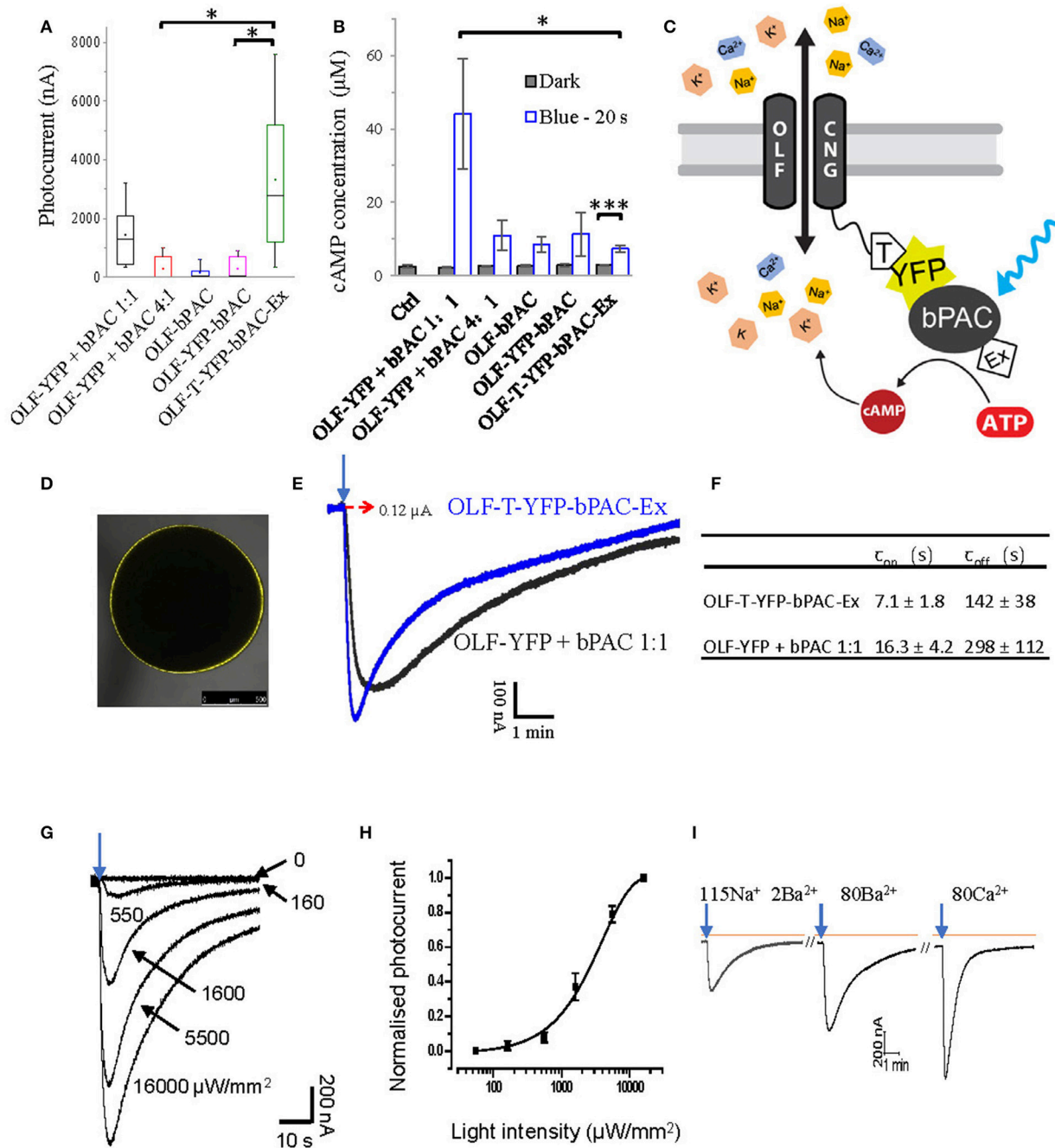


FIGURE 1 | Design of a light-gated Ca^{2+} -permeant cation channel. **(A)** Photocurrents of *Xenopus* oocytes expressing the bovine olfactory cyclic nucleotide gated channel (OLF) and the photoactivatable adenylyl cyclase (bPAC) and various fusion constructs. Total cRNA amounts were adjusted to keep the copies of injected OLF constant. Ratios of cRNA mixtures are indicated. Experiments were performed employing blue light illumination (0.2 s, 1 mW/mm², 473 nm, $n = 6$). **(B)** cAMP production of different OLF and bPAC fusion constructs or mixes; blue light (473 nm, 0.3 mW/mm²); $n = 3$ experiments, each with 6 oocytes; error bars = SD. **(C)** Schematic of the designed OLF (T537S) and bPAC fusion construct. T, plasma membrane trafficking signal; Ex, ER export signal. **(D)** Fluorescence picture of *Xenopus* oocyte expressing OLF-T-YFP-bPAC-Ex. **(E)** Example photocurrent of OLF-T-YFP-bPAC-Ex and 1:1 mixture of OLF and bPAC. Holding potential -60 mV; illumination with 473 nm blue light, 1 mW/mm², red dashed arrow indicates 0 nA. **(F)** Kinetics of photocurrents in oocytes expressing OLF-T-YFP-bPAC-Ex and 1:1 mixture of OLF and bPAC. Light intensity was adjusted to evoke currents of ~ 0.6 μA. $n = 3$, error bars = SD. **(G)** Example OLF-T-YFP-bPAC-Ex photocurrent traces from 1 oocyte induced by 1 s 473 nm light of different intensities, ~ 15 min recovery time in the dark for each illumination. **(H)** OLF-T-YFP-bPAC-Ex photocurrents induced by light of different intensities. $n = 4$, error bars = SD. **(I)** A current recording trace from an oocyte expressing OLF-T-YFP-bPAC-Ex with 1 s blue light (473 nm, 550 μW/mm²) illumination and switching bath solutions containing different cations (115Na^+ 2Ba^{2+} : 115 mM NaCl, 2 mM BaCl₂; 80Ba^{2+} : 80 mM BaCl₂; 80Ca^{2+} : 80 mM CaCl₂). All buffers contain 1 mM MgCl₂, 5 mM HEPES and pH adjusted to 7.6 . Orange line indicates basal current, arrows indicate light pulse, ~ 15 min recovery time in the dark between each illumination.

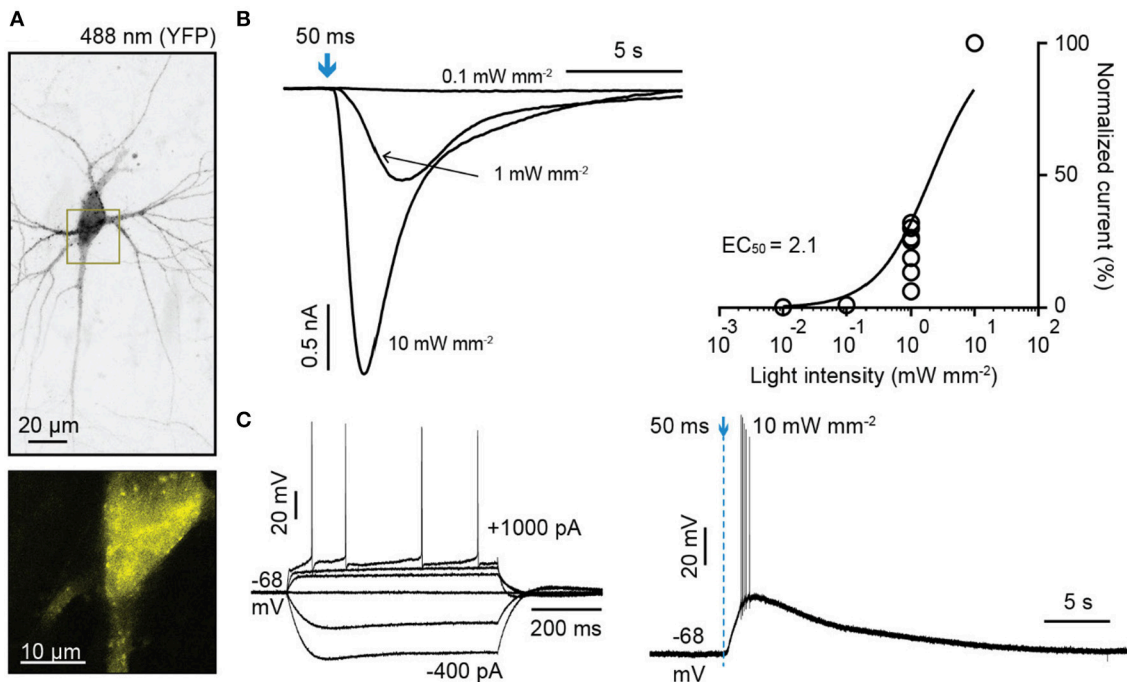


FIGURE 2 | Characterization of light-gated OLF channel in hippocampal neurons. **(A)** Top: Maximum intensity projection of confocal images of hippocampal neurons 6 days after electroporation with DNA encoding OLF-T-YFP-bPAC-Ex (OLF-bP) and mKate2 (excitation 488 nm). Bottom: Single plane of the YFP signal of indicated area in **(A)** (dark yellow box). **(B)** Left: Sample photocurrents evoked by a 50 ms light pulse (470 nm) of different intensity in hippocampal neurons expressing mKate2 and OLF-bP. Right: Light intensity-response relationship fitted with a quadratic equation. Photocurrents are normalized to the maximum current recorded from each neuron. $n = 6$. **(C)** Left: Whole-cell responses to current injections from -400 to $1,000$ pA in an OLF-bP expressing hippocampal neuron. Right: Action potentials of the same cell generated by applying a short 470 nm light flash (50 ms at 10 mW/mm²).

Therefore, we introduced a plasma membrane trafficking signal (T, AA sequence: KSRITSEGEYIPLDQIDINV) between the OLF channel and YFP and added an ER export signal (Ex, AA sequence: FCYENEV) (Gradinaru et al., 2010) to the C-terminal end, as shown in **Figure 1C**. The T and Ex sequences were used to improve the plasma membrane targeting of halorhodopsin and bacteriorhodopsin in mammalian neurons effectively (Gradinaru et al., 2010). The new construct, OLF-T-YFP-bPAC-Ex, showed good expression in *Xenopus* oocytes (**Figure 1D**) and larger photocurrents than the other fusion constructs or the co-expressed OLF channel and soluble bPAC (**Figure 1A**). Interestingly, when illuminated, OLF-T-YFP-bPAC-Ex also produced the smallest increase in cytosolic cAMP (**Figure 1B**).

To compare the kinetics of OLF-T-YFP-bPAC-Ex photocurrents with the kinetics of the co-expressed OLF and bPAC (OLF-YFP + bPAC 1:1), photocurrents of ~ 600 nA were elicited. The fusion construct showed faster onset and offset of the photocurrents than did the co-expression of OLF-YFP and soluble bPAC (**Figures 1E,F**). The half-saturation light intensity of Olf-T-YFP-bPAC-Ex with 1 s light flash was determined to be ~ 2.8 mW/mm² (**Figures 1G,H**).

OLF is a non-selective cation channel with high Ca²⁺ permeability. In oocytes, it showed high conductance with Ba²⁺, which is a cation most equivalent to Ca²⁺ (**Figure 1I**). The Ca²⁺ buffer also generated a big current but it should be mixed

with the endogenous Ca²⁺-activated Cl⁻ channel current. The faster recovery time in Ca²⁺ buffer suggested the high Ca²⁺ concentration blocking effect of the OLF channel (Frings et al., 1995; Dzeja et al., 1999).

OLF-T-YFP-bPAC-Ex (OLF-bP) also induced photocurrents in hippocampal pyramidal neurons (**Figure 2**). The half-saturation light intensity of OLF-bP with a 50 ms light flash in neurons was ~ 2.1 mW/mm² (**Figure 2B**). A 50 ms, 10 mW/mm², 470 nm flash slowly depolarized neurons and evoked action potentials (**Figure 2C**).

Generation of a Light-Gated Potassium Channel

Recently, a cyclic nucleotide gated K⁺ channel from *S. thermophila*, SthK, was described (Brams et al., 2014; Kesters et al., 2015). We fused SthK with T-YFP-bPAC-Ex to generate a light-gated potassium channel, SthK-T-YFP-bPAC-Ex (**Figure 3A**, SthK-bP). In 5 mM extracellular K⁺, oocytes expressing SthK-bP had outward photocurrents that increased with increasing light intensities (1 s, 473 nm, 16 to 5,500 μ W/mm²; **Figure 3B**). The half-saturation light intensity of SthK-bP with a 1 s light flash was determined to be ~ 500 μ W/mm² (**Figure 3C**).

We applied 5 s illumination to SthK-bP expressing oocytes, which evoked photocurrents that persisted for several minutes, during which we changed the extracellular K⁺ concentration

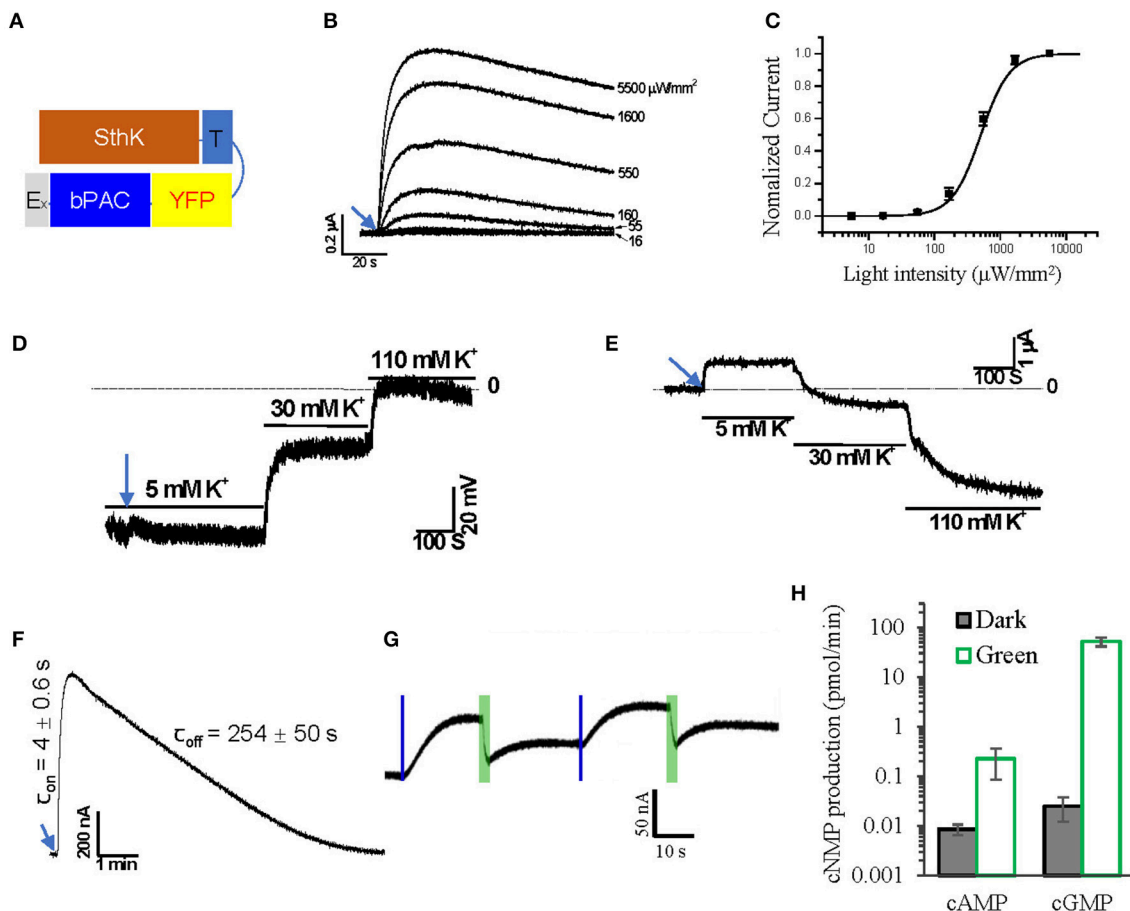


FIGURE 3 | Design of a light-gated potassium channel. **(A)** Schematic of the designed SthK and bPAC fusion construct. **(B)** Representative Photocurrent traces recorded from *Xenopus* oocytes injected with 2 ng SthK-T-YFP-bPAC-Ex (SthK-bP) activated by 1 s blue light (473 nm) of different intensities, ~30 min recovery time in the dark for each illumination. **(C)** Normalized currents against light intensity curve fitted monoexponentially. The half-maximal light intensity value was determined to be 500 $\mu\text{W}/\text{mm}^2$; $n = 4$, error bars = SEM. **(D)** Representative traces of membrane potential recording while switching bath solutions containing 5, 30, and 110 mM K^+ after 5 s blue light (473 nm, 550 $\mu\text{W}/\text{mm}^2$) illumination. **(E)** Representative traces of current recording (holding at -40 mV) while switching bath solutions containing 5, 30 and 110 mM K^+ after 5 s blue light (473 nm, 550 $\mu\text{W}/\text{mm}^2$) illumination. **(F)** On and off kinetics of SthK-bP photocurrents in oocytes with 1 s blue light (473 nm, 550 $\mu\text{W}/\text{mm}^2$) illumination; for values, $n = 4$, error bars = SD. **(G)** Representative photocurrent traces from oocytes co-injected with 1.2 ng SthK-bP and 5 ng BeCyclop cRNA in *Xenopus* oocytes. Currents were induced by 200 ms blue light (473 nm, 550 $\mu\text{W}/\text{mm}^2$) illumination and reduced by 3 s green light (532 nm, 1 mW/mm^2) illumination. **(H)** cAMP and cGMP production of *Xenopus* oocyte membranes co-expressing SthK-bP and BeCyclop in the dark or light (532 nm, 80 $\mu\text{W}/\text{mm}^2$). $n = 3$, error bars = SD.

to verify the K^+ permeability of the fusion construct. Both membrane voltage (Figure 3D) and the currents recorded at -40 mV (Figure 3E) showed a high dependence on extracellular K^+ , confirming that SthK-bP is highly permeable to K^+ . The opening of SthK-bP is faster than OLF-bP and the closing is slower (Figure 3F). This is in good accordance with the lower EC_{50} of SthK for cAMP ($3.7 \pm 0.55 \mu\text{M}$) (Altenhofen et al., 1991) than that of OLF/T537S ($14 \pm 4 \mu\text{M}$) (Brams et al., 2014).

The SthK channel is reported to be activated by cAMP, with cGMP as an antagonist (Kesters et al., 2015). We therefore co-expressed SthK-bP with BeCyclop, a green light-activated guanylyl cyclase (Gao et al., 2015). A short blue light flash (0.2 s, 550 $\mu\text{W}/\text{mm}^2$, 473 nm) activated the bPAC and initiated outward currents. Applying green light (3 s, 1 mW/mm^2 , 532 nm, selective for BeCyclop), to

increase cGMP, attenuated the currents (Figure 3G). The illumination time and light intensities were adjusted to produce enough cGMP upon green light illumination. However, the cAMP-induced current was not fully blocked and we found that the 532 nm illumination still activated bPAC slightly (Figure 3H).

We then expressed SthK-bP in rat hippocampal neurons together with the red fluorescent protein mKate2 (Figures 4A,B). Short flashes of blue light (50 ms, 470 nm) induced outward currents that were light intensity-dependent (Figures 4C,E,F). The currents reversed at -100.5 mV close to the calculated reversal potential of -104 for K^+ (Figure 4D). We then tested whether the hyperpolarization induced by activating SthK-bP would be sufficient to block action potentials (Figure 4G). A single light flash (50 ms, 470 nm, 1 mW/mm^2) completely

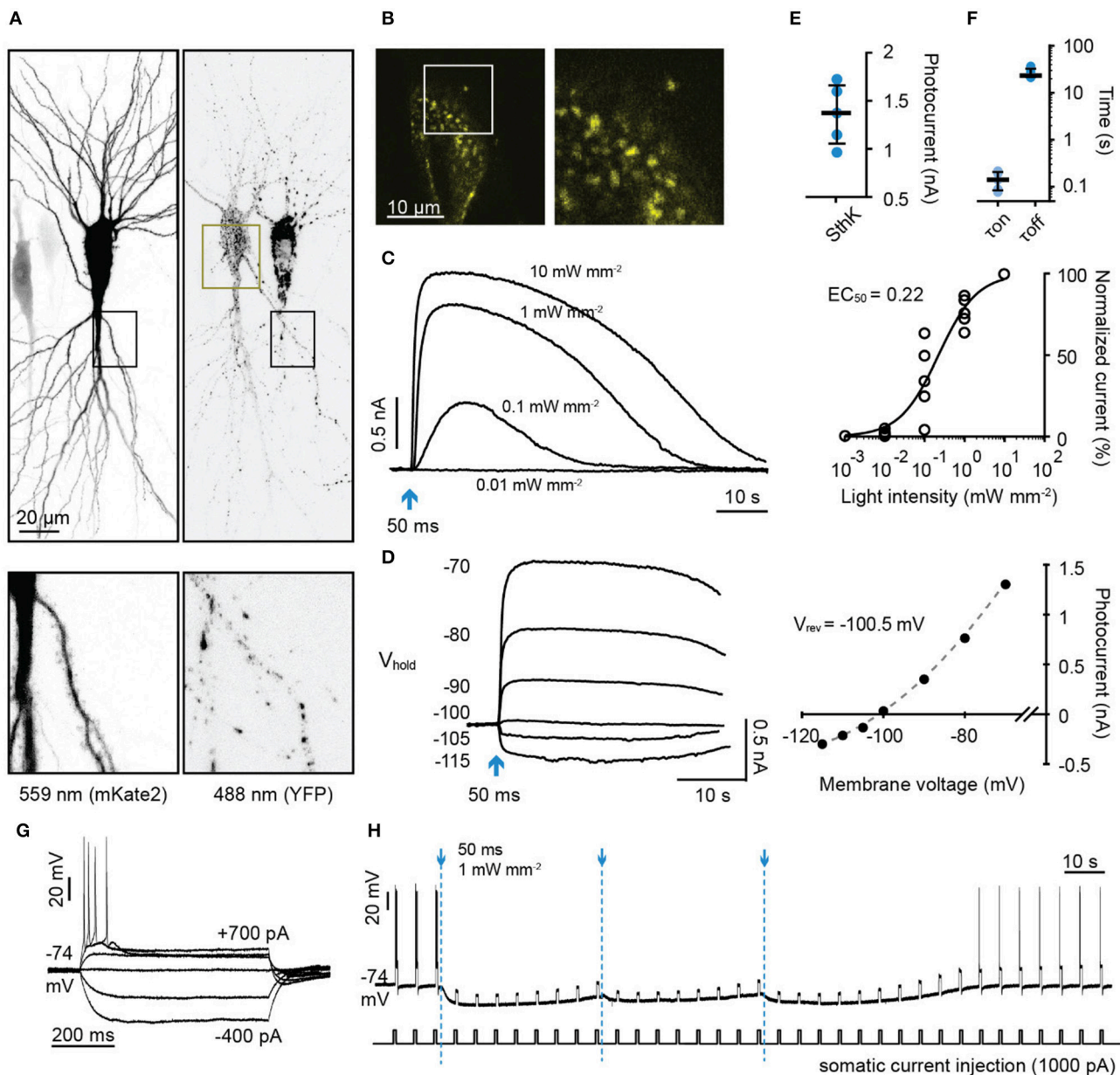


FIGURE 4 | Characterization of a light-gated potassium channel in hippocampal neurons. **(A)** Maximum intensity projection of confocal images of hippocampal neurons 3 days after electroporation with DNA encoding SthK-bP and mKate2 (left: excitation 559 nm; right: excitation 488 nm). Lower images are close up of the regions indicated by dark boxes. **(B)** Single plane of the YFP signal of the region indicated in **(A)** (dark yellow box). **(C)** Left: Sample photocurrents evoked by a 50 ms light pulse (470 nm) of different intensity in a hippocampal neuron expressing mKate2 and SthK-bP. The holding potential was -70 mV. Right: Light intensity-response relationship fitted with a quadratic equation. Photocurrents are normalized to the maximum current recorded in each neuron. $n = 5$. **(D)** Left: Sample traces of photocurrents recorded from a SthK-bP expressing neuron when stimulated with 0.1 mW/mm^2 , 470 nm light (50 ms) while holding the cell at membrane potentials from -70 mV down to -115 mV. Baselines are aligned. Right: Current-voltage plot. A non-linear fit was applied to determine the K^+ equilibrium potential (-100.5 mV). **(E)** Photocurrent amplitude recorded from neurons expressing mKate2 and SthK-bP when stimulated with 1 mW/mm^2 470 nm light. Shown are individual data points, median and 25–75% interquartile range, $n = 5$; median peak current SthK-bP 1.37 nA . **(F)** Kinetics of SthK-bP; data obtained from traces when the stimulation intensity was 1 mW/mm^2 (470 nm, 50 ms); $n = 5$. **(G)** Whole-cell responses to current injections from -400 to 700 pA in SthK-bP expressing hippocampal neuron. **(H)** Action potentials generated by repeated somatic current injection ($1,000 \text{ pA}$, 600 ms , ISI 5 s) were blocked for 3 min by 3 470 nm light flashes at 40 second intervals (50 ms at 1 mW/mm^2); same neuron as in **(G)**.

blocked action potentials induced by 600 ms $1,000 \text{ pA}$ current injections for around 1 min. This complete blockade of action potentials was extended to 3 min by repeatedly flashing blue light

at 40 second intervals (**Figure 4H**). SthK-bP could be activated strongly by 400 and 470 nm light and very slightly by 530 nm light (**Supplementary Figure 1**).

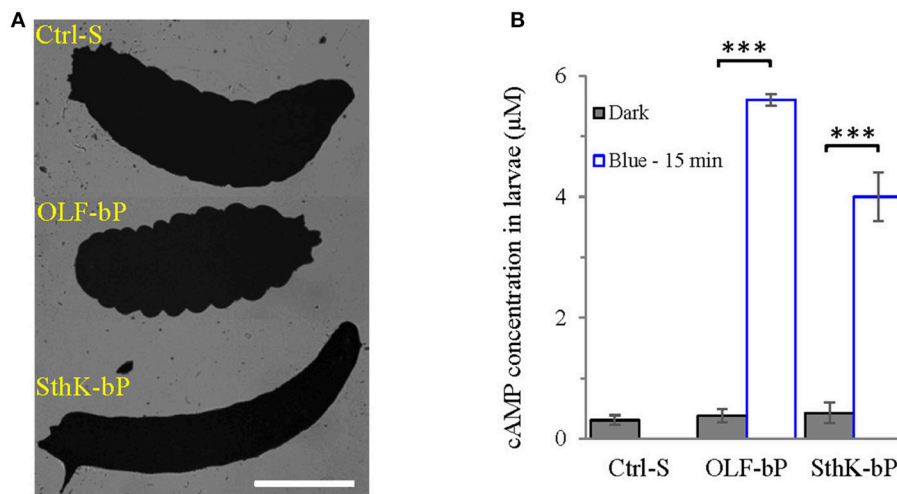


FIGURE 5 | Functional expression of OLF-bP and SthK-bP in *Drosophila* larval motoneurons. **(A)** Expression of OLF-bP and SthK-bP in the larval motoneurons showed different phenotypes upon continuous blue light illumination, Ctrl-S = UAS-SthK-T-YFP-bPAC-Ex/+, Scale bar = 1 mm. **(B)** Light induced cAMP production in larvae expressing OLF-bP and SthK-bP in motoneurons, blue light (473 nm, 0.3 mW/mm²), $n = 3$ experiments, each with 6 larvae, error bars = SD. To calculate the final cAMP concentration in larvae, we assumed 1 larva has a volume of 2 μ l.

Expression of Light-Gated CNG Channels in *Drosophila* Larvae

The two optimized constructs for light-induced Na⁺/Ca²⁺ permeability and K⁺-selective permeability, OLF-bP and SthK-bP, were used to generate transgenic flies. The target genes were placed under the control of the UAS promoter to allow crossing with Gal4 lines.

We obtained expression in motoneurons by crossing the UAS-OLF-T-YFP-bPAC-Ex and UAS-SthK-T-YFP-bPAC-Ex flies with the ok6-Gal4 line (Sanyal, 2009).

The larvae expressing OLF-bP and SthK-bP in motoneurons were paralyzed upon continuous blue light illumination, with a clearly observable body contraction for OLF-bP and body extension for SthK-bP larvae (Figure 5A). These observations fit the known effects of increased Na⁺/Ca²⁺ and K⁺ permeability in *Drosophila* motoneurons: Depolarization and Ca²⁺ influx yield increased intracellular Ca²⁺, synaptic transmission and muscle contraction, whereas increased K⁺ permeability hyperpolarizes motoneurons, synaptic transmission is blocked and muscles relax.

Fifteen minute illumination with blue light (473 nm, 0.3 mW/mm²) induced a ~15-fold cAMP concentration increase (for the whole larva) for OLF-bP larvae and ~10-fold for SthK-bP (Figure 5B) demonstrating the light-dependent cyclase activity of these constructs in transgenic larvae.

To investigate the distribution of OLF-bP and SthK-bP in motoneurons (ok6-GAL driver), immunohistochemistry of larval ventral nerve cords (VNCs) and neuromuscular junctions (NMJs) was performed (Figure 6). Both constructs show expression in motoneuron cell bodies of the VNC. While OLF-bP displays agglomeration within somata, SthK-bP localizes uniformly to cell body membranes. Neither construct could be detected in neuronal arborizations at the NMJ.

Optogenetic Control of Larval Motility

Both OLF-bP and SthK-bP effectively paralyzed *Drosophila* larvae upon illumination with blue light (Videos 1, 2). To quantify the paralyzing effect, we recorded movements of larvae, expressing different constructs, and used the FIM (FTIR-based Imaging Method) tracking system to analyze and calculate posture- and motion-related parameters (Schmidt et al., 2014; Cosentino et al., 2015). As shown in Figure 7, Videos 3, 4, larvae expressing OLF-bP (Figures 7A,B) and SthK-bP (Figures 7C,D) in motoneurons were completely immobile during the 30 s blue light illumination (470 nm, 1.6 mW/cm²).

Larvae of the three control lines, UAS-OLF-T-YFP-bPAC-Ex/+ (Ctrl-O), UAS-SthK-T-YFP-bPAC-Ex/+ (Ctrl-S), and OK6-Gal4/+ (Ctrl-G), transiently slowed at the start of blue illumination but resumed their normal motion within seconds (Figure 7E, see asterisks). This transient response is a normal behavior of the larvae toward the changing light conditions. We also used shorter light pulses to see the effect of varying light dose on larval locomotion. SthK-bP larvae were more light-sensitive than OLF-bP larvae. The motility of OLF-bP larvae was obviously affected with 2 s (470 nm, 25 μ W/cm²) illumination (Figure 8A) whereas SthK-bP larvae already showed a clear response to 0.5 s illumination (Figure 8B). The three controls only showed a mild and fast recovered natural response to 5 s illumination (Figure 8C). This difference in sensitivity between OLF-bP and SthK-bP correlates with their cAMP sensitivity. The cAMP EC₅₀, for SthK is $3.7 \pm 0.55 \mu$ M (Altenhofen et al., 1991), and for OLF/T537S is $14 \pm 4 \mu$ M (Brams et al., 2014). Recovery from paralysis was also faster for shorter light pulses (Figure 8). Channel closing relies on diffusion and hydrolysis of cAMP, which will take longer when the intracellular cAMP reaches higher concentrations.

We also observed that even under red light, larvae expressing SthK-bP in motoneurons showed lower motility than control

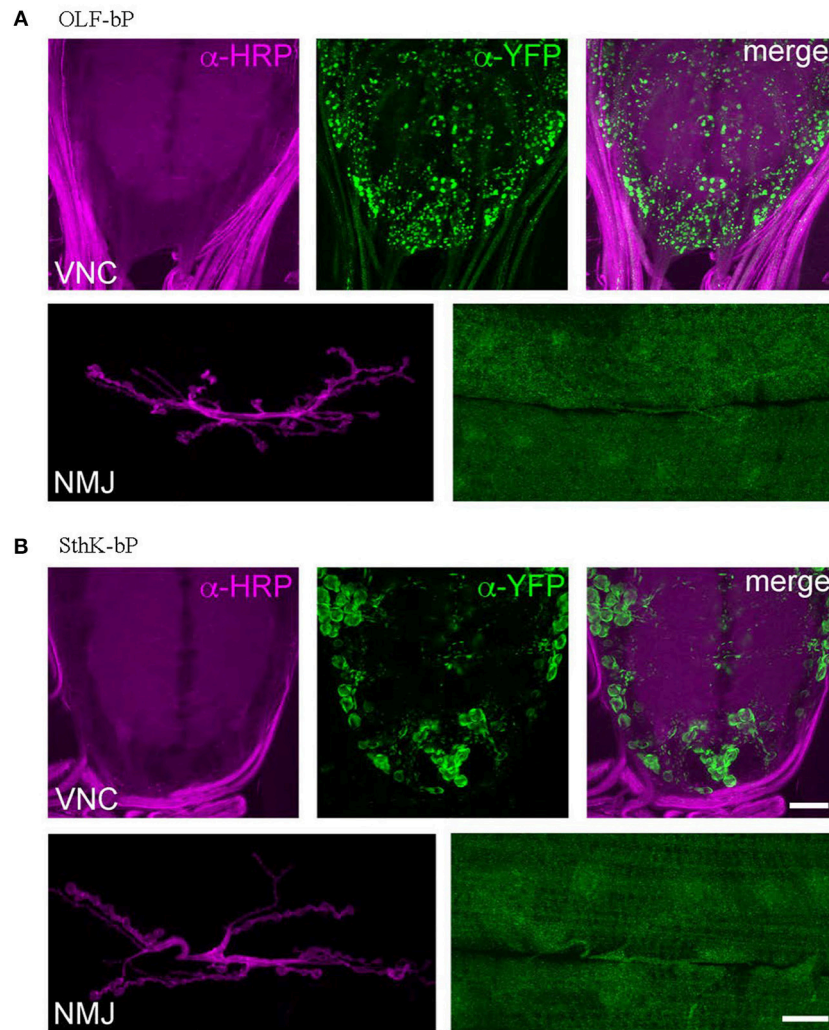


FIGURE 6 | Expression of OLF-bP and SthK-bP in larval motoneurons. **(A)** Staining against YFP (green) reveals a clustered distribution of OLF-bP in motoneuron somata (larval VNC, upper panels), while no signal was detected at the NMJ (lower panels). Anti-HRP (horseradish peroxidase; magenta) was employed to stain neuronal membranes. **(B)** SthK-bP is enriched at cell body membranes in the VNC (upper panels). Similar to OLF-bP, no signal was detected at the NMJ (lower panels). Scale bars: 20 μ m.

larvae (**Figure 7D**). This observation might indicate that endogenous cAMP partially activates SthK due to its high cAMP affinity ($EC_{50} = 3.7 \pm 0.55 \mu$ M).

As additional controls, we generated two further fly strains expressing either OLF or bPAC. Larvae expressing OLF alone [UAS-OLF-T-YFP-Ex/OK6-Gal4 (OLF)], showed no significant light response (**Figure 7F**). To create a membrane-bound bPAC control, we fused bPAC to the CD8 membrane anchor, which was previously used to target GFP to the plasma membrane in *Drosophila* (Lee and Luo, 1999). The OK6-Gal4/UAS-CD8-YFP-bPAC (CD8-bP) larvae showed a significant slowing of locomotion upon blue light illumination (470 nm, 1.6 mW/cm²) but did not become paralyzed in contrast to the larvae expressing either channel together with bPAC (**Figure 7G**). This is not surprising, as increased cAMP (via forskolin) is known to increase neurotransmitter release from

larval motoneurons (Cheung et al., 2006), which could increase muscle tone and account for the changes in locomotion observed here. Indeed, body length decreased in these larvae when illuminated, indicative of muscle contraction (**Figure 9G**). The velocity of CD8-bP larvae dropped to 66% upon illumination, while OLF-bP larvae slowed to 15% and SthK-bP larvae to 6% (**Figure 7H**).

Fifteen minute blue light (473 nm, 0.3 mW/mm²) illumination generated an ~ 18 -fold increase in cAMP for CD8-bP larvae (**Figure 7I**), which is similar to the bPAC activity of OLF-bP animals.

Optogenetic Control of *Drosophila* Larval Body Length

While activation of OLF-bP and SthK-bP both paralyze the larvae, their respective phenotypes are opposing as already shown

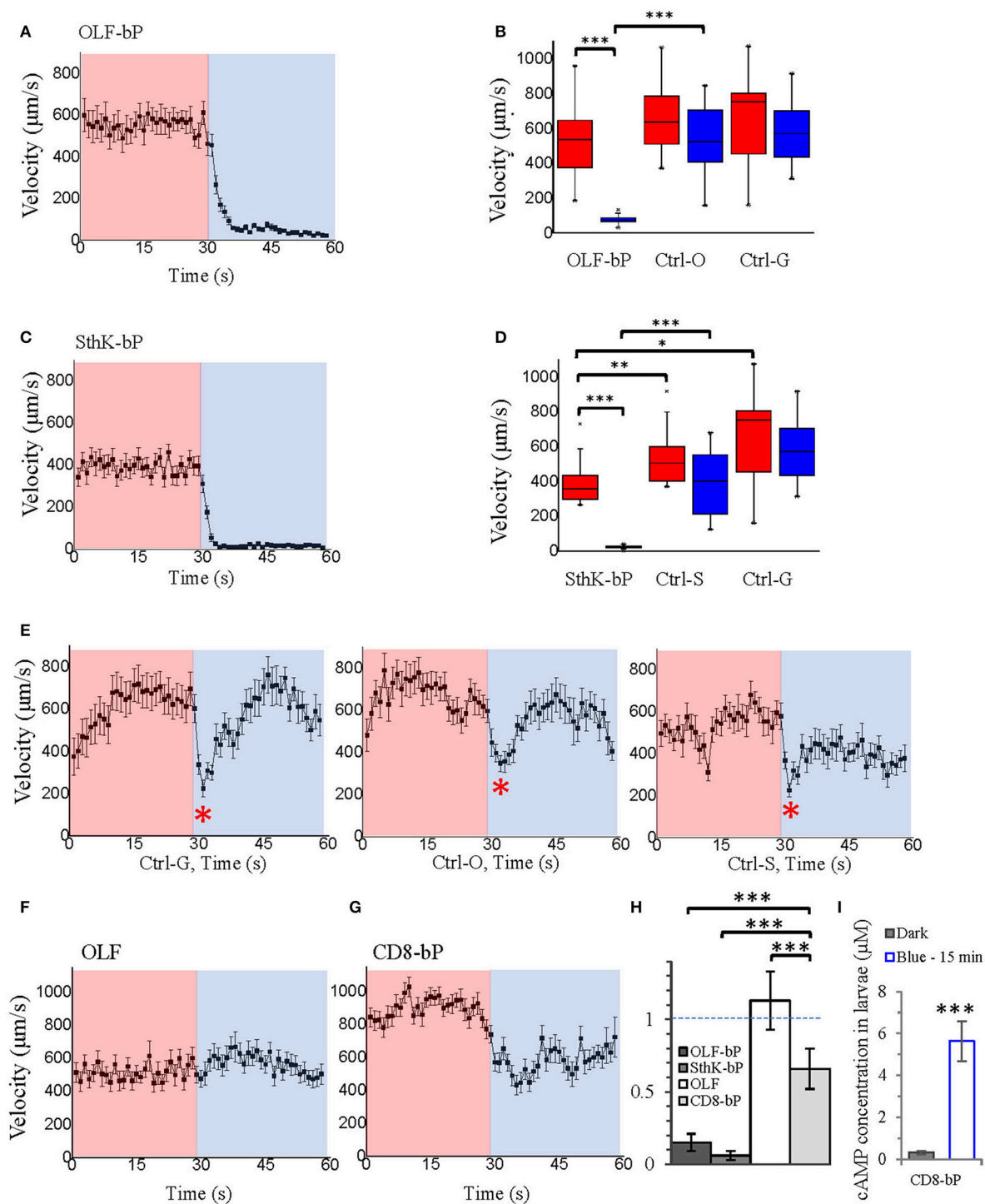


FIGURE 7 | Optogenetic control of *Drosophila* larval motility. **(A)** Velocity of 3rd instar *Drosophila* larvae expressing OLF-bP in motoneurons under red and blue light. **(B)** Box plot of velocity data from OLF-bP expressing larvae and controls under red light and blue light conditions, Ctrl-G = +/OK-Gal4; Ctrl-O = UAS-OLF-T-YFP-bPAC-Ex/+-. **(C)** Velocity of 3rd instar *Drosophila* larvae expressing SthK-bP in motoneurons under red and blue light. **(D)** Box plot of velocity data from SthK-bP expressing larvae and controls under red light and blue light conditions. **(E)** Velocity of different *Drosophila* control larvae under red and blue light. For box plot graph, box line represents median, box edges represent 25 and 75 percentiles, whiskers represent 1 and 99 percentiles. **(F)** Velocity of *Drosophila* larvae expressing OLF-T-YFP-Ex (OLF) in motoneurons under control conditions (red) followed by 30 s of blue light illumination. **(G)** Velocity of *Drosophila* larvae expressing CD8-YFP-bPAC (CD8-bP) in motoneurons under control conditions followed by 30 s of blue light illumination. For A-G, $n = 20$ for each genotype; error bars = SEM. Red light (620 nm, $0.1 \mu\text{W}/\text{cm}^2$), blue light (470 nm, $1.6 \text{ mW}/\text{cm}^2$). **(H)** Light to dark velocity ratios of different genotypes. $n = 19$, error bars = SD. **(I)** Light induced cAMP production of larvae expressing CD8-bP in motoneurons, blue light (473 nm, $0.3 \text{ mW}/\text{mm}^2$). $n = 3$ experiments, each with six larvae, error bars = SD. To calculate the final cAMP concentration in larvae, we assumed that one larva has a volume of $2 \mu\text{l}$.

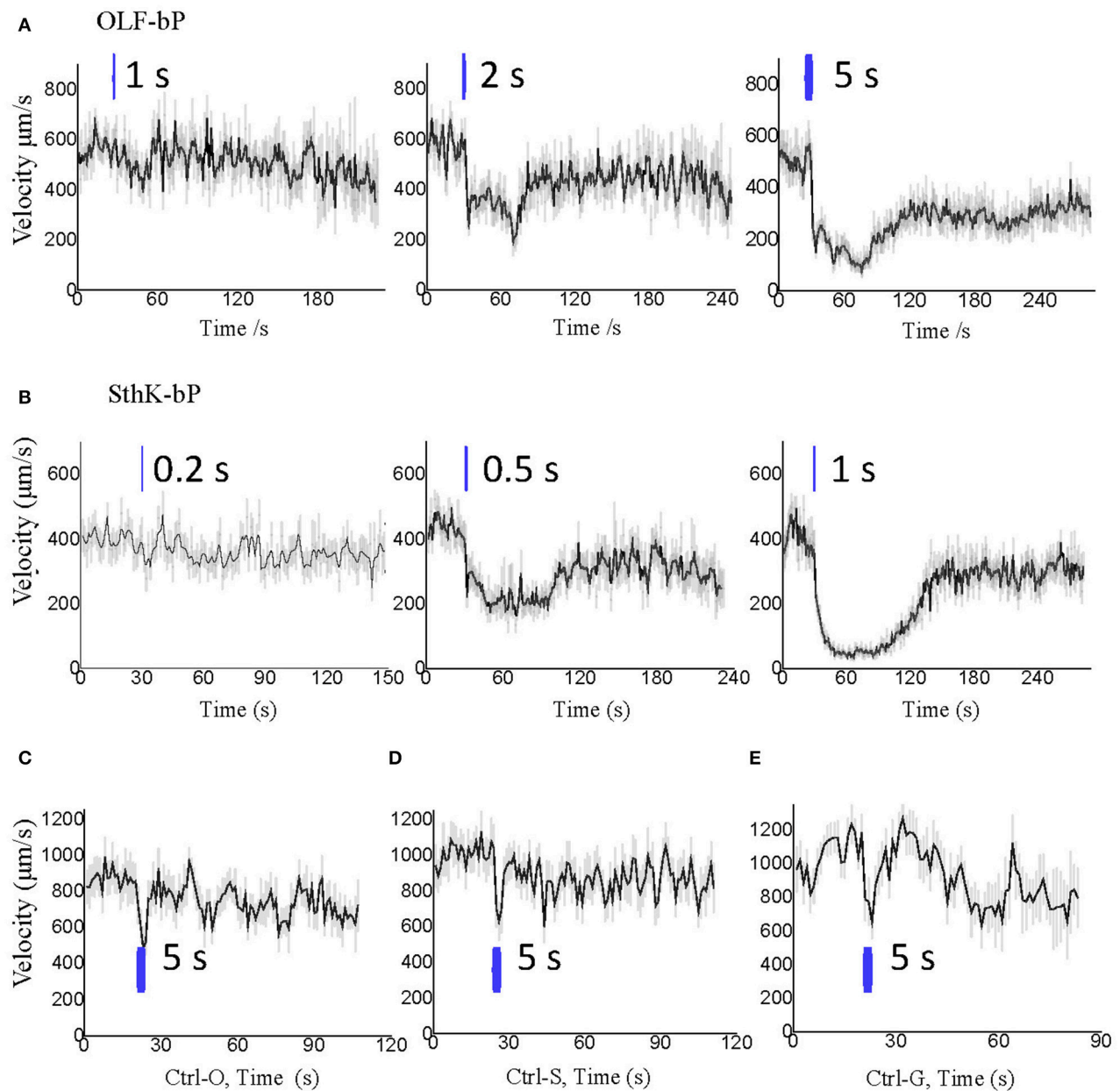


FIGURE 8 | Optogenetic control of *Drosophila* larval motility with short illumination. **(A)** Velocity changes of 3rd instar *Drosophila* larvae expressing OLF-bP in motoneurons with 1, 2, and 5 s blue light illumination. **(B)** Velocity changes of 3rd instar *Drosophila* larvae expressing SthK-bP in motoneurons with 0.2, 0.5, and 1 s blue light illumination. **(C–E)** Velocity changes of 3 control lines with 5 s blue light illumination. For all, $n = 20$ for each genotype [except for **(C)**, here $n = 16$]; error bars (gray) = SEM. Control red light conditions (620 nm, $0.1 \mu\text{W}/\text{cm}^2$), blue light (470 nm $25 \mu\text{W}/\text{cm}^2$).

in **Figure 5A**, Video 1 and 2. OLF-bP led to body contraction and SthK-bP led to body extension. To quantify this opposing effect caused by OLF-bP and SthK-bP, we compared the impact on the larval body length upon illumination (**Figure 9**). While OLF-bP larvae contracted to around 80% of their previous body length (**Figures 9A,B**), SthK-bP larvae extended to around 116% (**Figures 9C,D**). This correlates well with the ion selectivity of the two CNG channels. OLF is a channel most permeable

for Ca^{2+} and Na^{+} , which would activate the motoneuron and lead to muscle contraction, while SthK is a K^{+} -selective channel which would inhibit the motoneuron and lead to muscle relaxation. In contrast, control larvae did not change their body length in response to illumination, further confirming the channel-specific phenotype (**Figure 9E**). The influences of blue light illumination on body length were statistically significant for both OLF-bP and SthK-bP larvae while control

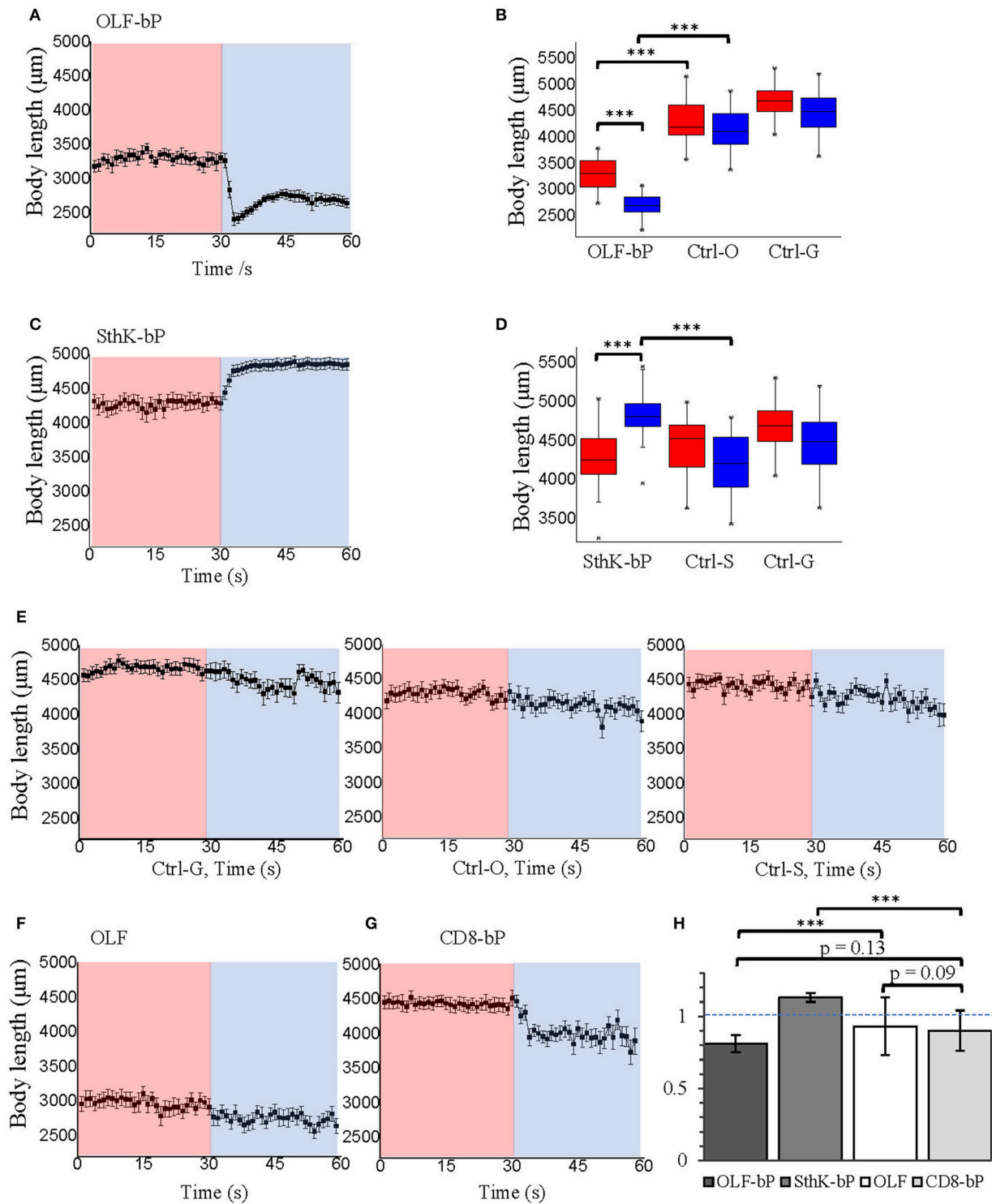
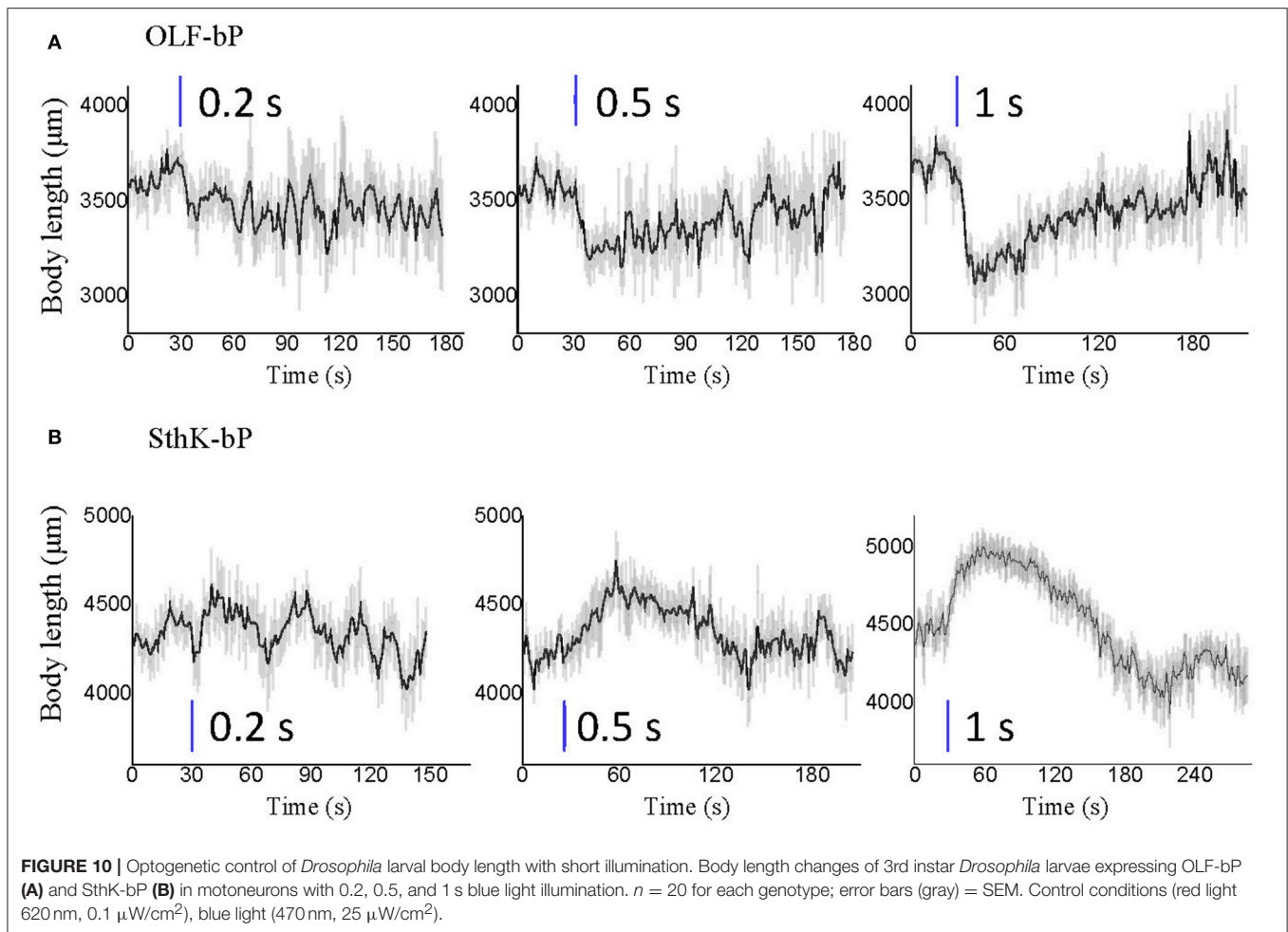


FIGURE 9 | Optogenetic control of *Drosophila* larval body length with long illumination. **(A)** Body length of 3rd instar *Drosophila* larvae expressing OLF-bP in motoneurons under red and blue light. **(B)** Box plot of body length data from OLF-bP expressing larvae and controls under red light and blue light conditions. **(C)** Body length of 3rd instar *Drosophila* larvae expressing SthK-bP in motoneurons under red and blue light. **(D)** Box plot of body length data from SthK-bP expressing larvae and controls under red light and blue light conditions. For box plot graph **(B,D)**, box line represents median, box edges represent 25 and 75 percentiles, whiskers represent 1 and 99 percentiles. **(E)** Body length of different *Drosophila* control larvae under red and blue light. Body length changes of 3rd instar *Drosophila* larvae expressing OLF **(F)** and CD8-bP **(G)** in motoneurons under control conditions followed by 30 s of blue light illumination. For **A–G**, $n = 20$ for each genotype; error bars = SEM. Red light (620 nm, $0.1 \mu\text{W}/\text{cm}^2$), blue light (470 nm, $1.6 \text{ mW}/\text{cm}^2$). **(H)** Light to dark body length ratios of different genotypes. $n = 19$, error bars = SD.



larvae were not significantly different upon blue illumination (Figures 9B,D).

The channel-only-control, OLF in motoneurons, also showed no response to light regarding the body-length (Figure 9F). The membrane-bound bPAC control, CD8-bP in motoneurons, showed slight light-induced contraction (Figure 9G) possibly due to a cAMP-induced increase of neurotransmitter release from larval motoneurons (Cheung et al., 2006). Here, larval body length contracted to 90% upon illumination, while OLF-bP larvae contracted to 81% and SthK-bP larvae to 113% (Figure 9H).

In addition, for OLF-bP and the channel-only-control, OLF, both larvae and pupae were smaller (Figures 9B,F, for pupae see Supplementary Figures 2A,B), which suggests a probable effect of endogenous cAMP or cGMP on OLF and OLF-bP. It is worth mentioning here that the OLF/T537S mutant we are using here is very sensitive to cGMP with an EC_{50} of $0.7 \pm 0.2 \mu\text{M}$ (Brams et al., 2014).

Both the body contracting effect of OLF-bP and the body stretching effect of SthK-bP appeared to be fully reversible after blue light illumination, with a light-dose-dependent recovery time (Figure 10). Interestingly, both OLF-bP and SthK-bP larvae showed obvious body size changes, already with 0.5 s blue light illumination (470 nm, $25 \mu\text{W}/\text{cm}^2$).

DISCUSSION

We designed tools for light-activated $\text{Na}^+/\text{Ca}^{2+}$ and K^+ permeability, combining bPAC and different CNG channels, optimized the fusion strategy and first tested their properties in *Xenopus* oocytes. The optimized fusion constructs were then shown to be effective at activating and inhibiting hippocampal neurons and were subsequently tested in *Drosophila* larval motoneurons with an easily interpretable readout (Pauls et al., 2015). Illumination led to body contraction with highly Ca^{2+} permeable OLF-bP, or extension with K^+ selective SthK-bP. Both constructs paralyze the larvae effectively upon short light flashes.

There is high demand for an improved optogenetic inhibitory tool since the currently available inhibitory tools are not always effective. Whether ACRs hyperpolarize or depolarize cells depends on the intracellular Cl^- concentration (Mahn et al., 2016; Wiegert and Oertner, 2016). Hyperpolarizing light-activated pumps were shown to be able to inhibit action potentials (Zhang et al., 2007) but only at high light intensities and still with low turnover and efficiency. Sustained inhibition with proton pump-type tools may induce a pH-dependent Ca^{2+} influx and leads to increased spontaneous neurotransmitter release (Mahn et al., 2016). Hyperpolarization by halorhodopsin

may also result in enhanced synaptic transmission (Mattingly et al., 2018). A powerful light activated K^+ channel has therefore been high on many wish lists.

The new SthK-bP induced large outward K^+ currents and effectively inhibited hippocampal neurons. Furthermore, based on the narrow activation spectrum in the blue range and high light sensitivity of bPAC, it should be possible to combine SthK-bP with red light-activated ChRs such as Chrimson (Klapoetke et al., 2014) for modulating activation and inhibition of one cell with two colors. Detailed characterization of the inhibition effect and further optimization of SthK-bP are necessary in the future. This should be focused on two aspects, modifying the cAMP affinity and improving targeting to axons and presynaptic compartments.

When employing such synthetic optogenetic tools, the effects of raising intracellular cAMP need to be taken into consideration. Cyclic AMP is an important second messenger that may itself induce physiological changes which could be cell type and developmental stage dependent. The new tools have been optimized to produce little cAMP very close to the channels to minimize bulk increases in cAMP. However, bPAC only controls are needed to discriminate between the effects of cAMP, Ca^{2+} and K^+ .

Endogenous cAMP and cGMP may also directly activate the channels independently of light-induced cAMP. This is a likely explanation for the smaller size of *Drosophila* larvae and pupae expressing OLF-bP and the channel alone. Larvae expressing SthK-bP in motoneurons, turned out to move slightly slower. This might also be due to activation of the channels by endogenous cAMP. We also observed that expression of OLF-bP and SthK-bP in motoneurons leads to eclosion failure limiting their use to larvae.

Several strategies can be applied to overcome this problem and to enable the application of these tools in adult flies. Firstly, an inducible gene expression strategy can be applied, such as temperature-sensitive gene expression using tubGAL80ts

(McGuire et al., 2004). Secondly, it may be possible to develop OLF or SthK mutants with lower cAMP and cGMP sensitivities.

In summary, we have generated new and efficient tools for optogenetic manipulation of Ca^{2+} or K^+ permeability. These tools work efficiently in *Xenopus* oocytes, *Drosophila* larvae and hippocampal cultures.

AUTHOR CONTRIBUTIONS

SG and GN designed the molecular tools. SG and JY-S performed the experiments in *Xenopus* oocytes. SB carried out the *Drosophila* work with the help of DP, NE, RJK, and SG. OC performed experiments and analyzed data from hippocampal neurons and together with CG wrote parts of the manuscript. SG and GN wrote the first draft and all authors revised the paper and approved the final version to be published.

ACKNOWLEDGMENTS

This work was funded by grants from the German Research Foundation to GN (SFB 1047/A03, TRR 166/A03), CEG (SFB1328/A07, FOR2419/P07), and RJK (FOR 2149/P03, SFB 1047/A05, TRR 166/B04, KI1460/4-1). GN acknowledges support provided by the Prix-Louis-Jeantet. We would like to thank Shang Yang for help with the cAMP assay, Sabine Graf for preparing hippocampal slice cultures, Nicole Scholz and Tobias Langenhan for providing the CD8 DNA, Divya Sachidanandan and Andreas S. Thum for supporting fly work and confocal imaging, respectively. We would also like to thank Charlotte Förster, Thomas Oertner, Christian Wegener, and Dirk Rieger for providing support, discussion, and suggestions.

SUPPLEMENTARY MATERIAL

The Supplementary Material for this article can be found online at: <https://www.frontiersin.org/articles/10.3389/fnins.2018.00643/full#supplementary-material>

REFERENCES

- Airan, R. D., Thompson, K. R., Fenno, L. E., Bernstein, H., and Deisseroth, K. (2009). Temporally precise *in vivo* control of intracellular signalling. *Nature* 458, 1025–1029. doi: 10.1038/nature07926
- Altenhofen, W., Ludwig, J., Eismann, E., Kraus, W., Bonigk, W., and Kaupp, U. (1991). B. Control of ligand specificity in cyclic nucleotide-gated channels from rod photoreceptors and olfactory epithelium. *Proc. Natl. Acad. Sci. U. S. A.* 88, 9868–9872. doi: 10.1073/pnas.88.21.9868
- Banghart, M., Borges, K., Isacoff, E., Trauner, D., and Kramer, R. (2004). H. Light-activated ion channels for remote control of neuronal firing. *Nat. Neurosci.* 7, 1381–1386. doi: 10.1038/nn1356
- Bi, A. D., Cui, J. J., Ma, Y. P., Olshevskaya, E., Pu, M. L., Dizhoor, A. M., et al. (2006). Ectopic expression of a microbial-type rhodopsin restores visual responses in mice with photoreceptor degeneration. *Neuron*, 50, 23–33. doi: 10.1016/j.neuron.2006.02.026
- Boyden, E. S., Zhang, F., Bamberg, E., Nagel, G., and Deisseroth, K. (2005). Millisecond-timescale, genetically targeted optical control of neural activity. *Nat. Neurosci.* 8, 1263–1268. doi: 10.1038/nn1525
- Brams, M., Kusch, J., Spurny, R., Benndorf, K., and Ulens, C. (2014). Family of prokaryote cyclic nucleotide-modulated ion channels. *Proc. Natl. Acad. Sci. U. S. A.* 111, 7855–7860. doi: 10.1073/pnas.1401917111
- Cheung, U., Atwood, H. L., and Zucker, R. S. (2006). Presynaptic effectors contributing to cAMP-induced synaptic potentiation in *Drosophila*. *J. Neurobiol.* 66, 273–280. doi: 10.1002/neu.20218
- Chow, B. Y., Han, X., Dobry, A. S., Qian, X., Chuong, A. S., Li, M., et al. (2010). High-performance genetically targetable optical neural silencing by light-driven proton pumps. *Nature* 463, 98–102. doi: 10.1038/nature08652
- Cosentino, C., Alberio, L., Gazzarrini, S., Aquila, M., Romano, E., Cermenati, S., et al. (2015). Optogenetics. Engineering of a light-gated potassium channel. *Science* 348, 707–710. doi: 10.1126/science.aaa2787
- Dawydow, A., Gueta, R., Ljaschenko, D., Ullrich, S., Hermann, M., Ehmann, N., et al. (2014). Channelrhodopsin-2-XXL, a powerful optogenetic tool for low-light applications. *Proc. Natl. Acad. Sci. U.S.A.* 111, 13972–7. doi: 10.1073/pnas.1408269111
- Dzeja, C., Hagen, V., Kaupp, U. B., and Frings, S. (1999). Ca^{2+} permeation in cyclic nucleotide-gated channels. *Embo J.* 18, 131–144. doi: 10.1093/emboj/18.1.131
- Frings, S., Seifert, R., Godde, M., and Kaupp, U. (1995). Profoundly different calcium permeation and blockage determine the specific

- function of distinct cyclic nucleotide-gated channels. *Neuron* 15, 169–179. doi: 10.1016/0896-6273(95)90074-8
- Gao, S. Q., Nagpal, J., Schneider, M. W., Kozjak-Pavlovic, V., Nagel, G., and Gottschalk, A. (2015). Optogenetic manipulation of cGMP in cells and animals by the tightly light-regulated guanylyl-cyclase opsin CyclOp. *Nat. Commun.* 6:8046. doi: 10.1038/ncomms9046
- Gee, C. E., Ohmert, I., Wiegert, J. S., and Oertner, T. (2017). Preparation of slice cultures from rodent hippocampus. *Cold Spring Harb. Protoc.* 2017: pdb prot094888. doi: 10.1101/pdb.prot094888
- Govorunova, E. G., Sineshchekov, O. A., Janz, R., Liu, X. Q., and Spudich, J. (2015). Natural light-gated anion channels: A family of microbial rhodopsins for advanced optogenetics. *Science* 349, 647–650. doi: 10.1126/science.aaa7484
- Gradinaru, V., Zhang, F., Ramakrishnan, C., Mattis, J., Prakash, R., Diester, I., et al. (2010). Molecular and cellular approaches for diversifying and extending optogenetics. *Cell* 141, 154–165. doi: 10.1016/j.cell.2010.02.037
- He, L., Zhang, Y., Ma, G., Tan, P., Li, Z., Zang, S., et al. (2015). Near-infrared photoactivatable control of Ca(2+) signaling and optogenetic immunomodulation. *Elife* 4:e10024. doi: 10.7554/eLife.10024
- Iseki, M., Matsunaga, S., Murakami, A., Ohno, K., Shiga, K., Yoshida, K., et al. (2002). A blue-light-activated adenylyl cyclase mediates photoavoidance in *Euglena gracilis*. *Nature* 415, 1047–1051. doi: 10.1038/4151047a
- Ishizuka, T., Kakuda, M., Araki, R., and Yawo, H. (2006). Kinetic evaluation of photosensitivity in genetically engineered neurons expressing green algae light-gated channels. *Neurosci. Res.* 54, 85–94. doi: 10.1016/j.neures.2005.10.009
- Kesters, D., Brams, M., Nys, M., Wijckmans, E., Spurny, R., Voets, T., et al. (2015). Structure of the SthK carboxy-terminal region reveals a gating mechanism for cyclic nucleotide-modulated ion channels. *PLoS ONE* 10:e0116369. doi: 10.1371/journal.pone.0116369
- Klapoetke, N. C., Murata, Y., Kim, S. S., Pulver, S. R., Birdsey-Benson, A., Cho, Y. K., et al. (2014). Independent optical excitation of distinct neural populations. *Nat. Methods* 11, 338–346. doi: 10.1038/nmeth.2836
- Kleinlogel, S., Feldbauer, K., Dempksi, R. E., Fotis H., Wood P. G., Bamann, C., et al. (2011). Ultra light-sensitive and fast neuronal activation with the Ca(2+)-permeable channelrhodopsin CatCh. *Nat. Neurosci.* 14, 513–518. doi: 10.1038/nn.2776
- Kyung, T., Lee, S., Kim, J. E., Cho, T., Park, H., Jeong, Y. M., et al. (2015). Optogenetic control of endogenous Ca(2+) channels *in vivo*. *Nat. Biotechnol.* 33, 1092–1096. doi: 10.1038/nbt.3350
- Lee, T., and Luo, L. (1999). Mosaic analysis with a repressible cell marker for studies of gene function in neuronal morphogenesis. *Neuron* 22, 451–461. doi: 10.1016/S0896-6273(00)80701-1
- Li, X., Gutierrez, D. V., Hanson, M. G., Han, J., Mark, M. D., Chiel, H., et al. (2005). Fast noninvasive activation and inhibition of neural and network activity by vertebrate rhodopsin and green algae channelrhodopsin. *Proc. Natl. Acad. Sci. U. S. A.* 102, 17816–17821. doi: 10.1073/pnas.0509030102
- Lin, J. Y., Knutsen, P. M., Muller, A., Kleinfeld, D., and Tsien, R. Y. (2013). ReaChR: a red-shifted variant of channelrhodopsin enables deep transcranial optogenetic excitation. *Nat. Neurosci.* 16, 1499–1508. doi: 10.1038/nn.3502
- Ljaschenko, D., Ehmann, N., and Kittel, R. J. (2013). Hebbian plasticity guides maturation of glutamate receptor fields *in vivo*. *Cell Rep.* 3, 1407–1413. doi: 10.1016/j.celrep.2013.04.003
- Mahn, M., Prigge, M., Ron, S., Levy, R., and Yizhar, O. (2016). Biophysical constraints of optogenetic inhibition at presynaptic terminals. *Nat. Neurosci.* 19, 554–556. doi: 10.1038/nn.4266
- Mattingly, M., Weineck, K., Costa, J., and Cooper, R. L. (2018). Hyperpolarization by activation of halorhodopsin results in enhanced synaptic transmission: neuromuscular junction and CNS circuit. *PLoS ONE* 13:e0200107. doi: 10.1371/journal.pone.0200107
- McGuire, S. E., Mao, Z., and Davis, R. L. (2004). Spatiotemporal gene expression targeting with the TARGET and gene-switch systems in *Drosophila*. *Sci. STKE* 2004:pl6. doi: 10.1126/stke.2202004pl6
- Nagel, G., Brauner, M., Liewald, J. F., Adeishvili, N., Bamberg, E., and Gottschalk, A. (2005). Light activation of channelrhodopsin-2 in excitable cells of *Caenorhabditis elegans* triggers rapid behavioral responses. *Curr. Biol.* 15, 2279–2284. doi: 10.1016/j.cub.2005.11.032
- Nagel, G., Ollig, D., Fuhrmann, M., Kateriya, S., Mustl, A. M., Bamberg, E., et al. (2002). Channelrhodopsin-1: a light-gated proton channel in green algae. *Science* 296, 2395–2398. doi: 10.1126/science.1072068
- Nagel, G., Szellas, T., Huhn, W., Kateriya, S., Adeishvili, N., Berthold, P., et al. (2003). Channelrhodopsin-2, a directly light-gated cation-selective membrane channel. *Proc. Natl. Acad. Sci. U. S. A.* 100, 13940–13945. doi: 10.1073/pnas.1936192100
- Pauls, D., von Essen, A., Lyutova, R., van Giesen, L., Rosner, R., Wegener, C., et al. (2015). Potency of transgenic effectors for neurogenetic manipulation in *Drosophila* larvae. *Genetics* 199, 25–37. doi: 10.1534/genetics.114.172023
- Risse, B., Berh, D., Otto, N., Klambt, C., and Jiang, X. (2017). FIMTrack: an open source tracking and locomotion analysis software for small animals. *PLoS Comput. Biol.* 13:e1005530. doi: 10.1371/journal.pcbi.1005530
- Risse, B., Thomas, S., Otto, N., Lopmeier, T., Valkov, D., Jiang, X., et al. (2013). FIM, a novel FTIR-based imaging method for high throughput locomotion analysis. *PLoS ONE* 8:e53963. doi: 10.1371/journal.pone.0053963
- Ryu, M. H., Moskvina, O. V., Silberg-Liberles, J., and Gomelsky, M. (2010). Natural and engineered photoactivated nucleotidyl cyclases for optogenetic applications. *J. Biol. Chem.* 285, 41501–41508. doi: 10.1074/jbc.M110.177600
- Sanyal, S. (2009). Genomic mapping and expression patterns of C380, OK6 and D42 enhancer trap lines in the larval nervous system of *Drosophila*. *Gene Expr. Patterns* 9, 371–380. doi: 10.1016/j.gep.2009.01.002
- Scheib, U., Stehfest, K., Gee, C. E., Korschen, H. G., Fudim, R., Oertner, T. G., et al. (2015). The rhodopsin-guanylyl cyclase of the aquatic fungus *Blastocladiella emersonii* enables fast optical control of cGMP signaling. *Sci. Sign.* 8: rs8. doi: 10.1126/scisignal.aab0611
- Schmidt, D., Tillberg, P. W., Chen, F., and Boyden, E. S. (2014). A fully genetically encoded protein architecture for optical control of peptide ligand concentration. *Nat. Commun.* 5:5019. doi: 10.1038/ncomms4019
- Scholz, N., Guan, C., Niebler, M., Grotemeyer, A., Maiellaro, I., Gao, S., et al. (2017). Mechano-dependent signaling by Latrophilin/CIRL quenches cAMP in proprioceptive neurons. *Elife* 6:28360. doi: 10.7554/eLife.28360
- Schröder-Lang, S., Schwarzel, M., Seifert, R., Strunker, T., Kateriya, S., Looser, J., et al. (2007). Fast manipulation of cellular cAMP level by light *in vivo*. *Nat. Methods* 4, 39–42. doi: 10.1038/nmeth975
- Stewart, B. A., Atwood, H. L., Renger, J. J., Wang, J., and Wu, C. F. (1994). Improved stability of *Drosophila* larval neuromuscular preparations in haemolymph-like physiological solutions. *J. Comp. Physiol. A* 175, 179–191. doi: 10.1007/BF00215114
- Stierl, M., Stumpf, P., Udvari, D., Gueta, R., Hagedorn, R., Losi, A., et al. (2011). Light modulation of cellular cAMP by a small bacterial photoactivated adenylyl cyclase, bPAC, of the soil bacterium *beggiatoa*. *J. Biol. Chem.* 286, 1181–1188. doi: 10.1074/jbc.M110.185496
- Venken, K. J., He, Y., Hoskins, R. A., and Bellen, H. J. (2006). P[acman]: a BAC transgenic platform for targeted insertion of large DNA fragments in *D. melanogaster*. *Science* 314, 1747–1751. doi: 10.1126/science.1134426
- Wiegert, J. S., Gee, C. E., and Oertner, T. G. (2017). Single-Cell Electroporation of Neurons. *Cold Spring Harb. Protoc.* 2017: pdb prot094904. doi: 10.1101/pdb.prot094904
- Wiegert, J. S., and Oertner, T. G. (2016). How (not) to silence long-range projections with light. *Nat. Neurosci.* 19, 527–528. doi: 10.1038/nn.4270
- Zhang, F., Wang, L. P., Brauner, M., Liewald, J. F., Kay, K., Watzke, N., et al. (2007). Multimodal fast optical interrogation of neural circuitry. *Nature* 446, 633–639. doi: 10.1038/nature05744

Conflict of Interest Statement: The authors declare that the research was conducted in the absence of any commercial or financial relationships that could be construed as a potential conflict of interest.

Copyright © 2018 Beck, Yu-Strzelczyk, Pauls, Constantin, Gee, Ehmann, Kittel, Nagel and Gao. This is an open-access article distributed under the terms of the Creative Commons Attribution License (CC BY). The use, distribution or reproduction in other forums is permitted, provided the original author(s) and the copyright owner(s) are credited and that the original publication in this journal is cited, in accordance with accepted academic practice. No use, distribution or reproduction is permitted which does not comply with these terms.



High-Density μ LED-Based Optical Cochlear Implant With Improved Thermomechanical Behavior

Eric Klein^{1*}, Christian Gossler¹, Oliver Paul^{1,2} and Patrick Ruther^{1,2*}

¹ Department of Microsystems Engineering (IMTEK), University of Freiburg, Freiburg, Germany, ² BrainLinks-BrainTools, Cluster of Excellence, University of Freiburg, Freiburg, Germany

OPEN ACCESS

Edited by:

Ferruccio Pisanello,
Fondazione Istituto Italiano di
Tecnologia, Italy

Reviewed by:

Leonardo Sacconi,
Università degli Studi di Firenze, Italy
Aseema Mohanty,
Columbia University, United States

*Correspondence:

Eric Klein
eric.klein@imtek.de
Patrick Ruther
ruther@imtek.de

Specialty section:

This article was submitted to
Neural Technology,
a section of the journal
Frontiers in Neuroscience

Received: 11 July 2018

Accepted: 04 September 2018

Published: 01 October 2018

Citation:

Klein E, Gossler C, Paul O and
Ruther P (2018) High-Density
 μ LED-Based Optical Cochlear
Implant With Improved
Thermomechanical Behavior.
Front. Neurosci. 12:659.
doi: 10.3389/fnins.2018.00659

This study reports the realization of an optical cochlear implant (oCI) with optimized thermomechanical properties for optogenetic experiments. The oCI probe comprises 144 miniaturized light-emitting diodes (μ LEDs) distributed along a bendable, 1.5-cm-long, 350- μ m-wide and 26- μ m-thick probe shaft, individually controlled via a $n \times p$ matrix interconnection. In contrast to our earlier approach based on polyimide (PI) and epoxy resin with different thermal expansion coefficients, the μ LEDs and interconnecting wires are now embedded into a triple-layer stack of a single, biocompatible, and highly transparent epoxy material. The new material combination results in a pronounced reduction of thermomechanical bending in comparison with the material pair of the earlier approach. We developed a spin-coating process enabling epoxy resin layers down to 5 μ m at thickness variations of less than 7% across the entire carrier wafer. We observed that the cross-linking of epoxy resin layers strongly depends on the spin-coating parameters which were found to be correlated to a potential separation of epoxy resin components of different densities. Furthermore, various metallization layers and corresponding adhesion promoting layers were investigated. We identified the combination of silicon carbide with a titanium-based metallization to provide the highest peeling strength, achieving an adhesion to epoxy improved by a factor of two. In order to obtain a high process yield, we established a stress-free implant release using the electrochemical dissolution of a sacrificial aluminum layer. The direct comparison of oCI probe variants using a single epoxy material and the combination of PI and epoxy resin revealed that the epoxy-resin-only probe shows minimal thermomechanical probe bending with a negligible hysteresis. The thermal probe characterization demonstrated that the temperature increase is limited to 1 K at μ LED DC currents of up to 10 mA depending on the stimulation duration and the medium surrounding the probe. The optical output power and peak wavelengths of the new oCI variant were extracted to be 0.82 mW and 462 nm when operating the μ LEDs at 10 mA, 10 kHz, and a duty cycle of 10%. The optical power corresponds to a radiant emittance of 407 mW/mm², sufficient for optogenetic experiments using channelrhodopsin-2.

Keywords: cochlear implant, optogenetics, micro light-emitting diode (μ LED), thermomechanical behavior, epoxy

INTRODUCTION

With more than 400,000 implanted systems, cochlear implants (CIs) currently represent the most successful neuroprosthetic device (Zeng and Canlon, 2015). In general, CIs comprise up to 22 electrodes arranged along a slender implantable probe with a typical length of up to 30 mm and diameters between 0.25 (distal end) and 0.6 mm (apical position). They are implanted into the scala tympani of the cochlea through the round window and are used to electrically stimulate the spiral ganglion neurons (SGNs) to partially restore hearing. Most CIs are implanted in very young children starting at the age of 6 months as they learn much faster to handle the electrical signals produced by a CI, which improves the early development of their hearing and speaking capabilities (Conner et al., 2006). Nonetheless, older children and adults, suffering from a sudden hearing loss, receive CIs as well. However, despite hearing restoration, both groups of patients encounter the main drawback of classical CIs, which is the limited frequency resolution as a consequence of the wide current spreading in the scala tympani (Kral et al., 1998; Wheeler et al., 2007; Zeng et al., 2008). This restriction in terms of frequency resolution is taken into account by the stimulation algorithms of modern CIs, offering patients a reasonable comprehension of speech (Zeng et al., 2008). Although improvements have been achieved with advanced stimulation techniques (Zhu et al., 2012), even children with early implantations and therefore a good result of hearing restoration are rarely able to conduct conversations in noisy environments or to appreciate music.

A promising approach to overcome the limitations of classical CIs is offered by optogenetics (Jeschke and Moser, 2015). Optogenetics enables the direct interaction with neurons using light-sensitive opsins integrated into the neuronal cell membranes (Deisseroth et al., 2006; Yizhar et al., 2011). The most widely used opsin is channelrhodopsin-2 (ChR2) with a peak sensitivity at 470 nm (Pashaie et al., 2014) matching the emission spectra of highly efficient gallium nitride (GaN) light-emitting diodes (LED). CIs designed for optical stimulation have been proposed to integrate linear arrays of micro LEDs (μ LEDs) on a slender, bendable probe allowing the direct optical stimulation of the SGNs (Goßler et al., 2014). This approach of a so-called optical CI (oCI) promises neuronal stimulation with improved spatial resolution, thereby improving the frequency decoding by a factor of 10 depending on the number of applicable μ LEDs and on the cellular selectivity.

Several approaches for a controlled delivery of light into neuronal tissue have been previously described. Often, the technical interfaces have taken advantage of optical glass fibers (Aravanis et al., 2007; Zhang et al., 2007; Pisanello et al., 2017) guiding the light from an external light source, e.g., a solid state laser or a high-power LED, to the area of interest. This approach has the advantage that light with a broad range of wavelengths matching the sensitivity spectrum of various opsins can be delivered. However, there are several reasons why optical fibers are far from optimal as an oCI: a first reason is the need for an external light source; secondly, the mechanical stiffness of the optical glass fibers is hardly compatible with the bending radii of the cochlea; thirdly, even if the bending problem was solved, the

internal reflection needed for light guiding is strongly reduced in bent fibers. The direct integration of laser diode (LD) chips with light guiding structures, as described in Park et al. (2011), Kampasi et al. (2016), and Schwaerzle et al. (2017), overcomes at least the size constraints of an external light source. However, it imposes restrictions in terms of applicable wavelengths due to the limited commercial availability of compact, unpackaged LD chips.

A more promising approach is based on the integration of LEDs either as bare LED chips (Kwon et al., 2013a; Ayub et al., 2017; Ji et al., 2017) or as thin-film μ LEDs (Goßler et al., 2014; Hahn et al., 2014; Wu et al., 2015; Ayub et al., 2016; Klein et al., 2016; Scharf et al., 2016) on the implantable probe. In the case of bare LED chips, the probe design needs to fit to the size of available chips with typical lateral dimensions of $220 \times 270 \mu\text{m}^2$ and a thickness of 50 μm or more (Schwaerzle et al., 2016). The integration of these LED chips has been achieved using wire bonding and adhesive fixation (Ji et al., 2017), which has been accompanied by a pronounced size increase due to the wire bonds. Alternatively, flip-chip bonding (Ayub et al., 2016; Schwaerzle et al., 2016) on either flexible or stiff substrates has enabled smaller system dimensions limited only by the size of the LED chips. As an example, Schwaerzle et al. (2016) presented an oCI based on 10 individually controllable LED chips on a custom-made polyimide (PI) carrier substrate; with this system, the optical evocation of auditory brainstem responses (ABRs) has been demonstrated. Nevertheless, the size of commercially available LED chips has remained an obstacle to higher lateral resolutions in LED arrangement and a reduction of the implant bending radii required for reaching deeper positions in the cochlea (Jeschke and Moser, 2015).

The above limitations can be circumvented by the approach of Goßler et al. (2014) integrating linear μ LED arrays on flexible PI substrates using a wafer-level laser lift-off (LLO) transfer of the μ LEDs. As a result, the oCI width was successfully reduced to 380 μm and 15 μ LEDs with a size of $150 \times 150 \mu\text{m}^2$ were integrated on the probe. The μ LEDs were controlled in groups of five via three individually addressable electrical channels. The wafer-level transfer and assembly process enable hundreds of these μ LEDs of minimal lateral dimensions to be handled in parallel, which could not realistically be achieved by flip-chip bonding. The fabrication process of this oCI variant relies on different polymers, i.e., PI and epoxy resin, serving as the substrate and for encapsulation, respectively. The mismatch in the coefficients of thermal expansion (CTEs) of the two polymers caused a pronounced mechanical bending of the oCI upon temperature changes during probe processing and encapsulation or simply by activating the μ LEDs. This bending made implantation into the windings of the cochlea difficult because the implant was curled in the wrong direction. Finally, the mismatch in the CTEs leads to mechanical stress within the implant itself which potentially causes delamination between the polymer layers and thus the failure of the oCI.

The study presented here addresses in particular the thermomechanical behavior of the oCI by replacing its PI substrate by an epoxy layer. This is the same material that is already used as an underfill during the LLO process and for the

encapsulation of the top n-contact metallization. In comparison to the state of the art, the study demonstrates a pronounced increase in the number of integrated μ LEDs while reducing the overall probe width. The thermomechanical behavior of the new oCI variant is successfully improved over that of the hybrid PI/epoxy probe. Aside from the optical probe characterization, i.e., μ LED center wavelength and radiant flux, the study further evaluates the temperature increase on the probe surface due to μ LED operation which needs to be limited to 1 K for a safe *in vivo* probe application.

MATERIALS AND METHODS

Design of the oCI

The oCI developed in this study is schematically shown in **Figure 1A**. It comprises 144 individually addressable μ LEDs controlled via 12 n-contact and 12 p-contact pads using a 12×12 matrix interconnection scheme. The contact pads are located on the oCI base with in-plane dimensions of $1500 \times 680 \mu\text{m}^2$. The top n-metallization of the μ LED comprises a circular aperture with a diameter of $50 \mu\text{m}$ confining the light emission from the μ LED. The μ LEDs are distributed along the 1.5-cm-long, $350\text{-}\mu\text{m}$ -wide, and $26\text{-}\mu\text{m}$ -thick flexible oCI shaft at a pitch of $100 \mu\text{m}$. The oCI metallization interfacing the n- and p-doped GaN of the μ LEDs is embedded in a three-layer polymer stack whose individual components each serve a specific task. The bottom layer (layer #1) represents the substrate comprising the

p-contact metallization onto which the μ LEDs are transferred using the LLO process. The second polymer layer (layer #2) plays the role of an underfill during the LLO process and electrically insulates the n-contact and p-contact metallizations from each other. Finally, the third polymer (layer #3) serves as the passivation layer of the n-contact metallization. Obviously, these layers need to offer process compatibility and biocompatibility as well as a high optical transparency at the peak emission wavelength of 462 nm of the applied GaN μ LEDs. Two oCI variants, i.e., the hybrid oCI, as introduced by Gößler et al. (2014), and the epoxy-resin-only variant developed here, are analyzed in this study. In the case of the hybrid oCI, a stack of one PI and two epoxy resin thin films is used for layers #1 to #3, as illustrated with the cross-section in **Figure 1B**. More specifically, these are the PI U-Varnish-S (UBE Industries Ltd., United States) and the epoxy resin E301 (Epoxy-Technologies, United States). In contrast, the novel epoxy-resin-only oCI comprises three layers of E301 (**Figure 1C**). As the CTEs of the used PI and epoxy resin are mismatched by a factor of 13 (see **Table 1**; Epoxy Technology; UBE Industries Ltd., United States¹), a strong residual bending of the oCI probes has resulted in the hybrid probe. This was observed following oCI processing and thermal cycling, i.e., by operating the μ LEDs and locally heating the oCI. By replacing the PI substrate, the mechanical structure of the oCI is expected to benefit of an improved thermomechanical homogeneity minimizing the residual probe bending.

¹http://www.epotek.com/site/administrator/components/com_products/assets/files/Style_Uploads/301.pdf

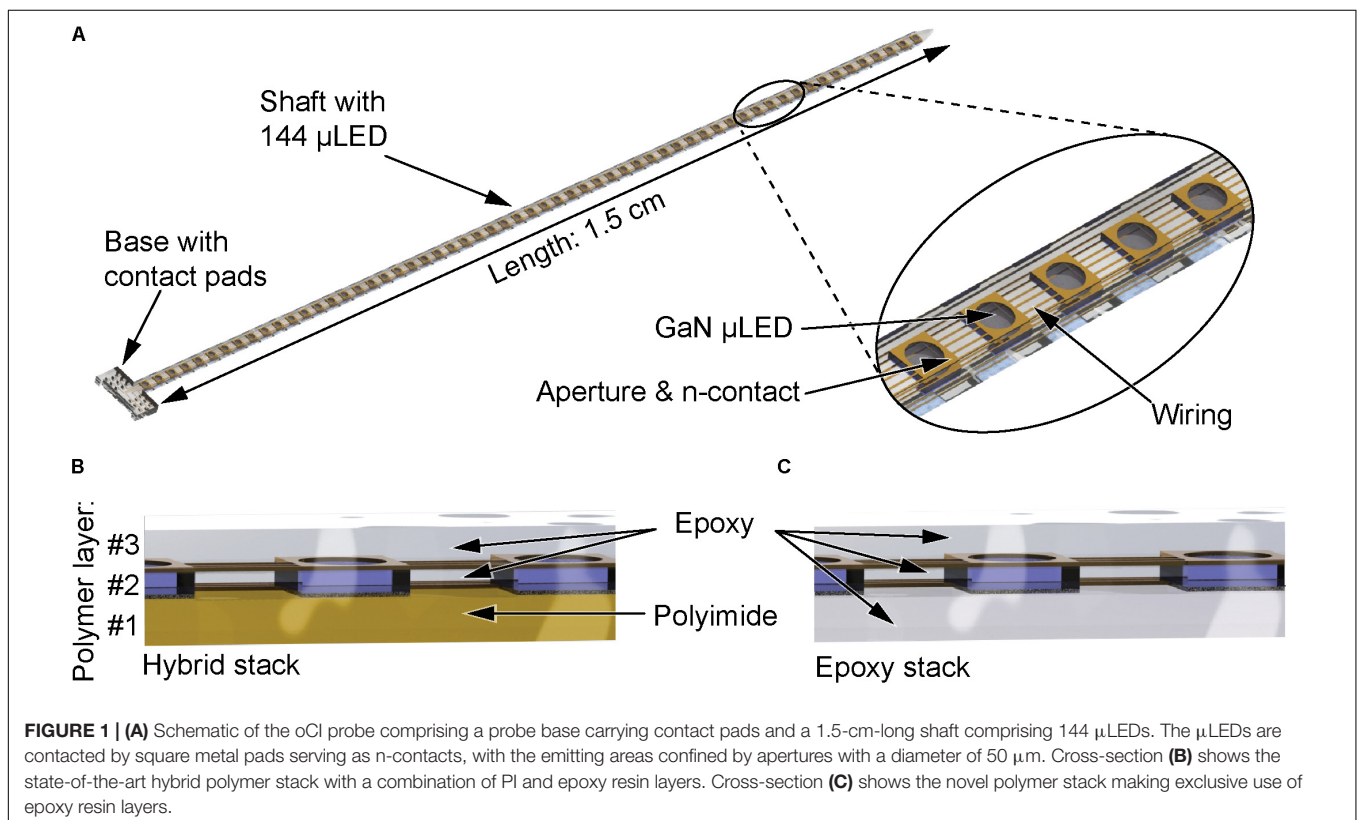


TABLE 1 | Physical properties of the polymers polyimide U-Varnish-S and epoxy resin E301 used to realize oCI probes.

Material	Transmission @ 470 nm	Curing temperature	Bio- compatibility	Peel-off from SiO ₂	Solvent	CTE α_{th} (10 ⁻⁶ K ⁻¹)
U-Varnish-S (UBE Industries Ltd., United States)	25–35%	450°C	Not specified	Possible	NMP	3
E301 (Epoxy Technology)	> 99%	80°C	Yes	Not possible	None	38

TABLE 2 | Materials applied during oCI fabrication.

Material	Function	Thickness	Deposition
Silicon (Si)	Carrier substrate initially used for the polymer substrates	525 μ m	–
Sapphire	Carrier substrate of μ LEDs and polymer substrate	626 μ m	–
Epoxy resin E301 (E301)	oCI substrate	10 μ m	Spin-coating
	Underfill	6 μ m	Dip-coating
	Passivation	10 μ m	Spin-coating
Polyimide (PI)	oCI substrate	5 μ m	Spin-coating
Gallium nitride (GaN)	μ LED	6 μ m	Epitaxial growth
Silicon oxide (SiO _x)	To facilitate PI release	200 nm	PECVD
Silicon nitride (Si _x N _y)	Passivation of GaN mesas and protective film for underfill		PECVD
Aluminum (Al)	Sacrificial layer	1 μ m	Sputter deposition
Gold (Au)	p-contact	5 nm	Evaporation
	Metal tracks	400 nm	Sputter deposition
Indium (In)	Bonding metal	4 μ m	Evaporation
Tungsten-titanium (WTi)	Diffusion barrier	200 nm	Sputter deposition
	Contact layer during Al dissolution	200 nm	
Platinum (Pt)	Diffusion barrier	50 nm	Sputter deposition
	Adhesion promoter	40 nm	
Silver (Ag)	Reflective p-contact	100 nm	Evaporation
Nickel (Ni)	Formation and adhesion of p-contact	5 nm	Evaporation
Titanium (Ti)	Adhesion promoter	40 nm	Sputter deposition
	Diffusion barrier		

Materials

The oCI combines components realized using the materials listed in **Table 2** indicating the respective material functionalities. As described in further detail in the section “Wafer Bonding Process”, μ LEDs are transferred from a sapphire fabrication wafer to a polymer substrate comprising the p-contact metallization using epoxy resin as an underfill. It serves the purpose of mechanically stabilizing the μ LEDs during the LLO process. The n-contact metallization, which is processed on the underfill after LLO, is subsequently passivated by another epoxy resin layer.

The basic process compatibility of the oCI materials has already been demonstrated in previous work: (i) μ LEDs have been realized on sapphire wafers (Goßler et al., 2014; Ayub et al., 2016; Klein et al., 2016), (ii) indium (In) has been deposited as a bonding material on μ LED mesas (Klein et al., 2016), and (iii) the μ LEDs have been transferred wafer-wise onto polymer (Goßler et al., 2014) and silicon (Si) (Ayub et al., 2016) substrates using LLO and epoxy resin underfill. In order to improve the thermomechanical behavior of the oCI probes, the PI substrate comprising the p-contact metallization originally processed on Si carrier wafers had to be replaced

by an epoxy resin layer. For this purpose, some fabrication steps needed to be developed. They targeted the spin-coating of the epoxy resin serving as polymer layer #1 and its release from a carrier substrate. In contrast to PI, which is easily peeled off a silicon oxide (SiO₂) naturally grown on silicon (Si) carrier wafers (Goßler et al., 2014), sapphire carrier substrates will be introduced in the newly established process. The main reason behind this additional change in oCI processing is the residual mechanical stress which strongly affects the wafer-level μ LED bonding. This is in particular the case when μ LEDs realized on sapphire are transferred onto Si substrates. Again, the mechanical stress is caused by differences in the CTEs, in this case those of sapphire and Si, as discussed in detail in Klein et al. (2016).

These new material modifications required the following process developments and optimizations:

- spin-coating of a solvent-free epoxy resin film to achieve thin polymer layers with homogeneous thicknesses down to 5 μ m enabling a complete layer curing;
- layer adhesion between the epoxy resin layer and the gold-based oCI p-contact metallization;

- probe release from the carrier substrate exerting minimal mechanical stress on the oCI probes.

Material properties of layers #2 and #3 are subject to some requirements in view of oCI processing and probe functionality. These are

- that the epoxy resin of polymer layer #2, i.e., of the underfill, be solvent-free and cure at temperatures below 170°C with minimal material shrinkage. The first request is due to the fact that the material needs to be cured in the narrow gap between the sapphire-carrying μ LED wafer and the carrier wafer of the polymer substrate, where the exchange of solvents by diffusion is limited; the requirement about curing temperature and shrinkage aims at ensuring the integrity of the gold (Au)–In-based bond between the μ LED and oCI p-contact metallization;
- that the polymer layer #3, i.e., the probe passivation, be highly transparent at the μ LED wavelength around 460 nm and fulfill the same restrictions regarding thermal budget.

Upon considering these requirements, we chose the epoxy resin E301 as the material of choice since it is optically transparent and cures below 170°C, the critical temperature for the μ LED bond. The used polymers in the oCI and their process behaviors are summarized in **Table 1**.

oCI Fabrication

A schematic of the oCI manufacturing process is shown in **Figure 2**. This wafer-level process can be split into the fabrication sequences of (i) the μ LEDs on a sapphire wafer (**Figure 2A**), (ii) the polymer substrate with p-contact metallization (**Figure 2B**), and (iii) the μ LED transfer and bonding with subsequent n-contact metallization and passivation (**Figure 2C**). The μ LED process applies epitaxial growth of GaN by metalorganic vapor phase epitaxy and needs to be performed on a sapphire substrate at temperatures above 1000°C to achieve high LED efficiencies (Nakamura, 1991). Although the polymer substrate is processed on a carrier wafer using moderate temperatures, i.e., max. 450°C, sapphire is used as well in order to minimize the thermomechanical stress during the wafer-level bonding that had affected the structures in the case of Si substrate wafers (Klein et al., 2016).

GaN-Based μ LED Process

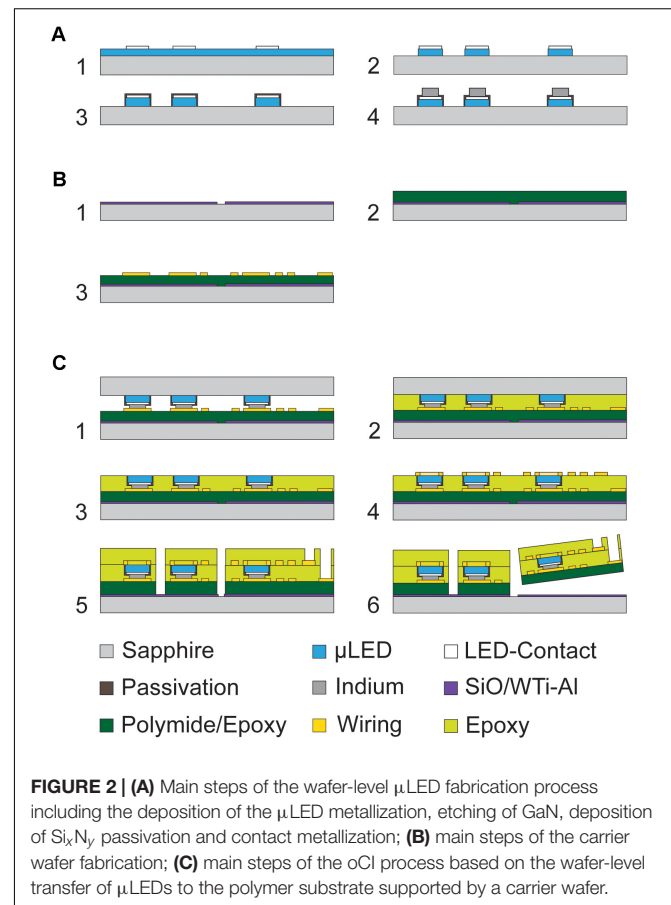
The μ LED process applies commercial GaN-on-sapphire wafers. It starts with cleaning the GaN surface by dipping the wafers for 5 min into 5 vol.% hydrochloric acid (HCl) followed by the first photolithography step using an image reversal photoresist (AZ5214E, Microchemicals, Ulm, Germany). Then 5 nm of nickel (Ni) and 5 nm of Au are deposited by evaporation in order to create the first layer of the p-contact metallization of the p-doped GaN. Following resist lift-off, the p-contacts are annealed in oxygen atmosphere at 550°C to lower the contact resistance; at this step, a Ni oxide forms at the surface. The Ni oxide is subsequently removed by oxalic acid to achieve an interface with low contact resistance (Mengzhe et al., 2009) and high optical transmittance through this first layer of the p-contact. Using the

same photolithography mask and AZ5214E photoresist, 100 nm of silver (Ag) is evaporated onto the preprocessed p-contact to form the reflective part of the p-contact. A second annealing step in nitrogen (N_2) atmosphere performed at 400°C forms the final contact with a reflectivity of 81% at 470 nm and a contact resistance of $2.9 \times 10^{-4} \Omega\text{cm}^2$.

Next, a diffusion barrier is deposited onto the Ag-based p-contact metallization. It serves as a protection of the p-contact and underlying GaN against In diffusion. The In is later used as a bond metal. The diffusion barrier comprises 200 nm of tungsten titanium (WTi; composition of 90% W and 10% Ti) and 50 nm of platinum (Pt) as an adhesion promoter for the In bond metal. The p-contact and the diffusion barrier are schematically shown in **Figure 2A1**.

A photoresist masking layer (AZ9260, Microchemicals, Ulm, Germany) with a thickness of 15 μm is used to pattern the GaN layer in a chlorine-based plasma etch process and to form the μ LEDs structures. The etch process is performed in an inductively coupled plasma etcher at a reduced power of 170 W, resulting in an etch rate of 660 nm/min. This moderate etch rate avoids high temperatures and maintains the photoresist integrity. Following the resist strip, 6- μm -high GaN mesas structures with p-contacts are obtained, as schematically shown in **Figure 2A2**.

The GaN μ LED mesas are then passivated with a layer of silicon nitride (Si_xN_y , 1 μm) applied by plasma-enhanced



chemical vapor deposition (PECVD). This layer serves as a protective film of the μ LED sidewalls against short circuits. The Si_xN_y on the sapphire surface between the μ LED mesas is structured using a 10- μm -thick AZ9260 photoresist mask and reactive ion etching (RIE). As a result, only the μ LED mesas and their respective metallization are covered with Si_xN_y (**Figure 2A3**). The exposed sapphire substrate between the GaN mesas and the μ LED structures is next covered by an additional 50-nm-thin PECVD Si_xN_y layer. It is later needed as a protective film against the polymer underfill used during the LLO process.

In order to prepare the μ LED wafer for bonding onto the polymer substrate on its carrier wafer, a 4- μm -thick In layer is deposited on the 6- μm -high μ LED mesas. The In patterns are defined using a bi-layer lift-off process applying a 12- μm -high layer of LOR 30B photoresist (MicroChem, MA, United States) and a 7- μm -thick AZ4533 photoresist (Microchemicals, Ulm, Germany). With this protection in place, the Si_xN_y passivation on the μ LED p-contact and diffusion barrier is then opened using RIE. Subsequently, the In bond layer is evaporated, as described in Klein et al. (2016), and patterned by lifting off the bi-layer photoresist stack to finalize the μ LED process (**Figure 2A4**).

Polymer Substrate Process

The process sequence to realize the polymer substrates of the oCIs is illustrated in **Figure 2B**. In contrast to the state-of-the-art hybrid oCIs (Goßler et al., 2014), in this study the process is performed on sapphire wafers to avoid thermal stress during the In-based wafer bonding, which had hampered earlier systems (Klein et al., 2016). In order to compare both oCI variants, i.e., the hybrid and epoxy-resin-only structures, we realized two polymer substrate variants, as described in detail in the following sections.

PI-based oCI probes

In the case of PI, a 200-nm-thin PECVD SiO_x layer is deposited on the sapphire carrier wafer in order to enable the final probe peel-off. This oxide layer is structured using a photoresist layer (AZ1518, Microchemicals, Ulm, Germany) and RIE such that SiO_x remains only in those wafer areas where the implants are realized (**Figure 2B1**). In the other areas the sapphire surface therefore remains exposed. This ensures that the PI film optimally adheres directly to the carrier wafer minimizing the effect of a potential PI delamination on the implants, thus increasing the process control and fabrication yield.

Following the carrier wafer preparation, PI is spin-coated to a thickness of 5 μm and then cured in N_2 atmosphere at a peak temperature of 450°C (**Figure 2B2**). This is followed by the deposition of the p-side metallization of the μ LEDs using a bi-layer lift-off process applying a 1- μm -thin lift-off resist (LOR10B, MicroChem, MA, United States) in combination with a 3- μm -thick positive photoresist (AZ1518). Prior to the metal deposition, the PI surface is cleaned and activated in argon (Ar) plasma followed by the sputter-deposition of 40 nm of Pt, 400 nm of Au, and 40 nm of Ti without breaking the vacuum. The Pt film serves as the adhesion promoter to PI while Au is the highly conductive part of the metal stack. In the subsequent wafer-level bonding process, the top Ti film prohibits the diffusion of In along the metal tracks. The lift-off is performed using a lift-off

tool applying dimethyl sulfoxide with high-pressure to the wafer surface. Subsequently, the wafer is rinsed to ensure a clean substrate surface. In the final step of the polymer substrate fabrication, the Ti layer is removed on the contact pads in order to enable the wafer-level bonding by In–Au reflow. This Ti etch step is performed with a 4- μm -thick photoresist (AZ4533) using hydrofluoric acid (HF, 1%) for 15 s to expose the Au underneath (**Figure 2B3**).

Epoxy-resin-only oCI probes

In the case of the epoxy-resin-based oCI substrates, the carrier wafer has to be equipped with a sacrificial layer as epoxy resin can neither be peeled from the sapphire substrate nor from the SiO_x layer used in the case of the PI substrates. We addressed this challenge by applying a sacrificial aluminum (Al) layer which is later dissolved by anodic metal dissolution (Metz et al., 2005) for oCI probe release. This Al film is deposited on an additional, conductive WTi layer which remains unaffected by the sacrificial Al removal. This WTi layer is necessary to guarantee electrical contact throughout the entire release and thus ensures the complete Al removal. We applied a 200-nm-thin WTi film and a 1- μm -thick Al layer which are sputter-deposited and evaporated, respectively. This layer stack is then structured into areas of $1 \times 2 \text{ cm}^2$ enabling the local lift-off of 12 oCIs per area. The masking is done using the AZ4533 photoresist followed by selective etching of Al and WTi at 50°C using a commercial Al-etchant [mixture of phosphoric, nitric, and acetic acids diluted in water at a ratio of 12:3:1:3 (Westberg et al., 1996)] and hydrogen peroxide (H_2O_2 , 20 wt.%), respectively.

Spin-coating – Following the carrier wafer preparation, the epoxy resin E301 needs to be deposited with homogenous layer thickness. Similar to PI, spin-coating was chosen as the deposition method. As the E301 resin consists of two components that have to be mixed prior to layer deposition and as it does not contain any solvent, spin-coating this material presents several challenges compared to others such as photoresist or the solvent-based epoxy resin SU-8.

First, the E301 layer does not dry during spin-coating like solvent-based films. Furthermore, it has a low interfacial energy with sapphire, which leads to the formation of thicker islands rather than a homogeneous layer. Island formation most often starts at the edges and the middle of the carrier wafer. In order to suppress this effect, the adhesion promoter Protek B3 Prime (Brewer Science, Rolla, MO, United States) is applied; it basically provides a surface silanization. We use a dehydration bake (205°C, 5 min) and a primer baking step (205°C, 1 min) between which the adhesion promoter is spin-coated. Spin-coating E301 on a primed wafer shows a much improved wetting as a consequence of which the E301 no longer collapses into islands. Nevertheless, the material still starts creeping toward the wafer center within a minute after spin-coating, hence reducing the wafer area covered by E301. In order to prevent this undesired effect, the E301-coated wafer needs to be transferred to a hotplate within seconds to initiate the curing procedure in particular at the interface between primer and epoxy resin. We chose a hot plate temperature of 75°C, which is below the evaporation temperature of both E301 components. The curing

temperature was kept constant for 3 h; it was then ramped up to 120°C within 10 min; the wafer is kept at that temperature for additional 12 h.

During the process development, we evaluated the effect of the spinning speed (between 1,000 and 7,000 rpm in steps of 1,000 rpm) and spinning duration (between 2 and 30 s) on layer thickness, thickness homogeneity, and material cross-linking.

Metallization – In addition to the spin-coating parameters, the adhesion of the subsequently deposited layers needs to be evaluated as well. In the case of the epoxy-resin-based oCI probes, only the adhesion of the p-contact metallization has to be analyzed. This is because the E301 underfill is expected to adhere inseparable to an already cured E301 layer. In this study we investigated layer stacks of chromium Cr/Au/Ti, Pt/Au/Ti, and Ti/Au/Ti where Au (400 nm) serves as the conductive part of the wiring, and the upper Ti layer (40 nm) acts as a diffusion barrier during the subsequent μ LED transfer process. For the first metal layer, we tested Pt, Ti, and Cr. These are commonly used to improve the layer adhesion (Vancea et al., 1989; Ordonez et al., 2012a). The metal stacks are sputter-deposited and patterned by the lift-off technique.

As adhesion promoters we tested (i) surface silanization by spin-coating and from the vapor phase at 120°C, (ii) a 20-nm-thin silicon carbide (SiC) film deposited using PECVD at 100°C, and (iii) the chemical treatment of the epoxide functional groups by dipping the epoxy resin layers into 37 wt.% HCl intended to split the epoxy rings into pairs of hydroxyl groups.

Wafer Bonding Process

The third sequence of the oCI fabrication process transfers the μ LEDs from the sapphire wafer to the polymer substrate supported by its carrier wafer. The respective wafer bond applies an In–Au interdiffusion bonding process (Goßler et al., 2014). For wafer bonding, the μ LED wafer is aligned upside down with respect to the Au pads on the polymer substrate using the mask aligner MA/BA6 (Karl Süss, Garching, Germany). The dual wafer sandwich is then transferred to the wafer bonder SB6 (Karl Süss, Garching, Germany) where a pressure of 80 kPa is applied at 140°C for 30 min under vacuum (Klein et al., 2016) [see cross-section in **Figure 2C1**].

The gap between both sapphire wafers mainly resulting from GaN mesas and the In bond metal is filled with an epoxy resin to mechanically stabilize the μ LEDs during the subsequent LLO process. The polymeric underfill is performed by exposing the wafer sandwich under vacuum to liquid epoxy resin. Once the wafer has been immersed into the epoxy, a pressure of 1 bar is applied using N_2 atmosphere. The combination of an initial vacuum followed by applying a pressure facilitates the capillary gap filling (**Figure 2C2**). In general, only a small void remains at the wafer center. It is usually smaller than 5% of the total wafer area. The epoxy resin is cured at room temperature (RT) for 12 h followed by a temperature ramp to 120°C at which the wafer remains for 12 h. This procedure ensures that none of the epoxy resin components evaporates prior to the completion of their cross-linking.

Laser Lift-Off

Next, the μ LED sapphire wafer is released in a LLO process using a 248 nm excimer laser (3D-Micromac, Germany, Chemnitz) (Goßler et al., 2014). During the LLO process, the individual μ LEDs are delaminated first using a laser fluence of 800 mJ/cm² followed by the delamination of the underfill at 500 mJ/cm². This sequence prevents the fracture of the μ LEDs by the compression waves caused by the decomposition of GaN into Ga and N_2 under the laser light. After the laser has been processed the entire wafer, the sapphire wafer can simply be lifted off using tweezers (**Figure 2C3**). In preparation of the deposition of the n-side metallization, residual Ga on the μ LED surface is removed using a 5-min-long exposure to ammonia (NH₃, 5 vol.%).

Probe Metallization, Patterning, and Release

Similar to the p-side wiring, we apply an Au-based metallization stack, where Ti is applied as the first metal, as it provides a better adhesion to the epoxy underfill. The metallized wafer with μ LEDs connected on both sides is shown in **Figure 2C4**. The last layer of epoxy resin is then again applied by spin-coating. The rough surface of the second epoxy layer resulting from the LLO is favorable enough for layer adhesion so that no adhesion promoter is needed. The epoxy resin is cured for 3 h at 75°C followed by 12 h at 120°C. Subsequently, a 30- μ m-thick photoresist etch mask (AZ9260) is applied to open the contact pads and to trench the polymer stack by RIE down to the substrate for probe separation (**Figure 2C5**). The process is similar to that described in Goßler et al. (2014) and Ayub et al. (2016).

In the case where PI is used as the polymer substrate, the oCI probes can be simply peeled off the carrier wafer one by one using tweezers. In the epoxy substrate case, the sacrificial Al layer is removed using anodic metal dissolution, thereby releasing the oCIs (Westberg et al., 1996). To connect the Al layer a spring-loaded needle connects the wafer surface in dedicated etch openings (300 × 300 μ m²) between the oCIs. The Al layer is dissolved by immersing the entire wafer into 0.1 M saline solution and applying a voltage of 1.6 V with respect to the solution. The counter electrode is made of a ceramic substrate coated with Pt. The etch openings in the polymer layer provide electrical contact to a field of 12 oCIs which are released from the carrier wafer and are ready to be picked up from the solution using tweezers. In general, the sacrificial layer approach benefits the oCI samples by a pronounced reduction in mechanical stress during the release.

Process Evaluation and oCI Probe Characterization

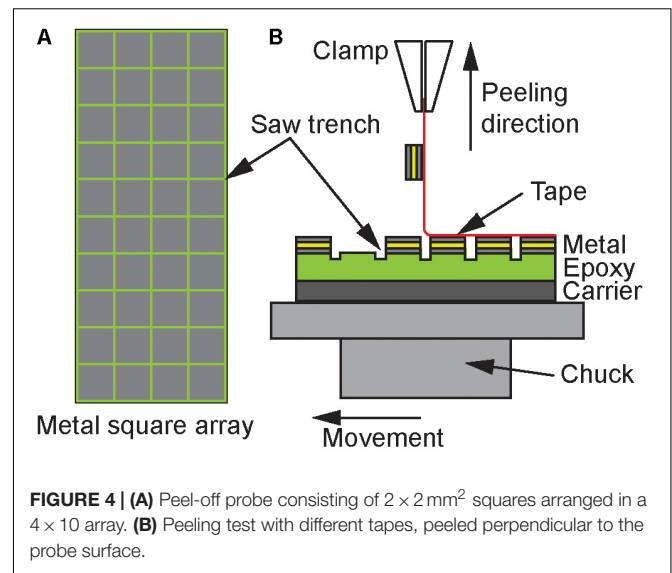
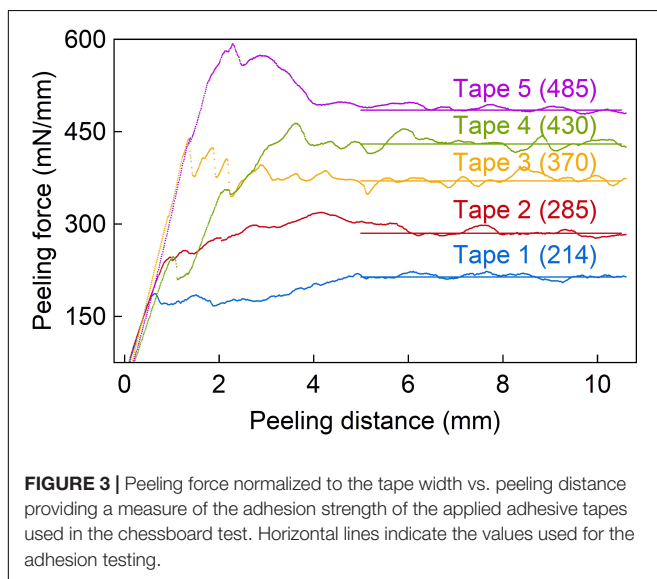
Characterization of the Spin-Coated Epoxy Resin Layers

The spin-coated epoxy resin thickness was measured using the profilometer P11 (Tencor, Milpitas, CA, United States) as a function of spinning parameters at nine positions across the 4-inch wafers by cutting out squares of the epoxy film with a size of ca. 2 × 2 mm². Aside from the complete, homogenous

coverage of the carrier wafer, a complete cross-linking of the spin-coated epoxy resin is crucial. Depending on the spin-coating parameters, we observed that some E301 layers remained sticky on the surface, indicating an incomplete cross-linking of the material. Due to the used deposition process, differential scanning calorimetry, which is widely applied to analyze the cross-linking of epoxide materials (Montserrat et al., 2003) could not be used here. The main reason is that 5 mg of material would be required for such an analysis while spin-coating covers the 4-inch wafers with just 10 μ g of epoxy resin. Instead, the etch rate of differently spin-coated E301 layers processed in an oxygen plasma was used as a measure of the level of cross-linking. In order to extract the epoxy resin etch rates and process uniformity across the test wafers, we measured the layer thicknesses h_{ini} and h_{etch} before and after plasma etching at nine positions, as described above. The etch rates are compared to the etch rate of bulk E301 samples cured under standard conditions to achieve more than 99% cross-linking (Epoxy Technology). All test samples including the bulk sample have been processed on 4-inch wafers representing an etch load above 99% which allows to eliminate the influence of any masking layer. During the etch process the wafers are actively cooled while the wafer temperature is monitored in order to exclude the influence of an increased temperature on the etch rate. It was found that the etch rate decreases with increased level of cross-linking.

Metal Layer Adhesion

The metal layer adhesion to E301 was tested for several adhesion promoters using an extended peel-off test. The adhesive tapes used here have the same carrier material but different adhesion properties. These are first characterized on a sputtered Ti layer representing the uppermost surface of the metal stack to be analyzed (section “Epoxy-resin-only oCI probes”). The adhesive strength between different tapes and the Ti is shown in **Figure 3** with the peeling force per tape width as a function of peeling



distance. These measurements indicate a difference in the peeling force by a factor of 2.2 between the weakest and strongest tape.

The metal layer stack deposited onto the epoxy resin E301 is subdivided into a 4×10 array with squares of $2 \times 2 \text{ mm}^2$ separated by 200- μm -wide trenches realized using a wafer saw that partially cuts into the underlying E301 layer. The peeling tests under 90° , as illustrated in **Figure 4**, use different tapes with a width of 12 mm slightly overlapping the array to eliminate edge effects. The adhesive strength of the metal layer stacks is evaluated using the number of metal squares remaining on the wafer after peel-testing with the adhesive tapes of different adhesive strengths.

Thermomechanical Behavior

To investigate the thermomechanical behavior of the hybrid and epoxy-resin-only oCI samples, both types of implants have been exposed to a heat ramp from RT to 100°C and subsequently cooling down to RT. For this purpose, the oCI probes are placed in a glass container to minimize any perturbation from air convection and to enable visual observation using a microscope. The glass container is heated using a hot plate while the temperature is monitored by a PT100 temperature sensor. The temperature was raised and reduced in steps of 5 K and kept constant for 2 min to stabilize the temperature of the oCI.

Thermal Characterization

The temperature increase on the probe surface was monitored using an infrared camera (PI 450, Optris GmbH, Berlin, Deutschland) while one μLED was operated with DC of up to 10 mA. The probe under test was either floating in air, or immersed into agarose gel (0.5 wt.%, Agar-Agar, Roth, Karlsruhe, Germany) or water both kept at a temperature of 37°C mimicking the body temperature. In the case of agarose gel and water, the probe surface to be measured with the IR camera was covered by 5 μm of the immersion material adjusted using a precise translational stage. The opposite side of the probe was facing the bulk of the immersion material with a thickness of at least 10 mm.

Optical Characterization of oCI Probes

The oCI probes are optically characterized using an integration sphere (ISP-50-I-USB, Ocean Optics, Ostfildern, Germany) (Schwaerzle et al., 2017). The probes mounted on a PCB and wire bonded to it are operated with a drive current between 0 and 10 mA while the radiant flux and the spectrum of emitted wavelengths are measured.

RESULTS AND DISCUSSION

Process Validation

Spin-Coating

Spin-coating test series at various spin speeds and spin durations revealed a maximum thickness variation of the E301 epoxy resin of 7%, measured between the wafer center and a radius of 45 mm. In contrast to solvent-based polymer solutions such as PI, this high thickness homogeneity is independent of the spin-coating parameters. It is caused by the fact that E301 is solvent-free and levels itself during the curing procedure.

Figure 5 shows the achieved epoxy resin layer thicknesses as a function of spin speed for different spin durations. For all samples the curing procedure mentioned earlier was followed. Wafers with spin durations longer than 10 s showed a highly sticky surface. They were rejected because the stickiness indicates a partial separation of the two E301 components inhibiting the complete curing of the material. In case of the test samples coated with spin durations of 2, 3, 5, and 10 s at different spin speeds epoxy resin films with a non-sticky surface and thicknesses between 3.8 and 62.5 μm are achieved. Layers thinner than 3.8 μm could not be obtained, even for spin speeds above 5,000 rpm and independent on the spin duration.

Cross-Linking

Figure 6 shows the epoxy layer etch rate in oxygen plasma normalized to the bulk etch rate of 520 ± 20 nm/min as a function of the spin duration for various spin speeds. A clear increase of

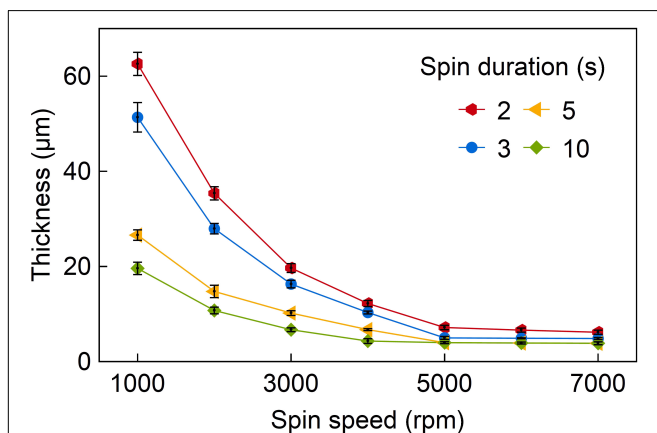


FIGURE 5 | Spin-coating curve of epoxy resin E301 with the achieved layer thickness as a function of spin speed for different spin durations. A minimum layer thickness of 3.8 μm is achieved.

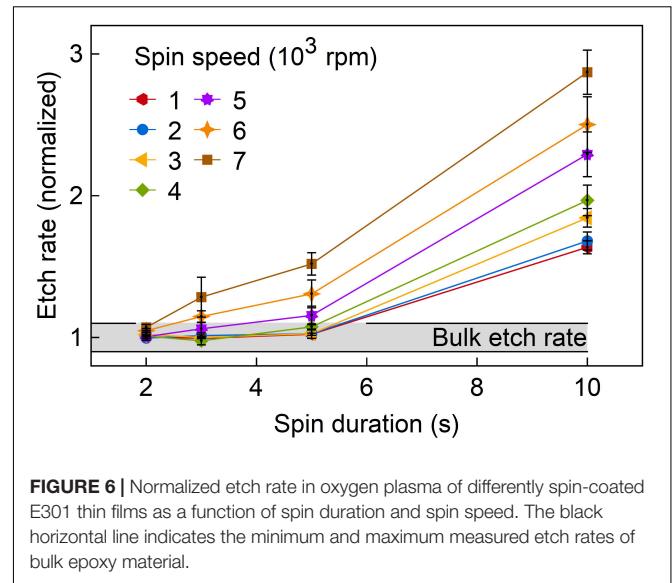


FIGURE 6 | Normalized etch rate in oxygen plasma of differently spin-coated E301 thin films as a function of spin duration and spin speed. The black horizontal line indicates the minimum and maximum measured etch rates of bulk epoxy material.

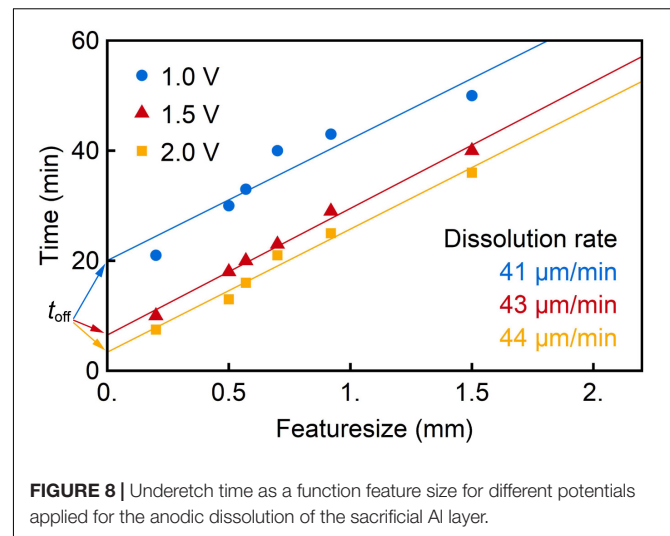
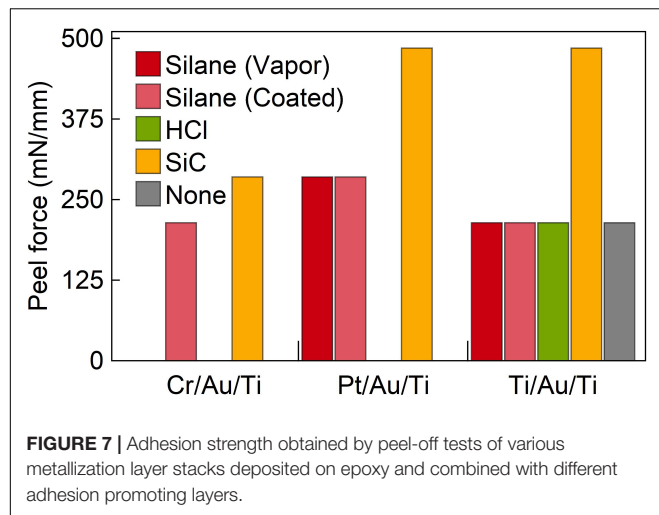
the etch rate with longer spin durations as well as for higher spin speeds is found. Obviously, the highest etch rates are achieved for a spin duration of 10 s independent on spin speed. This indicates the lowest cross-linking rate as already observed with the sticky epoxy layer surfaces for spin durations longer than 10 s.

In addition, wafers coated with long spin durations and high spin speeds showed larger deviations of the etch rate across the wafer. The highest etch rates were observed towards the wafer edge. The observed correlation between spin-coating parameters and etch rates indicates that centrifugal forces separate the epoxy resin components from each other which leads to an incomplete cross-linking of the E301 layers. This separation occurs as component A has a density of $\rho_A = 1.15 \text{ g/cm}^3$ while the density of component B is $\rho_B = 0.87 \text{ g/cm}^3$ (Epoxy Technology). In conclusion, monitoring the etch rate of epoxy resin thin films represents a practicable way to compare layer properties with a bulk E301 reference sample. It allows to judge whether there is a significant separation of epoxy components reducing the cross-linking ability of the mixture.

Metallization

This study tested three different metal layer stacks, i.e., Cr/Au/Ti, Pt/Au/Ti, and Ti/Au/Ti, and combined them with four adhesion promoting processes, namely surface silanization (vapor phase and spin-coating), epoxy resin exposure to HF, and deposition of a SiC layer. The results are summarized in **Figure 7**. The given peeling force correlates with the peeling strength of the applied adhesive tapes, i.e., Tape 1 to Tape 5.

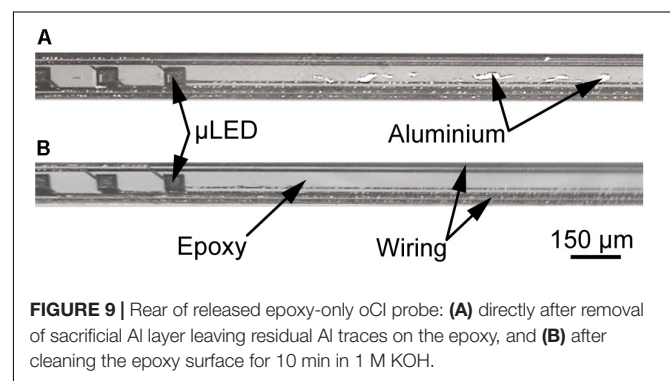
Obviously, SiC provides the best layer adhesion independent on which metal stack is used. Following a study by Ordonez et al. (2012b), this result was expected for Pt but is now established for Cr and Ti as well. The silanization approach was best in case of the Pt/Au/Ti stack, but still lower in adhesion strength than the films on SiC. Surface modification of the functional epoxide group by exposure to HF shows no increase in adhesion for any of the tested metal stacks.



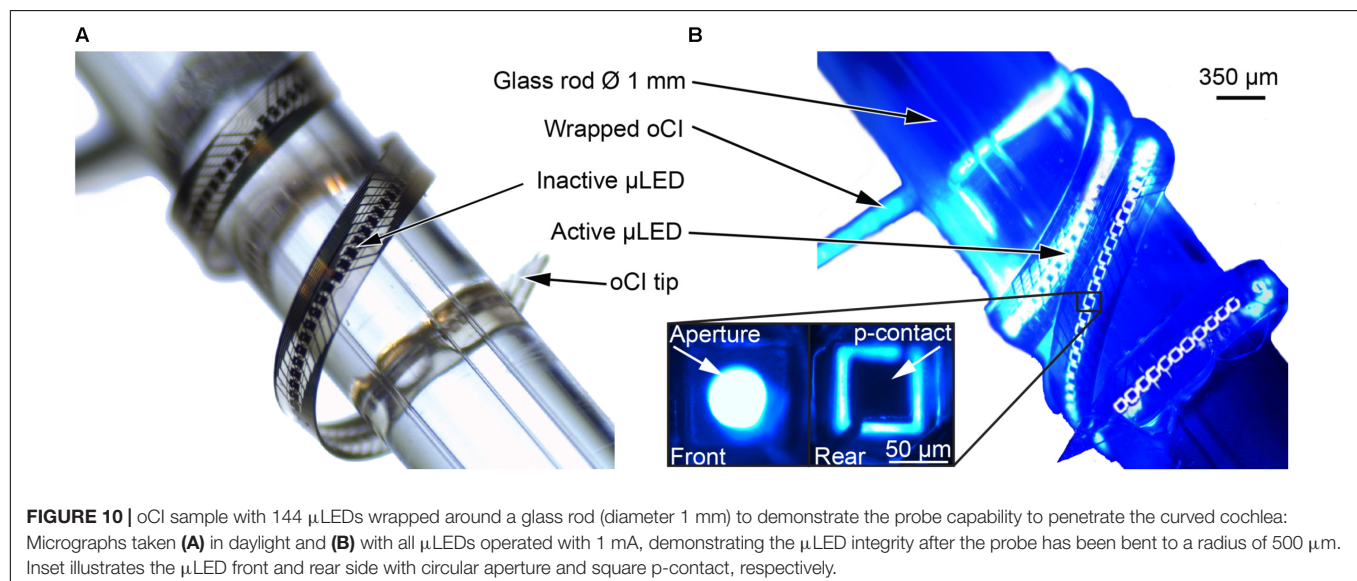
Due to the fact that Ti is easier to structure by wet and dry etching than Pt, and that it is also used as the upper metal layer, the decision was to take Ti in the form of the Ti/Au/Ti sandwich in order to ensure the adhesion on E301.

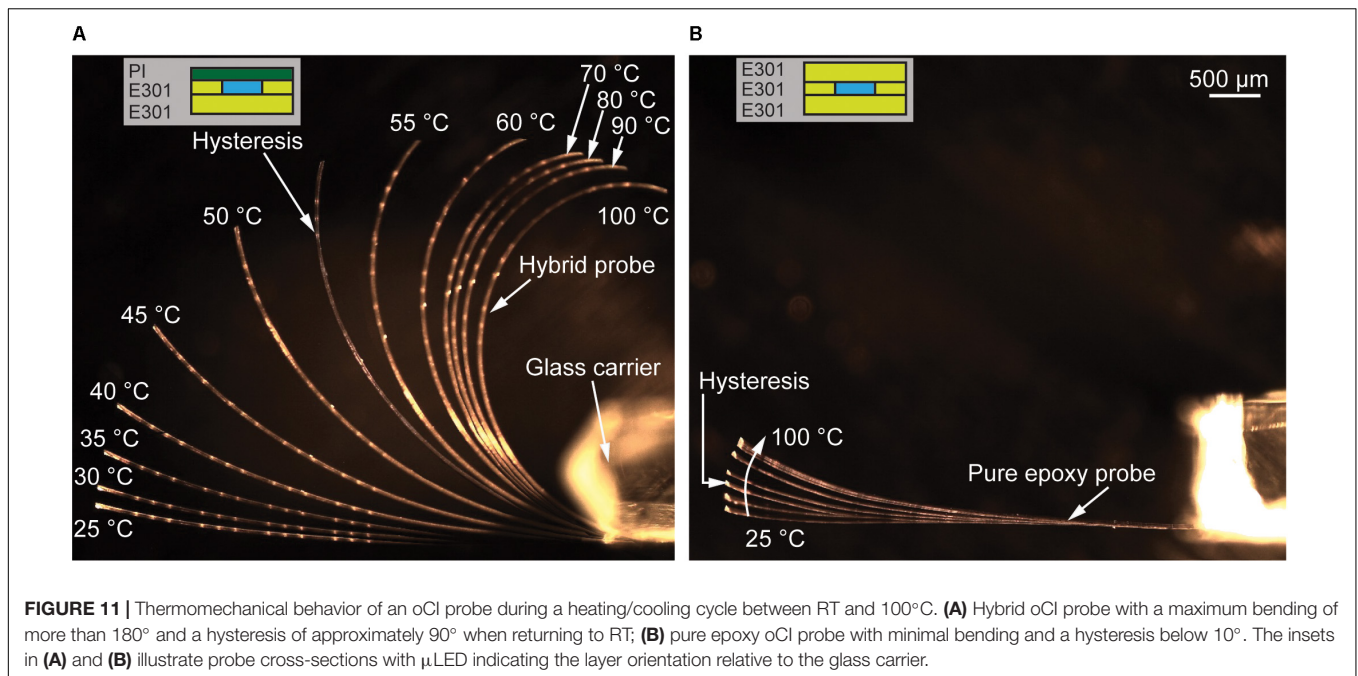
Sacrificial Aluminum Release

Investigating the sacrificial Al removal showed that the absolute dissolution time for different structure sizes linearly depends on the feature size to be released, as demonstrated in **Figure 8**. The linearity indicates that the process is not diffusion limited as would be expected in a purely chemical etching process where reaction products must be removed by diffusion. The dissolution rate investigated depends only on the current flow and therefore on the applied voltage. The temporal offset t_{off} , shown in **Figure 8**, originates from Al in the 40- μ m-wide etch trenches between individual probes. It needs to be dissolved before the



dissolution of the Al underneath the oCI structures starts. As soon as these trenches are opened, the probe underetching proceeds until the samples are released.





After successful release, some Al residues were found on the rear of the probes, as shown in **Figure 9A**. It is assumed that the dissolution process of Al depends on the release rate along grain boundaries. This can lead to Al islands losing their electrical contact to the underlying WTi layer. This stops their further dissolution. To remove these Al residuals, probes are etched in 1 M potassium hydroxide (KOH) for 10 min, which results in a clean probe (**Figure 9B**).

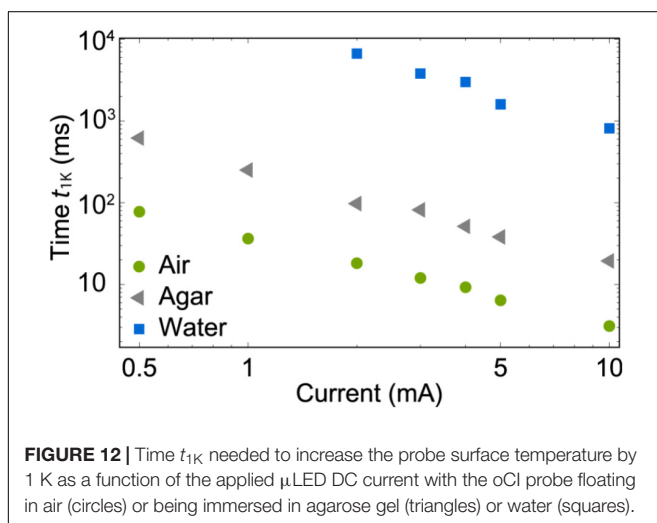
oCI Characterization

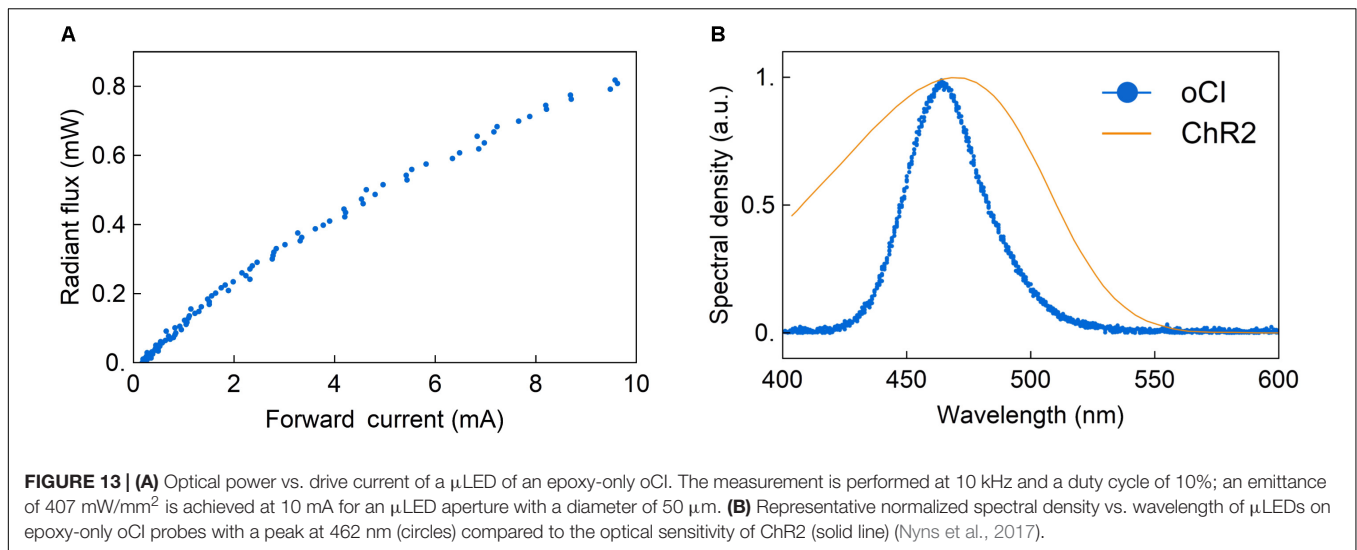
Based on the process parameters identified in this study, oCI probes with 144 μ LEDs were realized as hybrid oCIs based on a PI substrate and as epoxy-resin-only probes using three layers of E301. The example of an epoxy-resin-only probe is shown

in **Figure 10**. All 144 μ LEDs can be addressed and operated as indicated on the right-hand side of **Figure 10**. To demonstrate the ability of the oCI to wind into a cochlea, it was successfully wrapped around a glass rod with a diameter of 1 mm, resulting in a bending radius of 500 μ m.

Thermomechanical Behavior

The overarching aim of the technical developments described here is the optimization of the thermomechanical behavior of oCI probes. This behavior is determined by the different CTEs of the applied materials, namely PI and the epoxy resin E301 (Goßler et al., 2014), causing thermomechanical stress in the oCI and probe bending. We therefore compare a hybrid oCI probe with an epoxy-only sample by varying the temperature between RT and 100°C. **Figure 11** shows probe side views of both probe variants taken at several temperatures when increasing the temperature from RT and cooling back from 100°C to RT. The remaining probe bending indicates a mechanical hysteresis in the thermomechanical probe response. As shown in **Figure 11A**, the hybrid oCI bends toward the PI side by more than 180° resulting in a bending radius of 1.65 mm. Already at 80°C, the probe tip points in the opposite direction compared to the original orientation at RT. In contrast, the pure epoxy oCI just bends slightly within the same temperature interval. This bending is due to a small variation in the thickness of the first and third polymer layers of the oCI, caused by applying the same spin-coating parameters for both layers but having different surfaces. After cooling both oCIs down to RT, a hysteresis is observed, which is likely caused by the glass transition temperature of E301 around 55°C. In conclusion, irreversible bending is induced into the oCI. In the case of the hybrid oCI, this hysteresis deflects the tip by about 90°. This is a significant challenge when trying to implant the probe into





the cochlea: in fact a probe curling into the opposite direction would be required for the μ LED to directly face the SGNs. The increased CTE of E301 above its glass transition temperature is reflected in the increased bending between 40 and 60°C, as shown in **Figure 11A**. The pure epoxy oCI shows only a small hysteresis. It is deflected by about 10° from its original position, which is still suitable for probe implantation into the cochlea.

Thermal Characterization

Figure 12 shows the time t_{1K} needed to increase the probe temperature by 1 K as a function of the μ LED DC current varied between 0.5 and 10 mA and the material surrounding the probe. As expected, the surface temperature is strongly dependent on the immersion material, i.e., the fastest temperature increase is observed when the probe is floating in air. In this case, the 1 K-limit is already reached within $t_{1K} = 3$ ms at a maximum μ LED current of 10 mA. In contrast, due to the high thermal conductivity of water of ca. 0.62 Wm⁻¹ K⁻¹ heat dissipation is highly increased resulting in an increased rise time t_{1K} of 800 ms. In contrast, a value of $t_{1K} = 11$ ms is obtained for the agarose gel immersed probe applying a DC current of 10 mA. This faster probe heating is presumably caused by a reduced convection in agarose gel compared to water.

Optical Characterization

The optical characterization of the integrated μ LED using the integrating sphere revealed a radiant flux of a single μ LED of 0.82 mW at a forward current of 10 mA, as shown in **Figure 13A**. This corresponds to an emittance of 407 mW/mm², referred to an emitting surface with a diameter of 50 μ m. A slightly non-linear response is obtained, indicating a drop of the μ LED efficiency caused by thermal and non-thermal effects. The thermal response is increased due to the fact that the oCI probe was operated in air and was thus thermally well isolated. As demonstrated by Schwaerzle et al. (2016) and replicated in our thermal experiments, operating an LED-based probe in contact with agarose gel taking the role of a heat sink, the temperature

increase can be minimized, thus optimizing the LED efficiency. As indicated in **Figure 13B**, the peak wavelength is at 462 nm, which is suitable for the stimulation of ChR2.

CONCLUSION

This work developed and validated a new fabrication process of optical CIs based on a single biocompatible and optically highly transparent epoxy resin used as substrate and passivation materials. We substituted the PI substrate initially used by Gößler et al. (2014) by the epoxy resin E301. This development was motivated by the fact that the existing hybrid oCI probe variant is hampered by a pronounced residual and thermomechanical probe bending due to the CTE difference of the implemented materials.

The process development included a dedicated spin-coating procedure of the solvent-free epoxy resin E301 to guarantee layers of homogeneous thickness. Optimizing two spin-coating parameters, namely spin speed and spin duration, we reliably achieved layer thicknesses between 3.8 and 62.5 μ m. In order to prevent the uncured films from collapsing into E301 islands an appropriate adhesion promoter has been introduced in combination with a fast curing procedure applied immediately after spin-coating. Epoxy layers with a nearly perfect surface and homogenous thicknesses with a maximum variation of 7% across 4-inch wafers were achieved.

Since the cross-linking of the epoxy layers strongly depends on the spin-coating parameters, the process window was analyzed using a plasma-based dry etching process of the epoxy resin layers. It was introduced in this study to replace differential scanning calorimetry which cannot be applied in the case of thin-film materials spin-coated to carrier wafers. Depending on the spin speed and spin duration, we observed etch rates increased by a factor of up to 3 compared to optimally cured E301 bulk samples. Fully cured epoxy layers with etch rates similar to bulk material were achieved for a variety of spin

speed and spin duration combinations enabling a wider range of layer thicknesses. As an example, the thinnest epoxy layer with a thickness of 5 μm that could be cured completely was achieved at 5,000 rpm and with a spin duration of 3 s. On the other hand, long and fast spin-coating resulted in a separation of the two components of E301. This resulted in an incomplete curing, as indicated by the increased etch rate in the oxygen plasma.

In order to guarantee the probe integrity, we optimized the layer adhesion between the μ LED metallization and the underlying polymer substrate. Various metal layer compositions and adhesion promoters were tested. It was found that SiC in combination with Pt or Ti layers leads to the best results, with a peeling force of at least 485 mN/mm as extracted using a peeling test. Titanium was finally chosen for the oCI metallization as it can be structured by wet and dry etching and as it has already been established as the upper layer of the metallization stack.

The probe release of the epoxy-only probes required in addition the introduction of a structured sacrificial Al layer. It is deposited on a permanent WTi layer which provides the electrical contact during the anodic metal dissolution. The dissolution time was found to be linearly dependent on the distance to be undercut on the oCI wafer. The absolute time to lift an oCI using this technique was determined to be 23 min. In contrast to the peel-off approach used for PI layers on SiO_x , the method has the clear advantage of allowing a stress-free probe release. From the process compatibility point of view, the peel-off should also be considered to be used for PI-based ribbon cables used for Si-based neural implants (Kisban et al., 2009), electrocorticography (ECoG) electrode arrays (Rubehn et al., 2009) or cuff-electrodes (Schuettler et al., 2000).

The study presented here compared two oCI variants, i.e., a conventional hybrid probe based on PI and epoxy resin as well as an epoxy-based device composed of a three-layer epoxy stack. We demonstrated that the epoxy-only variant is definitely superior as far as its thermomechanical response is concerned. The epoxy-only probe shows minimal bending and a strongly reduced thermomechanical hysteresis. This is a clear advantage for probe implantation into the cochlea.

The thermal probe characterization revealed that the temperature increase can be safely limited to 1 K depending on the μ LED DC current, the stimulation duration, and the medium surrounding the μ LED probe. Using agarose gel as a tissue phantom, the 1 K-limit is reached within ca. 11 ms applying a DC current of 10 mA. In contrast, a stimulation duration of 800 ms is needed to reach this temperature increase when the probe is immersed into water. It has to be kept in mind that it is yet unclear whether the medium inside the cochlea can be thermally modeled by agarose gel or liquid water as done in our tests. In comparison to pulse lengths below 10 ms, as typically applied *in vivo* (Hernandez et al., 2014), the temperature increase of our μ LEDs can in any case be safely limited to 1 K.

The realized oCI probe with 144 individually controllable μ LEDs offers radiant flux and emittance values of 0.82 mW and 407 mW/mm² per μ LED at DC currents of 10 mA, respectively, well exceeding the optical threshold of 1–4 mW/mm² (Boyden

et al., 2005; Deisseroth et al., 2006). With a peak wavelength of 462 nm and the given emittance, the optical probe reported here perfectly matches the requirements of optogenetic neuronal experiments based on ChR2.

The technology presented in this study can easily be transferred to other fields of optogenetic applications where probe flexibility and highly resolved μ LED patterns are needed. As an example, it is conceivable to temporarily stiffen the linear arrays presented here using a biodegradable material (Boyden et al., 2005; Gilgunn et al., 2012) or an inserter tool (Barz et al., 2015; Felix et al., 2013), enabling a probe implantation into cortical tissue. Once implanted, the highly flexible probe will be beneficial in view of a long-term applications at minimal tissue reaction. Similarly, flexible two-dimensional (2D) μ LED arrays realized using our technological approach will provide a high lateral resolution to stimulate the brain tissue while the probe itself adapts to the corrugated brain surface at minimal bending forces. A combination of 2D μ LED arrays with state-of-the-art ECoG electrodes arrays (Kozai and Kipke, 2009) is also foreseeable providing simultaneously highly resolved optogenetic stimulation and electrophysiological recordings (Stieglitz et al., 2009). Aside from basic neuroscientific research, we are convinced that the technology is applicable as well in the field of cardiology, i.e., as optogenetic cardiac pacemaker or defibrillator (Kwon et al., 2013b; Bruegmann et al., 2016; Crocini et al., 2016; Diaz-Maue et al., 2018).

AUTHOR CONTRIBUTIONS

EK processed the oCIs, developed the epoxy thin-film process, performed the experiments, analyzed the measurement data, prepared the figures, and contributed the manuscript. EK and CG developed the oCIs and realized the photolithography masks. OP and PR discussed the technical concepts and experimental results, and finalized the manuscript. All authors reviewed the manuscript.

FUNDING

This research received funding from the project optical CI founded by the Federal Ministry of Education and Research (BMBF, No. 13N13728). The article processing charge was funded by the German Research Foundation (DFG) and the University of Freiburg in the funding programme Open Access Publishing.

ACKNOWLEDGMENTS

We acknowledge the technical support by the cleanroom service center (RSC) team of the Department of Microsystems Engineering (IMTEK), University of Freiburg, in matters of cleanroom fabrication. Furthermore, we would like to thank the Laboratory for Biomedical Microtechnology at IMTEK for giving access to its peel-off measurement setup.

REFERENCES

- Aravanis, A. M., Wang, L. P., Zang, F., Meltzer, L. A., Mogri, M. Z., Schneider, M. B., et al. (2007). An optical neural interface: in vivo control of rodent motor cortex with integrated fiberoptic and optogenetic technology. *J. Neural Eng.* 3, S143–S156. doi: 10.1088/1741-2560/4/3/S02
- Ayub, S., Gentet, L. J., Fiáth, R., Schwaerzle, M., Borel, M., David, F., et al. (2017). Hybrid intracerebral probe with integrated bare LED chips for optogenetic studies. *Biomed. Microdevices* 19:49. doi: 10.1007/s10544-017-0190-3
- Ayub, S., Gossler, C., Schwaerzle, M., Klein, E., Paul, O., Schwarz, U. T., et al. (2016). High-density probe with integrated thin-film micro light emitting diodes (μ LEDs) for optogenetic applications. *Proc. IEEE MEMS Conf.* 379–382. doi: 10.1109/MEMSYS.2016.7421640
- Barz, F., Ruther, P., Takeuchi, S., and Paul, O. (2015). Flexible silicon-polymer neural probe rigidified by dissolvable insertion vehicle for high-resolution neural recording with improved duration. *Proc. IEEE MEMS Conf.* 636–639. doi: 10.1109/MEMSYS.2015.7051036
- Boyden, E. S., Zhang, F., Bamberg, E., Nagel, G., and Deisseroth, K. (2005). Millisecond-timescale, genetically targeted optical control of neural activity. *Nat. Neurosci.* 8, 1263–1268. doi: 10.1038/nn1525
- Bruegmann, T., Boyle, P. M., Vogt, C. C., Karathanos, T. V., Arevalo, H. J., Fleischmann, B. K., et al. (2016). Optogenetic defibrillation terminates ventricular arrhythmia in mouse hearts and human simulations. *J. Clin. Investig.* 126, 3894–3904. doi: 10.1172/JCI88950
- Conner, C. M., Craig, H. K., Raudenbush, S. W., Heavner, K., and Zwolan, T. A. (2006). The age at which young deaf children receive cochlear implants and their vocabulary and speech-production growth: is there an added value for early implantation? *Ear Hear.* 27, 628–644. doi: 10.1097/01.aud.0000240640.59205.42
- Crocini, C., Ferrantini, C., Coppini, R., Scardigli, M., Yan, P., Loew, L. M., et al. (2016). Optogenetics design of mechanistically-based stimulation patterns for cardiac defibrillation. *Sci. Rep.* 6:35628. doi: 10.1038/srep35628
- Deisseroth, K., Feng, G., Majewska, A., Miesenböck, G., Ting, A., and Schnitzer, M. (2006). Next-generation optical technologies for illuminating genetically targeted brain circuits. *J. Neurosci.* 26:10380. doi: 10.1523/JNEUROSCI.3863-06.2006
- Diaz-Maue, L., Schwaerzle, M., Ruther, P., Luther, S., and Richter, C. (2018). Follow the light - from low-energy defibrillation to multi-site photostimulation. *Conf. Proc. IEEE Eng. Med. Biol. Soc.*
- Felix, S. H., Shah, K. G., Tolosa, V. M., Sheth, H. J., Tooker, A. C., Delima, T. L., et al. (2013). Insertion of flexible neural probes using rigid stiffeners attached with biodissolvable adhesive. *J. Vis. Exp.* 79:e50609. doi: 10.3791/50609
- Gilgunn, P. J., Khilwani, R., Kozai, T. D. Y., Weber, D. J., Cui, X. T., Ozdoganlar, O. B., et al. (2012). An ultra-compliant, scalable neural probe with molded biodissolvable delivery vehicle. *Proc. IEEE MEMS Conf.* 56–59. doi: 10.1109/MEMSYS.2012.6170092
- Gößler, C., Bierbrauer, C., Moser, R., Kunzer, M., Holc, K., Pletschen, W., et al. (2014). GaN-based micro-LED arrays on flexible substrates for optical cochlear implants. *J. Phys. D Appl. Phys.* 20:205401. doi: 10.1088/0022-3727/47/20/205401
- Hahn, B., Galler, B., and Engl, K. (2014). Development of high-efficiency and high-power vertical light emitting diodes. *Japn. J. Appl. Phys.* 53:100208. doi: 10.7567/JJAP.53.100208
- Hernandez, V. H., Gehrt, A., Reuter, K., Jing, Z., Jeschke, M., Schulz, A. M., et al. (2014). Optogenetic stimulation of the auditory pathway. *Am. Soc. Clin. Investig.* 124, 1114–1129. doi: 10.1172/JCI69050
- Jeschke, M., and Moser, T. (2015). Considering optogenetic stimulation for cochlear implants. *Hear. Res.* 322, 224–234. doi: 10.1016/j.heares.2015.01.005
- Ji, B., Wang, M., Kang, X.-Y., Gu, X., Li, C., Yang, B., et al. (2017). Flexible optoelectric neural interface integrated wire-bonding μ LEDs and microelectrocorticography for optogenetics. *IEEE Trans. Electron Devices* 64, 2008–2015. doi: 10.1109/TED.2016.2645860
- Kampasi, K., Stark, E., Seymour, J., Na, K., Winful, H. G., Wise, K., et al. (2016). Fiberless multicolor neural optoelectrode for in vivo circuit analysis. *Sci. Rep.* 6:30961. doi: 10.1038/srep30961
- Kisban, S., Kennntner, J., Janssen, P., Metzen, R. V., Herwik, S., Bartsch, U., et al. (2009). A novel assembly method for silicon-based neural devices. *IFMBE Proc.* 2, 107–110. doi: 10.1007/978-3-642-03889-1_29
- Klein, E., Gossler, C., Paul, O., Schwarz, U. T., and Ruther, P. (2016). High-yield indium-based wafer bonding for large-area multi-pixel optoelectronic probes for neuroscience. *Proc. IEEE MEMS Conf.* 453–455. doi: 10.1109/MEMSYS.2017.7863440
- Kozai, T. D. Y., and Kipke, D. R. (2009). Insertion shuttle with carboxyl terminated self-assembled monolayer coatings for implanting flexible polymer neural probes in the brain. *J. Neurosci. Methods* 184, 199–205. doi: 10.1016/j.jneumeth.2009.08.002
- Kral, A., Hartmann, R., Mortazavi, D., and Klinke, R. (1998). Spatial resolution of cochlear implants: the electrical field and excitation of auditory afferents. *Hear. Res.* 121, 11–28. doi: 10.1016/S0378-5955(98)00061-6
- Kwon, K. Y., Khomenko, A., Hag, M., and Li, W. (2013a). Integrated slanted microneedle-LED array for optogenetics. *Conf. Proc. IEEE Eng. Med. Biol. Soc.* 2013, 249–252. doi: 10.1109/EMBC.2013.6609484
- Kwon, K. Y., Sirowatka, B., Weber, A., and Li, W. (2013b). Opto- μ ECOG array: a hybrid neural interface with transparent μ ECOG electrode array and integrated LEDs for optogenetics IEEE transactions on biomedical circuits and systems, 7, 593–600. *IEEE Trans. Biomed. Circuits Syst.* 7, 593–600. doi: 10.1109/TBCAS.2013.2282318
- Mengzhe, L., Qin, C., Tingjing, Y., Shuming, Z., and Lianghui, C. (2009). NiO removal of Ni/Au Ohmic contact to p-GaN after annealing. *J. Semiconductors* 30:026001. doi: 10.1088/1674-4926/30/2/026001
- Metz, S., Bertsch, A., and Renaud, P. (2005). Partial release and detachment of microfabricated metal and polymer structures by anodic metal dissolution. *J. Microelectromech. Syst.* 14, 383–391. doi: 10.1109/JMEMS.2004.839328
- Montserrat, S., Flaquer, C., Paces, P., and Malek, J. (2003). Effect of the crosslinking degree on curing kinetics of an epoxy-anhydride system. *J. Appl. Polym. Sci.* 56, 1413–1421. doi: 10.1002/app.1995.070561104
- Nakamura, S. (1991). GaN growth using GaN buffer layer. *Japn. J. Appl. Phys.* 30, L1705–L1707. doi: 10.1143/JJAP.30.L1705
- Nyns, E. C. A., Kip, A., Bart, C. I., Plomp, J. J., Zeppenfeld, K., Schalij, M. J., et al. (2017). Optogenetic termination of ventricular arrhythmias in the whole heart: towards biological cardiac rhythm management. *Eur. Heart J.* 38, 2132–2136. doi: 10.1093/eurheartj/ehw574
- Ordóñez, J. S., Boehler, C., Schuettler, M., and Stieglitz, T. (2012a). Improved polyimide thin-film electrodes for neural implants. in *Conf. Proc. IEEE Eng. Med. Biol. Soc.* 2012, 5134–5137. doi: 10.1109/EMBC.2012.6347149
- Ordóñez, J. S., Boehler, C., Schuettler, M., and Stieglitz, T. (2012b). Long-term adhesion studies of polyimide to inorganic and metallic layers. *MRS Online Proc. Library Arch.* 1466, 7–13. doi: 10.1557/opl.2012.1198
- Park, H., Shin, H.-J., Cho, I.-J., Yoon, E., Suh, J.-K. F., Im, M., et al. (2011). The first neural probe integrated with light source (blue laser diode) for optical stimulation and electrical recording. in *Conf. Proc. IEEE Eng. Med. Biol. Soc.* 2011, 2961–2964. doi: 10.1109/IEMBS.2011.6090813
- Pashaie, R., Anikeeva, P., Lee, J., Prakash, R., Yizhar, O., Prigge, M., et al. (2014). Optogenetic brain interfaces. *IEEE Rev. Biomed. Eng.* 7, 3–29. doi: 10.1109/RBME.2013.2294796
- Pisanello, F., Mandelbaum, G., Pisanello, M., Oldenburg, I. A., Sileo, L., Markowitz, J. E., et al. (2017). Dynamic illumination of spatially restricted or large brain volumes via a single tapered optical fiber. *Nature Neurosci.* 20, 1180–1188. doi: 10.1038/nn.4591
- Rubehn, B., Bosman, C., Oostenveld, R., Fries, P., and Stieglitz, T. (2009). A MEMS-based flexible multichannel ECoG-electrode array. *J. Neural Eng.* 6:036003. doi: 10.1088/1741-2560/6/3/036003
- Scharf, R., Tsunematsu, T., McAlinden, N., Dawson, M. D., Sakata, S., and Mathieson, K. (2016). Depth-specific optogenetic control in vivo with a scalable, high-density μ LED neural probe. *Sci. Rep.* 6:28381. doi: 10.1038/srep28381
- Schneider, F., Grimm, C., and Hegemann, P. (2015). Biophysics of channelrhodopsin. *Annu. Rev. Biophys.* 44, 167–186. doi: 10.1146/annurev-biophys-060414-034014
- Schuettler, M., Koch, K. P., Stieglitz, T., Scholz, O., Haberer, W., Keller, R., et al. (2000). Multichannel neural cuff electrodes with integrated multiplexer circuit. *Conf. Proc. IEEE Eng. Med. Biol. Soc.* 624–629. doi: 10.1109/MMB.2000.893861
- Schwaerzle, M., Nehlich, J., Ayub, S., Paul, O. M., and Ruther, P. (2016). LED-based optical cochlear implant on highly flexible triple layer polyimide substrates. *Proc. IEEE MEMS Conf.* 395–398. doi: 10.1109/MEMSYS.2016.7421644

- Schwaerzle, M., Paul, O. M., and Ruther, P. (2017). Compact silicon-based optrode with integrated laser diode chips, SU-8 waveguides and platinum electrodes for optogenetic applications. *J. Micromech. Microeng.* 27, 065004-1–065004-11.
- Stieglitz, T., Rubehn, B., Henle, C., Kisban, S., Herwik, S., Ruther, P., et al. (2009). “Brain-computer interfaces: an overview of the hardware to record neural signals from the cortex,” in *Neurotherapy: Progress in Restorative Neuroscience and Neurology*, eds V. Joost, E. M. Hol, H. Inge, W. Jan, A. B. Bergen, G. J. Boer, and D. F. Swaab (New York, NY: Elsevier), 297–315. doi: 10.1016/S0079-6123(09)17521-0
- Vancea, J., Reiss, G., Schneider, F., Bauer, K., and Hoffmann, H. (1989). Substrate effects on the surface topography of evaporated gold films: a scanning tunnelling microscopy investigation. *Surface Sci.* 218, 108–126. doi: 10.1016/0039-6028(89)90622-5
- Westberg, D., Paul, O., Andersson, G. I., and Baltes, H. (1996). Surface micromachining by sacrificial aluminium. *J. Micromech. Microeng.* 6, 376–384. doi: 10.1088/0960-1317/6/4/004
- Wheeler, A., Archbold, S., Gregory, S., and Skipp, A. (2007). Cochlear implants: the young people’s perspective. *J. Deaf. Stud. Deaf. Edu.* 12, 303–316. doi: 10.1093/deafed/enm018
- Wu, F., Stark, E., Ku, P.-C., Wise, K. D., Buzaki, G., and Yoon, E. (2015). Monolithically integrated LEDs on silicon neural probes for high-resolution. *Neuron* 88, 1136–1148. doi: 10.1016/j.neuron.2015.10.032
- Yizhar, O., Fenno, L., Davidson, T., Mogri, M., and Deisseroth, K. (2011). Optogenetics in neural systems. *Neuron* 71, 9–34. doi: 10.1016/j.neuron.2011.06.004
- Zeng, F. G., and Canlon, B. (2015). Recognizing the journey and celebrating the achievement of cochlear implants. *Hear. Res.* 332, 1–3. doi: 10.1016/j.heares.2015.02.003
- Zeng, G., Rebscher, S., Harrison, W. V., Sun, X., and Feng, H. (2008). Cochlear implants: system design, integration, and evaluation. *IEEE Rev. Biomed. Eng.* 1, 115–142. doi: 10.1109/RBME.2008.2008250
- Zhang, F., Wang, L. P., Brauner, M., Liewald, J. F., Kay, K., Watzke, N., et al. (2007). Multimodal fast optical interrogation of neural circuitry. *Nature* 446, 633–639. doi: 10.1038/nature05744
- Zhu, Z., Tang, Q., Zeng, F.-G., Guan, T., and Ye, D. (2012). Cochlear-implant spatial selectivity with monopolar, bipolar and tripolar stimulation. *Hear. Res.* 283, 45–58. doi: 10.1016/j.heares.2011.11.005

Conflict of Interest Statement: The authors declare that the research was conducted in the absence of any commercial or financial relationships that could be construed as a potential conflict of interest.

Copyright © 2018 Klein, Gossler, Paul and Ruther. This is an open-access article distributed under the terms of the Creative Commons Attribution License (CC BY). The use, distribution or reproduction in other forums is permitted, provided the original author(s) and the copyright owner(s) are credited and that the original publication in this journal is cited, in accordance with accepted academic practice. No use, distribution or reproduction is permitted which does not comply with these terms.



Organelle Optogenetics: Direct Manipulation of Intracellular Ca^{2+} Dynamics by Light

Toshifumi Asano^{1†}, Hiroyuki Igarashi^{2†}, Toru Ishizuka³ and Hiromu Yawo^{2,3*}

¹ Department of Cell Biology, Graduate School of Medical and Dental Sciences, Tokyo Medical and Dental University, Tokyo, Japan, ² Department of Physiology and Pharmacology, Tohoku University Graduate School of Medicine, Sendai, Japan, ³ Department of Developmental Biology and Neuroscience, Tohoku University Graduate School of Life Sciences, Sendai, Japan

OPEN ACCESS

Edited by:

John A. Assad,
Harvard Medical School,
United States

Reviewed by:

Grigori Rychkov,
University of Adelaide, Australia
Francesco Lodola,
Fondazione Istituto Italiano di
Tecnologia, Italy

*Correspondence:

Hiromu Yawo
hiromu.yawo.c7@tohoku.ac.jp

[†]These authors have contributed
equally to this work

Specialty section:

This article was submitted to
Neural Technology,
a section of the journal
Frontiers in Neuroscience

Received: 27 February 2018

Accepted: 25 July 2018

Published: 17 August 2018

Citation:

Asano T, Igarashi H, Ishizuka T and
Yawo H (2018) Organelle
Optogenetics: Direct Manipulation of
Intracellular Ca^{2+} Dynamics by Light
Front. Neurosci. 12:561.
doi: 10.3389/fnins.2018.00561

As one of the ubiquitous second messengers, the intracellular Ca^{2+} , has been revealed to be a pivotal regulator of various cellular functions. Two major sources are involved in the initiation of Ca^{2+} -dependent signals: influx from the extracellular space and release from the intracellular Ca^{2+} stores such as the endoplasmic/sarcoplasmic reticulum (ER/SR). To manipulate the Ca^{2+} release from the stores under high spatiotemporal precision, we established a new method termed “organelle optogenetics.” That is, one of the light-sensitive cation channels (channelrhodopsin-green receiver, ChRGR), which is Ca^{2+} -permeable, was specifically targeted to the ER/SR. The expression specificity as well as the functional operation of the ER/SR-targeted ChRGR (ChRGR_{ER}) was evaluated using mouse skeletal myoblasts (C2C12): (1) the ChRGR_{ER} co-localized with the ER-marker KDEL; (2) no membrane current was generated by light under whole-cell clamp of cells expressing ChRGR_{ER}; (3) an increase of fluorometric Ca^{2+} was evoked by the optical stimulation (OS) in the cells expressing ChRGR_{ER} in a manner independent on the extracellular Ca^{2+} concentration ($[\text{Ca}^{2+}]_o$); (4) the $\Delta F/F_0$ was sensitive to the inhibitor of sarco/endoplasmic reticulum Ca^{2+} -ATPase (SERCA) and (5) the store-operated Ca^{2+} entry (SOCE) was induced by the OS in the ChRGR_{ER}-expressing cells. Our organelle optogenetics effectively manipulated the ER/SR to release Ca^{2+} from intracellular stores. The use of organelle optogenetics would reveal the neuroscientific significance of intracellular Ca^{2+} dynamics under spatiotemporal precision.

Keywords: channelrhodopsin, endoplasmic reticulum, sarcoplasmic reticulum, ER/SR, muscle, C2C12, store-operated Ca^{2+} entry (SOCE), super-resolution microscopy

INTRODUCTION

The intracellular Ca^{2+} , as one of the second messengers, plays a pivotal role in any kind of cell by conducting information (Berridge et al., 1998; Bagur and Hajnóczky, 2017). The Ca^{2+} signals that emerge from the external input, such as extracellular signaling molecules, are subsequently transduced for the activation of various signaling molecules to coordinate a wide variety of cell functions (Kakiuchi and Yamazaki, 1970; Berridge et al., 2003). When a murine myoblast, C2C12, was compelled to express one of the chimeric channelrhodopsins, channelrhodopsin-green receiver (ChRGR), a patterned optical stimulation (OS) induced an oscillation of membrane

potential and accelerated the assembly of sarcomere, the smallest contractile unit in muscle fibers in a manner dependent on the increase of intracellular Ca^{2+} ($[\text{Ca}^{2+}]_i$) (Asano et al., 2015). Therefore, the cyclic $[\text{Ca}^{2+}]_i$ elevation is assumed to be necessary for the sarcomere assembly. However, it has yet to be elucidated whether it is a sufficient condition without Ca^{2+} influx through a plasma membrane.

So far, the mobilization of intracellular Ca^{2+} has been investigated through pharmacological methods using drugs or caged compounds (Morad et al., 1988; Kaplan and Somlyo, 1989; Adams et al., 1997). However, these methods are limited in the spatiotemporal resolution because of the rapid diffusion of reagents in the cytoplasm. On the other hand, the optical control of Ca^{2+} signaling in mammalian cells would render two major advantages over conventional approaches: high spatiotemporal resolution and tunability of the magnitude in a manner dependent on the light energy. The Ca^{2+} signaling could be initiated through either influx from the extracellular space or efflux from the internal Ca^{2+} stores such as the endoplasmic/sarcoplasmic reticulum (ER/SR) (Bagur and Hajnóczky, 2017). Here, we established our state-of-the-art method “organelle optogenetics.” This method manipulates the Ca^{2+} release from Ca^{2+} stores under high spatiotemporal precision. In fact, one of the light-responsive cation channels (ChRGR) was specifically targeted to ER/SR, and subsequently illuminated to induce Ca^{2+} release from these organelles as well as their depletion.

MATERIALS AND METHODS

Plasmids

A cDNA fragment encoding ChRGR-Venus (Wen et al., 2010) was amplified by PCR and subcloned into EcoRI sites in pCAGGS by In-Fusion cloning (Takara Bio, Shiga, Japan). To generate a ChRGR with an ER-retention motif (ChRGR_{ER}), a cDNA encoding Gln⁴⁷⁶⁵-Ile⁴⁸⁶⁶ of mouse ryanodine receptor 2 (NM_023868) was inserted in-frame between ChRGR and Venus using the AgeI restriction site by In-Fusion cloning. The construct was verified by DNA sequencing.

Cell Culture and Transfection

The current-voltage (*I-V*) relationship of the ChRGR photocurrent was assessed using the ND 7/23 cell—a hybrid cell lines derived from neonatal rat dorsal root ganglia neurons fused with the mouse neuroblastoma (Wood et al., 1990). ND 7/23 cells were grown on a poly-L-lysine (Sigma-Aldrich, St Louis, MO)-coated coverslip in Dulbecco’s modified Eagle’s medium (DMEM, Wako Pure Chemical Industries, Osaka, Japan) supplemented with 10% fetal bovine serum (Biological Industries, Kibbutz Beit-Haemek, Israel) under a 5% CO_2 atmosphere at 37°C. The cells were maintained for no more than ten passages and grown to 80–90% confluence in the culture dish. The expression plasmids were transiently transfected in ND 7/23 cells using Effectene Transfection Reagent (Qiagen, Hilden, Germany) according to the manufacturer’s instructions. The medium was supplemented with 2.5 μM all-*trans* retinal at 6 h after transfection. Electrophysiological recordings were then

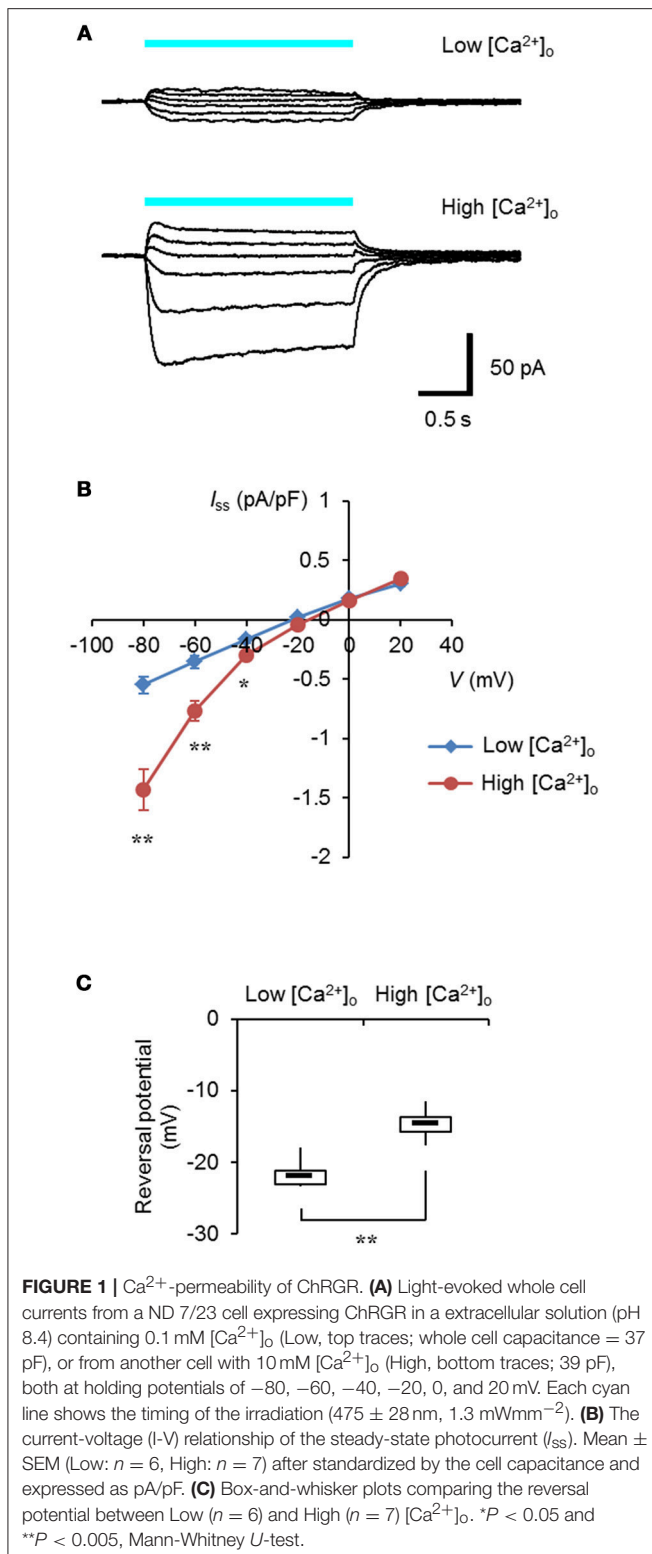
conducted 24–48 h after the transfection. Successfully transfected cells were identified by the presence of Venus fluorescence.

The C2C12 cell is a myoblast line derived from mouse skeletal muscle (RIKEN Cell Bank, Tsukuba, Japan), which has been used as one of model systems of skeletal muscle development and differentiation. The cells were maintained for no more than fifteen passages and kept at 37°C with a 5% CO_2 atmosphere in Dulbecco’s Modified Eagle’s Medium (DMEM, Wako Pure Chemical Industries), which was supplemented with 20% fetal bovine serum (Invitrogen, Carlsbad, CA), 100 units/mL penicillin, and 100 $\mu\text{g}/\text{mL}$ streptomycin (Sigma-Aldrich). C2C12 myoblasts were grown to 80–90% confluence on a collagen-coated coverslip, transfected with plasmids using either Effectene or Lipofectamine 2000 (Invitrogen) and used for patch clamp and calcium imaging experiments.

Electrophysiology

All experiments were conducted at room temperature ($23 \pm 2^\circ\text{C}$). The *I-V* relationship of the ChRGR photocurrent was investigated as previously described (Ishizuka et al., 2006) using an EPC-8 amplifier (HEKA Electronic, Lambrecht, Germany) under a whole-cell patch clamp configuration. The data were filtered at 1 kHz, sampled at 10 kHz (Digdata1440 A/D, Molecular Devices Co., Sunnyvale, CA) and stored in a computer (pCLAMP 10.3, Molecular Devices). The internal pipette solution for whole-cell voltage-clamp recordings from ND7/23 cells contained (in *mmol*): 120 N-methyl-D-glucamine, 50 tetraethylammonium (TEA)-Cl, 10 EGTA, 50 HEPES, 5 MgCl_2 , 2.5 MgATP , adjusted to pH 8.4 with HCl. The low Ca^{2+} extracellular solution contained (in *mmol*): 100 N-methyl-D-glucamine, 50 HEPES, 0.1 CaCl_2 , 46.9 MgCl_2 , 11 glucose, adjusted to pH 8.4 with HCl whereas the high Ca^{2+} solution contained (in *mmol*): 100 N-methyl-D-glucamine, 50 HEPES, 10 CaCl_2 , 37 MgCl_2 , 11 glucose, adjusted to pH 8.4 with HCl. The directly measured liquid junction potential was -3.4 mV for either the low Ca^{2+} or the high Ca^{2+} external solution and was not compensated for. The photocurrent was evoked by a light from SpectraX light engine (Lumencor Inc., Beaverton, OR) at a wavelength (nm, >90% of the maximum) of 475 ± 28 nm. The power of light was directly measured under microscopy by a visible light-sensing thermopile (MIR-101Q, SSC Co., Ltd., Kuwana City, Japan) that was 1.3 mWmm^{-2} on the specimen.

The myoblasts expressing either ChRGR-Venus or that with the ER retention signal (ChRGR_{ER}-Venus) were identified by Venus fluorescence using a conventional epifluorescence microscope (BX51WI, Olympus, Tokyo, Japan), which was equipped with a 60 \times water-immersion objective lens (LUMplanPI/IR60x, Olympus) and a filter cube (excitation, 495 nm; dichroic mirror, 505 nm; barrier filter, 515 nm). Photocurrents were recorded as previously described (Ishizuka et al., 2006) using an Axopatch 200B amplifier (Molecular Devices Co., Sunnyvale, CA) under a whole-cell patch clamp configuration. The data were filtered at 1 kHz, sampled at 10 kHz (Digdata1440A, Molecular Devices) and stored in a computer (pCLAMP 10.2, Molecular Devices). The standard extracellular Tyrode’s solution contained (in *mmol*): 138 NaCl, 3 KCl, 2.5 CaCl_2 , 1.25 MgCl_2 , 10 HEPES, 4 NaOH, and 11 glucose (pH



7.4 adjusted with HCl). The standard patch pipette solution contained (in mmol): 120 CsOH, 100 glutamic acid, 0.2 EGTA, 10 HEPES, 2.5 MgCl_2 , 3 MgATP , 0.3 Na_2GTP , and 0.1 leupeptin

(pH 7.4 adjusted with CsOH) for the voltage clamp. To test the optical responses, we used a cyan LED (505 ± 15 nm, LXHL-NE98, Philips Lumileds Lighting Co., San Jose, USA), which was regulated by a pulse generator (SEN-7203, Nippon Koden, Japan) and pCLAMP 10.2 computer software. Its power density through an objective lens was 1.6 mWmm^{-2} when focused on the specimen.

Immunohistochemistry

Cells were fixed with 4% paraformaldehyde/PBS and blocked in 0.1% Triton X-100/PBS containing 5% goat serum for 1 h. The samples were subsequently treated overnight with the primary antibodies, i.e., rat monoclonal anti-GFP IgG2a (1/1000, GF090R, Nacalai Tesque, Kyoto, Japan) and mouse monoclonal anti-KDEL (1/100, sc-58774, Santa Cruz Biotechnology, CA, USA) diluted in 0.1% Triton X-100/PBS containing 5% goat serum, and then incubated for 2 h with the secondary antibodies, i.e., Alexa Fluor 488-conjugated goat anti-rat IgG (Invitrogen) and Alexa Fluor 555-conjugated goat anti-mouse IgG (Invitrogen), diluted at 1/200 in 0.1% Triton X-100/PBS containing 5% goat serum. The specimens were washed three times with PBS between treatments and mounted with ProLong Gold antifade mounting medium (Invitrogen). These procedures were performed at room temperature. Super-resolution images were taken under TCS SP8 STED 3X (Leica, Wetzlar, Germany) with the STED (depletion) laser at 660 nm and white light laser. Alexa488 was excited at 488 nm and detected between 489 and 550 nm (gate, 1.5–6.5 ns) and Alexa555 was excited at 561 nm and detected between 563 and 680 nm (gate, 0.5–6.5 ns).

Real Time Ca^{2+} Imaging

Cells were transfected with ChRGR_{ER} and the red fluorescent Ca^{2+} probe R-CaMP1.07 (Ohkura et al., 2012) plasmids simultaneously using Lipofectamine 2000. After 24 h, the red fluorescent signal of R-CaMP1.07 was acquired using a high-speed laser-scanning confocal microscopy system (A1R, Nikon, Tokyo, Japan) equipped with $16 \times$ water-immersion objectives (0.8 NA), a 561-nm DPSS laser, a 405/488/561/640-nm dichroic mirror and a 580 ± 23 nm bandpass filter. The OS was given by high power 7-unit LED (450 ± 10 nm, LXML-PR01, Lumileds Lighting, USA). The images were sampled at 30 fps (resonant scan; 512×128 pixels) and analyzed using ImageJ software while regions of interest (ROIs) were each set to cover a single cell under visual identification. The fluorescence intensity in each ROI was sampled as the time series of digits and analyzed with Excel software (Microsoft Japan, Tokyo, Japan). The fluorescence change was defined as $\Delta F/F_0 = (F_t - F_0)/F_0$, where F_t is the fluorescence intensity at time t , and F_0 is the average baseline fluorescence 1 s before the stimulation. The averaged $\Delta F/F_0$ within 300 ms during the stimulation was used as the magnitude of the Ca^{2+} transient. The imaging experiment was performed under superfusion with normal extracellular Tyrode's solution containing (in mmol): 138 NaCl, 3 KCl, 2 CaCl_2 , 1 MgCl_2 , 10 HEPES, 4 NaOH, and 11 glucose (pH 7.4 adjusted with HCl), then switched to the Ca^{2+} -free extracellular Tyrode's solution containing (in mmol): 138 NaCl, 3 KCl, 5 MgCl_2 , 10 HEPES, 4 NaOH, 1 Na_2EGTA and 11 glucose (pH 7.4 adjusted with HCl).

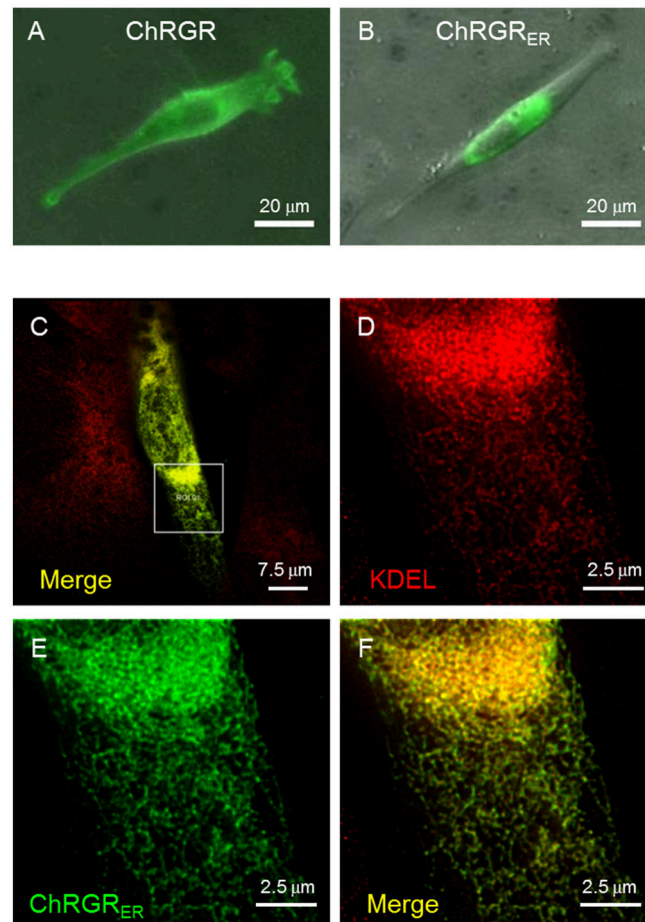


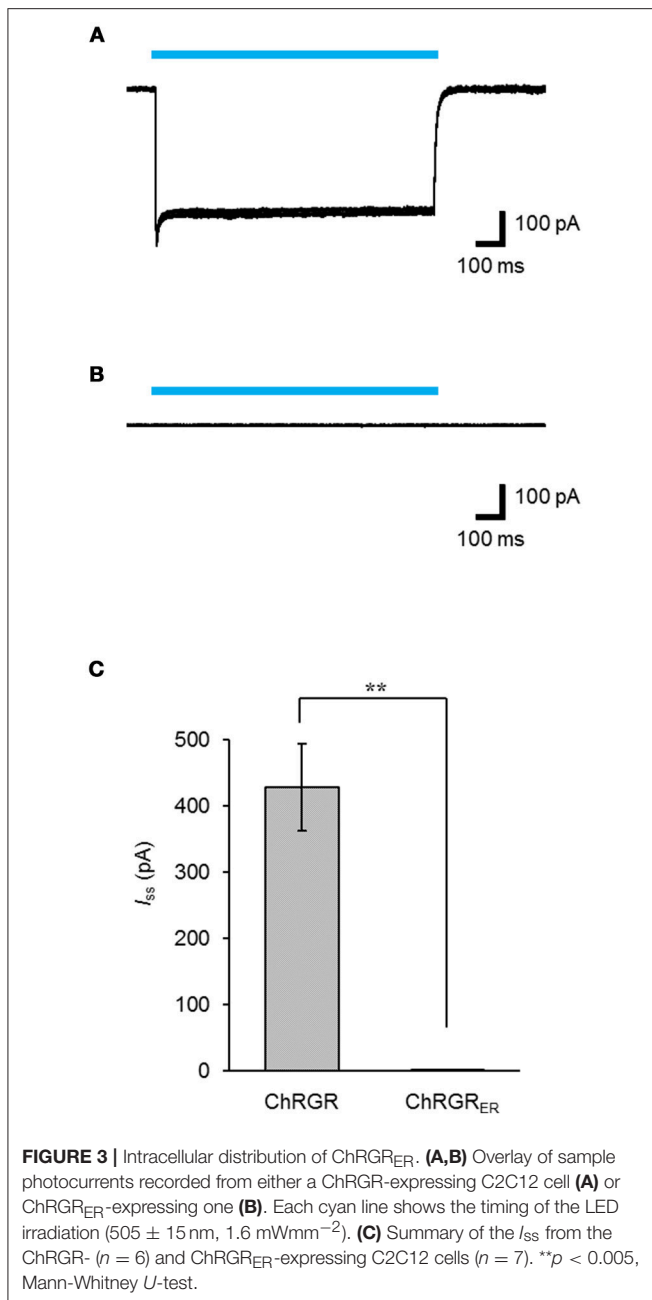
FIGURE 2 | Cellular expression of ChRGR_{ER}. **(A)** Image of Venus fluorescence of a typical C2C12 cell expressing ChRGR. **(B)** Another typical C2C12 cell expressing ChRGR_{ER}. **(C)** Merged image of super-resolution microscopy (STED) of C2C12 immunostained for Venus (green) and ER-marker KDEL (red) at low magnification. **(D–F)** The ROI encircled in **(C)** was enlarged for each color channel; KDEL **(D, red)**, Venus **(E, green)**, and the merge **(F)**.

The store depletion and the subsequent store-operated Ca^{2+} entry (SOCE) were investigated for the ChRGR_{ER}-expressing C2C12 myoblasts co-transfected with R-GECO1, a red-shifted fluorescent Ca^{2+} -sensor (Zhao et al., 2011), under superfusion with the Ca^{2+} -free Tyrode's solution containing (in *mmol*): 138 NaCl, 3 KCl, 3.75 MgCl_2 , 10 HEPES, 4 NaOH, and 11 glucose (pH 7.4 adjusted with HCl), then switched to the standard Tyrode's solution containing (in *mmol*): 138 NaCl, 3 KCl, 2.5 CaCl_2 , 1.25 MgCl_2 , 10 HEPES, 4 NaOH and 11 glucose (pH 7.4 adjusted with HCl). In some experiments thapsigargin (TG, 2–5 μM , Tocris Bioscience, Bristol, UK) was included in the Ca^{2+} -free solution. For the store depletion experiments, images of R-GECO1 fluorescence were acquired using a laser-scanning confocal microscopy system (A1R, Nikon) equipped with 16 \times water-immersion objectives (0.8 NA). A fiber-coupled 451-nm laser source (Optohub, Saitama, Japan) was used for the optical stimulation. The free end of the optic fiber (core diameter; 50 μm , Doric Lenses, Quebec City, Canada) was placed close to the C2C12 cell. The power of light was directly measured at the free end of the optic fiber, and was 18.7 μW . For the SOCE

experiments, images of R-GECO1 fluorescence were acquired every 10 s on a FV1200 confocal laser scanning microscope (Olympus) equipped with a 40 \times UPlanSApo objective lens using the 559 nm excitation and 590 nm emission long pass filter sets. The OS ($475 \pm 10 \text{ nm}$, 2.8 mWmm^{-2}) were applied at 20 Hz with 10 ms duration and 100 pulses between imaging sequences. The store-operated Ca^{2+} entry (SOCE) was monitored using Ca^{2+} add-back protocol after treating with either OS or TG in a Ca^{2+} -free Tyrode's solution. The $\Delta F/F_0$ after Ca^{2+} add-back was expressed by averaging 20 s of peak value after changing $[\text{Ca}^{2+}]_0$.

Statistics

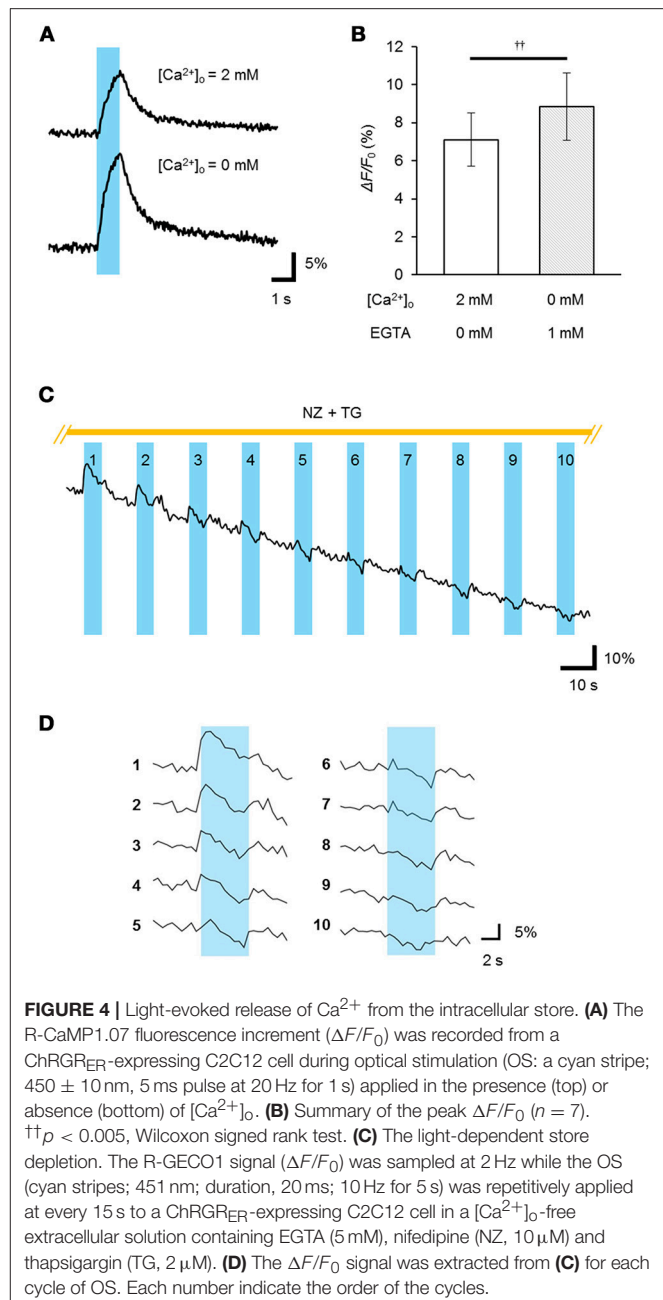
All data in the text and figures are expressed as the mean \pm SEM and evaluated using the Mann-Whitney *U*-test for the unpaired data, the Wilcoxon signed rank test for the paired data, and the one-way Kruskal-Wallis test by ranks for multi-group data to determine statistical significance, unless stated otherwise. It was judged as statistically insignificant when $P > 0.05$.



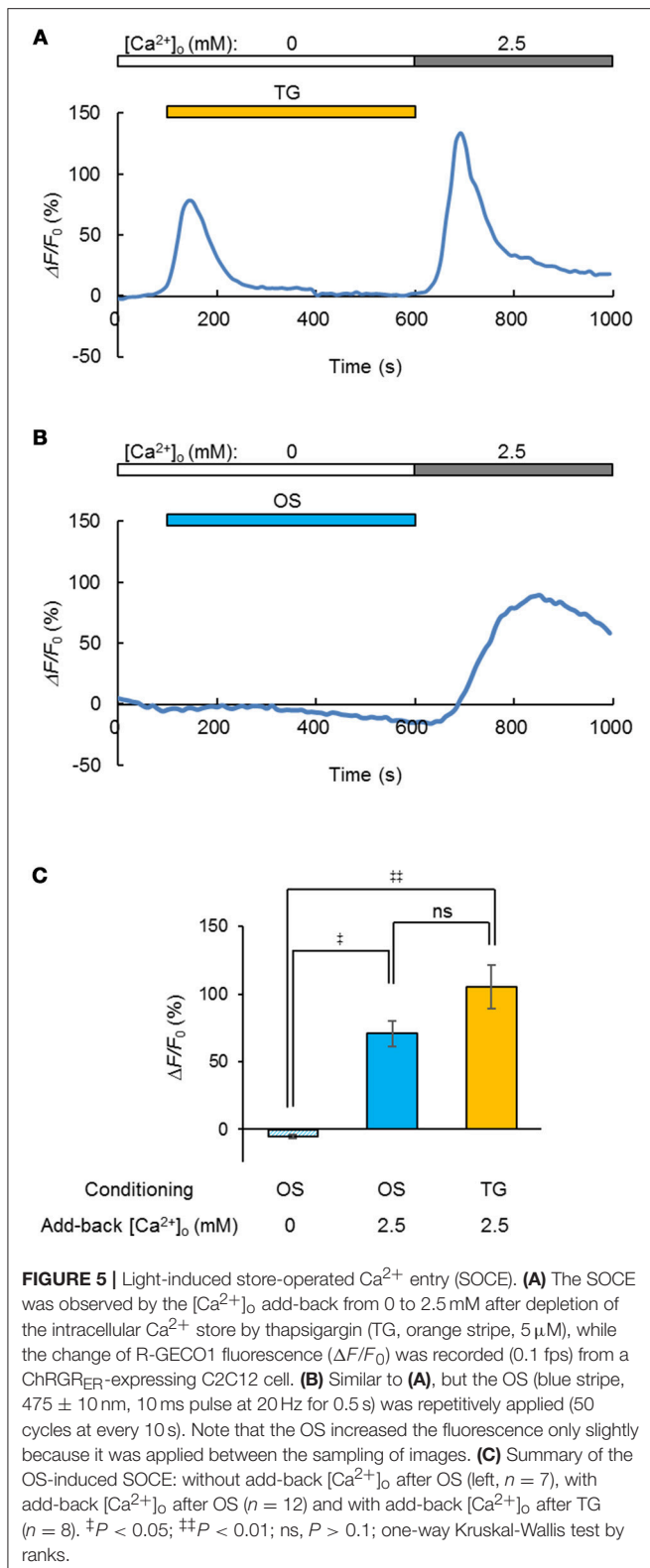
RESULTS

Characterization of ER-Targeting Channelrhodopsin

It was expected that selective control of the intracellular Ca^{2+} dynamics could be achieved by the specific targeting of light-sensitive actuators to the ER/SR membrane. Expanding the optogenetic toolbox enabled us to choose the optimal light-sensitive actuator depending on the experimental context (Mattis et al., 2011; Schneider et al., 2013). One of the chimeric channelrhodopsins, ChRGR, was characterized by the red-shifted light absorbance spectrum and lower desensitization over ChR2



(Wen et al., 2010), and it effectively facilitated myogenesis in a manner dependent on light when expressed in C2C12 myoblasts (Asano et al., 2015). As shown in **Figures 1A,B**, when ChRGR was expressed in ND 7/23 cells, which are optimal for the voltage control with negligible dye coupling (Hososhima et al., 2015), showed inward-rectifying photocurrents in the presence of 10 mM $[\text{Ca}^{2+}]_o$ and not with 0.1 mM $[\text{Ca}^{2+}]_o$. Indeed, the reversal potential of the photocurrent was -14 ± 0.8 mV in 10 mM $[\text{Ca}^{2+}]_o$ whereas it was -22 ± 0.8 mV in 0.1 mM $[\text{Ca}^{2+}]_o$ with significant difference (**Figure 1C**). Therefore, ChRGR would be suitable for optogenetic manipulation of the Ca^{2+} dynamics.



We then tested the ER/SR localization of ChRGR, connecting a sequence consisting of the 3rd-4th transmembrane helices of mouse ryanodine receptor 2 at its C-terminus end (hereafter

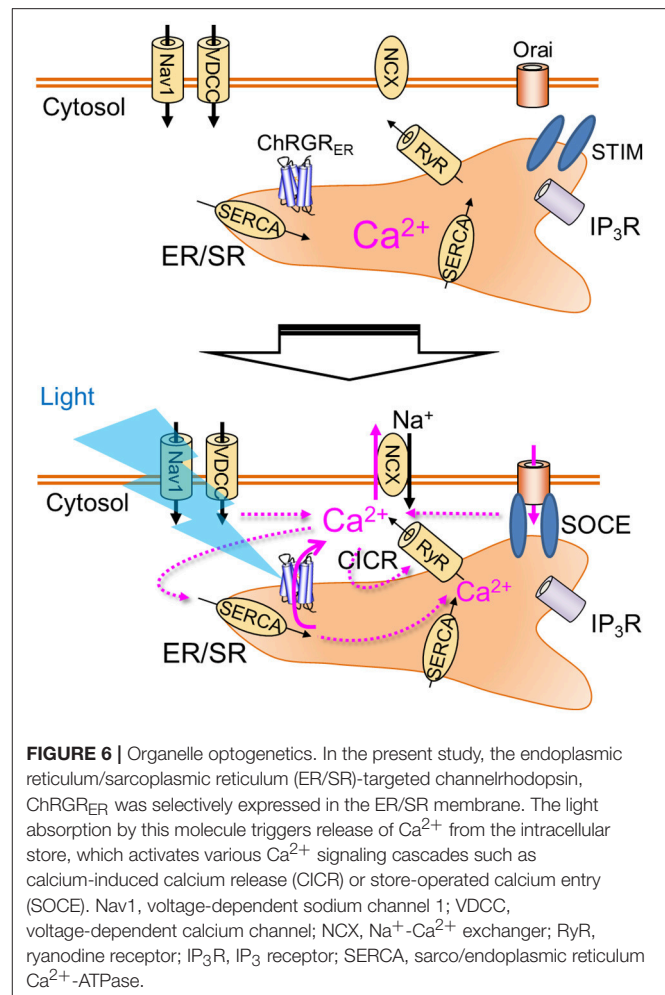


FIGURE 6 | Organelle optogenetics. In the present study, the endoplasmic reticulum/sarcoplasmic reticulum (ER/SR)-targeted channelrhodopsin, ChRGR_{ER} was selectively expressed in the ER/SR membrane. The light absorption by this molecule triggers release of Ca^{2+} from the intracellular store, which activates various Ca^{2+} signaling cascades such as calcium-induced calcium release (CICR) or store-operated calcium entry (SOCE). Nav1, voltage-dependent sodium channel 1; VDCC, voltage-dependent calcium channel; NCX, Na^+ - Ca^{2+} exchanger; RyR, ryanodine receptor; IP₃R, IP₃ receptor; SERCA, sarco/endoplasmic reticulum Ca^{2+} -ATPase.

called ChRGR_{ER}). The expression patterns of ChRGR and the ChRGR_{ER} were visualized by Venus, which was tagged at their C-terminus (Figures 2A,B). The signal of ChRGR_{ER}-Venus was confined in the peri-nucleus region in contrast to the conventional ChRGR-Venus, which localized in the plasma membrane with the original membrane targeting property (Wen et al., 2010; Asano et al., 2015). To further examine the precise localization, ChRGR_{ER}-expressing C2C12 cells were immunostained for ER/SR-marker KDEL and subsequently observed under the STED super-resolution microscopy (Figures 2C–F). As shown in Figure 2F and Movie S1, the Venus fluorescence was mostly co-localized with the KDEL signal.

Leaked expression of ChRGR_{ER} in the plasma membrane caused by miss-targeting or overexpression would hamper the precise regulation of the intracellular Ca^{2+} dynamics. To determine whether functional ChRGR_{ER} was incorporated in the plasma membrane, we performed patch clamp experiments under the whole-cell voltage clamp configuration. Cyan light (505 ± 15 nm; 1.58 mWmm⁻²; 1 s) evoked a photocurrent of 428 ± 65 pA ($n = 6$) in the ChRGR-expressing cells (Figure 3A). On the other hand, the photocurrent was negligible

for the ChRGR_{ER}-expressing cells ($n = 7$) even with the same light stimulation (**Figure 3B**), with significant difference (**Figure 3C**).

Functional Operation of ChRGR_{ER} in the Cell

To determine whether the ChRGR_{ER} was fully functional in the ER/SR, we performed real-time Ca^{2+} imaging using the red fluorescent Ca^{2+} indicator R-CaMP1.07 (Ohkura et al., 2012). The double positive cells with ChRGR_{ER}-Venus and R-CaMP1.07 were identified and stimulated with a train of pulses (5 ms at 20 Hz for 1 s) of blue LED light (4.5 mWmm^{-2} at 450 nm). In the standard extracellular milieu containing 2 mM Ca^{2+} , the ChRGR_{ER}-expressing cells responded to the light by $7.1 \pm 1.4\%$ ($n = 11$) red fluorescence $\Delta F/F_0$ (**Figures 4A,B**). When the perfusing solution was switched to the $[\text{Ca}^{2+}]_o$ -free solution containing 1 mM EGTA, the $\Delta F/F_0$ signal was significantly enhanced to $8.8 \pm 1.8\%$ by the same light. However, the light-dependent $\Delta F/F_0$ was reduced with the repetitive OS when the Ca^{2+} entry was suppressed by the external EGTA and nifedipine and the ER/SR uptake were blocked by thapsigargin (**Figures 4C,D**). In fact, the $\Delta F/F_0$ ranged from -15 to -11% of the initial value at the end of the repetition (10–50 cycles, $n = 3$).

Generally, the depletion of Ca^{2+} from the ER/SR induced Ca^{2+} entry through the plasma membrane and facilitated the subsequent uptake of Ca^{2+} (store-operated Ca^{2+} entry, SOCE) by the coupling between STIM and Orai proteins (Prakriya and Lewis, 2015). Indeed, when the Ca^{2+} store in a C2C12 cell was depleted by treatment with thapsigargin ($5 \mu\text{M}$) in a $[\text{Ca}^{2+}]_o$ -free milieu, the entry of Ca^{2+} was evident from the $[\text{Ca}^{2+}]_i$ increase upon the add-back of $[\text{Ca}^{2+}]_o$ to 2.5 mM (**Figure 5A**). Similarly, a significant Ca^{2+} entry was observed when the OS was repetitively applied before the $[\text{Ca}^{2+}]_o$ add-back (**Figure 5B**), yet was negative in a $[\text{Ca}^{2+}]_o$ -free milieu (**Figure 5C**). In summary, a significant SOCE was observed after OS of the ChRGR_{ER}-expressing C2C12 cells (**Figure 5C**).

DISCUSSION

This paper demonstrated for the first time specific control of intracellular Ca^{2+} dynamics by light with the application of organelle optogenetics using an ER/SR-targeted channelrhodopsin, ChRGR_{ER}, that includes the 4th transmembrane helix of ryanodine receptor as an ER-retention motif (Bhat and Jianjie, 2002). This conclusion was supported by the following evidences: (1) the localization pattern of ChRGR_{ER} was 3-dimensionally merged with the ER markers even when examined under the super-resolution microscopy; (2) whole cell patch clamp recording detected the photocurrent in the ChRGR-expressing C2C12 cells but not in the ChRGR_{ER}-expressing ones; (3) the fluorometric Ca^{2+} signal ($\Delta F/F_0$) was induced by the OS in the ChRGR_{ER}-expressing cells even in the absence of $[\text{Ca}^{2+}]_o$ (see also **Movie S2**). It was even larger than that in the presence of $[\text{Ca}^{2+}]_o$, probably due to the reduction of basal $[\text{Ca}^{2+}]_i$; (4) the $\Delta F/F_0$ was sensitive to

the SERCA inhibitor (thapsigargin). (5) the SOCE was induced by the OS in the ChRGR_{ER}-expressing cells. The organelle optogenetics (**Figure 6**) would thus enable the regulation of not only the intracellular Ca^{2+} release from ER/SR but also the subsequent activation of other internal Ca^{2+} signaling cascades such as calcium-induced calcium release (CICR) (Endo et al., 1977) or SOCE (Soboloff et al., 2012; Bagur and Hajnóczky, 2017). Although prevalent in every cell, tissue, and organ of any living organism, the consequences of the spatiotemporal dynamics of intracellular Ca^{2+} have not been extensively studied because of technical limitations in differentiating between the two major sources of Ca^{2+} mobilization: the extracellular milieu and the internal Ca^{2+} stores. Therefore, the present optogenetic manipulation of ER/SR would represent a breakthrough in elaborating its physiological significance, such as the triggering of the sarcomere assembly (Ferrari et al., 1996, 1998; Li et al., 2004). Accumulating evidence has indicated that intracellular Ca^{2+} stores similarly have an important functional role in neurons; for example, somatodendritic signaling, synaptic transmission and plasticity (Simpson et al., 1995; Bouchard et al., 2003; Collin et al., 2005; Segal and Korkotian, 2014, 2015) in addition to being involved in neurodegenerative diseases such as Alzheimer's (Villegas et al., 2014; Zhang et al., 2016). Further improvements in optogenetic molecular tools, targeting and expression techniques, and optical systems will enable the precise manipulation of intracellular Ca^{2+} in neuroscience.

AUTHOR CONTRIBUTIONS

TA, HI, TI, and HY conceived, designed, and performed the experiments, and analyzed the data. HI, TI, and HY contributed reagents, materials, and analysis tools. All authors drafted and reviewed the manuscript.

ACKNOWLEDGMENTS

The authors thank H. Kato (Leica Microsystems K.K., Tokyo, Japan) for technical assistance and B. Bell (Sendai, Japan), and M. Bettle (Toronto, Canada) for language assistance. This work was supported by Grants-in-Aid for Scientific Research (KAKENHI) from the Ministry of Education, Culture, Sports, Science, and Technology (MEXT), Japan (15J05551 to HI, 10J07170 to TA, 25290002 and 17K19437 to TI, 15H01413, 25250001 and 15K15025 to HY), JST, Strategic International Collaborative Research Program, SICORP and the Tohoku University Division for Interdisciplinary Advanced Research and Education (DIARE) to HI.

SUPPLEMENTARY MATERIAL

The Supplementary Material for this article can be found online at: <https://www.frontiersin.org/articles/10.3389/fnins.2018.00561/full#supplementary-material>

Movie S1 | Three-dimensional expression of ChRGR_{ER} in a cell. Images of super-resolution microscopy (STED) of C2C12 immunostained for Venus (green)

and ER-marker KDEL (red) were merged for the same ROI shown in **Figure 1C**. Scale, 2 μm .

Movie S2 | Representative movies of light-induced intracellular Ca^{2+} increase in a ChRGE_{ER}-expressing C2C12 cell. **(A,B)** The R-GECO1 signals were sampled at 2 Hz and the fluorescence intensity (F) was imaged during an optical stimulation

(OS: 451 nm; duration, 20 ms; 10 Hz for 5 s) in the presence **(A)** and absence **(B)** of extracellular Ca^{2+} ($[\text{Ca}^{2+}]_o$). The images were sampled at 2 Hz and pseudocolor-displayed at 20 Hz. Scale bar, 10 μm . **(C,D)** The changes ($\Delta F/F_0$) of R-GECO1 fluorescence of ROIs above the cells shown in **(A,B)**, respectively. Each OS was indicated as a cyan stripe.

REFERENCES

- Adams, S. R., Lev-Ram, V., and Tsien, R. Y. (1997). A new caged Ca^{2+} , azid-1, is far more photosensitive than nitrobenzyl-based chelators. *Chem. Biol.* 4, 867–878. doi: 10.1016/S1074-5521(97)90119-8
- Asano, T., Ishizuka, T., Morishima, K., and Yawo, H. (2015). Optogenetic induction of contractile ability in immature C2C12 myotubes. *Sci. Rep.* 5:8317. doi: 10.1038/srep08317
- Bagur, R., and Hajnóczky, G. (2017). Intracellular Ca^{2+} sensing: its role in calcium homeostasis and signaling. *Mol. Cell* 66, 780–788. doi: 10.1016/j.molcel.2017.05.028
- Berridge, M. J., Bootman, M. D., and Lipp, P. (1998). Calcium—a life and death signal. *Nature* 395, 645–648. doi: 10.1038/27094
- Berridge, M. J., Bootman, M. D., and Roderick, H. L. (2003). Calcium signalling: dynamics, homeostasis and remodelling. *Nat. Rev. Mol. Cell Biol.* 4, 517–529. doi: 10.1038/nrm1155
- Bhat, M. B., and Jianjie, M. (2002). The transmembrane segment of ryanodine receptor contains an intracellular membrane retention signal for Ca^{2+} release channel. *J. Biol. Chem.* 277, 8597–8601. doi: 10.1074/jbc.M107609200
- Bouchard, R., Pattarini, R., and Geiger, J. D. (2003). Presence and functional significance of presynaptic ryanodine receptors. *Prog. Neurobiol.* 69, 391–418. doi: 10.1016/S0304-0082(03)00053-4
- Collin, T., Marty, A., and Llano, I. (2005). Presynaptic calcium stores and synaptic transmission. *Curr. Opin. Neurobiol.* 15, 275–281. doi: 10.1016/j.conb.2005.05.003
- Endo, M., Fabiato, A., and Fabiato, F. (1977). Calcium release from the sarcoplasmic reticulum. *Physiol. Rev.* 57, 71–108. doi: 10.1152/physrev.1977.57.1.71
- Ferrari, M. B., Ribbeck, K., Hagler, D. J., and Spitzer, N. C. (1998). A calcium signaling cascade essential for myosin thick filament assembly in *Xenopus* myocytes. *J. Cell Biol.* 141, 1349–1356. doi: 10.1083/jcb.141.6.1349
- Ferrari, M. B., Rohrbough, J., and Spitzer, N. C. (1996). Spontaneous calcium transients regulate myofibrillogenesis in embryonic *Xenopus* myocytes. *Dev. Biol.* 178, 484–497. doi: 10.1006/dbio.1996.0233
- Hososhima, S., Sakai, S., Ishizuka, T., and Yawo, H. (2015). Kinetic evaluation of photosensitivity in bi-stable variants of chimeric channelrhodopsins. *PLoS ONE* 10:e0119558. doi: 10.1371/journal.pone.0119558
- Ishizuka, T., Kakuda, M., Araki, R., and Yawo, H. (2006). Kinetic evaluation of photosensitivity in genetically engineered neurons expressing green algae light-gated channels. *Neurosci. Res.* 54, 85–94. doi: 10.1016/j.neures.2005.10.009
- Kakiuchi, S., and Yamazaki, R. (1970). Calcium dependent phosphodiesterase activity and its activating factor (PAF) from brain studies on cyclic 3',5'-nucleotide phosphodiesterase (III). *Biochem. Biophys. Res. Commun.* 41, 1104–1110. doi: 10.1016/0006-291X(70)90199-3
- Kaplan, J. H., and Somlyo, A. P. (1989). Flash photolysis of caged compounds: new tools for cellular physiology. *Trends Neurosci.* 12, 54–59. doi: 10.1016/0166-2236(89)90136-7
- Li, H., Cook, J. D., Terry, M., Spitzer, N. C., and Ferrari, M. B. (2004). Calcium transients regulate patterned actin assembly during myofibrillogenesis. *Dev. Dyn.* 229, 231–242. doi: 10.1002/dvdy.10428
- Mattis, J., Tye, K. M., Ferenczi, E. A., Ramakrishnan, C., O'Shea, D. J., Prakash, R., et al. (2011). Principles for applying optogenetic tools derived from direct comparative analysis of microbial opsins. *Nat. Methods* 9, 159–172. doi: 10.1038/nmeth.1808
- Morad, M., Davies, N., Kaplan, J., and Lux, H. (1988). Inactivation and block of calcium channels by photo-released Ca^{2+} in dorsal root ganglion neurons. *Science* 241, 842–844. doi: 10.1126/science.2457253
- Ohkura, M., Sasaki, T., Kobayashi, C., Ikegaya, Y., and Nakai, J. (2012). An improved genetically encoded red fluorescent Ca^{2+} indicator for detecting optically evoked action potentials. *PLoS ONE* 7:e39933. doi: 10.1371/journal.pone.0039933
- Prakriya, M., and Lewis, R. S. (2015). Store-operated calcium channels. *Physiol. Rev.* 95, 1383–1436. doi: 10.1152/physrev.00020.2014
- Schneider, F., Gradmann, D., and Hegemann, P. (2013). Ion selectivity and competition in channelrhodopsins. *Biophys. J.* 105, 91–100. doi: 10.1016/j.bpj.2013.05.042
- Segal, M., and Korkotian, E. (2014). Endoplasmic reticulum calcium stores in dendritic spines. *Front. Neuroanat.* 8:64. doi: 10.3389/fnana.2014.00064
- Segal, M., and Korkotian, E. (2015). Roles of calcium stores and store-operated channels in plasticity of dendritic spines. *Neuroscientist* 22, 477–485. doi: 10.1177/1073858415613277
- Simpson, P. B., Challiss, R. A., and Nahorski, S. R. (1995). Neuronal Ca^{2+} stores: activation and function. *Trends Neurosci.* 18, 299–306. doi: 10.1016/0166-2236(95)93919-0
- Soboloff, J., Rothberg, B. S., Madesh, M., and Gill, D. L. (2012). STIM proteins: dynamic calcium signal transducers. *Nat. Rev. Mol. Cell Biol.* 13, 549–565. doi: 10.1038/nrm3414
- Villegas, R., Martinez, N. W., Lillo, J., Pihan, P., Hernandez, D., Twiss, J. L., et al. (2014). Calcium release from intra-axonal endoplasmic reticulum leads to axon degeneration through mitochondrial dysfunction. *J. Neurosci.* 34, 7179–7191. doi: 10.1523/JNEUROSCI.4784-13.2014
- Wen, L., Wang, H., Tanimoto, S., Egawa, R., Matsuzaka, Y., Mushiaka, H., et al. (2010). Opto-current-clamp actuation of cortical neurons using a strategically designed channelrhodopsin. *PLoS ONE* 5:e12893. doi: 10.1371/journal.pone.0012893
- Wood, J. N., Bevan, S. J., Coote, P. R., Dunn, P. M., Harmar, A., Hogan, P., et al. (1990). Novel cell lines display properties of nociceptive sensory neurons. *Proc. Biol. Sci.* 241, 187–194. doi: 10.1098/rspb.1990.0084
- Zhang, H., Sun, S., Wu, L., Pchitskaya, E., Zakharova, O., Fon Tacer, K., et al. (2016). Store-operated calcium channel complex in postsynaptic spines: a new therapeutic target for Alzheimer's disease treatment. *J. Neurosci.* 36, 11837–11850. doi: 10.1523/JNEUROSCI.1188-16.2016
- Zhao, Y., Araki, S., Wu, J., Teramoto, T., Chang, Y. F., Abdelfattah, A. S., et al. (2011). An expanded palette of genetically encoded Ca^{2+} indicators. *Science* 333, 1888–1891. doi: 10.1126/science.1208592

Conflict of Interest Statement: The authors declare that the research was conducted in the absence of any commercial or financial relationships that could be construed as a potential conflict of interest.

Copyright © 2018 Asano, Igarashi, Ishizuka and Yawo. This is an open-access article distributed under the terms of the Creative Commons Attribution License (CC BY). The use, distribution or reproduction in other forums is permitted, provided the original author(s) and the copyright owner(s) are credited and that the original publication in this journal is cited, in accordance with accepted academic practice. No use, distribution or reproduction is permitted which does not comply with these terms.

Advantages of publishing in Frontiers



OPEN ACCESS

Articles are free to read
for greatest visibility
and readership



FAST PUBLICATION

Around 90 days
from submission
to decision



HIGH QUALITY PEER-REVIEW

Rigorous, collaborative,
and constructive
peer-review



TRANSPARENT PEER-REVIEW

Editors and reviewers
acknowledged by name
on published articles

Frontiers

Avenue du Tribunal-Fédéral 34
1005 Lausanne | Switzerland

Visit us: www.frontiersin.org

Contact us: info@frontiersin.org | +41 21 510 17 00



REPRODUCIBILITY OF RESEARCH

Support open data
and methods to enhance
research reproducibility



DIGITAL PUBLISHING

Articles designed
for optimal readership
across devices



FOLLOW US

@frontiersin



IMPACT METRICS

Advanced article metrics
track visibility across
digital media



EXTENSIVE PROMOTION

Marketing
and promotion
of impactful research



LOOP RESEARCH NETWORK

Our network
increases your
article's readership